



저작자표시-비영리-변경금지 2.0 대한민국

이용자는 아래의 조건을 따르는 경우에 한하여 자유롭게

- 이 저작물을 복제, 배포, 전송, 전시, 공연 및 방송할 수 있습니다.

다음과 같은 조건을 따라야 합니다:



저작자표시. 귀하는 원저작자를 표시하여야 합니다.



비영리. 귀하는 이 저작물을 영리 목적으로 이용할 수 없습니다.



변경금지. 귀하는 이 저작물을 개작, 변형 또는 가공할 수 없습니다.

- 귀하는, 이 저작물의 재이용이나 배포의 경우, 이 저작물에 적용된 이용허락조건을 명확하게 나타내어야 합니다.
- 저작권자로부터 별도의 허가를 받으면 이러한 조건들은 적용되지 않습니다.

저작권법에 따른 이용자의 권리는 위의 내용에 의하여 영향을 받지 않습니다.

이것은 [이용허락규약\(Legal Code\)](#)을 이해하기 쉽게 요약한 것입니다.

[Disclaimer](#)

공학박사 학위논문

소듐이차전지용 저가 고용량 복합인  
산염계 양극 소재 연구

Design of cost-efficient mixed-phosphate  
cathode materials for Na rechargeable batteries

2016 년 2 월

서울대학교 대학원

재료공학부

김 형 섭

## **Abstract**

# **Design of cost-efficient mixed-phosphate cathode materials for Na rechargeable batteries**

Kim, Hyungsub

Department of Materials Science and Engineering

College of Engineering

Seoul National University

Recent global warming and the exhaustion of fossil fuel concerns have accelerated advancements to develop renewable energy sources. To cope with ever growing energy demand and supply sustainable energy in an efficient way, large-scale energy storage systems (ESSs) have become an important area of research in recent years. Among various candidates, Na-ion batteries (NIBs) are considered to be the optimal choice for these applications because of the availability and low cost of sodium, as well as the similar electrochemistry to the established Li-ion battery technology. In this respect, the search for new electrode materials for NIBs based

on low cost redox couples such as Fe or Mn has been intensively performed in recent years.

For better electrode materials for NIBs, my prime interest is in designing new mixed-phosphate compounds based on low cost transition metal redox couples such as  $\text{Fe}^{2+}/\text{Fe}^{3+}$  and  $\text{Mn}^{2+}/\text{Mn}^{3+}$ . In **Chapter 2**, a new iron-based mixed polyanion compound,  $\text{Na}_4\text{Fe}_3(\text{PO}_4)_2(\text{P}_2\text{O}_7)$ , for NIBs is introduced. Structural characterization of a newly synthesized mixed-polyanion compound with three-dimensional Na pathways was performed using combined X-ray and neutron diffraction studies. The electrode exhibited average potential  $\sim 3.2$  V (vs.  $\text{Na}^+/\text{Na}$ ) and energy density of  $320 \text{ Wh kg}^{-1}$ . Also, the reversible electrode operation was found from ion-exchanged sample of  $\text{Li}_3\text{NaFe}_3(\text{PO}_4)_2(\text{P}_2\text{O}_7)$  in Li-ion cells. The electrode delivers about 92 % of theoretical capacity ( $\sim 140 \text{ mAh g}^{-1}$ ) with an average voltage of 3.4 V (vs.  $\text{Li}^+/\text{Li}$ ). This research firstly suggested that a significant opportunity exists to explore new open-framework electrodes for NIBs with high electrochemical performances by combination of  $(\text{PO}_4)^{3-}$  and  $(\text{P}_2\text{O}_7)^{4-}$  polyanions.

In **Chapter 3**, I investigated the electrochemical mechanism of  $\text{Na}_x\text{Fe}_3(\text{PO}_4)_2(\text{P}_2\text{O}_7)$  ( $1 \leq x \leq 4$ ) in Na-ion cells using first principles calculations and experiments. I discovered that the de/sodiation of the  $\text{Na}_x\text{Fe}_3(\text{PO}_4)_2(\text{P}_2\text{O}_7)$  electrode occurs *via* one-phase reaction with a reversible  $\text{Fe}^{2+}/\text{Fe}^{3+}$  redox reaction. The electrode accompanies an exceptionally small volumetric change of less than 4% during electrochemical cycling, which is attributed to the open framework of polyanion compounds with flexible  $\text{P}_2\text{O}_7$  dimer in the structure. Although the

structural distortion in  $\text{NaFe}_3(\text{PO}_4)_2(\text{P}_2\text{O}_7)$  reduces Na de/intercalation kinetics at the last step of charge resulting in incomplete utilization of Na ( $\sim 82\%$  of theoretical capacity), high rate capability was confirmed with the negligible capacity reduction from C/20 to C/5. Also, stable cycle retention up to 20 cycles were confirmed. *In situ* X-ray diffraction (XRD) and differential scanning calorimetry (DSC) revealed that the partially charged electrodes,  $\text{Na}_x\text{Fe}_3(\text{PO}_4)_2(\text{P}_2\text{O}_7)$  ( $1 \leq x \leq 4$ ), are thermally stable up to  $530\text{ }^\circ\text{C}$ . The understanding of electrochemical mechanism of  $\text{Na}_x\text{Fe}_3(\text{PO}_4)_2(\text{P}_2\text{O}_7)$  ( $1 \leq x \leq 4$ ) shown here will give a direction to the optimization of the new  $\text{Na}_4\text{Fe}_3(\text{PO}_4)_2(\text{P}_2\text{O}_7)$  electrode for Na rechargeable batteries.

**Chapter 4** introduces a new 3.8 V-class manganese-based mixed-polyanion compound,  $\text{Na}_4\text{Mn}_3(\text{PO}_4)_2(\text{P}_2\text{O}_7)$ , for Na rechargeable batteries. The electrode shows a highly reversible electrochemical activities with a high  $\text{Mn}^{2+}/\text{Mn}^{3+}$  redox potential of  $3.84\text{ V}$  (vs.  $\text{Na}^+/\text{Na}$ ) and the largest energy density of  $416\text{ Wh kg}^{-1}$  yet reported for a manganese-based polyanion cathode. *Ex situ* XRD and X-ray absorption spectroscopy (XAS) studies revealed that the reversible multi-phase reaction occurs during electrochemical cycling. Although Jahn-Teller distortion of  $\text{Mn}^{3+}$  causes large volume change  $\sim 7\%$  upon charge reaction, the Na ion mobility is not decreased, rather it is increased. It is due to the unique Jahn-Teller distortion in the crystal structure, which opens up Na diffusion channels. This feature stabilize the electrode, providing high power capability and cycle stability in Na-

ion cells. I believe that this compound could be a new strong competitor for large scale NIBs based on its high voltage, large energy density and cycle stability.

Although the iron- and manganese-based electrode materials display promising electrochemical activities in Na-ion cells as shown from **Chapter 2-4**, the low energy density of  $\text{Na}_4\text{Fe}_3(\text{PO}_4)_2(\text{P}_2\text{O}_7)$  electrode and large volume change with multiple structural transitions in  $\text{Na}_4\text{Mn}_3(\text{PO}_4)_2(\text{P}_2\text{O}_7)$  electrode upon electrochemical cycling are still big challenges for its application to large-scale ESSs. In **Chapter 5**, I will introduce Fe- and Mn-based binary metal mixed-phosphate cathodes,  $\text{Na}_4\text{Mn}_x\text{Fe}_{3-x}(\text{PO}_4)_2(\text{P}_2\text{O}_7)$  ( $x = 1, 2$ ), which is successfully synthesized for the first time here. The electrochemical analysis of these binary mixed-phosphate materials shows that the substitution of Mn in the structure increases the energy density by utilizing  $\text{Mn}^{2+}/\text{Mn}^{3+}$  redox couples and upshifts the  $\text{Fe}^{2+}/\text{Fe}^{3+}$  redox potential in Na-ion cells. *Ex situ* structural investigation reveals that they operate *via* one-phase reaction upon charge and discharge processes with a remarkably low volume change of 2.07 % for  $\text{Na}_4\text{MnFe}_2(\text{PO}_4)_2(\text{P}_2\text{O}_7)$ , which is one of the lowest value among Na battery cathodes reported thus far. With a merit of open framework structure and low volume change, more than a half of the theoretical capacity is obtained at 20 C from both electrodes, and in the case of the  $\text{Na}_4\text{MnFe}_2(\text{PO}_4)_2(\text{P}_2\text{O}_7)$  electrode, it exhibits a stable cycle performances up to 3,000 cycles at 1C and room temperature. I believe that these materials can be a strong competitor for large-scale Na-ion battery cathodes based on their low costs, long-term cycle stability and high energy density.

**Keywords** : Energy storage, Na rechargeable battery, Cost-efficient electrode,  
Cathode materials, Mixed-phosphate,

**Student Number** : 2012-30917

# Table of Contents

<b>Abstract</b> .....	<b>i</b>
<b>Table of Contents</b> .....	<b>vi</b>
<b>List of Figures</b> .....	<b>x</b>
<b>List of Tables</b> .....	<b>xvii</b>
<b>Chapter 1. Introduction</b> .....	<b>1</b>
1.1 Research Background.....	1
1.2 References .....	5
<b>Chapter 2. New iron-Based Mixed-Phosphate Cathodes for Lithium and Sodium Rechargeable Batteries</b> .....	<b>9</b>
2.1 Introduction.....	9
2.2 Experimental.....	12
2.3 Results and Discussion .....	17
2.3.1 Synthesis and characterization of $\text{Na}_4\text{Fe}_3(\text{PO}_4)_2(\text{P}_2\text{O}_7)$ .....	17
2.3.2 Electrochemical properties of $\text{Na}_4\text{Fe}_3(\text{PO}_4)_2(\text{P}_2\text{O}_7)$ in Na-ion cells	27
2.3.3 Desodiation mechanism of $\text{Na}_{4-x}\text{Fe}_3(\text{PO}_4)_2(\text{P}_2\text{O}_7)$ .....	29
2.3.4 Electrochemical properties of $\text{Li}_3\text{NaFe}_3(\text{PO}_4)_2(\text{P}_2\text{O}_7)$ in Li-ion cells	
.....	38

2.4 Conclusion .....	42
2.5 References .....	43
<b>Chapter 3. Understanding the electrochemical mechanism of the new iron-based mixed-phosphate <math>\text{Na}_4\text{Fe}_3(\text{PO}_4)_2(\text{P}_2\text{O}_7)</math> in a Na rechargeable battery.....</b>	<b>47</b>
3.1 Introduction .....	47
3.2 Experimental .....	49
3.3 Results and Discussion .....	53
3.3.1 Synthesis and electrochemical properties of $\text{Na}_4\text{Fe}_3(\text{PO}_4)_2(\text{P}_2\text{O}_7)$ ..	53
3.3.2 Ex situ XRD studies on $\text{Na}_{4-x}\text{Fe}_3(\text{PO}_4)_2(\text{P}_2\text{O}_7)$ .....	57
3.3.3 Structural analyses of $\text{Na}_{4-x}\text{Fe}_3(\text{PO}_4)_2(\text{P}_2\text{O}_7)$ using first principles calculation .....	63
3.3.4 Neutron diffraction studies on $\text{NaFe}_3(\text{PO}_4)_2(\text{P}_2\text{O}_7)$ .....	70
3.3.5 XANES analyses of $\text{Na}_{4-x}\text{Fe}_3(\text{PO}_4)_2(\text{P}_2\text{O}_7)$ .....	76
3.3.6 Electrochemical mechanism studies using GITT and PITT .....	80
3.3.7 Phase diagram of $\text{Na}_{4-x}\text{Fe}_3(\text{PO}_4)_2(\text{P}_2\text{O}_7)$ .....	81
3.4 Conclusion .....	87
3.5 References .....	88

**Chapter 4. Anomalous Jahn-Teller behavior in manganese-based mixed-phosphate cathode for sodium ion batteries ..... 91**

4.1 Introduction .....	91
4.2 Experimental .....	95
4.3 Result and Discussion .....	101
4.3.1 Synthesis and characterization of $\text{Na}_4\text{Mn}_3(\text{PO}_4)_2(\text{P}_2\text{O}_7)$ .....	101
4.3.2 Electrochemical properties of $\text{Na}_4\text{Mn}_3(\text{PO}_4)_2(\text{P}_2\text{O}_7)$ .....	109
4.3.3 Structural evolution of the $\text{Na}_{4-x}\text{Mn}_3(\text{PO}_4)_2(\text{P}_2\text{O}_7)$ electrode during cycling ( $0 \leq x \leq 3$ ) .....	116
4.3.4 Local structural analyses of $\text{Na}_{4-x}\text{Mn}_3(\text{PO}_4)_2(\text{P}_2\text{O}_7)$ ( $0 \leq x \leq 3$ ) using <i>ex situ</i> XAS .....	122
4.3.5 DFT study on $\text{Na}_{4-x}\text{Mn}_3(\text{PO}_4)_2(\text{P}_2\text{O}_7)$ ( $0 \leq x \leq 3$ ) .....	125
4.4 Conclusion .....	147
4.5 References .....	148

**Chapter 5. Highly stable iron- and manganese-based cathodes for long-lasting sodium rechargeable batteries ..... 154**

5.1 Introduction .....	154
5.2 Experimental .....	158
5.3 Result and Discussion .....	161

5.3.1 Synthesis and structural characterization of $\text{Na}_4\text{Mn}_x\text{Fe}_{3-x}(\text{PO}_4)_2(\text{P}_2\text{O}_7)$ ( $x = 0, 1, 2, 3$ ) .....	161
5.3.2 Electrochemical investigation of $\text{Na}_4\text{Mn}_x\text{Fe}_{3-x}(\text{PO}_4)_2(\text{P}_2\text{O}_7)$ ( $x = 0, 1,$ 2, 3) electrodes .....	173
5.3.3 Electrochemical mechanism of $\text{Na}_4\text{Mn}_x\text{Fe}_{3-x}(\text{PO}_4)_2(\text{P}_2\text{O}_7)$ ( $x = 1, 2$ ) electrodes upon charge/discharge processes .....	180
5.3.4 Electrochemical properties of $\text{Na}_4\text{Mn}_x\text{Fe}_{3-x}(\text{PO}_4)_2(\text{P}_2\text{O}_7)$ ( $x = 1, 2$ ) electrodes at various conditions .....	186
5.4 Conclusion .....	192
5.5 References .....	193
<b>Chapter 6. Summary .....</b>	<b>197</b>
<b>Abstract in Korean .....</b>	<b>199</b>
<b>Curriculum Vitae .....</b>	오류! 책갈피가 정의되어 있지 않습니다.

## List of Figures

**Figure 2-1.** Thermogravimetric analysis and differential scanning calorimetry (TGA/DSC) of the precursor used for the solid-state synthesis of  $\text{Na}_4\text{Fe}_3(\text{PO}_4)_2(\text{P}_2\text{O}_7)$ .

**Figure 2-2.** (a) Schematic representation of  $\text{Na}_4\text{Fe}_3(\text{PO}_4)_2(\text{P}_2\text{O}_7)$ . (b) Rietveld refinement of the neutron diffraction patterns of  $\text{Na}_4\text{Fe}_3(\text{PO}_4)_2(\text{P}_2\text{O}_7)$ . The observed and calculated intensities are represented by the red markers and the black solid line, respectively. The bottom blue line represents the difference between the observed and calculated patterns. Bragg positions for  $\text{Na}_4\text{Fe}_3(\text{PO}_4)_2(\text{P}_2\text{O}_7)$  are represented as green markers, and the  $\text{NaFePO}_4$  ( $\sim 4\%$ ) impurity is shown as purple markers. (c) The 3D sodium diffusion paths in the  $\text{Na}_4\text{Fe}_3(\text{PO}_4)_2(\text{P}_2\text{O}_7)$  structure.

**Figure 2-3.** Detailed schematics of the Na channel along the  $b$ - $c$  plane and the diphosphate connection between the  $[\text{Fe}_3\text{P}_2\text{O}_{13}]_\infty$  layers are presented in (a). The sodium sites along the  $a$ - and  $b$ -axes in the structure of  $\text{Na}_4\text{Fe}_3(\text{PO}_4)_2(\text{P}_2\text{O}_7)$  are shown in (b) and (c), respectively. The four different Na sites in the structure of  $\text{Na}_4\text{Fe}_3(\text{PO}_4)_2(\text{P}_2\text{O}_7)$  are shown in (d).

**Figure 2-4.** *In-situ* high-temperature X-ray diffraction (XRD) patterns of  $\text{Na}_4\text{Fe}_3(\text{PO}_4)_2(\text{P}_2\text{O}_7)$  in the temperature range of 25–650°C under an Ar atmosphere. The  $\text{NaFePO}_4$  peaks start to significantly evolve above 550°C.

**Figure 2-5.** Calculated main diffusion motion along the  $b$ -axis as illustrated in (a) and (b). (c) The activation barrier of sodium from one Na1 site to another Na1 site.

**Figure 2-6.** (a) Galvanostatic charge/discharge profiles of  $\text{Na}_4\text{Fe}_3(\text{PO}_4)_2(\text{P}_2\text{O}_7)$  under a C/40 rate and the calculated average voltage at each region. The inset shows the  $dQ/dV$  curve of initial charge/discharge profiles. (b) Cycle performance of a Na cell under C/40 and C/20 rates.

**Figure 2-7.** XRD patterns of  $\text{Na}_x\text{Fe}_3(\text{PO}_4)_2(\text{P}_2\text{O}_7)$  ( $x = 1, 4$ ).

**Figure 2-8.** Mössbauer spectra of  $\text{Na}_x\text{Fe}_3(\text{PO}_4)_2(\text{P}_2\text{O}_7)$  ( $x = 1, 4$ ).

**Figure 2-9.** Integrated spin as a function of integration radius around Fe in  $\text{Na}_{4-x}\text{Fe}_3(\text{PO}_4)_2(\text{P}_2\text{O}_7)$  ( $x = 0, 3$ ).

**Figure 2-10.** TGA/DSC analysis of the desodiated phase of  $\text{NaFe}_3(\text{PO}_4)_2(\text{P}_2\text{O}_7)$ .

**Figure 2-11.** *In-situ* high-temperature XRD patterns of  $\text{NaFe}_3(\text{PO}_4)_2(\text{P}_2\text{O}_7)$  for a temperature range of 25–650°C under an Ar atmosphere.

**Figure 2-12.** (a) XRD patterns of  $\text{Li}_3\text{NaFe}_3(\text{PO}_4)_2(\text{P}_2\text{O}_7)$ . The reference sodium phase of  $\text{Na}_4\text{Fe}_3(\text{PO}_4)_2(\text{P}_2\text{O}_7)$  is represented below. (b) Calculated voltage and galvanostatic charge/discharge profiles of the Li cell under a C/20 rate at 298 K and calculated voltage profiles; (c) cyclability of the Li-ion cell under C/5 at 333 K. (d) The rate capability of  $\text{Li}_3\text{NaFe}_3(\text{PO}_4)_2(\text{P}_2\text{O}_7)$  in the Li-ion cell.

**Figure 3-1.** (a) Rietveld refinement of  $\text{Na}_4\text{Fe}_3(\text{PO}_4)_2(\text{P}_2\text{O}_7)$  using XRD. A schematic representation of  $\text{Na}_4\text{Fe}_3(\text{PO}_4)_2(\text{P}_2\text{O}_7)$  is illustrated in the inset. (b) Galvanostatic charge/discharge profiles of  $\text{Na}_4\text{Fe}_3(\text{PO}_4)_2(\text{P}_2\text{O}_7)$  in a Na-ion cell at the C/20 rate. The inset presents the cycle performance at various C-rates (C/20, C/10, and C/5).

**Figure 3-2.** (a) Scanning electron microscopy (SEM) and (b) transmission electron microscopy (TEM) images of  $\text{Na}_4\text{Fe}_3(\text{PO}_4)_2(\text{P}_2\text{O}_7)$  showing that the primary particle sizes are about 100 – 200 nm and that the crystallinity is good.

**Figure 3-3.** (a) *Ex situ* XRD patterns of  $\text{Na}_4\text{Fe}_3(\text{PO}_4)_2(\text{P}_2\text{O}_7)$  in a Na-ion cell during the charge/discharge process. Amplified XRD patterns in the  $2\theta$  range of 8 to 19° are illustrated in (b).

**Figure 3-4.** X-ray diffraction (XRD) patterns of  $\text{Na}_x\text{Fe}_3(\text{PO}_4)_2(\text{P}_2\text{O}_7)$  ( $1 \leq x \leq 4$ ) powder samples synthesized by chemical desodiation.

**Figure 3-5.** (a)  $a$ , (b)  $b$ , (c)  $c$  lattice parameters and (d) lattice volume change of  $\text{Na}_x\text{Fe}_3(\text{PO}_4)_2(\text{P}_2\text{O}_7)$  as a function of Na composition ( $x$ ).

**Figure 3-6.** (a)  $a$ , (b)  $b$ , (c)  $c$  lattice parameters, and (d) lattice volume change of  $\text{Na}_x\text{Fe}_3(\text{PO}_4)_2(\text{P}_2\text{O}_7)$  as a function of Na composition ( $x$ ). The black, blue, and red

rectangle markers represent the lattice parameters of *ex situ* electrode samples during the initial charge, discharge, and second charge, respectively.

**Figure 3-7.** DFT formation energies of  $\text{Na}_x\text{Fe}_3(\text{PO}_4)_2(\text{P}_2\text{O}_7)$  at various configurations of  $x$ .

**Figure 3-8.** (a) Local structure schematics of  $\text{Na}_x\text{Fe}_3(\text{PO}_4)_2(\text{P}_2\text{O}_7)$  around Fe sites and integrated spin as a function of integration radius around Fe in  $\text{Na}_x\text{Fe}_3(\text{PO}_4)_2(\text{P}_2\text{O}_7)$  ((b)  $x = 4$ , (c)  $x = 3$ , (d)  $x = 2$ , and (e)  $x = 1$ ).

**Figure 3-9.** Structure schematics of  $\text{Na}_x\text{Fe}_3(\text{PO}_4)_2(\text{P}_2\text{O}_7)$  at (a)  $x = 2$  and (b)  $x = 1$  from first principles calculations.

**Figure 3-10.** (a) Rietveld refinement of  $\text{NaFe}_3(\text{PO}_4)_2(\text{P}_2\text{O}_7)$  using ND. (b) Local structure schematics around Fe1 and P(3) – O – P(4) bond angle comparison table as a function of Na content ( $x$ ) in  $\text{Na}_x\text{Fe}_3(\text{PO}_4)_2(\text{P}_2\text{O}_7)$  from ND analysis.

**Figure 3-11.** XANES spectra during first (a) charge and (b) discharge. XANES spectra of the as-prepared state and of the end of charge and end of discharge states are shown in (c).

**Figure 3-12.** X-ray absorption near-edge structure (XANES) spectra of the  $\text{Na}_x\text{Fe}_3(\text{PO}_4)_2(\text{P}_2\text{O}_7)$  electrode during the second charge.

**Figure 3-13.** XANES spectra of chemically prepared  $\text{Na}_x\text{Fe}_3(\text{PO}_4)_2(\text{P}_2\text{O}_7)$  ( $1 \leq x \leq 4$ ) samples.

**Figure 3-14.** PITT measurements of  $\text{Na}_4\text{Fe}_3(\text{PO}_4)_2(\text{P}_2\text{O}_7)$  during (a) charging and (b) discharging.

**Figure 3-15.** Differential scanning calorimetry (DSC) spectra of  $\text{Na}_x\text{Fe}_3(\text{PO}_4)_2(\text{P}_2\text{O}_7)$  ( $1 \leq x \leq 4$ ).

**Figure 3-16.** *In situ* high-temperature XRD of desodiated powder samples of  $\text{Na}_x\text{Fe}_3(\text{PO}_4)_2(\text{P}_2\text{O}_7)$  at (a)  $x = 3.2$ , (b)  $x = 2.72$ , (c)  $x = 2.21$ , and (d)  $x = 1.71$ .

**Figure 3-17.** Phase diagram of  $\text{Na}_x\text{Fe}_3(\text{PO}_4)_2(\text{P}_2\text{O}_7)$  ( $1 < x < 4$ ).

**Figure 4-1.** Free energies of  $\text{Na}_4\text{Mn}_3(\text{PO}_4)_2\text{P}_2\text{O}_7$  with various magnetic configurations.

**Figure 4-2.** Rietveld refinement of (a) XRD and (b) ND patterns of  $\text{Na}_4\text{Mn}_3(\text{PO}_4)_2(\text{P}_2\text{O}_7)$ . The  $\text{NaMnPO}_4$  impurities are shown by the purple markers. (c) Schematic representation of  $\text{Na}_4\text{Mn}_3(\text{PO}_4)_2(\text{P}_2\text{O}_7)$  based on the ND analyses.

**Figure 4-3.** SEM images of (d) the as-synthesized and (e) carbon-coated  $\text{Na}_4\text{Mn}_3(\text{PO}_4)_2(\text{P}_2\text{O}_7)$ . (f) TEM image of the carbon-coated  $\text{Na}_4\text{Mn}_3(\text{PO}_4)_2(\text{P}_2\text{O}_7)$ .

**Figure 4-4.** (a) Charge/discharge profiles of  $\text{Na}_4\text{Mn}_3(\text{PO}_4)_2(\text{P}_2\text{O}_7)$  at a rate of C/20. Cycles at a rate of C/20 are shown in the inset. (b)  $dQ/dV$  plots for  $\text{Na}_4\text{Mn}_3(\text{PO}_4)_2(\text{P}_2\text{O}_7)$ .

**Figure 4-5.** The discharge profiles of  $\text{Na}_4\text{Mn}_3(\text{PO}_4)_2(\text{P}_2\text{O}_7)$  at various rates of C/20 to 20C at (c) 25°C and (d) 60°C.

**Figure 4-6.** A Ragone plot of  $\text{Na}_4\text{Mn}_3(\text{PO}_4)_2(\text{P}_2\text{O}_7)$  and other representative Fe- and Mn-based polyanion cathode materials for NIBs.<sup>15, 27, 28, 30, 45, 46</sup>

**Figure 4-7.** The cycle performance of  $\text{Na}_4\text{Mn}_3(\text{PO}_4)_2(\text{P}_2\text{O}_7)$  in Na-ion cells at (f) C/5 and 25°C, and (g) 1C and 60°C.

**Figure 4-8.** (a) Galvanostatic charge/discharge profiles of  $\text{Na}_4\text{Mn}_3(\text{PO}_4)_2(\text{P}_2\text{O}_7)$  at a rate of C/20. (b) *Ex situ* XRD patterns of  $\text{Na}_4\text{Mn}_3(\text{PO}_4)_2(\text{P}_2\text{O}_7)$  electrodes during charge/discharge in a Na-ion cell. Changes in the (c) *a*, (d) *b*, (e) *c* lattice parameters and (f) the lattice volume following charging and discharging.

**Figure 4-9.** Rietveld refinement of the XRD patterns of (c) fully charged and (d) discharged electrodes.

**Figure 4-10.** *Ex situ* XRD patterns of  $\text{Na}_{4-x}\text{Mn}_3(\text{PO}_4)_2(\text{P}_2\text{O}_7)$  during the second charge/discharge cycle. The black, red, blue and green dotted curves corresponds to the  $\alpha$ -,  $\beta$ -,  $\gamma$ - and  $\delta$ -phases, respectively.

**Figure 4-11.** The XANES spectra of *ex situ* electrode samples of  $\text{Na}_{4-x}\text{Mn}_3(\text{PO}_4)_2(\text{P}_2\text{O}_7)$  ( $0 \leq x \leq 3$ ) during (a) charge and (b) discharge. The EXAFS

spectra of *ex situ* electrode samples of  $\text{Na}_{4-x}\text{Mn}_3(\text{PO}_4)_2(\text{P}_2\text{O}_7)$  ( $0 \leq x \leq 3$ ) during (c) charge and (d) discharge.

**Figure 4-12.** XANES spectra of the *ex situ* electrode samples of  $\text{Na}_{4-x}\text{Mn}_3(\text{PO}_4)_2(\text{P}_2\text{O}_7)$  ( $0 \leq x \leq 3$ ) during (a) the second charging and (b) discharging. *Ex situ* EXAFS spectra of  $\text{Na}_{4-x}\text{Mn}_3(\text{PO}_4)_2(\text{P}_2\text{O}_7)$  ( $0 \leq x \leq 3$ ) electrode samples (c) during the second charging and (d) discharging.

**Figure 4-13.** (a) Formation energy plot of  $\text{Na}_{4-x}\text{Mn}_3(\text{PO}_4)_2(\text{P}_2\text{O}_7)$  ( $0 \leq x \leq 3$ ). (b) Lattice parameters of each phase in  $\text{Na}_{4-x}\text{Mn}_3(\text{PO}_4)_2(\text{P}_2\text{O}_7)$  ( $0 \leq x \leq 3$ ), both from the DFT calculations and the experiments. (c) Calculated structures of (left)  $\text{Na}_4\text{Mn}_3(\text{PO}_4)_2(\text{P}_2\text{O}_7)$ , (centre)  $\text{Na}_3\text{Mn}_3(\text{PO}_4)_2(\text{P}_2\text{O}_7)$  and (right)  $\text{NaMn}_3(\text{PO}_4)_2(\text{P}_2\text{O}_7)$ .

**Figure 4-14.** Spin integration of Mn ions in (a)  $\text{Na}_4\text{Mn}_3(\text{PO}_4)_2(\text{P}_2\text{O}_7)$ , (b)  $\text{Na}_3\text{Mn}_3(\text{PO}_4)_2(\text{P}_2\text{O}_7)$  and (c)  $\text{NaMn}_3(\text{PO}_4)_2(\text{P}_2\text{O}_7)$ .

**Figure 4-15.** Partial Density of States (pDOS) of (a)  $\text{Na}_4\text{Mn}_3(\text{PO}_4)_2(\text{P}_2\text{O}_7)$ , (b)  $\text{Na}_3\text{Mn}_3(\text{PO}_4)_2(\text{P}_2\text{O}_7)$  and (c)  $\text{NaMn}_3(\text{PO}_4)_2(\text{P}_2\text{O}_7)$ .

**Figure 4-16.** The magnified local structure of  $\text{Na}_{4-x}\text{Mn}_3(\text{PO}_4)_2(\text{P}_2\text{O}_7)$  ( $x = 0, 1, 3$ ). The bond lengths between Mn and O ions are listed in the table below.

**Figure 4-17.** The XRD patterns of  $\text{Na}_{4-x}\text{Mn}_3(\text{PO}_4)_2(\text{P}_2\text{O}_7)$  ((a)  $x = 0$ , (b)  $x = 3$ ) from experiments and DFT calculations.

**Figure 4-18.** Na diffusion pathways in (a)  $\text{Na}_4\text{Mn}_3(\text{PO}_4)_2(\text{P}_2\text{O}_7)$ , (b)  $\text{Na}_3\text{Mn}_3(\text{PO}_4)_2(\text{P}_2\text{O}_7)$  and (c)  $\text{NaMn}_3(\text{PO}_4)_2(\text{P}_2\text{O}_7)$ .

**Figure 4-19.** Bond distance change of (a)  $\Delta(\text{Me}-\text{O})$  and (b)  $\Delta(\text{P}-\text{O})$  in  $\text{Na}_4\text{Me}_3(\text{PO}_4)_2(\text{P}_2\text{O}_7)$  ( $\text{Me}=\text{Mn}, \text{Fe}$ ) after full charge.

**Figure 4-20.** Na diffusion pathways in  $\text{NaFe}_3(\text{PO}_4)_2(\text{P}_2\text{O}_7)$  with an activation energy below 500 meV.

**Figure 4-21.** Magnified diffusion pathways of Na ions from the Na1 to Na4 sites (shown by the black circles in Figure 4-18a and c) in (a)  $\text{Na}_4\text{Mn}_3(\text{PO}_4)_2(\text{P}_2\text{O}_7)$  and (b)  $\text{NaMn}_3(\text{PO}_4)_2(\text{P}_2\text{O}_7)$ .

**Figure 4-22.** Magnified diffusion pathways of Na ions from Na1 to Na4 site in (a)  $\text{Na}_4\text{Fe}_3(\text{PO}_4)_2(\text{P}_2\text{O}_7)$  and (b)  $\text{NaFe}_3(\text{PO}_4)_2(\text{P}_2\text{O}_7)$ .

**Figure 4-23.** Galvanostatic intermittent titration technique (GITT) profiles of  $\text{NaMn}_3(\text{PO}_4)_2(\text{P}_2\text{O}_7)$  and  $\text{Na}_4\text{Fe}_3(\text{PO}_4)_2(\text{P}_2\text{O}_7)$  in Na-ion cells.

**Figure 5-1.** a) XRD patterns and b) cell parameters of  $\text{Na}_4\text{Mn}_x\text{Fe}_{3-x}(\text{PO}_4)_2(\text{P}_2\text{O}_7)$  ( $x = 0, 1, 2, 3$ ). Rietveld refinement of ND patterns of  $\text{Na}_4\text{Mn}_x\text{Fe}_{3-x}(\text{PO}_4)_2(\text{P}_2\text{O}_7)$  (c)  $x = 1$ , d)  $x = 2$ ). Occupied Fe and Mn ions in three different transition metal sites with their fraction in color are described in the inset of ND patterns.

**Figure 5-2.** Rietveld refinement of the XRD patterns of  $\text{Na}_4\text{Mn}_x\text{Fe}_{3-x}(\text{PO}_4)_2(\text{P}_2\text{O}_7)$  (a)  $x = 0$ , b)  $x = 1$ , c)  $x = 2$ , d)  $x = 3$ ). The elemental composition from inductively coupled plasma (ICP) analyses and the cell parameters and reliability factors from Rietveld refinement are illustrated in the table.

**Figure 5-3.** XANES spectra at c) Fe and d) Mn k-edges of  $\text{Na}_4\text{Mn}_x\text{Fe}_{3-x}(\text{PO}_4)_2(\text{P}_2\text{O}_7)$  ( $x = 0, 1, 2, 3$ ). EXAFS spectra are shown in the inset.

**Figure 5-4.** Rietveld refinement of synchrotron XRD patterns of  $\text{Na}_4\text{Mn}_x\text{Fe}_{3-x}(\text{PO}_4)_2(\text{P}_2\text{O}_7)$  (a)  $x = 1$ , b)  $x = 2$ ). Structure schematics are presented in the inset of XRD patterns.

**Figure 5-5.** Simulated neutron diffraction (ND) patterns of  $\text{Na}_4\text{Mn}_x\text{Fe}_{3-x}(\text{PO}_4)_2(\text{P}_2\text{O}_7)$  (a-d)  $x = 1$ , (e-h)  $x = 2$ . Four different simulated models are presented at each composition ( $x = 1, 2$ ) with a different atomic distribution of Fe and Mn in three different transition metal sites.

**Figure 5-6.** Scanning electron microscopy (SEM) images of  $\text{Na}_4\text{Mn}_x\text{Fe}_{3-x}(\text{PO}_4)_2(\text{P}_2\text{O}_7)$  ((a)  $x = 0$ , (b)  $x = 1$ , (c)  $x = 2$ , (d)  $x = 3$ ).

**Figure 5-7.** Galvanostatic a) charge / b) discharge curves of  $\text{Na}_4\text{Mn}_x\text{Fe}_{3-x}(\text{PO}_4)_2(\text{P}_2\text{O}_7)$  ( $x = 0, 1, 2, 3$ ) at the C-rate of C/20. c) The magnified figure of discharge curves around  $\text{Fe}^{2+}/\text{Fe}^{3+}$  redox potentials. For the clear comparison of electrochemical profiles, we used the data from second charge/discharge reaction.

**Figure 5-8.** Energy densities of  $\text{Na}_4\text{Mn}_x\text{Fe}_{3-x}(\text{PO}_4)_2(\text{P}_2\text{O}_7)$  ( $x = 0, 1, 2, 3$ ) electrodes at the C-rate of C/20 at room temperature.

**Figure 5-9.** CV curves upon a) anodic and b) cathodic scans. c) The magnified figure of CV plot around 2.8 V upon cathodic scan.

**Figure 5-10.** Galvanostatic intermittent titration technique (GITT) profiles of  $\text{Na}_4\text{Mn}_x\text{Fe}_{3-x}(\text{PO}_4)_2(\text{P}_2\text{O}_7)$  ( $x = 1, 2$ ) at the C-rate of C/50 with 4h relaxation times.

**Figure 5-11.** *Ex situ* XRD patterns of  $\text{Na}_4\text{Mn}_x\text{Fe}_{3-x}(\text{PO}_4)_2(\text{P}_2\text{O}_7)$  (a)  $x = 1$ , b)  $x = 2$ ) during electrochemical charge/discharge reactions in Na-ion cells. c) Lattice parameter and cell volume changes upon charge/discharge reactions in Na-ion cells. d) Comparison of volume changes on charging in various Fe- and Mn-based cathodes for Na-ion batteries. e) The Fe and Mn k-edge XANES spectra of  $\text{Na}_4\text{Mn}_x\text{Fe}_{3-x}(\text{PO}_4)_2(\text{P}_2\text{O}_7)$  ( $x = 1, 2$ ) upon charge reactions in Na-ion cells.

**Figure 5-12.** *Ex situ* XRD patterns of  $\text{Na}_4\text{Mn}_x\text{Fe}_{3-x}(\text{PO}_4)_2(\text{P}_2\text{O}_7)$  (a)  $x = 1$ , b)  $x = 2$ ) during charge/discharge reactions in Na-ion cells.

**Figure 5-13.** X-ray absorption near edge structure (XANES) spectra near to Fe and Mn k-edges of  $\text{Na}_{4-y}\text{Mn}_x\text{Fe}_{3-x}(\text{PO}_4)_2(\text{P}_2\text{O}_7)$  ( $x = 1, 2$ ;  $0 \leq y \leq 3$ ) upon discharge reaction.

**Figure 5-14.** Galvanostatic discharge profiles of  $\text{Na}_4\text{Mn}_x\text{Fe}_{3-x}(\text{PO}_4)_2(\text{P}_2\text{O}_7)$  (a)  $x = 1$ , b)  $x = 2$ ) at different C-rates (C/20, C/10, C/5, 1C, 2C, 5C, 10C and 20C). The charge was conducted at a current rate of C/20.

**Figure 5-15.** A Ragone plot of  $\text{Na}_4\text{Mn}_x\text{Fe}_{3-x}(\text{PO}_4)_2(\text{P}_2\text{O}_7)$  and other representative Fe- and Mn-based polyanion cathode materials for NIBs. <sup>15,17,22,25,29,36-37</sup>

**Figure 5-16.** Galvanostatic discharge profiles of  $\text{Na}_4\text{Mn}_x\text{Fe}_{3-x}(\text{PO}_4)_2(\text{P}_2\text{O}_7)$  (a)  $x = 1$ , b)  $x = 2$ ) at different C-rates (C/20, C/10, C/5, 1C, 2C, 5C, 10C and 20C) in 60°C cell. The charge was conducted at a current rate of C/20.

**Figure 5-17.** a) The cycle performances of  $\text{Na}_4\text{Mn}_x\text{Fe}_{3-x}(\text{PO}_4)_2(\text{P}_2\text{O}_7)$  ( $x = 1, 2$ ) at C/20 and 25 °C. b) The cycle performance of  $\text{Na}_4\text{MnFe}_2(\text{PO}_4)_2(\text{P}_2\text{O}_7)$  at 1C and

25 °C. c) The cycle performance of  $\text{Na}_4\text{Mn}_x\text{Fe}_{3-x}(\text{PO}_4)_2(\text{P}_2\text{O}_7)$  ( $x = 1, 2$ ) at C/20 and 60 °C.

## List of Tables

**Table 2-1.** The detailed data for the structural refinement of  $\text{Na}_4\text{Fe}_3(\text{PO}_4)_2(\text{P}_2\text{O}_7)$  using ND patterns.

**Table 2-2.** Sodium vacancy activation barriers in the  $\text{Na}_4\text{Fe}_3(\text{PO}_4)_2(\text{P}_2\text{O}_7)$  structure.

**Table 2-3.** Lattice parameters of  $\text{Na}_x\text{Fe}_3(\text{PO}_4)_2(\text{P}_2\text{O}_7)$  ( $x = 4, 1$ ).

**Table 2-4.** Quadruple splitting, isomer shift values, and the ratio of each iron site in  $\text{Na}_x\text{Fe}_3(\text{PO}_4)_2(\text{P}_2\text{O}_7)$  ( $x = 4, 1$ ).

**Table 2-5.** Volumetric energy density of iron-based polyanion compounds.

**Table 3-1.** Schematic representations of  $\text{Na}_4\text{Fe}_3(\text{PO}_4)_2(\text{P}_2\text{O}_7)$  and order of sodium extraction from the structure of  $\text{Na}_x\text{Fe}_3(\text{PO}_4)_2(\text{P}_2\text{O}_7)$  ( $1 \leq x \leq 4$ ).

**Table 3-2.** Detailed structural information of  $\text{NaFe}_3(\text{PO}_4)_2(\text{P}_2\text{O}_7)$  analyzed by Rietveld refinement of the ND pattern.

**Table 3-3.** Bond valence parameters of each atom in  $\text{Na}_x\text{Fe}_3(\text{PO}_4)_2(\text{P}_2\text{O}_7)$  ( $x = 1, 4$ ).

**Table 4-1.** The structural data on  $\text{Na}_4\text{Mn}_3(\text{PO}_4)_2(\text{P}_2\text{O}_7)$  analyzed using Rietveld refinement of the XRD and ND patterns. Details of the measurement conditions, lattice parameters, reliability factors, atomic positions and bond valence data are also listed.

**Table 4-2.** Desodiation sequence and Mn oxidation states upon charging of  $\text{Na}_{4-x}\text{Mn}_3(\text{PO}_4)_2(\text{P}_2\text{O}_7)$  ( $0 \leq x \leq 3$ ) based on the DFT calculations.

**Table 4-3.** Bader charge analysis on  $\text{Na}_4\text{Mn}_3(\text{PO}_4)_2(\text{P}_2\text{O}_7)$  upon desodiation.

**Table 4-4.** The calculated activation barriers for Na diffusion in  $\text{Na}_{4-x}\text{Mn}_3(\text{PO}_4)_2(\text{P}_2\text{O}_7)$ . ( $x = 0, 1, 3$ )

**Table 4-5.** The calculated activation barriers for Na diffusion in  $\text{Na}_{4-x}\text{Fe}_3(\text{PO}_4)_2(\text{P}_2\text{O}_7)$ . ( $x = 0, 3$ )

**Table 4-6.** Distance from diffusing Na ions in the intermediate state to adjacent Mn ions and O ions.

**Table 5-1.** Fe and Mn occupancies in three different transition metal sites (TM1, 2 and TM3 sites).

**Table 5-2.** The detailed structural information of  $\text{Na}_4\text{Mn}_x\text{Fe}_{3-x}(\text{PO}_4)_2(\text{P}_2\text{O}_7)$  ( $x = 1, 2$ ). The measurement conditions and atomic information from Rietveld refinements are presented.

**Table 5-3.** TM-O bond lengths in  $\text{Na}_4\text{Mn}_x\text{Fe}_{3-x}(\text{PO}_4)_2(\text{P}_2\text{O}_7)$  ( $x = 0, 1, 2, 3$ ).

# Chapter 1. Introduction

## 1.1 Research Background

Recent global warming and the exhaustion of fossil fuel concerns have accelerated advancements to develop sustainable energy sources such as solar, wind, hydro and geothermal power. In this respect, storing the energy in large-scale energy storage system (ESS) has become a critical issue in 21st century to cope with the uneven energy generation and demands.<sup>1</sup> Although Li-ion battery (LIB) has been a great success in small and mid-sized portable devices, and recent advances in battery system introduced numerous promising candidates for large-scale EES such as Li air and sulfur batteries, the cost issues arising from the use of costly transition metals such as Ni and Co and the political issues related to the uneven global distribution of Li around world are still great challenges.<sup>2-4</sup> Considering that the low cost is the most critical factor for large-scale ESSs, Na-ion battery (NIB) can be the most appealing alternative to LIB because of the unlimited Na resources and similar electrochemistry to LIB.<sup>5-7</sup> Furthermore, the electrodes composed of Na guest ion and redox couples based on low cost transition metals such as Fe or Mn would be an optimal design for large scale ESSs. However, only a limited number of such materials have been reported to date.<sup>5-7</sup>

Recent studies have introduced a few important types of potential electrode materials such as layered oxides, Prussian blue analogues and transition metal-free organic electrodes.<sup>5-7</sup> Komaba et al. reported Fe- and Mn-based P2-type layered

oxide,  $\text{Na}_x[\text{Fe}_{1/2}\text{Mn}_{1/2}]\text{O}_2$ , with an high energy density of  $520 \text{ Wh kg}^{-1}$ . And following researches introduced numerous O3- and P2-type layered oxide electrodes.<sup>8-11</sup> Although these layered-type materials possess clear potential merits such as high capacity and energy density, the large volume change ( $>10\%$ ) during electrochemical cycling and the phase instability of the desodiated structure are among the largest obstacles.<sup>12-13</sup> Also, general O3- and P2-type sodium layered oxides are very hygroscopic, therefore they exhibit irreversible phase transformation in the air at room temperature.<sup>14</sup> Prussian blue analogues (PBAs) and organic compounds have also been intensively studied with a merit of low element cost, easy synthesis and high energy density.<sup>15-21</sup> Recently reported Fe- and Mn-based Prussian blue analogue by J. Song et al. showed that  $\text{Na}_2\text{MnFe}(\text{CN})_6$  delivers a high capacity of  $150 \text{ mAh g}^{-1}$  with a voltage of  $3.5 \text{ V}$ .<sup>22</sup> Also, H. W. Lee et al. reported that  $\text{Na}_2\text{Mn}_2(\text{CN})_6$  electrode shows the promising electrochemical properties with high capacity of  $209 \text{ mAh g}^{-1}$  in Na-ion cells.<sup>23</sup> While these materials display promising electrochemical properties in Na-ion cells, the dissolution issues in the electrolyte and the absence of Na ions in the electrode are still challenging to address.

The polyanion-based compounds have been extensively studied as an important group of potential electrode materials due to their structural stability and chemical diversity.<sup>24</sup> The general structure based on the polyanions provides the structural stability due to the strong X-O ( $X = \text{P, S, B, Si}$ ) covalent bonding in the structure, and the open rigid framework is beneficial for a small volume change upon

electrochemical cycling with a fast ionic mobility compared common layered materials. Moreover, its diversity in chemistry in terms of polyanion species, transition metals and the crystal structure offers many opportunities to find new electrode materials with high-performance and low-cost. To date, the search for cost efficient polyanion electrodes has focused on the phosphate-, pyrophosphate-, fluorophosphates-, fluorosulfate- and sulfate-based materials, including  $\text{NaFe}_x\text{Mn}_{1-x}\text{PO}_4$ ,  $\text{Na}_2\text{FeP}_2\text{O}_7$ ,  $\text{Na}_2\text{MnP}_2\text{O}_7$ ,  $\text{Na}_{4-x}\text{Fe}_{2+x/2}(\text{P}_2\text{O}_7)_2$ ,  $\text{Na}_2\text{FePO}_4\text{F}$ ,  $\text{Na}_2\text{MnPO}_4\text{F}$ ,  $\text{NaFeSO}_4\text{F}$ ,  $\text{Na}_2\text{Fe}(\text{SO}_4)_2 \cdot 2\text{H}_2\text{O}$  and  $\text{Na}_2\text{Fe}_2(\text{SO}_4)_3$ .<sup>25-34</sup> However, there are a number of challenges to be addressed; the iron-based cathodes suffered from low voltage below 3.0 V, and the manganese-based cathodes exhibit poor electrochemical performances, which is attributed to Jahn-Teller distortion ( $\text{Mn}^{3+}$ ) in the structure during battery cycling.

In the search for new rich chemistry in Na-containing polyanion compounds, there has been another state of the art approach which combines two different polyanions in the structure, namely, a mixed-polyanion system. This system was firstly examined by pioneering work of A. K. Pahdi *et al.*, and they showed that the combination between two different  $\text{Li}_3\text{Fe}_2(\text{PO}_4)_3$  and  $\text{Fe}_2(\text{PO}_4)_3$  phases produces new electrode material of  $\text{LiFe}_2(\text{SO}_4)_2(\text{PO}_4)$ .<sup>35</sup> Also, theoretical studies predicted that the combination of  $\text{XO}_3^{2 \text{ or } 3-}$  and  $\text{YO}_4^{3 \text{ or } 4-}$  ( $\text{X} = \text{C}, \text{B}; \text{Y} = \text{Si}, \text{As}, \text{P}$ ) could give a series of new  $\text{A}_z\text{Me}(\text{XO}_3)(\text{YO}_4)$  compounds ( $\text{A} = \text{Li}$  or  $\text{Na}$ ;  $\text{Me} =$  a transition metal; and  $z = 0-3$ ) which is suitable for cathode materials.<sup>36-37</sup> Recent experimental synthesis of new mixed-polyanion compounds,  $\text{Na}_7\text{V}_4(\text{P}_2\text{O}_7)_4\text{PO}_4$  and

$\text{Na}_3\text{MnPO}_4\text{CO}_3$ , showed that variety of combinations may lead to the discovery of a new open crystal framework with promising electrochemical properties.<sup>38-39</sup>

For better electrode materials for NIBs, my main objective of thesis study was to design a new mixed-polyanion compounds based on  $(\text{PO}_4)^{3-}$  and  $(\text{P}_2\text{O}_7)^{4-}$  as well as low cost transition metal redox couples such as  $\text{Fe}^{2+}/\text{Fe}^{3+}$  and  $\text{Mn}^{2+}/\text{Mn}^{3+}$ . The known mixed polyanion closest to my objective was  $\text{Na}_4\text{Me}_3(\text{PO}_4)_2(\text{P}_2\text{O}_7)$  (Me = a transition metal).<sup>40-41</sup> I designed and synthesized a new iron-based mixed-polyanion compound,  $\text{Na}_4\text{Fe}_3(\text{PO}_4)_2(\text{P}_2\text{O}_7)$ , for the first time using first principles calculation and experiments.<sup>42-43</sup> Also, the unique Jahn-Teller distortion of  $\text{Mn}^{3+}$  in a new 3.8 V-class manganese-based mixed-polyanion compound,  $\text{Na}_4\text{Mn}_3(\text{PO}_4)_2(\text{P}_2\text{O}_7)$ , was confirmed.<sup>44</sup> Finally, highly reversible electrode of  $\text{Na}_4\text{Mn}_x\text{Fe}_{3-x}(\text{PO}_4)_2(\text{P}_2\text{O}_7)$  ( $x = 1, 2$ ) with an extremely low volume change ( $\sim 2\%$ ) was introduced. I believe that the combination of high energy density, long-term cycle stability and low element cost of Fe and Mn makes the  $\text{Na}_4\text{Me}_3(\text{PO}_4)_2(\text{P}_2\text{O}_7)$  (Me = Fe or Mn) electrode as a strong competitor for large-scale Na-ion battery cathodes.

## 1.2 References

- (1) H. Chen, T. N. Cong, W. Yang, C. Tan, Y. Li, Y. Ding *Prog. Natural Sci.* **2009**, *19*, 291.
- (2) J. -M. Tarascon, M. Armand, *Nature* **2001**, *414*, 359–367.
- (3) M. Armand, J. -M. Tarascon, *Nature* **2008**, *451*, 652–657.
- (4) J.-M. Tarascon, *Nat. Chem.* **2010**, *2*, 510-510.
- (5) S.-W. Kim, D.-H. Seo, X. Ma, G. Ceder, K. Kang, *Adv. Energy Mater.* **2012**, *2*, 710-721.
- (6) H. Pan, Y.-S. Hu, L. Chen, *Energy Environ. Sci.* **2013**, *6*, 2338-2360.
- (7) D. Kundu, E. Talaie, V. Duffort, L. F. Nazar, *Angew. Chem. Int. Ed.* **2015**, *54*, 3431-3448.
- (8) N. Yabuuchi, M. Kajiyama, J. Iwatate, H. Nishikawa, S. Hitomi, R. Okuyama, R. Usui, Y. Yamada and S. Komaba, *Nat. Mater.*, **2012**, *11*, 512-517.
- (9) B. Mortemard de Boisse, D. Carlier, M. Guignard, C. Delmas, *J. Electrochem. Soc.* **2013**, *150*, A569-A574.
- (10) D. Kim, E. Lee, M. Slater, W. Lu, S. Rood, C. S. Johnson, *Electrochem. Commun.* **2012**, *18*, 66-69.
- (11) S. -M. Oh, S. -T. Myung, C. S. Yoon, J. Lu, J. Hassoun, B. Scrosati, K. Amine, Y. -K. Sun, *Nano Lett.* **2014**, *14*, 1620-1626.
- (12) R. Berthelot, D. Carlier and C. Delmas, *Nat. Mater.*, **2011**, *10*, 74-80.

- (13) S. Komaba, N. Yabuuchi, T. Nakayama, A. Ogata, T. Ishikawa and I. Nakai, *Inorg. Chem.*, **2012**, *51*, 6211-6220.
- (14) V. Duffort, E. Talaie, R. Black, and L.F. Nazar, *Chem. Mater.* **2015**, *27*, 2515-2524.
- (15) H. Chen, M. Armand, G. Demailly, F. Dolhem, P. Poizot, J.-M. Tarascon, *ChemSusChem* **2008**, *1*, 348-355.
- (16) Y. Liang, Z. Tao, J. Chen, *Adv. Energy Mater.* **2012**, *2*, 742-769.
- (17) M. Lee, J. Hong, H. Kim, H.-D. Lim, S. B. Cho, K. Kang, C. B. Park, *Adv. Mater.* **2014**, *26*, 2558-2565.
- (18) Y. You, X. Yu, Y. Yin, K.-W. Nam, Y.-G. Guo, *Nano Res.* **2015**, *8*, 117-128.
- (19) M. Pasta, C. D. Wessells, N. Liu, J. Nelson, M. T. McDowell, R. A. Huggins, M. F. Toney, Y. Cui, *Nat. Commun.* **2014**, *5*.
- (20) Y. You, X.-L. Wu, Y.-X. Yin, Y.-G. Guo, *Energy Environ. Sci.* **2014**, *7*, 1643-1647.
- (21) Y. Lu, L. Wang, J. Cheng, J. B. Goodenough, *Chem. Commun.* **2012**, *48*, 6544-6546.
- (22) J. Song, L. Wang, Y. Lu, J. Liu, B. Guo, P. Xiao, J. -J. Lee, X. -Q. Yang, G. Henkelman, J. B. Goodenough, *J. Am. Chem. Soc.* **2015**, *137*, 2658-2664.
- (23) H. -W. Lee, R. Y. Wang, M. Pasta<sup>1</sup>, S. W. Lee, N. Liu, Y. Cui, *Nat. Commun.* **2014**, *5*, 5280.
- (24) C. Masquelier and L. Croguennec, *Chem. Rev.* **2013**, *113*, 6552-6591.

- (25) K. T. Lee, T. N. Ramesh, F. Nan, G. Botton, L. F. Nazar, *Chem. Mater.* **2011**, *23*, 3593-3600.
- (26) J. Kim, H. Kim, I. Park, Y.-U. Park, J.-K. Yoo, K.-Y. Park, S. Lee, K. Kang, *Energy Environ. Sci.* **2013**, *6*, 830-834.
- (27) P. Barpanda, T. Ye, S.-i. Nishimura, S.-C. Chung, Y. Yamada, M. Okubo, H. Zhou, A. Yamada, *Electrochem. Commun.* **2012**, *24*, 116-119.
- (28) C. S. Park, H. Kim, R. A. Shakoor, E. Yang, S. Y. Lim, R. Kahraman, Y. Jung, J. W. Choi, *J. Am. Chem. Soc.* **2013**, *135*, 2787-2792.
- (29) K.-H. Ha, S. H. Woo, D. Mok, N.-S. Choi, Y. Park, S. M. Oh, Y. Kim, J. Kim, J. Lee, L. F. Nazar and K. T. Lee, *Adv. Energy Mater.*, **2013**, *3*, 689-689.
- (30) B. L. Ellis, W. R. M. Makahnouk, Y. Makimura, K. Toghill, L. F. Nazar, *Nat. Mater.* **2007**, *6*, 749-753.
- (31) S.-W. Kim, D.-H. Seo, H. Kim, K.-Y. Park, K. Kang, *Phys. Chem. Chem. Phys.* **2012**, *14*, 3299-3303.
- (32) P. Barpanda, G. Liu, Z. Mohamed, C. D. Ling, A. Yamada, *Solid State Ionics* **2014**, *268*, Part B, 305-311.
- (33) P. Barpanda, G. Oyama, C. D. Ling, A. Yamada, *Chem. Mater.* **2014**, *26*, 1297-1299.
- (34) P. Barpanda, G. Oyama, S.-i. Nishimura, S.-C. Chung, A. Yamada, *Nat. Commun.* **2014**, *5*.

- (35) A. K. Padhi, V. Manivannan, J. B. Goodenough, *J. Electrochem. Soc.* **1998**, *145*, 1518-1520.
- (36) G. Hautier, A. Jain, H. Chen, C. Moore, S. P. Ong, G. Ceder, *J. Mater. Chem.* **2011**, *21* (43), 17147–17153.
- (37) A. Jain, G. Hautier, C. Moore, B. Kang, J. Lee, H. Chen, N. Twu, G. Ceder, *J. Electrochem. Soc.* **2012**, *159* (5), 622–633.
- (38) S. Y. Lim, H. Kim, J. Chung, J. H. Lee, B. G. Kim, J.-J. Choi, K. Y. Chung, W. Cho, S.-J. Kim, W. A. Goddard, Y. Jung and J. W. Choi, *Proc. Nat. Acad. Sci. U. S. A.*, **2013**, *111*, 599-604.
- (39) H. Chen, Q. Hao, O. Zivkovic, G. Hautier, L.-S. Du, Y. Tang, Y.-Y. Hu, X. Ma, C. P. Grey, G. Ceder, *Chem. Mater.* **2013**, *25*, 2777-2786.
- (40) F. Sanz, C. Parada, J. Rojo, C. Ruiz-Valero, *Chem. Mater.* **2001**, *13* (4), 1334–1340.
- (41) R. Essehli, E. B. Bali, S. Benmokhtar, H. Fuess, I. Svoboda, S. Obbade, *J. Alloys Compd.* **2010**, *493* (1), 654–660.
- (42) H. Kim, I. Park, D.-H. Seo, S. Lee, S.-W. Kim, W. J. Kwon, Y.-U. Park, C. S. Kim, S. Jeon, K. Kang, *J. Am. Chem. Soc.* **2012**, *134*, 10369-10372.
- (43) H. Kim, I. Park, S. Lee, H. Kim, K.-Y. Park, Y.-U. Park, H. Kim, J. Kim, H.-D. Lim, W.-S. Yoon, K. Kang, *Chem. Mater.* **2013**, *25*, 3614-3622.
- (44) H. Kim, G. Yoon, I. Park, K.-Y. Park, B. Lee, J. Kim, Y.-U. Park, S.-K. Jung, H.-D. Lim, D. Ahn, S. Lee, K. Kang, *Energy Environ. Sci.* **2015**, *8*, 3325-3335.

## **Chapter 2. New iron-Based Mixed-Phosphate Cathodes for Lithium and Sodium Rechargeable Batteries**

(The content of this chapter has been published in *Journal of the American Chemical Society*. Reprinted with permission from [H. Kim et al., *J. Am. Chem. Soc.* **2012**, *134* (25), 10369-10372.]. Copyright (2012) American Chemical Society.)

### **2.1 Introduction**

An integral part of the new energy economy is to provide cost-effective, sustainable energy storage. Chemical energy storage in the form of batteries, in particular, the most advanced lithium-ion batteries, will contribute strongly to the energy storage picture. However, the cost-effectiveness per energy and the safety hazards regarding lithium-ion batteries have so far prohibited their widespread use in large-scale applications.

In this respect, the search for new polyanion compounds using iron as a redox center is of timely significance. Using naturally abundant iron as a full redox couple, combined with stabilization of the oxygen atoms within the crystal via the strong covalent bonds of the polyanion,<sup>1</sup> may significantly reduce the energy costs and safety concerns. This has led to the use of olivine lithium iron phosphate,  $\text{LiFePO}_4$ , as a popular cathode material for lithium-ion batteries.<sup>2,3</sup> Recent studies on polyanion materials using the  $\text{Fe}^{2+}/\text{Fe}^{3+}$  redox couple have identified new

compounds, such as fluorinated iron phosphate ( $\text{Li}_2\text{FePO}_4\text{F}$ ),<sup>4</sup> iron pyrophosphate ( $\text{Li}_2\text{FeP}_2\text{O}_7$ ),<sup>1,5</sup> fluorinated iron sulfate ( $\text{LiFeSO}_4\text{F}$ ),<sup>6,7</sup> iron silicate ( $\text{Li}_2\text{FeSiO}_4$ ),<sup>8</sup> and iron borate ( $\text{LiFeBO}_3$ ),<sup>9,10</sup> as alternatives. However, the synthesis of fluorinated compounds requires complex and costly procedures, and their theoretical capacities are hardly obtainable. Moreover, some of the fluorinated compounds such as  $\text{Li}_2\text{FePO}_4\text{F}$  are moisture sensitive, while the most moisture stable phase is  $\text{LiFePO}_4\text{F}$ .<sup>11,12</sup> Lithium iron silicates and iron borates are unable to provide sufficient voltage, and the specific capacity of  $\text{Li}_2\text{FeP}_2\text{O}_7$  is less than  $110 \text{ mAh g}^{-1}$ .

In the search for new iron-based lithium-containing cathode materials, our prime interest is in mixed-polyanion systems, which were examined by pioneering work of Goodenough et al.<sup>13,14</sup> Recently, mixed-polyanion compounds are refocused, and theoretical work predicted that the combination of  $\text{YO}_3^{2 \text{ or } 3-}$  and  $\text{XO}_4^{3 \text{ or } 4-}$  ( $Y = \text{C, B}$ ;  $X = \text{Si, As, P}$ ) could give a series of new  $\text{A}_x\text{M}(\text{YO}_3)(\text{XO}_4)$  compounds ( $A = \text{Li, Na}$ ;  $M = \text{a redox transition metal}$ ; and  $x = 0-3$ ) suitable for cathode materials.<sup>15,16</sup> The experimental synthesis of the mixed phosphate,  $\text{Li}_9\text{V}_3(\text{P}_2\text{O}_7)_3(\text{PO}_4)_2$ , with the vanadium  $\text{V}^{3+}/\text{V}^{5+}$  redox couple, showed promising electrochemical properties.<sup>17,18</sup> We believe that the variety of combinations among different polyanion groups may lead to the discovery of a new open crystal framework containing both lithium and iron.

One of our main objectives of this study was to synthesize materials based on the mixed polyanion groups of  $(\text{PO}_4)^{3-}$  and  $(\text{P}_2\text{O}_7)^{4-}$  with the  $\text{Fe}^{2+}/\text{Fe}^{3+}$  redox couple. Currently, the known mixed phosphate that is closest to our aim is

$\text{Na}_4\text{Me}_3(\text{PO}_4)_2(\text{P}_2\text{O}_7)$  (Me = Mn, Co, Ni, Mg).<sup>19,20</sup> However, to the best of our knowledge, an iron analogue with this composition has been neither synthesized nor documented in the materials database. It was expected that such an unreported compound would not be stable under conventional synthesis conditions, and may, therefore, require a special synthesis route. However, contrary to expectations,  $\text{Na}_4\text{Fe}_3(\text{PO}_4)_2(\text{P}_2\text{O}_7)$  was easily obtained using a simple solid-state method. Furthermore, from the first principles calculations, we found  $\text{Na}_4\text{Fe}_3(\text{PO}_4)_2(\text{P}_2\text{O}_7)$  to be a promising candidate for cathode materials in terms of its voltage and the mobility of alkali cations for Na-ion batteries. Finally, we showed that sodium could be topotactically ion-exchanged with lithium to produce a new lithium compound that inherited the good electrochemical properties of the parent sodium phase for lithium-ion batteries.

## 2.2 Experimental

**Synthesis of  $\text{Na}_4\text{Fe}_3(\text{PO}_4)_2(\text{P}_2\text{O}_7)$ :**  $\text{Na}_4\text{Fe}_3(\text{PO}_4)_2(\text{P}_2\text{O}_7)$  was synthesized using a simple solid-state method. Stoichiometric amounts of  $\text{Na}_4\text{P}_2\text{O}_7$  (95%, Aldrich),  $\text{Fe}_2\text{C}_2\text{O}_4 \cdot 2\text{H}_2\text{O}$  (99%, Aldrich), and  $\text{NH}_4\text{H}_2\text{PO}_4$  (98% ACS reagent, Aldrich) were used as the starting materials. These precursors were mixed by ball-milling with acetone for 24 h and then evaporating the acetone at 70°C for 12 h. The homogeneous mixed powder was fired at 300°C under flowing Ar for 6 h. The calcined powder was pelletized manually under 200 kg cm<sup>-2</sup> pressure using a disk-shaped mold. This sample was then heated again at 500°C for 12 h. For the electrode composite, pyromellitic acid (PA) ( $\text{C}_{10}\text{H}_6\text{O}_2$ , 96%, Alfa Aesar) was added during the ball-milling step to enhance the electrochemical properties (weight ratio of the active material: PA = 95:5).

**Synthesis of  $\text{NaFe}_3(\text{PO}_4)_2(\text{P}_2\text{O}_7)$ :** An oxidized sample of  $\text{NaFe}_3(\text{PO}_4)_2(\text{P}_2\text{O}_7)$  was prepared by stoichiometric amounts of  $\text{NO}_2\text{BF}_4$  (95%, Aldrich) in an acetonitrile solvent (anhydrous, 99.8%, Aldrich) according to the following reaction:



$\text{NO}_2\text{BF}_4$  was used as the oxidizing agent with a 5.1 V redox potential versus  $\text{Li}^+/\text{Li}$ .<sup>21-22</sup> The solution was stirred at 60°C for 12 h.  $\text{NaFe}_3(\text{PO}_4)_2(\text{P}_2\text{O}_7)$  was obtained by washing several times with acetonitrile.

**Synthesis of ion-exchanged  $\text{Li}_3\text{NaFe}_3(\text{PO}_4)_2(\text{P}_2\text{O}_7)$ :** The ion-exchange of  $\text{Na}_4\text{Fe}_3(\text{PO}_4)_2(\text{P}_2\text{O}_7)$  occurred in a 1M LiBr and 1-hexanol (anhydrous, 99%,

Aldrich) solution at 100–160°C for 24 h. The obtained  $\text{Li}_x\text{Na}_{4-x}\text{Fe}_3(\text{PO}_4)_2(\text{P}_2\text{O}_7)$  was optimized to  $\text{Li}_3\text{NaFe}_3(\text{PO}_4)_2(\text{P}_2\text{O}_7)$  (Li/Na ratio of 3:1).

**Structural characterization:** Powder X-ray diffraction (XRD) data of the synthesized  $\text{Na}_x\text{Fe}_3(\text{PO}_4)_2(\text{P}_2\text{O}_7)$  ( $x = 4, 1$ ) were collected using an X-ray diffractometer (Rigaku, D/MAX 2500) equipped with a Cu  $K\alpha$  radiation ( $\lambda = 1.5406 \text{ \AA}$ ). The data were recorded over a  $2\theta$  range of 5–100° at 4-s steps of 0.02°. The XRD data of  $\text{Li}_x\text{NaFe}_3(\text{PO}_4)_2(\text{P}_2\text{O}_7)$  ( $x = 3, 0$ ) were obtained over a  $2\theta$  range of 5–80°, with 0.01° steps per 2 s using an X-ray diffractometer an XRD (Bruker, New D8 Advance) at Research Institute of Advanced Materials, Seoul National University. Neutron diffraction (ND) analyses of  $\text{Na}_4\text{Fe}_3(\text{PO}_4)_2(\text{P}_2\text{O}_7)$  were performed to determine detailed structural information. ND data were obtained using a high-resolution powder diffractometer (HRPD) at the HANARO facility, Korea Atomic Energy Research Institute. The data were recorded at  $\lambda = 1.8348 \text{ \AA}$  with a step size of 0.05° over a  $2\theta$  range of 0–180°. Rietveld refinement of the XRD and ND patterns was performed using Fullprof software.<sup>23</sup> *In-situ* high-temperature XRD data were collected over a  $2\theta$  range of 5–60° with a scan rate of  $1^\circ \text{ min}^{-1}$  at each temperature using an X-ray diffractometer (Rigaku, D/MAX 2500).

**Mossbauer analysis:** The  $^{57}\text{Fe}$  Mössbauer spectra were recorded using a  $^{57}\text{Co}$  source (60 mCi) in a Rh matrix with the spectrometer moving at constant acceleration.

**Other analyses methods:** The atomic ratios of the elements, including Li, Na, Fe, and P, were confirmed by inductively-coupled plasma–atomic emission spectroscopy (ICP–AES, Thermo Jarrel Ash, Polyscan 60E, USA). The composition ratio of Na:Fe was confirmed to be 4.04:3 for  $\text{Na}_4\text{Fe}_3(\text{PO}_4)_2(\text{P}_2\text{O}_7)$  and 1.1:3 for  $\text{NaFe}_3(\text{PO}_4)_2(\text{P}_2\text{O}_7)$ . Thermal gravimetric analysis (TGA) and differential scanning calorimetry (DSC) were used to investigate the synthesis, temperature, and structural stability of the desodiated phase. Data were recorded at a heating rate of  $10^\circ\text{C min}^{-1}$  from room temperature to  $650^\circ\text{C}$  under an Ar atmosphere using a Setsys 16/18 thermogravimetric analyzer (SETARAM, France).

**First principles calculations:** Density functional theory (DFT) calculations were performed using the Vienna *ab initio* simulation package (VASP) code<sup>24</sup> with the spin-polarized generalized gradient approximation (GGA) and the Perdew–Burke–Ernzerhof (PBE) functional<sup>25</sup> for the exchange–correlation. A plane-wave basis set and the projector-augmented-wave (PAW) method were used as implemented in the VASP. Because GGA involves incomplete cancellation of the self-interaction, we used GGA+U<sup>26–27</sup>, which is a well-established approach for transition metal compounds to accurately calculate their structural and electronic properties. We used a U value of 4.3 eV for the Fe ion, which was previously determined from the self-consistent calculation of olivine phosphate. All calculations were performed in supercells ( $a \times 2b \times c$ ) of eight formula units of  $\text{Na}_4\text{Fe}_3(\text{PO}_4)_2(\text{P}_2\text{O}_7)$ . A plane-wave basis with a kinetic energy cutoff of 500 eV and appropriate *k*-point meshes were used to ensure that the total energies converged

within 5 meV per formula unit. The initial unit cells for the geometry optimizations were taken from our experimental structural data on  $\text{Na}_4\text{Fe}_3(\text{PO}_4)_2(\text{P}_2\text{O}_7)$ . The activation barrier for Na diffusion in  $\text{Na}_4\text{Fe}_3(\text{PO}_4)_2(\text{P}_2\text{O}_7)$  was calculated with the nudged-elastic-band (NEB) method in supercells ( $a \times 2b \times c$ ).<sup>28</sup> For these calculations, a Na ion was allowed to diffuse in the supercells of  $\text{Na}_{4-1/8}\text{Fe}_3(\text{PO}_4)_2(\text{P}_2\text{O}_7)$ . During the NEB calculation, all of the lattice parameters were fixed; however, all of the internal degrees of freedom were relaxed.

**Electrode fabrication:** Samples of the electrochemical active materials were mixed with super P and polyvinylidene fluoride (PVDF) at a weight ratio of 70:20:10 in N-methyl-2-pyrrolidone (99.5%, Aldrich) (NMP) solvent. The electrode was assembled by a CR2016-type coin cell using lithium metal (Hohsen Corp, Japan) as an anode for the Li-ion cell and sodium metal (sodium cube 99%, Aldrich) as an anode for the Na-ion cell. Ethylene carbonate/dimethyl carbonate (EC/DMC 1:1 v/v, Technosemichem) with 1M  $\text{LiPF}_6$  solution was used as an electrolyte for the Li-ion cell, and propylene carbonate (anhydrous 99.x%, Aldrich) with  $\text{NaClO}_4$  (99.x%, Aldrich) was used for the Na-ion cell. A separator (Celgard 2400) was used in both the Na- and Li-ion cells. Galvanostatic charge/discharge tests were carried out at various C-rates (2C, 1C, C/5, C/10, C/20, C/40) for both the Na phase and the Li phase. The cut-off voltage was in the range of 1.7–4.3 V for the Na-ion cell and 2.0–4.6 V for the Li-ion cell. The cyclic voltammogram was obtained at a scan rate of  $0.01 \text{ mV s}^{-1}$ .



## 2.3 Results and Discussion

### 2.3.1 Synthesis and characterization of $\text{Na}_4\text{Fe}_3(\text{PO}_4)_2(\text{P}_2\text{O}_7)$

$\text{Na}_4\text{Fe}_3(\text{PO}_4)_2(\text{P}_2\text{O}_7)$  was successfully synthesized via a conventional solid-state reaction at 500 °C (see Figure 2-1). The first calcination was performed at 300°C based on the endothermic peak in the range of 150–300 °C in DSC. The final firing was conducted at 450–500 °C, the flat region in the DSC results. The exothermic peak after 500 °C in the DSC analysis is attributed to the evolution of  $\text{NaFePO}_4$ . Figure 2-2a shows a schematic representation of the crystal. The crystal framework is composed of a 3D network of  $[\text{Fe}_3\text{P}_2\text{O}_{13}]_\infty$  infinite layers parallel to the b–c plane. The  $[\text{Fe}_3\text{P}_2\text{O}_{13}]_\infty$  layer is connected along the a-axis by  $\text{P}_2\text{O}_7$  groups, and this diphosphate connection produces large tunnels that can provide one of the Na-diffusion channels along the b-axis. The structural characterization based on neutron diffraction (ND) data, shown in Figure 2-2b, confirmed that the  $\text{Na}_4\text{Fe}_3(\text{PO}_4)_2(\text{P}_2\text{O}_7)$  is isostructural to  $\text{Na}_4\text{Co}_3(\text{PO}_4)_2(\text{P}_2\text{O}_7)$ , as reported by Sanz et al.<sup>16</sup> The Rietveld refinement with a space group of  $Pn2_1a$  identified that  $a = 18.07517(7) \text{ \AA}$ ,  $b = 6.53238(2) \text{ \AA}$ ,  $c = 10.64760(4) \text{ \AA}$ , and  $V = 1257.204(1) \text{ \AA}^3$ . The fitting was satisfactory ( $R_p = 1.92 \%$ ,  $R_1 = 1.98 \%$ ,  $R_F = 1.01 \%$ ). A detailed structural illustration of  $\text{Na}_4\text{Fe}_3(\text{PO}_4)_2(\text{P}_2\text{O}_7)$  and a summary of the crystal data can be found in Figure 2-3 and Table 2-1. A trace amount ( $< 4 \%$ ) of the  $\text{NaFePO}_4$  impurity was detected in the ND patterns, and the impurity formation gradually increased above 550 °C, as shown by in situ high-temperature X-ray diffraction

(XRD) analysis (Figure 2-4), thermal gravimetric analysis (TGA), and differential scanning calorimetry (DSC) results (Figure 2-1).

There are four symmetrically distinguishable Na sites in the crystal, and these are connected to each other throughout the 3D framework. Two Na sites (Na2 and Na3) formed by seven coordinated  $\text{NaO}_7$  polyhedra and  $\text{NaO}_6$  octahedra are present along the  $a$ -axis. Two other Na sites (Na1 and Na4), formed by  $\text{NaO}_6$  octahedra, are located on the  $b$ - $c$  plane, as shown in Figure 2-2c. All of the probable diffusion pathways among the four Na sites were examined by first principles calculations. Figure 2-2c illustrates the only energetically plausible Na diffusion paths, with activation barriers lower than 800 meV. The color gradient from yellow to green in Figure 2-2c indicates the site energies of Na during the migration along the path, from which we can identify the fast diffusion pathways of Na. While all Na sites are connected with reasonably low activation barriers, the Na diffusion in the large tunnel along the  $b$ -axis (Na1–Na1) shows the lowest activation barrier (see Table 2-2 for the activation barriers for each Na diffusion path). The Na moves sinusoidally along the  $b$ -axis due to the electrostatic repulsion from the neighboring iron, as shown in Figure 2-5b. It is interesting to note that the sinusoidal motion of Li along the 1D channel was also observed in  $\text{LiFePO}_4$ .<sup>29</sup> Figure 2-5 shows the detailed diffusion mechanism and the landscape of the activation barrier.

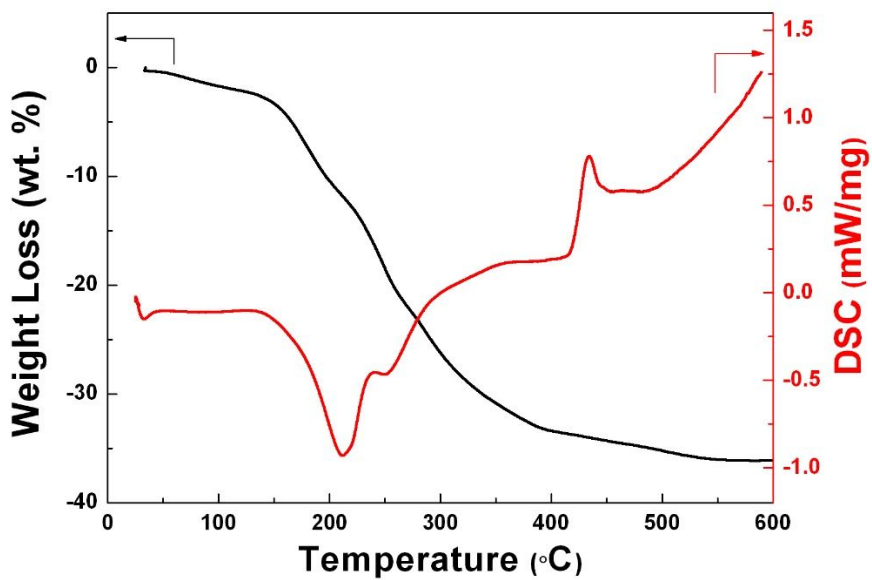


**Figure 2-1.** Thermogravimetric analysis and differential scanning calorimetry (TGA/DSC) of the precursor used for the solid-state synthesis of  $\text{Na}_4\text{Fe}_3(\text{PO}_4)_2(\text{P}_2\text{O}_7)$ .

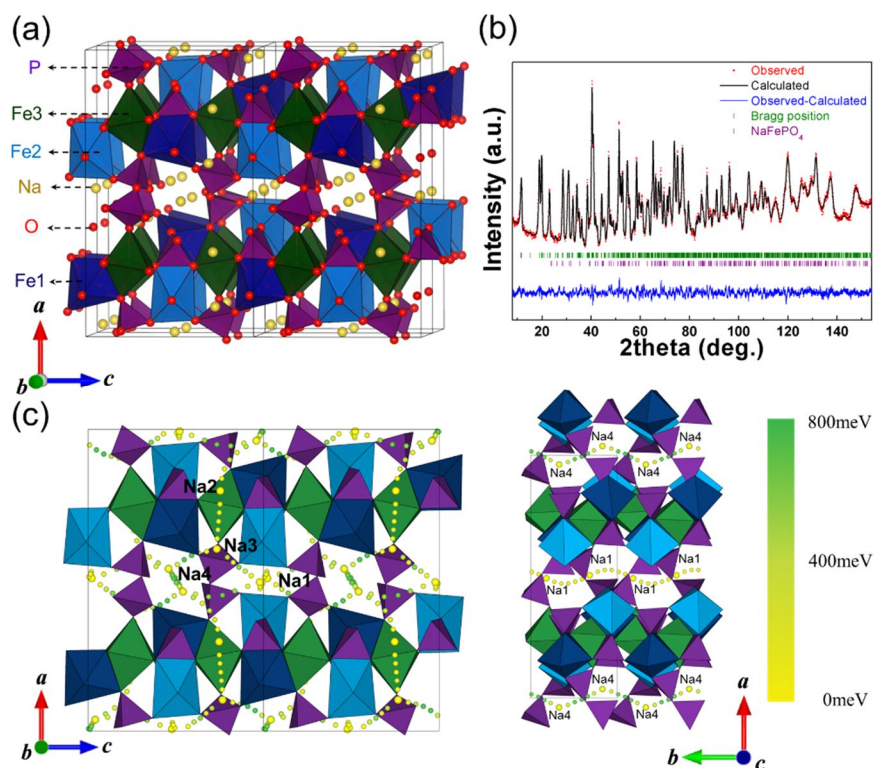


**Figure 2-2.** (a) Schematic representation of  $\text{Na}_4\text{Fe}_3(\text{PO}_4)_2(\text{P}_2\text{O}_7)$ . (b) Rietveld refinement of the neutron diffraction patterns of  $\text{Na}_4\text{Fe}_3(\text{PO}_4)_2(\text{P}_2\text{O}_7)$ . The observed and calculated intensities are represented by the red markers and the black solid line, respectively. The bottom blue line represents the difference between the observed and calculated patterns. Bragg positions for  $\text{Na}_4\text{Fe}_3(\text{PO}_4)_2(\text{P}_2\text{O}_7)$  are represented as green markers, and the  $\text{NaFePO}_4$  ( $\sim 4\%$ ) impurity is shown as purple markers. (c) The 3D sodium diffusion paths in the  $\text{Na}_4\text{Fe}_3(\text{PO}_4)_2(\text{P}_2\text{O}_7)$  structure.

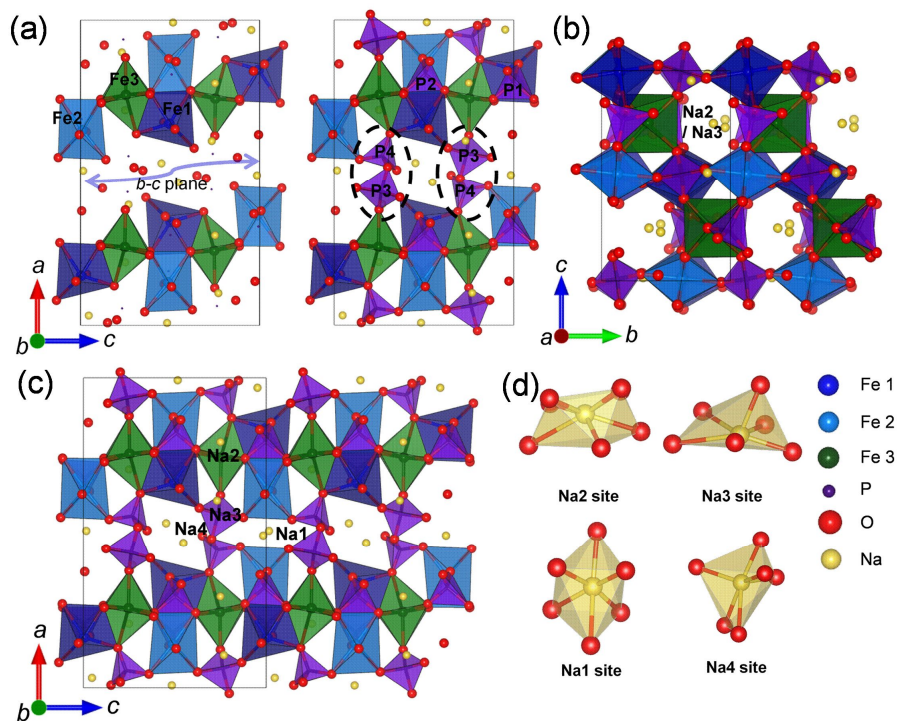


**Figure 2-3.** Detailed schematics of the Na channel along the  $b$ - $c$  plane and the diposphate connection between the  $[\text{Fe}_3\text{P}_2\text{O}_{13}]_\infty$  layers are presented in (a). The sodium sites along the  $a$ - and  $b$ -axes in the structure of  $\text{Na}_4\text{Fe}_3(\text{PO}_4)_2(\text{P}_2\text{O}_7)$  are shown in (b) and (c), respectively. The four different Na sites in the structure of  $\text{Na}_4\text{Fe}_3(\text{PO}_4)_2(\text{P}_2\text{O}_7)$  are shown in (d).

**Table 2-1.** The detailed data for the structural refinement of  $\text{Na}_4\text{Fe}_3(\text{PO}_4)_2(\text{P}_2\text{O}_7)$  using ND patterns.

Formula	$\text{Na}_4\text{Fe}_3(\text{PO}_4)_2(\text{P}_2\text{O}_7)$
Crystal system	Orthorhombic
Space group	$\text{Pn}2_1\text{a}$ (No. 33)
Lattice parameters	
$a$ (Å)	18.07517 (7)
$b$ (Å)	6.53238 (2)
$c$ (Å)	10.64760 (4)
Unitcell volume (Å <sup>3</sup> )	1257.204 (1)
Formula weight	623.38012
Source	Neutron
Temperature (K)	300K
Wave length (Å)	1.834333
$2\theta$ range	0 – 180°
Number of data points	3200
Number of reflections	1092
$R_p$ (%)	1.92
$R_I$ (%)	1.98
$R_F$ (%)	1.01
$\chi^2$	3.55

Atom	x	y	z	Biso
Fe1	0.3377(3)	0.138(3)	0.5042(9)	0.03(7)
Fe2	0.1402(3)	0.624(3)	0.4886(8)	0.03(7)
Fe3	0.2440(5)	0.358(4)	0.7469(11)	0.03(7)
P1	0.2950(6)	0.618(4)	0.502(2)	0.13(10)
P2	0.1772(5)	0.123(5)	0.4918(19)	0.13(10)
P3	0.5630(6)	0.488(4)	0.7382(14)	0.13(10)
P4	0.4446(7)	0.173(4)	0.7323(12)	0.13(10)
Na1	0.4923(13)	0.822(4)	0.984(2)	1.1(2)
Na2	0.2941(9)	0.868(4)	0.750(3)	1.1(2)
Na3	0.3949(11)	0.459(4)	0.2686(20)	1.1(2)
Na4	0.4681(12)	0.695(2)	0.5473(19)	1.1(2)
O1	0.2417(8)	0.590(3)	0.6136(16)	0.29(5)
O2	0.3563(8)	0.439(4)	0.4731(14)	0.29(5)
O3	0.3335(6)	0.814(4)	0.5351(12)	0.29(5)
O4	0.2414(7)	0.649(4)	0.3874(13)	0.29(5)
O5	0.2355(7)	0.138(4)	0.6097(12)	0.29(5)
O6	0.1258(7)	-0.071(4)	0.5074(13)	0.29(5)
O7	0.2299(7)	0.086(4)	0.3848(15)	0.29(5)
O8	0.1352(7)	0.302(4)	0.4674(12)	0.29(5)
O9	0.4819(7)	0.401(4)	0.7019(10)	0.29(5)
O10	0.5510(7)	0.595(4)	0.8760(12)	0.29(5)
O11	0.6225(6)	0.326(3)	0.7502(18)	0.29(5)
O12	0.5816(5)	0.634(4)	0.6339(12)	0.29(5)
O13	0.4558(6)	0.123(4)	0.8585(13)	0.29(5)

O14	0.3709(7)	0.191(4)	0.6882(12)	0.29(5)
O15	0.4915(7)	0.026(3)	0.6515(10)	0.29(5)

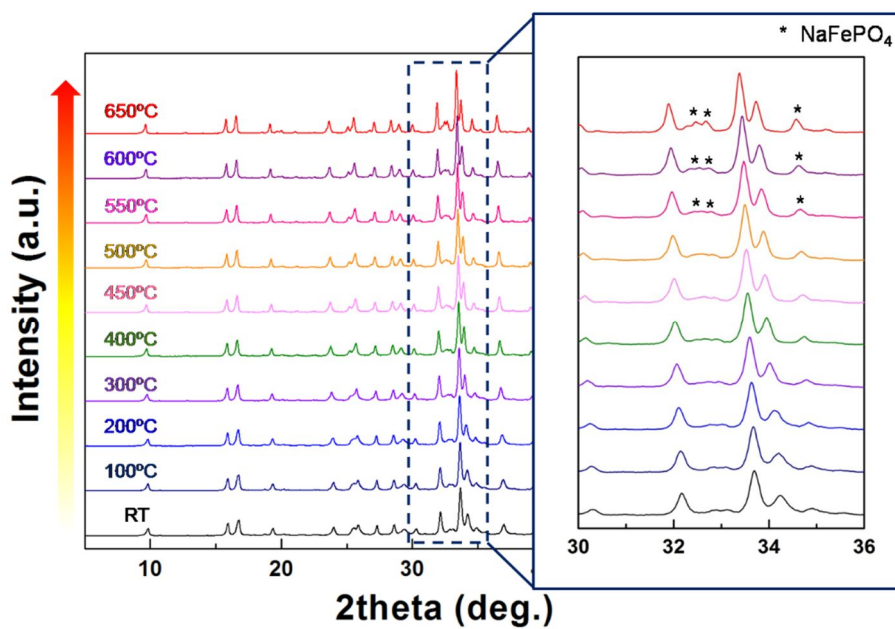


**Figure 2-4.** *In-situ* high-temperature X-ray diffraction (XRD) patterns of  $\text{Na}_4\text{Fe}_3(\text{PO}_4)_2(\text{P}_2\text{O}_7)$  in the temperature range of 25–650°C under an Ar atmosphere. The  $\text{NaFePO}_4$  peaks start to significantly evolve above 550°C.

**Table 2-2.** Sodium vacancy activation barriers in the  $\text{Na}_4\text{Fe}_3(\text{PO}_4)_2(\text{P}_2\text{O}_7)$  structure.

From (site)	To (site)	Activation energy (meV)
Na1	Na1	256meV
Na1	Na4	599meV
Na2	Na4	481meV
Na3-1	Na1	540meV
Na2	Na3	344meV
Na3	Na4	685meV
Na4	Na4	544meV

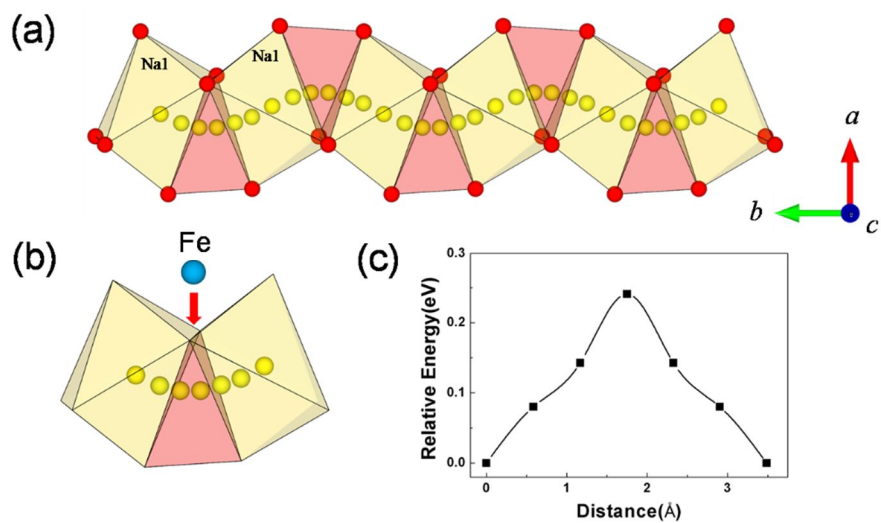


**Figure 2-5.** Calculated main diffusion motion along the *b*-axis as illustrated in (a) and (b). (c) The activation barrier of sodium from one Na1 site to another Na1 site.

### 2.3.2 Electrochemical properties of $\text{Na}_4\text{Fe}_3(\text{PO}_4)_2(\text{P}_2\text{O}_7)$ in Na-ion cells

Inspired by the feasible Na diffusion in the crystal, the electrochemical properties of  $\text{Na}_4\text{Fe}_3(\text{PO}_4)_2(\text{P}_2\text{O}_7)$  were tested in a Na cell. The Na cell was fabricated with  $\text{Na}_4\text{Fe}_3(\text{PO}_4)_2(\text{P}_2\text{O}_7)$  as the cathode, a sodium counter electrode as the anode, and  $\text{NaClO}_4$  in propylene carbonate (PC) as the electrolyte. Figure 2-6a shows the voltage trace as a function of sodium composition for  $\text{Na}_x\text{Fe}_3(\text{PO}_4)_2(\text{P}_2\text{O}_7)$  with a 4.3 V cutoff voltage in a Na cell. About 88 % of the theoretical capacity which can be considered as one electron reaction per Fe atom was obtained at the rate of C/40, with an average voltage of  $\sim 3.2$  V. The electrochemical activity centered around 3.2 V is consistent with the theoretical prediction of the voltage from the first principles calculations, as indicated in Figure 2-6a. It is noted that unusually high polarization is observable at the end of the first charge profile. We speculate that this phenomenon can be related to the local structural change occurring around the Na tunnels at the end of the charge. The examination of the structural evolution from first principles calculation reveals that  $\text{P}_2\text{O}_7$  dimer that constitutes the Na diffusion tunnels in the structure significantly distorts at  $1 \leq x \leq 2$  in  $\text{Na}_x\text{Fe}_3(\text{PO}_4)_2(\text{P}_2\text{O}_7)$ , while the precise relation between  $\text{P}_2\text{O}_7$  dimer distortion and the Na mobility is currently under investigation. Relatively good cycle performance was observed at both the C/40 rate and C/20 rate, as shown in Figure 2-6b.

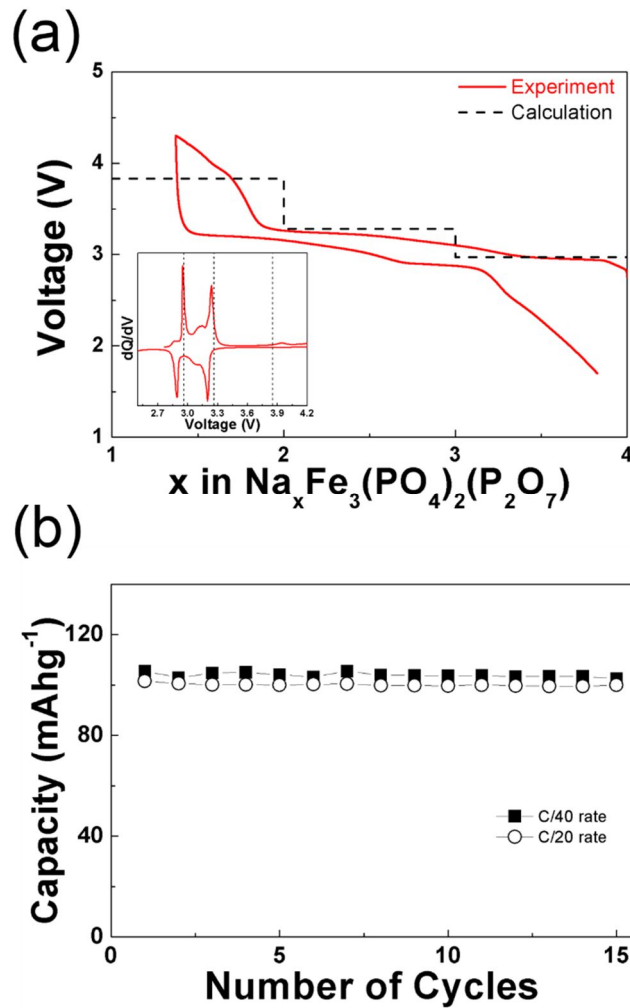


**Figure 2-6.** (a) Galvanostatic charge/discharge profiles of  $\text{Na}_4\text{Fe}_3(\text{PO}_4)_2(\text{P}_2\text{O}_7)$  under a C/40 rate and the calculated average voltage at each region. The inset shows the  $dQ/dV$  curve of initial charge/discharge profiles. (b) Cycle performance of a Na cell under C/40 and C/20 rates.

### 2.3.3 Desodiation mechanism of $\text{Na}_{4-x}\text{Fe}_3(\text{PO}_4)_2(\text{P}_2\text{O}_7)$

The mechanism by which sodium is extracted from  $\text{Na}_4\text{Fe}_3(\text{PO}_4)_2(\text{P}_2\text{O}_7)$  was studied by monitoring Mössbauer spectra and XRD patterns of  $\text{Na}_4\text{Fe}_3(\text{PO}_4)_2(\text{P}_2\text{O}_7)$  and fully charged  $\text{NaFe}_3(\text{PO}_4)_2(\text{P}_2\text{O}_7)$ . Figure 2-7 indicates that the comparison of the XRD patterns of the two samples did not show a significant change; this implies a topotactical de/insertion of the sodium ions. However, a change in the lattice parameters was observed. The values of  $a$ ,  $b$ , and the volume decreased when the three sodium ions were extracted, while the  $c$  lattice parameter increased significantly.

The volume change was less than 4 %, which is considerably low compared with other cathode materials.<sup>3,4,6</sup> The lattice parameters of each phase are tabulated in Table 2-3 along with the ND analysis, which showed the same trend. The comparison of Mössbauer spectra of the two samples clearly indicated that the  $\text{Fe}^{2+}/\text{Fe}^{3+}$  redox reaction mainly accompanies the de/sodiation shown in Figure 2-8. Mössbauer analysis in Figure 2-8 confirmed that most of the iron in  $\text{Na}_4\text{Fe}_3(\text{PO}_4)_2(\text{P}_2\text{O}_7)$  initially existed as  $\text{Fe}^{2+}$ . The blue, green, and purple lines in Mössbauer spectra represent the three distinct iron sites. The values of the quadruple splitting ( $\Delta E_Q$ ) and isomer shift ( $I_S$ ) are in good agreement with those observed in other  $\text{Fe}^{2+}$ -containing compounds.<sup>30</sup> However, when a full charge of  $\text{Na}_4\text{Fe}_3(\text{PO}_4)_2(\text{P}_2\text{O}_7)$  is complete, resulting in the formation of  $\text{NaFe}_3(\text{PO}_4)_2(\text{P}_2\text{O}_7)$ , the  $\Delta E_Q$  and  $I_S$  shift toward values typically observed for  $\text{Fe}^{3+}$ . A trace amount of  $\text{Fe}^{2+}$  detected was attributed to the  $\text{NaFePO}_4$  impurity, consistent with the ND study.

This result agrees with the first principles calculation of the Fe valence states for the two samples. The spin integration around Fe indicates that the valence of Fe is +2 for the as-prepared sample and +3 for the charged sample, as shown in Figure 2-9. Detailed information on  $\Delta E_Q$ , the  $I_S$  values, and the iron site ratios are provided in Table 2-4.

The thermal phase stability of the charged electrode is one of the indicators that determine the safety characteristics of the battery at elevated temperatures. The charged electrode,  $\text{NaFe}_3(\text{PO}_4)_2(\text{P}_2\text{O}_7)$ , was further investigated using TGA/ DSC measurements and in situ high-temperature XRD. TGA/ DSC analyses indicate that the desodiated phase was stable up to 500 °C, with only  $\sim 4\%$  weight loss (see Figure 2-10). An exothermic peak was observed around 530 °C, where the decomposition into  $\text{NaFeP}_2\text{O}_7$  and  $\text{Fe}_2\text{P}_2\text{O}_7$  was detected from the in situ high-temperature XRD results (see Figure 2-11). The high stability of the  $\text{NaFe}_3(\text{PO}_4)_2(\text{P}_2\text{O}_7)$  was comparable to that of charged olivine  $\text{LiFePO}_4$  and pyrophosphate  $\text{Li}_2\text{FeP}_2\text{O}_7$ ,<sup>3,5</sup> presenting intrinsically safe characteristics of polyanion-compound electrodes.

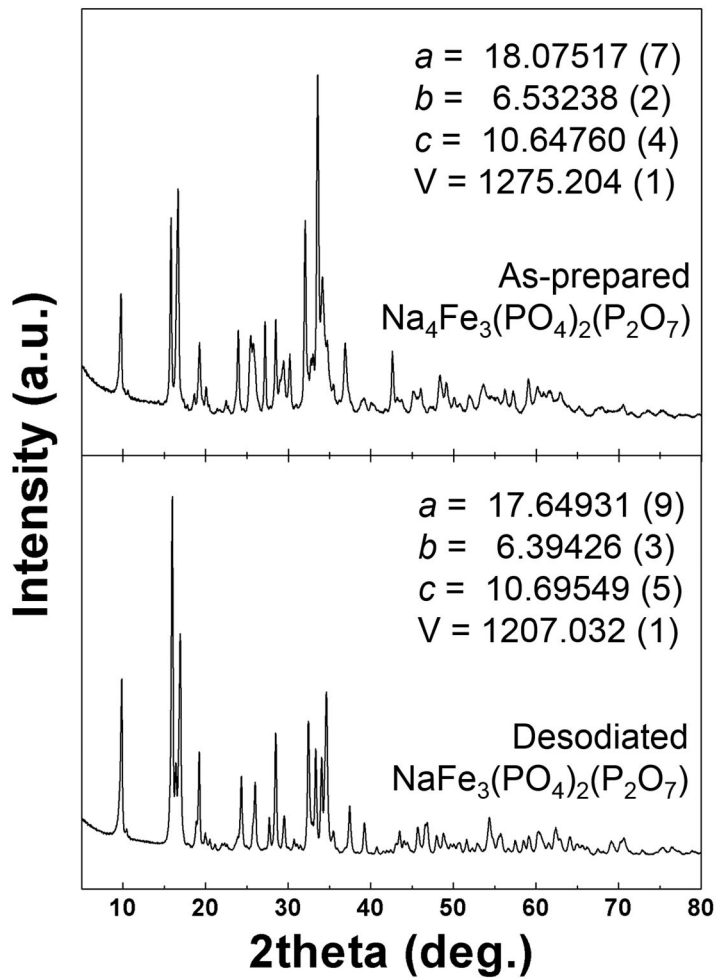


**Figure 2-7.** XRD patterns of  $\text{Na}_x\text{Fe}_3(\text{PO}_4)_2(\text{P}_2\text{O}_7)$  ( $x = 1, 4$ ).

**Table 2-3.** Lattice parameters of  $\text{Na}_x\text{Fe}_3(\text{PO}_4)_2(\text{P}_2\text{O}_7)$  ( $x = 4, 1$ ).

---

Sample	Source	$a$ (Å)	$b$ (Å)	$c$ (Å)	vol (Å <sup>3</sup> )
$\text{Na}_4\text{Fe}_3(\text{PO}_4)_2(\text{P}_2\text{O}_7)$	X-ray	18.0703 (1)	6.53193 (3)	10.64717 (5)	1256.723 (1)
	Neutron	18.07517 (7)	6.53238 (2)	10.64760 (4)	1257.204 (1)
$\text{NaFe}_3(\text{PO}_4)_2(\text{P}_2\text{O}_7)$	X-ray	17.6625(2)	6.39797(5)	10.69996(6)	1209.137 (1)
	Neutron	17.64931(9)	6.39426(3)	10.69549(5)	1207.032 (1)

---

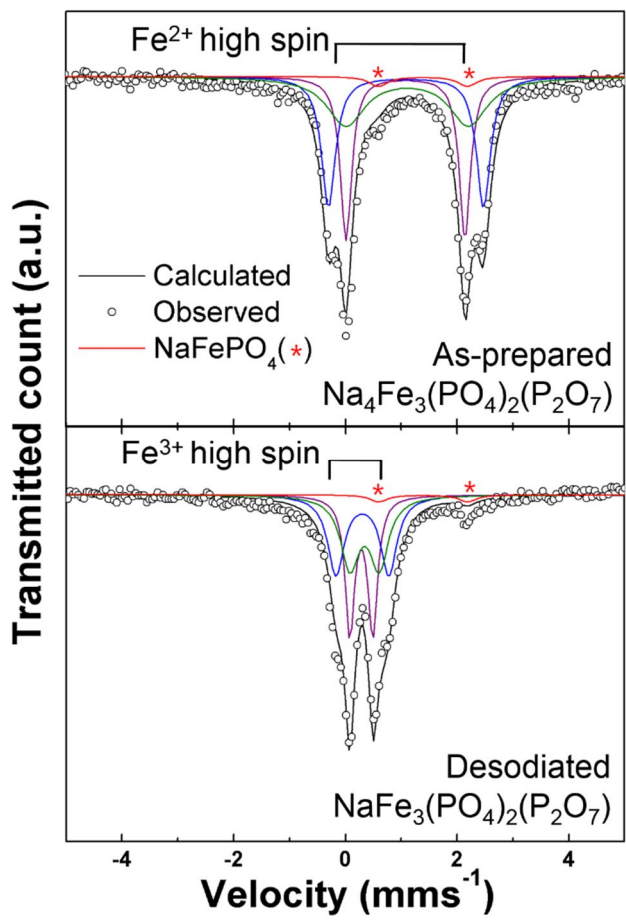


**Figure 2-8.** Mössbauer spectra of Na<sub>x</sub>Fe<sub>3</sub>(PO<sub>4</sub>)<sub>2</sub>(P<sub>2</sub>O<sub>7</sub>) (x = 1, 4).

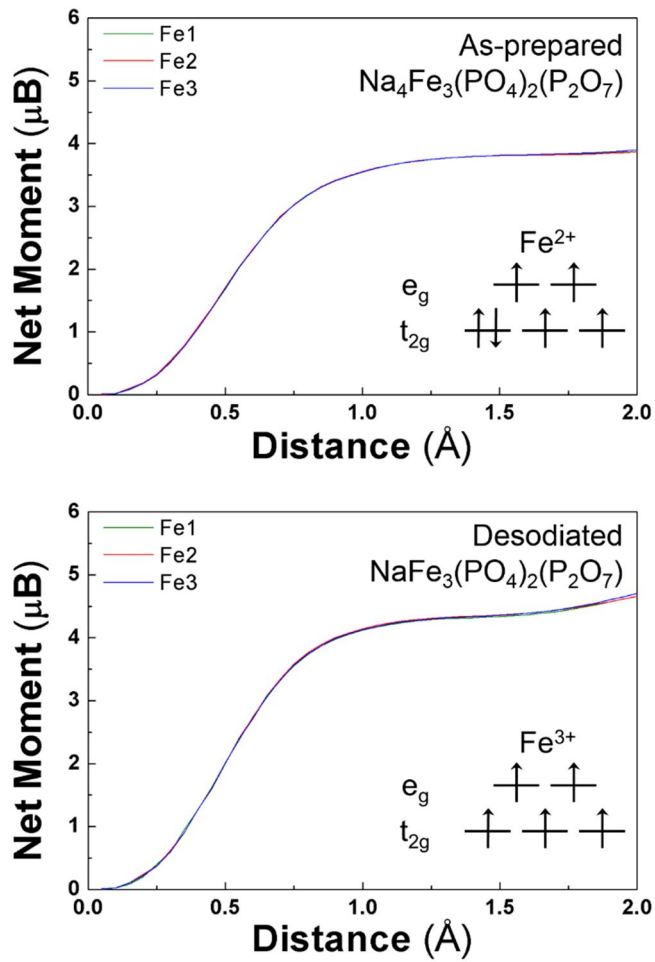


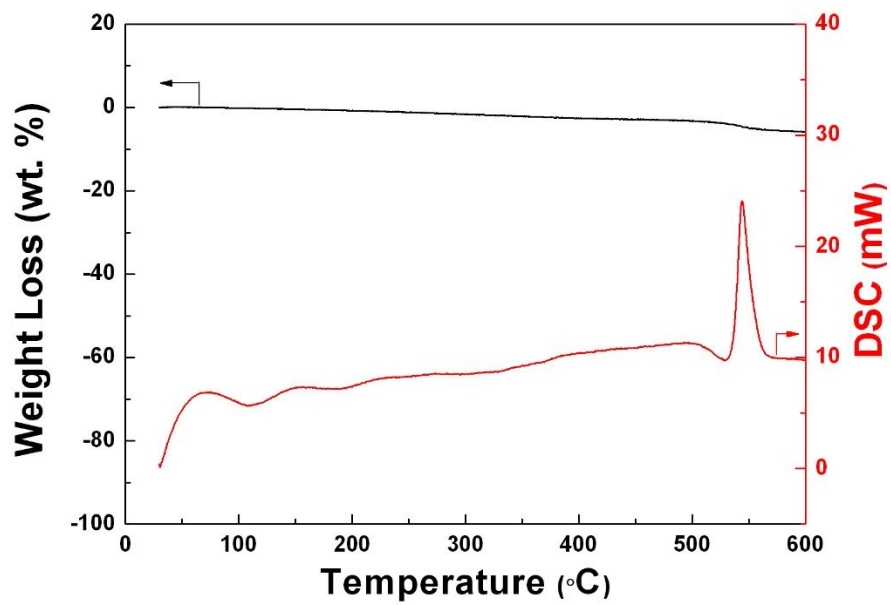
**Figure 2-9.** Integrated spin as a function of integration radius around Fe in  $\text{Na}_{4-x}\text{Fe}_3(\text{PO}_4)_2(\text{P}_2\text{O}_7)$  ( $x = 0, 3$ ).

**Table 2-4.** Quadruple splitting, isomer shift values, and the ratio of each iron site in  $\text{Na}_x\text{Fe}_3(\text{PO}_4)_2(\text{P}_2\text{O}_7)$  ( $x = 4, 1$ ).

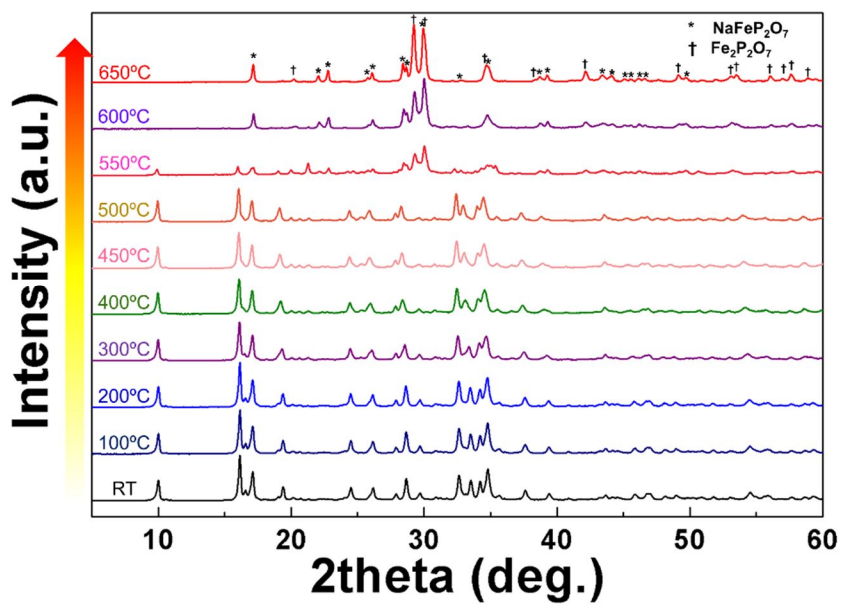
$\text{Na}_4\text{Fe}_3(\text{PO}_4)_2(\text{P}_2\text{O}_7)$	$\Delta E_Q$ (mm/s)	$\delta$ (mm/s)	Ratio (%)
Iron 1	2.1312	1.078	32.26
Iron 2	2.775	1.0875	32.26
Iron 3	2.1941	1.1095	32.26
$\text{NaFePO}_4$	1.5933	1.3917	3.23

$\text{NaFe}_3(\text{PO}_4)_2(\text{P}_2\text{O}_7)$	$\Delta E_Q$ (mm/s)	$\delta$ (mm/s)	Ratio (%)
Iron 1	0.4104	0.2842	32.26
Iron 2	0.9477	0.3026	32.26
Iron 3	0.5244	0.3413	32.26
$\text{NaFePO}_4$	1.5933	1.3917	3.23



**Figure 2-10.** TGA/DSC analysis of the desodiated phase of  $\text{NaFe}_3(\text{PO}_4)_2(\text{P}_2\text{O}_7)$ .



**Figure 2-11.** *In-situ* high-temperature XRD patterns of NaFe<sub>3</sub>(PO<sub>4</sub>)<sub>2</sub>(P<sub>2</sub>O<sub>7</sub>) for a temperature range of 25–650°C under an Ar atmosphere.

### 2.3.4 Electrochemical properties of $\text{Li}_3\text{NaFe}_3(\text{PO}_4)_2(\text{P}_2\text{O}_7)$ in Li-ion cells

The lithium analogue of  $\text{Na}_4\text{Fe}_3(\text{PO}_4)_2(\text{P}_2\text{O}_7)$  was produced via a topotactic ion-exchange of the Na cation to the Li cation within the lattice by refluxing in a solution of LiBr. Three Na ions were successfully replaced by Li ions in the lattice, while one Na remained in the structure, resulting in the production of  $\text{Li}_3\text{NaFe}_3(\text{PO}_4)_2(\text{P}_2\text{O}_7)$ . The Li/Na composition was confirmed to be 3.06:0.9 by inductively coupled plasma–atomic emission spectroscopy (ICP–AES). Figure 2-12a shows the XRD patterns of  $\text{Li}_3\text{NaFe}_3(\text{PO}_4)_2(\text{P}_2\text{O}_7)$ . The general patterns are similar to those of  $\text{Na}_4\text{Fe}_3(\text{PO}_4)_2(\text{P}_2\text{O}_7)$ , implying that the crystal framework was maintained. However, the lattice parameters were determined to be smaller,  $a = 16.8755$  (7) Å,  $b = 6.50413$  (17) Å, and  $c = 10.6453$  (3) Å, for  $\text{Li}_3\text{NaFe}_3(\text{PO}_4)_2(\text{P}_2\text{O}_7)$  from profile matching, due in part to the smaller ionic radius of Li compared with Na. In particular, a significant reduction of the  $a$  lattice was observed. We believe that the replacement of Na with Li in the  $(\text{Na}1)\text{O}_6$  and  $(\text{Na}4)\text{O}_6$  polyhedra located on the  $b$ – $c$  plane caused a significant distortion of the  $\text{P}_2\text{O}_7$  pillars, which induced the collapse of the interlayer spacing along the  $a$ -axis.

Electrochemical measurements on the Li-ion cell were performed with a Li metal anode in a 2016-type coin cell at 298 and 333 K. Figure 2-12b shows the voltage–lithium composition trace of  $\text{Li}_3\text{NaFe}_3(\text{PO}_4)_2(\text{P}_2\text{O}_7)$ . It should be noted that the electrochemical cycling of  $\text{Li}_3\text{NaFe}_3(\text{PO}_4)_2(\text{P}_2\text{O}_7)$  electrode did not show any noticeable change in Na contents. This implies that residual Na may play a role of pillar in the structure. Nevertheless, we believe that various environments such as

different C-rates, cutoff voltages, and particle sizes can affect the sodium contents in the structure of  $\text{Li}_3\text{NaFe}_3(\text{PO}_4)_2(\text{P}_2\text{O}_7)$ . About 92 % of the theoretical capacity was obtained at a C/20 rate with an average voltage of 3.4 V. The electrochemical activity centered around 3.4 V agrees with the voltage trace predicted from the first principles calculations, as indicated in Figure 2-12b. The average voltage of the  $\text{Li}_3\text{NaFe}_3(\text{PO}_4)_2(\text{P}_2\text{O}_7)$  is only slightly higher than that of  $\text{Na}_4\text{Fe}_3(\text{PO}_4)_2(\text{P}_2\text{O}_7)$ . It is attributed to the relative instability of Li ions in the crystal framework which is derived from a parent Na-phase. Relatively good cycle performance was observed, as shown Figure 2-12c. Almost 86 % of the initial discharge capacity was retained at 333 K after 100 cycles. The battery operation at higher current densities showed that  $\sim 75$  % of the initial capacity could be delivered in 1 h (1C rate) and  $\sim 60$  % even in 30 min (2C rate), suggesting that this electrode could sustain respectable rate capabilities (see Figure 2-12d). Note that this electrode was fabricated without any special efforts such as carbon-coating or nanosizing, and there exists about 4% inactive  $\text{NaFePO}_4$  impurity. We believe that further synthesis optimization can improve the electrochemical properties significantly. The excellent rate capability and cycle performance was attributed to the open and stable polyanion framework of the electrode material. The open framework is beneficial for fast ion transport, but may, in turn, sacrifice the volumetric energy density for practical use. Nevertheless, comparison with other iron-based polyanion cathodes reported so far showed that the volumetric energy density of  $\text{Li}_3\text{NaFe}_3(\text{PO}_4)_2(\text{P}_2\text{O}_7)$  is comparable to them as tabulated in Table S5.

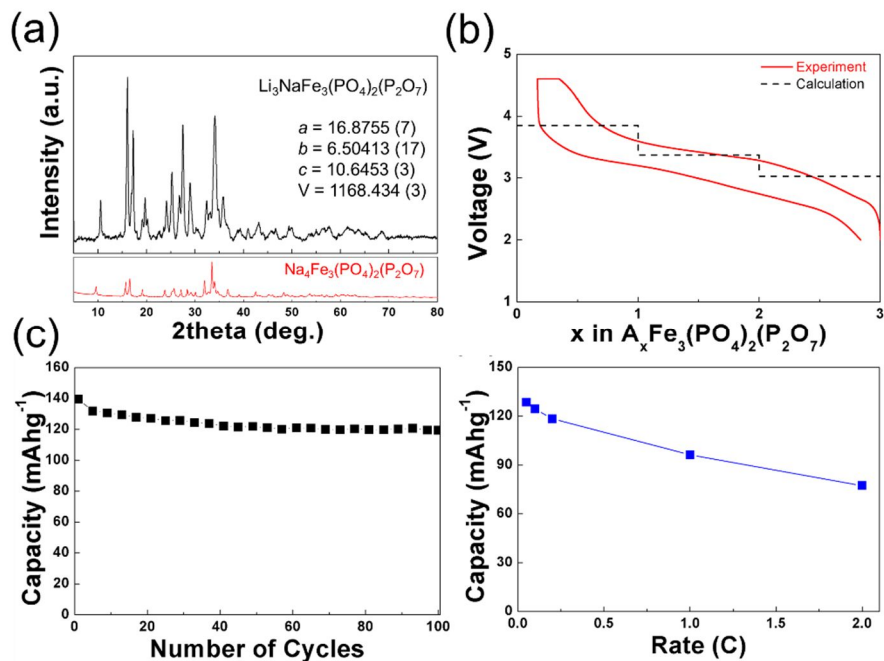


**Figure 2-12.** (a) XRD patterns of  $\text{Li}_3\text{NaFe}_3(\text{PO}_4)_2(\text{P}_2\text{O}_7)$ . The reference sodium phase of  $\text{Na}_4\text{Fe}_3(\text{PO}_4)_2(\text{P}_2\text{O}_7)$  is represented below. (b) Calculated voltage and galvanostatic charge/discharge profiles of the Li cell under a C/20 rate at 298 K and calculated voltage profiles; (c) cyclability of the Li-ion cell under C/5 at 333 K. (d) The rate capability of  $\text{Li}_3\text{NaFe}_3(\text{PO}_4)_2(\text{P}_2\text{O}_7)$  in the Li-ion cell.

**Table 2-5.** Volumetric energy density of iron-based polyanion compounds.

Designation	Voltage	Volumetric energy density	References
$\text{Li}_3\text{NaFe}_3(\text{PO}_4)_2(\text{P}_2\text{O}_7)$	3.4V	1550Wh/L	This work
Pyrophosphate, $\text{Li}_2\text{FeP}_2\text{O}_7$	3.5V	1200Wh/L	Ref. 1
$\text{Li}_2\text{FePO}_4\text{F}$	3.3V	1550Wh/L	Ref. 6
Tavorite, $\text{LiFeSO}_4\text{F}$	3.6V	1750Wh/L	Ref. 10
Tavorite, $\text{LiFePO}_4\text{F}$	2.75V	1290Wh/L	Ref. 31
Tavorite, $\text{LiFePO}_4\text{OH}$	2.4V	1220Wh/L	Ref. 32
Silicate, $\text{Li}_2\text{FeSiO}_4$	2.85V	1510Wh/L	Ref. 8
Olivine, $\text{LiFePO}_4$	3.3V	2010Wh/L	Ref. 2
$\text{Li}_3\text{Fe}_2(\text{PO}_4)_3$	2.8V	1110Wh/L	Ref. 13
$\text{LiFeP}_2\text{O}_7$	2.9V	1020Wh/L	

## 2.4 Conclusion

In conclusion, new mixed-polyanion-based compounds,  $\text{Li}_x\text{Na}_{4-x}\text{Fe}_3(\text{PO}_4)_2(\text{P}_2\text{O}_7)$  ( $x = 0, 3$ ), were successfully synthesized, and their energy densities were 380 and 460  $\text{Wh kg}^{-1}$  in sodium- and lithium-ion batteries, respectively. The respectable cathode activity in both sodium- and lithium-ion batteries was delivered without special efforts, such as carbon coating or nano-sizing. The combined  $(\text{PO}_4)^{3-}$  and  $(\text{P}_2\text{O}_7)^{4-}$  polyanion groups, which provided a new crystal framework that accommodated the naturally abundant Fe redox center and lithium/sodium ions, exhibited stable and fast cathode activity in lithium and sodium batteries. The emerging rich chemistry in mixed-polyanion materials suggests that significant opportunity exists to explore new low-cost, high-performance electrodes in this class of materials.

## 2.5 References

- (1) S. Nishimura, M. Nakamura, R. Natsui, A. Yamada, *J. Am. Chem. Soc.* **2010**, *132* (39), 13596–13597.
- (2) A. K. Padhi, K. Nanjundaswamy, J. B. Goodenough, *J. Electrochem. Soc.* **1997**, *144* (4), 1188–1194.
- (3) C. Delacourt, P. Poizot, J. -M. Tarascon, C. Masquelier, *Nat. Mater.* **2005**, *4*, 254–260.
- (4) B. L. Ellis, W. R. Makahnouk, Y. Makimura, K. Toghill, L. F. Nazar, *Nat. Mater.* **2007**, *6* (10), 749–753.
- (5) H. Kim, S. Lee, Y. -U. Park, H. Kim, J. Kim, S. Jeon, K. Kang, *Chem. Mater.* **2011**, *23* (17), 3930–3937.
- (6) N. Recham, J. -N. Chotard, L. Dupont, C. Delacourt, W. Walker, M. Armand, J. -M. Tarascon, *Nat. Mater.* **2009**, *9* (1), 68–74.
- (7) P. Barpanda, M. Ati, B. C. Melot, G. Rousse, J. N. Chotard, M. L. Doublet, M. T. Sougrati, S. -A. Corr, J. C. Jumas, J. -M. Tarascon, *Nat. Mater.* **2011**, *10* (10), 772–779.
- (8) A. Nyten, A. Abouimrane, M. Armand, T. Gustafsson, J. O. Thomas, *Electrochem. Commun.* **2005**, *7* (2), 156–160.
- (9) A. Yamada, N. Iwane, Y. Harada, S. -i. Nishimura, Y. Koyama, I. Tanaka, *Adv. Mater.* **2010**, *22* (32), 3583–3587.

- (10) D.-H. Seo, Y. -U. Park, S. -W. Kim, I. Park, R. Shakoob, K. Kang, *Phy. Rev. B* **2011**, *83*, 205127–1–8.
- (11) T. N. Ramesh, K. T. Lee, B. L. Ellis, L. F. Nazar, *Electrochem. Solid-State Lett.* **2010**, *13* (4), A43–A47.
- (12) B. L. Ellis, T. N. Ramesh, W. N. Rowan-Weetaluktuk, D. H. Ryan, L. F. Nazar, *J. Mater. Chem.* **2012**, *22*, 4759–4766.
- (13) A. K. Pahdi, K. S. Nanjundaswamy, C. Masquelier, S. Okada, J. B. Goodenough, *J. Electrochem. Soc.* **1997**, *144* (5), 1609–1613.
- (14) A. K. Padhi, V. Manivannan, J. B. Goodenough, *J. Electrochem. Soc.* **1998**, *145* (5), 1518–1520.
- (15) G. Hautier, A. Jain, H. Chen, C. Moore, S. P. Ong, G. Ceder, *J. Mater. Chem.* **2011**, *21* (43), 17147–17153.
- (16) A. Jain, G. Hautier, C. Moore, B. Kang, J. Lee, H. Chen, N. Twu, G. Ceder, *J. Electrochem. Soc.* **2012**, *159* (5), 622–633.
- (17) Q. Kuang, J. Xu, Y. Zhao, X. Chen, L. Chen, *Electrochim. Acta* **2011**, *56* (5), 2201–2205.
- (18) Q. Kuang, Z. Lin, Y. Zhao, X. Chen, L. Chen, *J. Mater. Chem.* **2011**, *21* (38), 14760–15765.
- (19) F. Sanz, C. Parada, J. Rojo, C. Ruiz-Valero, *Chem. Mater.* **2001**, *13* (4), 1334–1340.

- (20) R. Essehli, E. B. Bali, S. Benmokhtar, H. Fuess, I. Svoboda, S. Obbade, *J. Alloys Compd.* **2010**, 493 (1), 654–660.
- (21) A. R. Wizansky, P. E. Rauch, F. J. DiSalvo, *J. Solid State. Chem.* **1989**, 81, 203–207.
- (22) S. -W. Kim, J. Kim, H. Gwon, K. Kang, *J. Electrochem. Soc.* **2009**, 156 (8), A635– A638.
- (23) T. Roisnel, J. Rodriquez-Carvajal, *Transtec Publications*; 1999: **2001**, 118–123.
- (24) G. Kresse, J. Furthmuller, *Comput. Mater. Sci.* **1996**, 6, 15.
- (25) J. P. Perdew, K. Burke, M. Ernzerhof, *Phys. Rev. Lett.* **1996**, 77, 3865.
- (26) V. I. Anisimov, J. Zaanen, O. K. Andersen, *Phys. Rev. B* **1991**, 44, 943.
- (27) V. I. Anisimov, F. Aryasetiawan, A. I. Lichtenstein, *J. Phys. Condens. Matter* **1997**, 9, 767.
- (28) H. Jonsson, G. Mills, K. W. Jacobsen, B. J. Berne, title. in *Classical and Quantum Dynamics in Condensed Phase Simulations*, edited by D. Chandler, B. J. Berne, G. Ciccotti, & D. F. Coker (World Scientific, Singapore, 1998), p. 385
- (29) S. -i Nishimura, G. Kobayashi. K. Ohoyama, R. Kanno, M. Yashima, A. Yamada, *Nat. Mater.* **2008**, 7, 707–711.
- (30) A.-S. Andersson, B. Kalska, L. Haggström, J. –O. Thomas, *Solid State Ionics* **2000**, 130 (1), 41–52.

(31) N. Recham, J. –N. Chotard, J. –C. Jumas, L. Laffont, M. Armand, J. –M. Tarascon, *Chem. Mater.* **2010**, 22 (3), 1142-1148.

(32) M. S. Whittingham, Y. Song, S. Lutta, P. –Y. Zavalij, N. –A. Chernova, *J. Mater. Chem.* **2005**, 15, 3362-3379.

# **Chapter 3. Understanding the electrochemical mechanism of the new iron-based mixed-phosphate $\text{Na}_4\text{Fe}_3(\text{PO}_4)_2(\text{P}_2\text{O}_7)$ in a Na rechargeable battery**

(The content of this chapter has been published in *Chemistry of Materials*. Reprinted with permission from [H. Kim et al., *Chem. Mater.* **2013**, 25 (18), 3614-3622.]. Copyright (2013) American Chemical Society.)

## **3.1 Introduction**

Storing the energy from sustainable but intermittent resources, such as solar and wind energy, in a large-scale energy storage system (ESS) has become a critical issue in recent years. Although the Li rechargeable battery has been a great success in small portable electronics, and is on the verge of being used in mid-size applications such as hybrid electric vehicles (HEVs) and electric vehicles (EVs),<sup>1-3</sup> great challenges remain in its application to large-scale ESSs. In order to develop a stationary ESS connected to green and sustainable energy generators beyond the scale of HEVs and EVs, cost effectiveness is of foremost importance. While the significant cost reduction in cell making or maintenance would greatly benefit the development, in the aspects of material cost, batteries that are based on earth-abundant, readily available, and low-cost elements are highly desirable for large-scale ESSs. In particular, electrochemistry that utilizes an iron-based redox reaction combined with Na guest ions would be an optimal choice for such batteries because of the nearly unlimited availability of Na from seawater and the ready

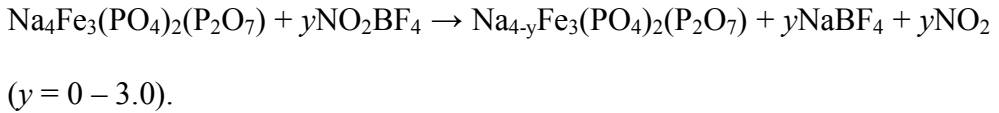
availability of iron. The intensive effort is focused on the development of new low-cost electrode materials. However, only a limited number of such materials has been reported to date ( $\text{NaFePO}_4$ ,  $\text{Na}_2\text{FePO}_4\text{F}$ ,  $\text{NaFeSO}_4\text{F}$ , and  $\text{Na}_2\text{FeP}_2\text{O}_7$ ).<sup>4-9</sup>

Recently, we reported a new iron-based mixed-polyanion compound,  $\text{Na}_4\text{Fe}_3(\text{PO}_4)_2(\text{P}_2\text{O}_7)$ , that shows promising electrochemical properties in both Na- and Li-ion cells.<sup>10</sup> A  $\text{Na}_4\text{Fe}_3(\text{PO}_4)_2(\text{P}_2\text{O}_7)$  electrode in a Na-ion cell exhibited an average voltage of 3.2 V (*vs.* Na), which is high compared to other polyanion-based cathodes, with a theoretical capacity of 129  $\text{mAhg}^{-1}$ .<sup>4-9</sup> Also, the open framework with three-dimensional (3D) Na channels enabled nearly full utilization of the theoretical capacity at reasonable current densities. However, a fundamental understanding of the electrochemical reaction mechanism and structural stability under various conditions, which is essential for further development of this promising cathode, had not yet been achieved.

Because the electrochemical reaction of a mixed-polyanion compound with a generally complex crystal structure may involve a complex structural evolution, we carefully combined neutron diffraction (ND), XRD, X-ray absorption spectroscopy (XAS), and first principles calculations for a structural characterization of  $\text{Na}_x\text{Fe}_3(\text{PO}_4)_2(\text{P}_2\text{O}_7)$  ( $1 \leq x \leq 4$ ). We discovered that the redox reaction of  $\text{Na}_x\text{Fe}_3(\text{PO}_4)_2(\text{P}_2\text{O}_7)$  in a Na-ion cell occurs mainly *via* a one-phase reaction with a small volumetric change of less than 4 %, despite significant distortion of the pyrophosphate ( $\text{P}_2\text{O}_7$ ) polyhedron occurring upon electrochemical cycling. Furthermore, the charged  $\text{Na}_x\text{Fe}_3(\text{PO}_4)_2(\text{P}_2\text{O}_7)$  ( $x < 4$ ) electrode is thermally stable at temperatures of more than 500 °C, irrespective of the state of charge (SOC).

## 3.2 Experimental

**Synthesis of  $\text{Na}_x\text{Fe}_3(\text{PO}_4)_2(\text{P}_2\text{O}_7)$  ( $1 \leq x \leq 4$ ):**  $\text{Na}_4\text{Fe}_3(\text{PO}_4)_2(\text{P}_2\text{O}_7)$  was synthesized via a conventional two-step solid-state method. The starting materials,  $\text{Na}_4\text{P}_2\text{O}_7$  (95 %, Aldrich),  $\text{Fe}_2\text{C}_2\text{O}_4 \cdot 2\text{H}_2\text{O}$  (99 %, Aldrich), and  $\text{NH}_4\text{H}_2\text{PO}_4$  (98 % ACS reagent, Aldrich), were mixed by ball milling with acetone for 24 h and dried at 70 °C for 12 h. The mixture was sintered at 300 °C for 6 h under flowing Ar. The calcined powder was then reground and pelletized under a pressure of 200 kg cm<sup>-2</sup> using a disk-shaped mold. The pelletized sample was again sintered at 500 °C for 12 h under an Ar flow. Desodiated samples,  $\text{Na}_x\text{Fe}_3(\text{PO}_4)_2(\text{P}_2\text{O}_7)$  ( $x < 4.0$ ), were prepared using stoichiometric amounts of  $y\text{NO}_2\text{BF}_4$  (95 %, Aldrich,  $y = 0 - 3.0$ ) in acetonitrile solvent (anhydrous, 99.8 %, Aldrich) according to the following reaction:



$\text{NO}_2\text{BF}_4$  is a strong oxidizing agent equivalent to a 4.8 V potential versus  $\text{Na}^+ / \text{Na}$ .<sup>11</sup> The solution was maintained at 60 °C for 12 h. Final products of the desodiated phases were obtained by washing with acetonitrile using a centrifuge.

**Characterization:** *Ex situ* XRD patterns of  $\text{Na}_x\text{Fe}_3(\text{PO}_4)_2(\text{P}_2\text{O}_7)$  ( $x = 1 - 4$ ) were recorded using an X-ray diffractometer (Bruker, D2 PHASER) with Cu K $\alpha$  radiation ( $\lambda = 1.5406 \text{ \AA}$ ). Each dataset was obtained over a  $2\theta$  range of 5 – 60 ° with a 0.01 step per 1.2 s. ND data of  $\text{NaFe}_3(\text{PO}_4)_2(\text{P}_2\text{O}_7)$  were collected using a

high-resolution powder diffractometer (HRPD) at the HANARO facility of the Korea Atomic Energy Research Institute. Data were recorded over a  $2\theta$  range of  $0 - 180^\circ$  with a step size of  $0.05^\circ$ . A constant wavelength of  $\lambda = 1.834333 \text{ \AA}$  was supplied by a Ge (331) single-crystal monochromator. *In situ* high-temperature XRD patterns were obtained over a  $2\theta$  range of  $5 - 60^\circ$  with a scan rate of  $1^\circ \text{ min}^{-1}$  at each temperature (room temperature  $\sim 650^\circ\text{C}$ ) using an X-ray diffractometer (Rigaku, D/MAX 2500). Particle size and crystallinity were examined by field-emission scanning electron microscopy (FESEM, SUPRA 55VP/Carl Zeiss) and transmission electron microscopy (TEM, Tecnai F20/FEI).

The valence states of iron in  $\text{Na}_x\text{Fe}_3(\text{PO}_4)_2(\text{P}_2\text{O}_7)$  ( $x = 1 - 4$ ) samples were investigated by X-ray absorption near-edge structure (XANES) analysis. The XAS experiments were performed at beamline 8C at the Pohang Accelerator Laboratory (PAL), Republic of Korea. Fe K-edge XANES spectra of  $\text{Na}_x\text{Fe}_3(\text{PO}_4)_2(\text{P}_2\text{O}_7)$  ( $x = 1 - 4$ ) samples were obtained in the transmission mode with an electron energy of 2.5 GeV and stored in the current range of 100 – 150 mA. Fe K-edge energy calibration was performed using Fe metal foil as a reference. A reference spectrum was simultaneously recorded for the *in situ* spectrum using Fe metal foil.

The structural stability of desodiated samples was investigated by DSC under an Ar atmosphere at a heating rate of  $10^\circ\text{C min}^{-1}$  from room temperature to  $650^\circ\text{C}$  using a SETSYS 16/18 thermogravimetric analyzer (SETARAM, France). Atomic ratios of Na to Fe in the powdered sample of  $\text{Na}_x\text{Fe}_3(\text{PO}_4)_2(\text{P}_2\text{O}_7)$  ( $x = 1 - 4$ ) were

determined by inductively coupled plasma-atomic emission spectroscopy (ICP-AES, Thermo Jarrel Ash, Polyscan 60E, USA).

**First-principles calculation method:** All *ab initio* calculations were performed with density functional theory (DFT) using the spin-polarized generalized-gradient approximation (GGA) from Perdew–Burke–Ernzerhof (PBE) and a Hubbard U parameter for Fe.<sup>12–15</sup> Additional details about the general method and parameters can be found in previous work.<sup>10</sup>

The crystal structure and Na/vacancy ordering of  $\text{Na}_x\text{Fe}_3(\text{PO}_4)_2(\text{P}_2\text{O}_7)$  ( $x = 1, 2, 3$ ) were evaluated by the *convex hull methodology*, which has been frequently used to evaluate the thermodynamic stability of intercalation compounds in battery fields.<sup>16–19</sup> We computed the *ab initio* energies of the 50 unique Na/vacancy orderings, which have been selected out of more than 8,000 random Na / vacancy orderings based on electrostatic energy calculations (by Ewald summation method<sup>20</sup>) for each integer  $x$  in  $\text{Na}_x\text{Fe}_3(\text{PO}_4)_2(\text{P}_2\text{O}_7)$ . Even though it is not as comprehensive as methods such as cluster expansions,<sup>21,22</sup> we believe 50 most plausible orderings out of  $\sim 8,000$  candidates based on electrostatic energy are the reasonable starting points for further *ab initio* calculations considering the heavy computational costs.

**Electrochemical tests:** Electrodes were fabricated using the active material  $\text{Na}_4\text{Fe}_3(\text{PO}_4)_2(\text{P}_2\text{O}_7)$ , super P, and polyvinylidene fluoride (PVDF) at a weight ratio of 70:20:10 in N-methyl-2-pyrrolidone (NMP) (99.5 %, Aldrich) solvent. The mixed slurry was pasted onto Al foil, and the NMP was allowed to evaporate at

120 °C for 3 h. The Na-ion cell was assembled in a CR2016-type coin cell in an Ar-filled glove box using sodium metal (sodium cube 99 %, Aldrich) as an anode and propylene carbonate (anhydrous 99.9 %, Aldrich) with 1 mol of NaClO<sub>4</sub> (99 %, Aldrich) as an electrolyte. A Celgard 2400 separator was used. Galvanostatic charge/discharge measurements were conducted at various C-rates (C/20, C/10 and C/5). The C-rate is based on the theoretical capacity of 129mAh g<sup>-1</sup>, which corresponds to 3 Na extraction / insertion of Na<sub>4</sub>Fe<sub>3</sub>(PO<sub>4</sub>)<sub>2</sub>(P<sub>2</sub>O<sub>7</sub>). Current densities for C/20, C/10 and C/5 rate measurements were 0.0117 mA cm<sup>-2</sup>, 0.0240 mA cm<sup>-2</sup> and 0.042 mA cm<sup>-2</sup>, respectively. The loading amount of active materials pasted onto an Al electrode was about 2 mg cm<sup>-2</sup>. *Ex situ* electrode samples were prepared in different charge and discharge states. Each sample was collected at a certain cut-off voltage with a 12 h relaxation time to measure the quasi-equilibrium state of the electrodes. Potentiostatic intermittent titration technique (PITT) measurements were carried out using a voltage step of 5 mV. The cut-off current in each individual titration corresponded to that of the C/50 rate. The voltage range for the PITT measurements was 2.0 – 4.3 V.

### 3.3 Results and Discussion

#### 3.3.1 Synthesis and electrochemical properties of $\text{Na}_4\text{Fe}_3(\text{PO}_4)_2(\text{P}_2\text{O}_7)$

$\text{Na}_4\text{Fe}_3(\text{PO}_4)_2(\text{P}_2\text{O}_7)$  was successfully synthesized using conventional solid-state methods at 500 °C. Rietveld refinement of the XRD pattern in Figure 3-1a confirmed that the structure of the as-prepared  $\text{Na}_4\text{Fe}_3(\text{PO}_4)_2(\text{P}_2\text{O}_7)$  can be indexed with the orthorhombic  $Pn2_1a$  space group.<sup>10</sup> The lattice parameters were  $a = 18.03744$  (11) Å,  $b = 6.52727$  (4) Å,  $c = 10.64413$  (7) Å, and  $V = 1253.189$  (1) Å<sup>3</sup>, which is comparable to those of the previous study, with low R-factors of  $R_p = 5.65$  %,  $R_I = 3.44$  %, and  $R_F = 2.14$  %.<sup>10</sup> A trace amount of maricite ( $\text{NaFePO}_4$ ) impurity (~4 wt%) was detected. The SEM and TEM analyses in Figure 3-2a and b show that the particle sizes of the crystalline  $\text{Na}_4\text{Fe}_3(\text{PO}_4)_2(\text{P}_2\text{O}_7)$  were about 100 – 200 nm.

The electrochemical properties of the  $\text{Na}_4\text{Fe}_3(\text{PO}_4)_2(\text{P}_2\text{O}_7)$  electrode in a Na-ion cell were examined at a C/20 rate in Figure 3-1b. The red and blue lines present the first and second charge/discharge profiles, respectively. About 82 % of the theoretical capacity was obtained at a C/20 rate with relatively good cycle stability. Good cycle performance was also observed at higher C-rates (C/20, C/10, and C/5) with only slight reduction of capacity, as shown in the inset of Figure 3-1 b.

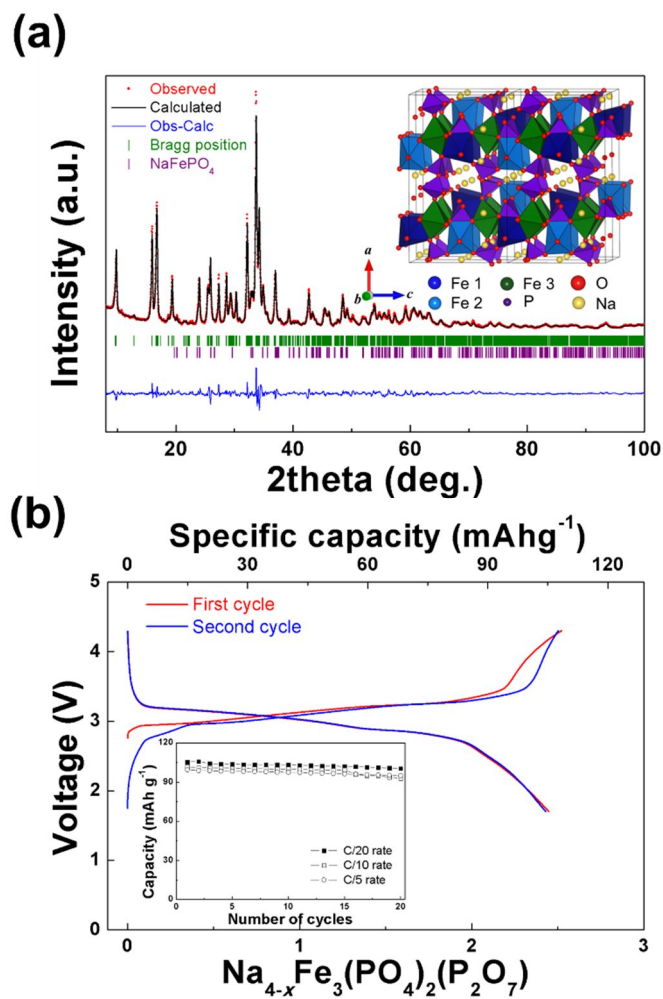


**Figure 3-1.** (a) Rietveld refinement of  $\text{Na}_4\text{Fe}_3(\text{PO}_4)_2(\text{P}_2\text{O}_7)$  using XRD. A schematic representation of  $\text{Na}_4\text{Fe}_3(\text{PO}_4)_2(\text{P}_2\text{O}_7)$  is illustrated in the inset. (b) Galvanostatic charge/discharge profiles of  $\text{Na}_4\text{Fe}_3(\text{PO}_4)_2(\text{P}_2\text{O}_7)$  in a Na-ion cell at

the  $C/20$  rate. The inset presents the cycle performance at various C-rates ( $C/20$ ,  $C/10$ , and  $C/5$ ).

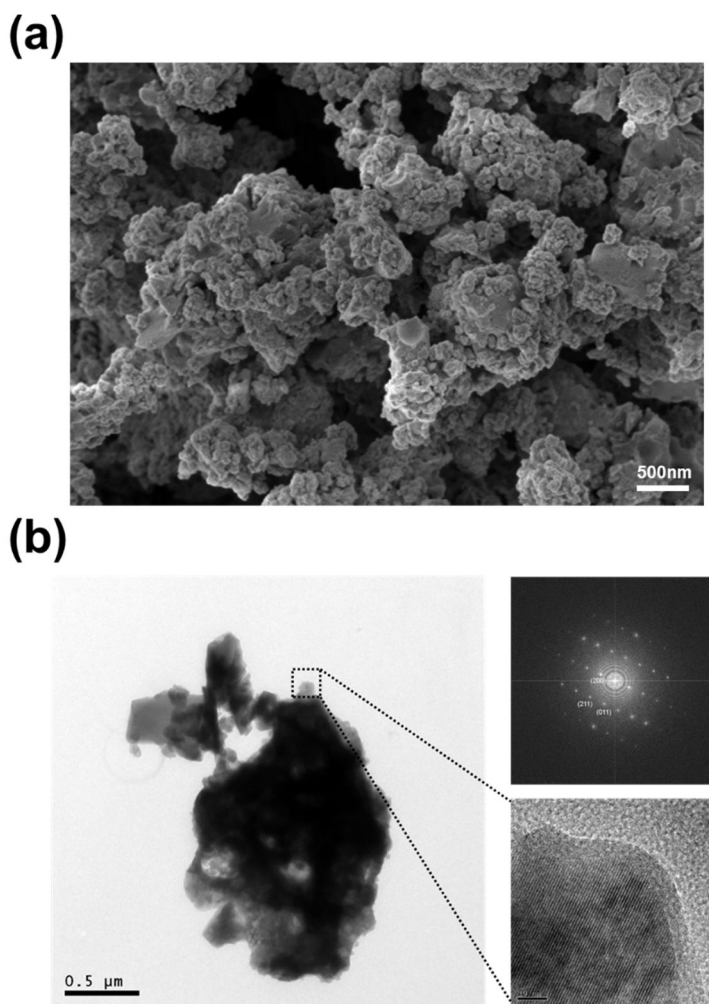


**Figure 3-2.** (a) Scanning electron microscopy (SEM) and (b) transmission electron microscopy (TEM) images of  $\text{Na}_4\text{Fe}_3(\text{PO}_4)_2(\text{P}_2\text{O}_7)$  showing that the primary particle sizes are about 100 – 200 nm and that the crystallinity is good.

### 3.3.2 Ex situ XRD studies on $\text{Na}_{4-x}\text{Fe}_3(\text{PO}_4)_2(\text{P}_2\text{O}_7)$

The structural evolution of the electrode material during cycling was analyzed by collecting electrodes at different states of charge in the first two cycles. Figure 3-3a shows *ex situ* XRD patterns of  $\text{Na}_x\text{Fe}_3(\text{PO}_4)_2(\text{P}_2\text{O}_7)$  during the charge/discharge process. Although the general patterns remained unchanged, implying a topotactic Na extraction from the mother structure, noticeable peak shifts of (200) and changes in peak intensity ratios, such as (011) / (210), were observed during the charge. The subsequent discharge to 1.7 V and further charge resulted in a completely reversible structural evolution. Closer examination of the amplified XRD patterns in the  $2\theta$  range of 8 to 19 ° in Figure 3-3b clearly shows peak shifts during the electrochemical reaction. Major peaks such as (200), (011), (002), and (210) gradually move to higher  $2\theta$  during Na extraction and return to their original values during reinsertion, which was attributed to continuous lattice volume change during cycling. The continuous peak shift in the series of *ex situ* XRD measurements is an indication of a one-phase-based electrochemical reaction of the  $\text{Na}_x\text{Fe}_3(\text{PO}_4)_2(\text{P}_2\text{O}_7)$  electrode in a Na rechargeable battery. This behavior is in clear contrast to those of simple polyanion compounds based on a similar Fe redox reaction, such as olivine  $\text{NaFePO}_4$  and  $\text{Na}_2\text{FeP}_2\text{O}_7$ , which are known to exhibit biphasic electrochemical reaction in Na-ion cells.<sup>5,9</sup>

For further structural characterization, we also prepared  $\text{Na}_x\text{Fe}_3(\text{PO}_4)_2(\text{P}_2\text{O}_7)$  ( $1 \leq x \leq 4$ ) samples from the chemical desodiation process. The XRD patterns of chemically prepared phases in Figure 3-4 show identical peak shifts and intensity

ratios as the *ex situ* XRD results. In Figure 3-5(a–d), the lattice parameters of chemically and electrochemically desodiated samples are plotted as a function of Na content; both show good agreement. Additionally, the figure shows the lattice parameters from first principles calculations. Experimental and theoretical quantification showed that  $a$ ,  $b$ , and  $V$  (lattice volume) linearly decrease upon Na extraction from  $\text{Na}_4\text{Fe}_3(\text{PO}_4)_2(\text{P}_2\text{O}_7)$ . This confirms again that the  $\text{Na}_x\text{Fe}_3(\text{PO}_4)_2(\text{P}_2\text{O}_7)$  electrode operates *via* a one-phase reaction during electrochemical cycling. However, we note that the  $c$  lattice parameter linearly increases up to  $x \sim 2$  but suddenly collapses at  $x \sim 1$ , contrary to the behavior of the  $a$  and  $b$  lattice parameters. This unusual phenomenon was reversibly observed from *ex situ* electrodes, as shown in Figure 3-6(a–d), and will be discussed later. Nevertheless, it is noteworthy that the volumetric change with the full charge and discharge is less than 4 %, which is one of the smallest volume changes reported for Na battery cathodes.<sup>4–9</sup> This small volume change is expected to contribute the stable cycle property as shown in Figure 3-1b. While the most of Na intercalation compounds show inherently large volumetric change during cycling due to large ionic size of Na compared to typical Li intercalation compounds, less than 4% volume change is remarkably small. We attributed this small volume change to the open and rigid framework of mixed polyanion crystal structure and believe this is one of the most important advantages of using mixed polyanion compounds as Na cathode materials.

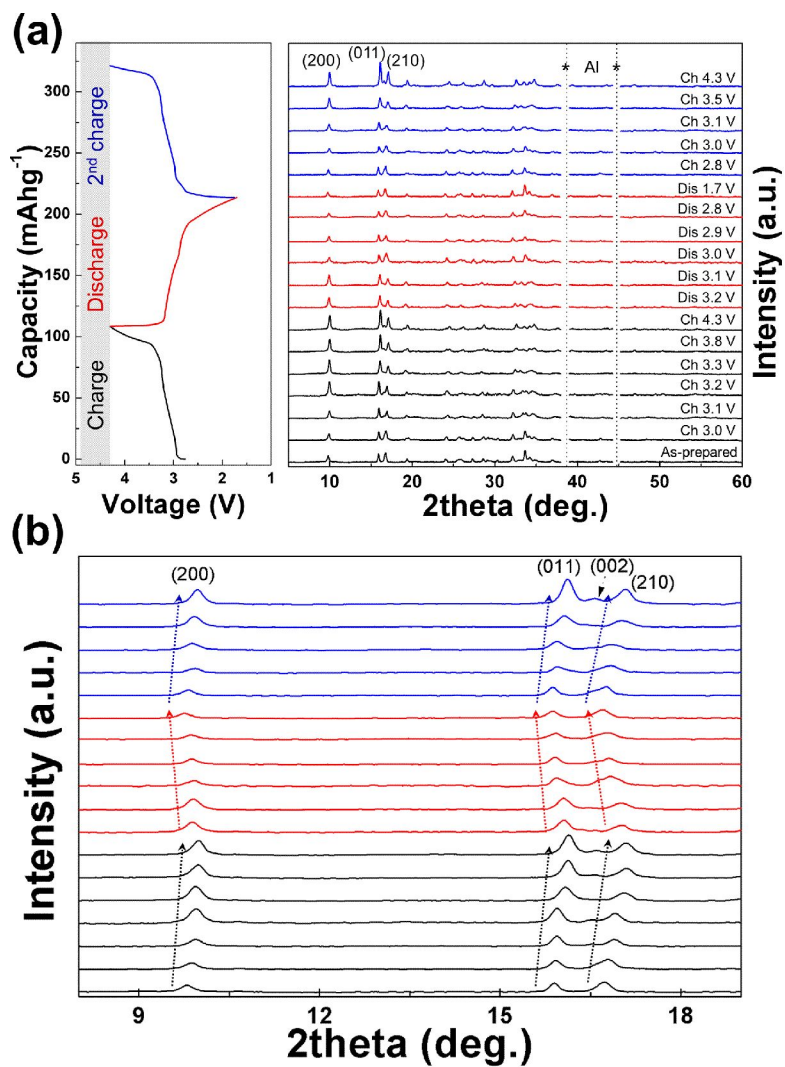


**Figure 3-3.** (a) *Ex situ* XRD patterns of  $\text{Na}_4\text{Fe}_3(\text{PO}_4)_2(\text{P}_2\text{O}_7)$  in a Na-ion cell during the charge/discharge process. Amplified XRD patterns in the  $2\theta$  range of 8 to  $19^\circ$  are illustrated in (b).

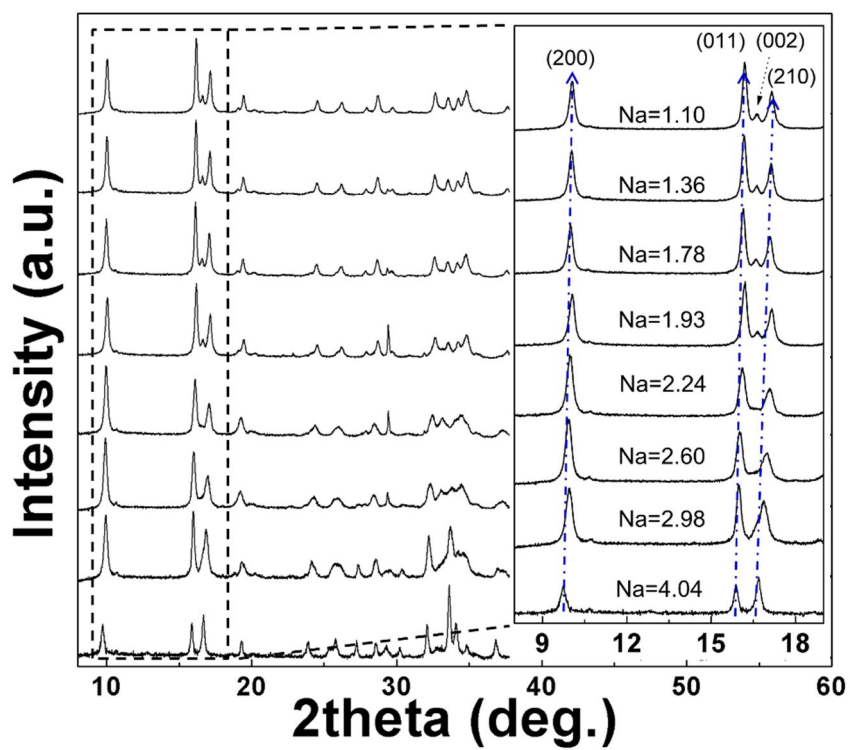


**Figure 3-4.** X-ray diffraction (XRD) patterns of  $\text{Na}_x\text{Fe}_3(\text{PO}_4)_2(\text{P}_2\text{O}_7)$  ( $1 \leq x \leq 4$ ) powder samples synthesized by chemical desodiation.

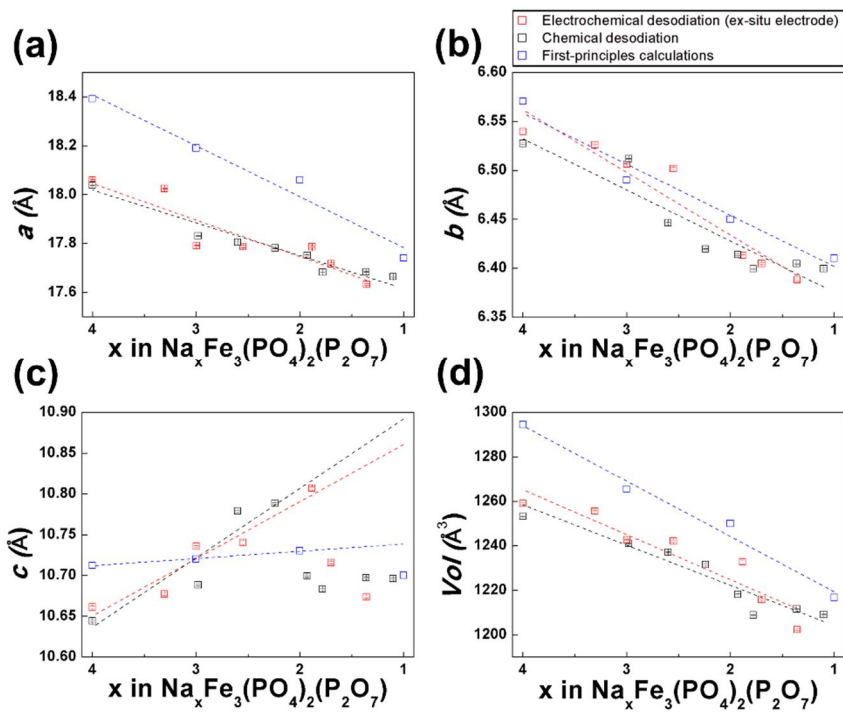


**Figure 3-5.** (a)  $a$ , (b)  $b$ , (c)  $c$  lattice parameters and (d) lattice volume change of  $\text{Na}_x\text{Fe}_3(\text{PO}_4)_2(\text{P}_2\text{O}_7)$  as a function of Na composition ( $x$ ).

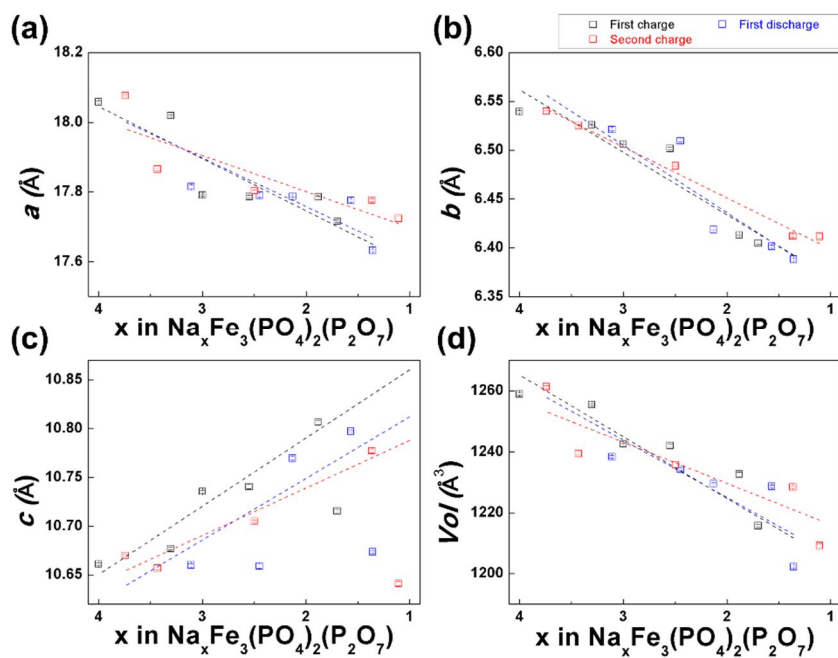


**Figure 3-6.** (a)  $a$ , (b)  $b$ , (c)  $c$  lattice parameters, and (d) lattice volume change of  $\text{Na}_x\text{Fe}_3(\text{PO}_4)_2(\text{P}_2\text{O}_7)$  as a function of Na composition ( $x$ ). The black, blue, and red rectangle markers represent the lattice parameters of *ex situ* electrode samples during the initial charge, discharge, and second charge, respectively.

### 3.3.3 Structural analyses of $\text{Na}_{4-x}\text{Fe}_3(\text{PO}_4)_2(\text{P}_2\text{O}_7)$ using first principles calculation

To understand the structural evolution during charge and discharge, we carefully investigated the intermediate states of  $\text{Na}_x\text{Fe}_3(\text{PO}_4)_2(\text{P}_2\text{O}_7)$  ( $x = 1 - 4$ ) using first principles calculations at each Na content. Figure 3-7 shows the formation energies of  $\text{Na}_x\text{Fe}_3(\text{PO}_4)_2(\text{P}_2\text{O}_7)$  structures with various Na-vacancy configurations as a function of Na composition. The convex hull  $\text{Na}_x\text{Fe}_3(\text{PO}_4)_2(\text{P}_2\text{O}_7)$  ( $1 \leq x \leq 4$ ) energy indicates that the presence of an intermediate phase is unlikely, implying a one-phase reaction of the  $\text{Na}_x\text{Fe}_3(\text{PO}_4)_2(\text{P}_2\text{O}_7)$  electrode, which is consistent with the *ex situ* results. The various Na-vacancy configurations from calculated intermediate states of  $\text{Na}_x\text{Fe}_3(\text{PO}_4)_2(\text{P}_2\text{O}_7)$  reveal that there are preferences in the order of Na extraction. Among four symmetrically different Na sites, shown in Table 3-1, the Na2 site in the five-coordinated polyhedra is extracted first from the structure. Once the Na in Na2 sites is fully extracted, half of the Na in Na1 and half of the Na in Na4 are extracted simultaneously. Finally, half of the Na in Na3 and the remaining Na in Na1 are extracted, leaving half of the Na3 and Na4 sites in  $\text{NaFe}_3(\text{PO}_4)_2(\text{P}_2\text{O}_7)$  occupied. The order of Na extraction is illustrated in Table 3-1. Sequential Na extraction from different sites also affects the charge distribution in transition metals. Figure 3-8 illustrates the number of spins integrated around Fe in the structure, from which the oxidation state of the transition metal can be estimated considering the spin configuration of the Fe orbitals in octahedral

coordination. As shown in Figure 3-8a, there are three different Fe sites in the structure. Initially, all of the Fe shows an identical magnetic moment corresponding to  $\text{Fe}^{2+}$  in Figure 3-8b. However, as Na is extracted from the Na2 site, the spin moment of the Fe1 site increases, indicating oxidation to  $\text{Fe}^{3+}$ , shown in Figure 3-8c. It is noteworthy that the Fe1 site is the nearest-neighbor site of Na2. Upon further desodiation, Figure 3-8d, Fe2 oxidizes from +2 to +3. We attribute the oxidation of Fe2 prior to Fe3 to effective electrostatic interactions among Fe ions. As the Fe3 octahedron shares an edge with the Fe1 octahedron, whose oxidation state is already +3, further oxidation to  $\text{Fe}^{3+}$  in Fe3 will be less favorable due to electrostatic repulsion. Instead, Fe in Fe2, which does not share an edge with Fe1, will be oxidized. Finally, Fe in the Fe3 site oxidizes to +3, as shown in Figure 3-8e.

The unusual *c*-lattice evolution at  $1 \leq x \leq 2$  in  $\text{Na}_x\text{Fe}_3(\text{PO}_4)_2(\text{P}_2\text{O}_7)$  can also be clearly detected at an atomic scale from first principles calculations. Figure 3-9(a-b) compares the calculated schematic structure of  $\text{Na}_2\text{Fe}_3(\text{PO}_4)_2(\text{P}_2\text{O}_7)$  and  $\text{NaFe}_3(\text{PO}_4)_2(\text{P}_2\text{O}_7)$ . The mother framework of  $\text{Na}_x\text{Fe}_3(\text{PO}_4)_2(\text{P}_2\text{O}_7)$  ( $x = 2, 1$ ) is not significantly altered with the Na ion extraction. However, distinct structural change is locally observed in  $\text{NaFe}_3(\text{PO}_4)_2(\text{P}_2\text{O}_7)$ . The amplified  $\text{FeO}_6$  and  $\text{PO}_4$  in Figure 3-9b show the significant distortion of  $\text{PO}_4$  (P4) in the  $\text{P}_2\text{O}_7$  dimer. It should be noted that this distortion was not observed in  $\text{Na}_4\text{Fe}_3(\text{PO}_4)_2(\text{P}_2\text{O}_7)$ ,  $\text{Na}_3\text{Fe}_3(\text{PO}_4)_2(\text{P}_2\text{O}_7)$ , and  $\text{Na}_2\text{Fe}_3(\text{PO}_4)_2(\text{P}_2\text{O}_7)$ . The distortion of  $\text{P}_2\text{O}_7$  also affects the Fe3 – Fe1 connection, which transforms from edge sharing to corner sharing when nearby Na4 sites are occupied. We believe that this structural change stems

from  $\text{Fe}^{3+} - \text{Fe}^{3+}$  repulsion in the  $[\text{Fe}_3\text{P}_2\text{O}_{13}]_\infty$  chain. As described earlier, Fe in the Fe3 site is oxidized to +3 when  $x$  finally reaches 1. Therefore, at the  $\text{NaFe}_3(\text{PO}_4)_2(\text{P}_2\text{O}_7)$  composition, Fe3 – Fe1 repulsion leads to corner sharing instead of edge sharing. The distance between Fe1 and Fe3 in  $\text{Na}_2\text{Fe}_3(\text{PO}_4)_2(\text{P}_2\text{O}_7)$  is 3.3 Å; Fe1 is in  $\text{Fe}^{3+}$  and Fe3 is in  $\text{Fe}^{2+}$ . However, the extraction of Na from  $\text{Na}_2\text{Fe}_3(\text{PO}_4)_2(\text{P}_2\text{O}_7)$  involving the oxidation of Fe in Fe3 sites does not lead to further reduction of the Fe1 – Fe3 distance. Instead, the  $\text{P}_2\text{O}_7$  dimer distorts such that the stronger electrostatic repulsion between the  $\text{Fe}^{3+}$  in Fe1, and Fe3 is effectively buffered. This distortion shifts the Fe1 site in the  $a$  direction, thus significantly reducing the  $c$  lattice parameter.

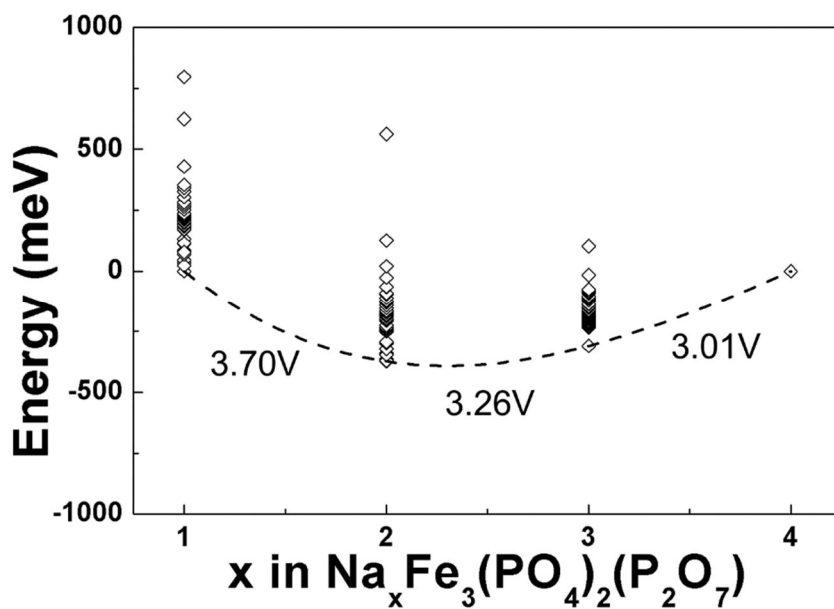
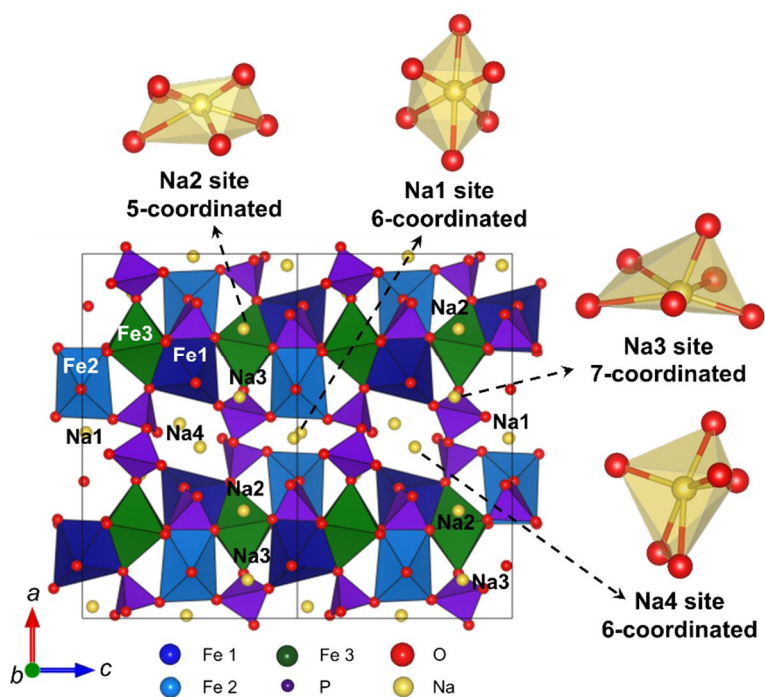


**Figure 3-7.** DFT formation energies of  $\text{Na}_x\text{Fe}_3(\text{PO}_4)_2(\text{P}_2\text{O}_7)$  at various configurations of  $x$ .



Composition	Space group	Na1 site	Na2 site	Na3 site	Na4 site
$\text{Na}_4\text{Fe}_3(\text{PO}_4)_2(\text{P}_2\text{O}_7)$	$Pn2_1a$	1.0	1.0	1.0	1.0
$\text{Na}_3\text{Fe}_3(\text{PO}_4)_2(\text{P}_2\text{O}_7)$	$Pn2_1a$	1.0	0	1.0	1.0
$\text{Na}_2\text{Fe}_3(\text{PO}_4)_2(\text{P}_2\text{O}_7)$	$Pn2_1a$	0.5	0	1.0	0.5
$\text{NaFe}_3(\text{PO}_4)_2(\text{P}_2\text{O}_7)$	$Pn2_1a$	0	0	0.5	0.5

**Table 3-1.** Schematic representations of  $\text{Na}_4\text{Fe}_3(\text{PO}_4)_2(\text{P}_2\text{O}_7)$  and order of sodium extraction from the structure of  $\text{Na}_x\text{Fe}_3(\text{PO}_4)_2(\text{P}_2\text{O}_7)$  ( $1 \leq x \leq 4$ ).

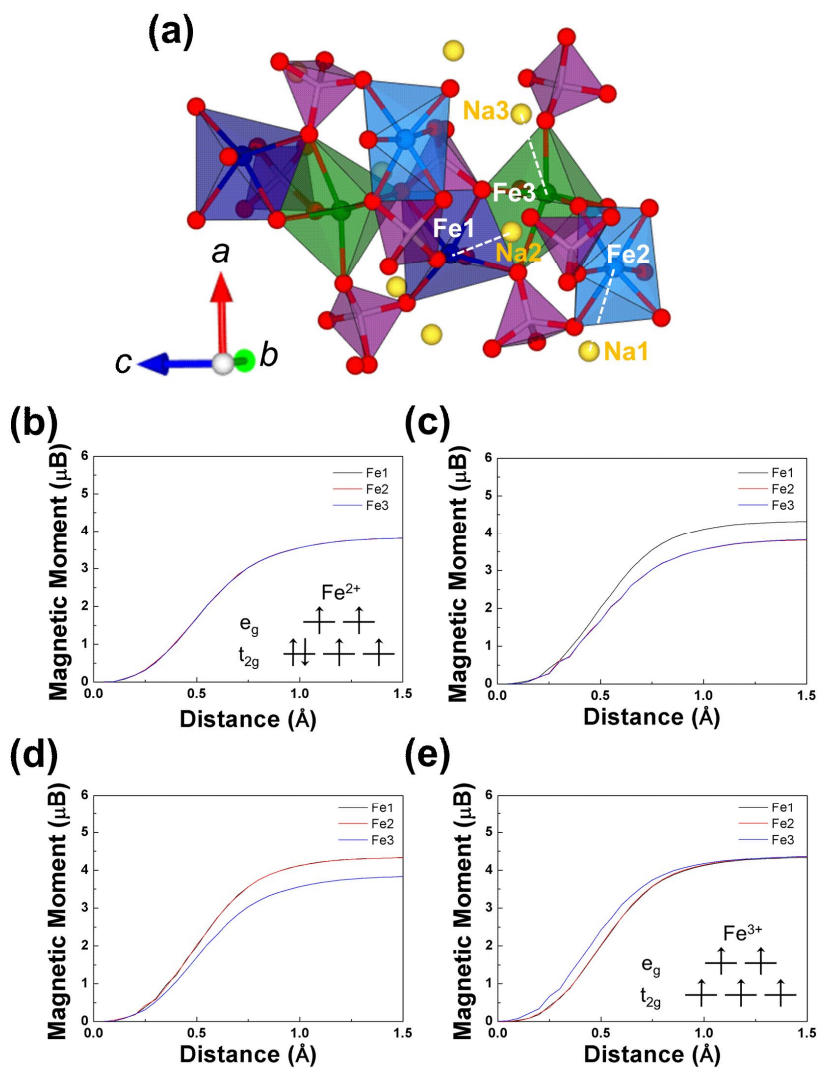


**Figure 3-8.** (a) Local structure schematics of  $\text{Na}_x\text{Fe}_3(\text{PO}_4)_2(\text{P}_2\text{O}_7)$  around Fe sites and integrated spin as a function of integration radius around Fe in  $\text{Na}_x\text{Fe}_3(\text{PO}_4)_2(\text{P}_2\text{O}_7)$  ((b)  $x = 4$ , (c)  $x = 3$ , (d)  $x = 2$ , and (e)  $x = 1$ ).

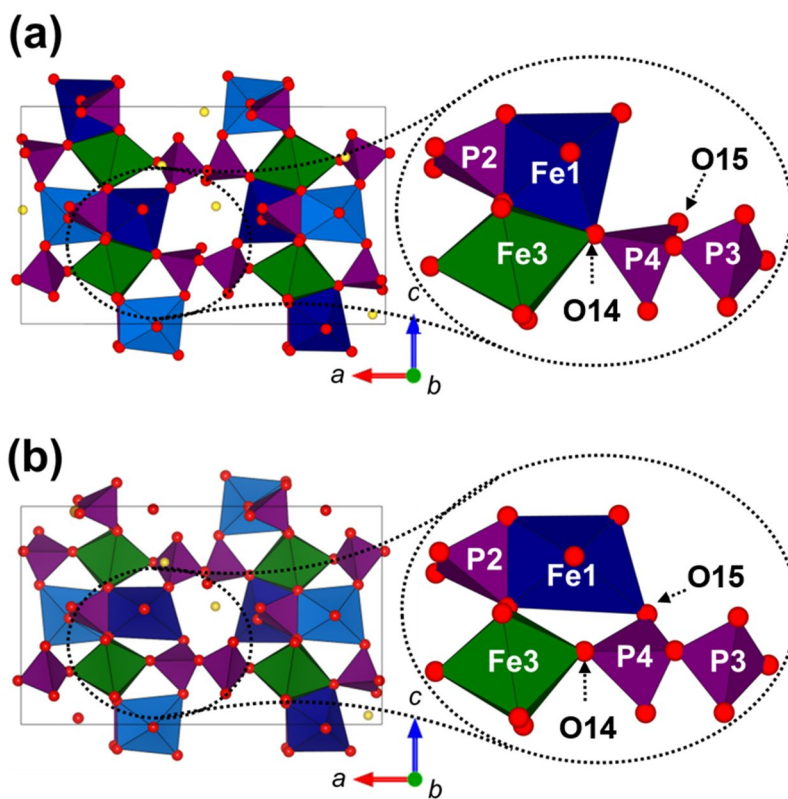


**Figure 3-9.** Structure schematics of  $\text{Na}_x\text{Fe}_3(\text{PO}_4)_2(\text{P}_2\text{O}_7)$  at (a)  $x = 2$  and (b)  $x = 1$  from first principles calculations.

### 3.3.4 Neutron diffraction studies on $\text{NaFe}_3(\text{PO}_4)_2(\text{P}_2\text{O}_7)$

This theoretical explanation was further confirmed by ND refinements of  $\text{NaFe}_3(\text{PO}_4)_2(\text{P}_2\text{O}_7)$ . Figure 3-10 presents the ND Rietveld refinement of  $\text{NaFe}_3(\text{PO}_4)_2(\text{P}_2\text{O}_7)$  and the corresponding local structure around the Fe1 and Fe3 sites. Detailed structural information from the ND patterns is presented in Table 3-2 and 3-3. It is interesting to note that the significant  $\text{P}_2\text{O}_7$  distortion in  $\text{NaFe}_3(\text{PO}_4)_2(\text{P}_2\text{O}_7)$  leads to a shift from edge sharing to corner sharing of  $\text{FeO}_6$  polyhedra between the Fe1 and Fe3 sites, in striking agreement with our first principles calculation. We further note that the local distortion in  $\text{NaFe}_3(\text{PO}_4)_2(\text{P}_2\text{O}_7)$  can affect Na diffusion. Since the local distortion involves a shift of Fe in Fe1 and the  $\text{P}_2\text{O}_7$  dimer that narrows Na diffusion tunnels, as indicated with the arrow in Figure 3-10b, the mobility of Na is potentially reduced at this composition of  $x \sim 1$ . As this distortion is mainly observed at  $1 \leq x \leq 2$  in  $\text{Na}_x\text{Fe}_3(\text{PO}_4)_2(\text{P}_2\text{O}_7)$  (Table in Figure 3-10b), it is believed to reduce the Na de/intercalation kinetics particularly in this region, and therefore to increase the polarization. Based on these results, we speculate that the incomplete utilization of Na (~82 % of theoretical capacity in Figure 3-1b) can be attributed to a large polarization developing at the last stage of charging, despite its apparent high rate capability as reflected in the negligible capacity reduction from C/20 to C/5.

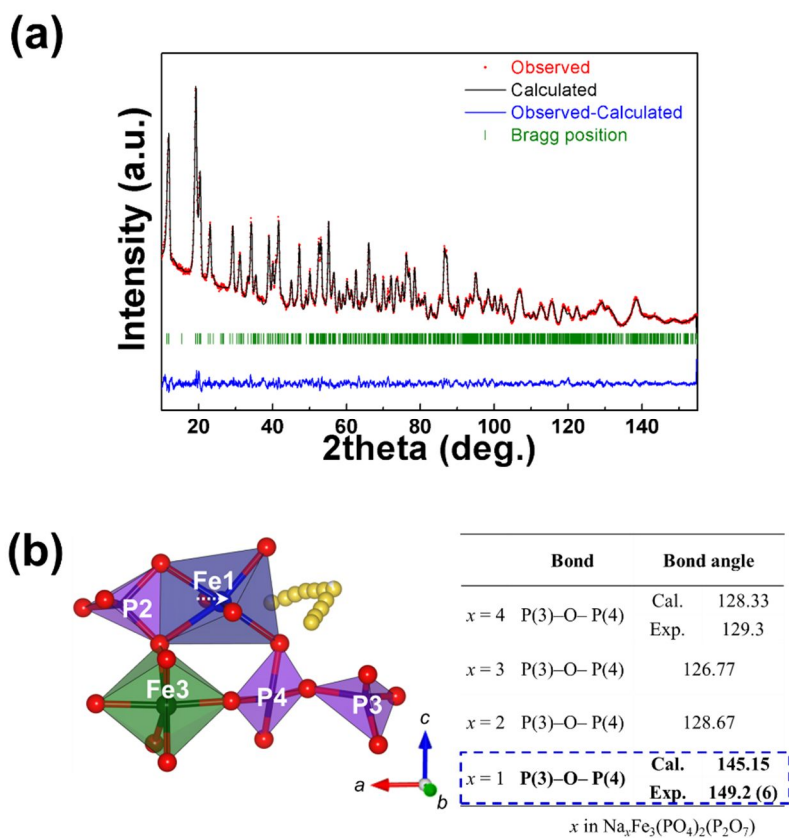


**Figure 3-10.** (a) Rietveld refinement of  $\text{NaFe}_3(\text{PO}_4)_2(\text{P}_2\text{O}_7)$  using ND. (b) Local structure schematics around Fe1 and P(3) – O – P(4) bond angle comparison table as a function of Na content ( $x$ ) in  $\text{Na}_x\text{Fe}_3(\text{PO}_4)_2(\text{P}_2\text{O}_7)$  from ND analysis.

**Table 3-2.** Detailed structural information of  $\text{NaFe}_3(\text{PO}_4)_2(\text{P}_2\text{O}_7)$  analyzed by Rietveld refinement of the ND pattern.

Formula	$\text{NaFe}_3(\text{PO}_4)_2(\text{P}_2\text{O}_7)$
Crystal system	Orthorhombic
Space group	$\text{Pn}2_1\text{a}$ (No. 33)
Lattice parameters	
$a$ (Å)	17.6613 (9)
$b$ (Å)	6.3966 (4)
$c$ (Å)	10.7012 (7)
Unitcell volume (Å <sup>3</sup> )	1208.948 (1)
Formula weight	531.42104
Source	Neutron
Temperature (K)	300K
Wave length (Å)	1.834333
$2\theta$ range	0 – 180°
Number of data points	3200
Number of reflections	905
$R_p$ (%)	1.91
$R_I$ (%)	1.82
$R_F$ (%)	0.999
$R_{wp}$ (%)	2.42
$\chi^2$	3.86

Atom	<i>x</i>	<i>y</i>	<i>z</i>	B <sub>iso</sub>	Occupancy
Fe1	0.3587 (5)	0.113 (4)	0.496 (1)	0.93 (9)	1.00
Fe2	0.1516 (4)	0.603 (4)	0.500 (1)	0.93 (9)	1.00
Fe3	0.2446 (7)	0.350 (4)	0.7652 (9)	0.93 (9)	1.00
P1	0.3064 (11)	0.595 (5)	0.496 (2)	0.6 (1)	1.00
P2	0.1997 (9)	0.102 (5)	0.493 (2)	0.6 (1)	1.00
P3	0.5733 (11)	0.472 (5)	0.742 (2)	0.6 (1)	1.00
P4	0.4279 (10)	0.248 (4)	0.752 (2)	0.6 (1)	1.00
Na3	0.409 (4)	0.468 (10)	0.312 (6)	1.0 (3)	0.13 (1)
Na4	0.485 (1)	0.794 (3)	0.534 (1)	1.0 (3)	0.87 (1)
O1	0.2387 (8)	0.5743 (5)	0.611 (2)	0.22 (5)	1.00
O2	0.3496 (10)	0.410 (4)	0.490 (2)	0.22 (5)	1.00
O3	0.3469 (9)	0.808 (5)	0.533 (1)	0.22 (5)	1.00
O4	0.2517 (8)	0.605 (4)	0.384 (2)	0.22 (5)	1.00
O5	0.2551 (9)	0.156 (5)	0.608 (2)	0.22 (5)	1.00
O6	0.1428 (10)	-0.053 (4)	0.520 (1)	0.22 (5)	1.00
O7	0.2518 (8)	0.078 (5)	0.395 (2)	0.22 (5)	1.00
O8	0.1427 (8)	0.327 (4)	0.462 (1)	0.22 (5)	1.00
O9	0.5107 (8)	0.325 (4)	0.7194 (10)	0.22 (5)	1.00
O10	0.5845 (7)	0.624 (5)	0.859 (1)	0.22 (5)	1.00
O11	0.6395 (8)	0.314 (4)	0.768 (1)	0.22 (5)	1.00
O12	0.5748 (8)	0.653 (4)	0.661 (1)	0.22 (5)	1.00
O13	0.4251 (9)	0.162 (4)	0.871 (1)	0.22 (5)	1.00
O14	0.3627 (7)	0.374 (4)	0.766 (2)	0.22 (5)	1.00
O15	0.4440 (7)	0.160 (4)	0.605 (1)	0.22 (5)	1.00

**Table 3-3.** Bond valence parameters of each atom in  $\text{Na}_x\text{Fe}_3(\text{PO}_4)_2(\text{P}_2\text{O}_7)$  ( $x = 1, 4$ ).

Atomic site	Coordination		Average Distance		Expected values	Bond valence	
	DFT	Exp.	DFT	Exp.		DFT	Exp.
Fe1	6.00	6.00	2.06 (2)	2.05 (1)	3.0	2.7 (1)	2.9 (1)
Fe2	6.00	6.00	2.0602 (3)	2.01 (1)	3.0	2.83 (5)	3.3 (1)
Fe3	6.00	6.00	2.06 (3)	2.05 (1)	3.0	2.8 (1)	2.78 (8)
P1	4.00	4.00	1.5547 (4)	1.56 (2)	5.0	4.746 (2)	4.8 (2)
P2	4.00	4.00	1.5564 (3)	1.56 (2)	5.0	4.73 (1)	5.1 (2)
P3	4.00	4.00	1.549 (4)	1.52 (2)	5.0	4.82 (6)	5.2 (2)
P4	4.00	4.00	1.551 (5)	1.52 (1)	5.0	4.82 (4)	5.5 (2)
Na3	4.00	6.00	2.4737	2.38 (1)	1.0	1.034	1.07 (4)
Na4	5.00	6.00	2.4842	2.427 (8)	1.0	0.991	1.09 (3)
O1	3.00	3.00	1.97 (2)	1.95 (2)	-2.0	-1.82 (3)	-1.67 (7)
O2	2.13	3.00	2.05 (1)	1.84 (2)	-2.0	-1.86 (3)	-2.4 (2)
O3	2.87	2.50	1.9 (1)	2.01 (2)	-2.0	-1.89 (3)	-1.8 (1)
O4	3.00	3.00	1.93 (1)	1.91 (1)	-2.0	-1.90 (3)	-2.1 (1)
O5	3.00	3.00	1.89 (1)	1.97 (1)	-2.0	-1.97 (6)	-1.72 (8)
O6	2.00	2.50	1.9 (2)	1.83 (2)	-2.0	-1.84 (4)	-1.9 (1)
O7	3.00	2.50	1.9 (1)	1.87 (1)	-2.0	-1.72 (7)	-2.6 (1)
O8	2.00	2.00	1.746 (8)	1.80 (3)	-2.0	-1.86 (1)	-1.5 (1)
O9	3.00	2.50	1.8 (2)	2.12 (1)	-2.0	-2.10 (4)	-2.6 (1)
O10	2.00	2.50	1.9 (2)	1.76 (2)	-2.0	-1.95 (1)	-1.7 (1)
O11	2.13	2.50	1.9 (1)	2.00 (1)	-2.0	-1.86 (4)	-1.8 (1)
O12	3.00	3.00	1.9 (2)	1.96 (1)	-2.0	-2.1 (1)	-2.3 (2)
O13	2.00	2.00	1.735 (7)	1.68 (2)	-2.0	-1.90 (1)	-2.4 (1)
O14	2.00	3.00	1.97 (4)	1.75 (2)	-2.0	-1.89 (8)	-2.1 (1)
O15	3.74	3.00	2.04 (4)	2.08 (1)	-2.0	-1.84 (3)	-1.92 (7)

Atomic site	Coordination		Average Distance		Expected values	Bond valence	
	DFT	Exp.	DFT	Exp.		DFT	Exp.
Fe1	6.00	6.00	2.169	2.138 (9)	2.0	1.913	2.09 (6)
Fe2	6.00	6.00	2.168	2.156 (9)	2.0	1.879	1.97 (6)
Fe3	5.00	5.00	2.114	2.10 (1)	2.0	1.812	1.86 (6)
P1	4.00	4.00	1.557	1.56 (1)	5.0	4.713	4.7 (2)
P2	4.00	4.00	1.560	1.54 (1)	5.0	4.669	5.1 (2)
P3	4.00	4.00	1.562	1.57 (1)	5.0	4.680	4.6 (2)
P4	4.00	4.00	1.564	1.51 (1)	5.0	4.673	5.6 (2)
Na1	6.00	6.00	2.412	2.37 (1)	1.0	1.186	1.37 (5)
Na2	7.00	7.00	2.532	2.51 (1)	1.0	1.000	1.07 (4)
Na3	5.00	5.00	2.451	2.44 (1)	1.0	0.933	1.00 (4)
Na4	6.00	6.00	2.537	2.51 (1)	1.0	0.882	0.94 (3)
O1	4.00	4.00	2.123	2.10 (1)	-2.0	1.897	2.00 (9)
O2	4.00	4.00	2.217	2.17 (1)	-2.0	1.874	1.75 (9)
O3	4.00	4.00	2.124	2.16 (2)	-2.0	1.947	2.0 (1)
O4	4.00	4.00	2.069	2.04 (1)	-2.0	1.987	2.09 (8)
O5	4.00	4.00	2.116	2.10 (1)	-2.0	1.915	1.81 (7)
O6	4.00	4.00	2.224	2.23 (2)	-2.0	1.816	1.8 (1)
O7	4.00	4.00	2.121	2.09 (1)	-2.0	1.874	2.09 (9)
O8	4.00	4.00	2.159	2.13 (2)	-2.0	1.891	2.4 (2)
O9	3.00	3.00	1.983	1.94 (2)	-2.0	1.902	2.00 (9)
O10	4.00	4.00	2.159	2.10 (1)	-2.0	1.886	1.81 (7)
O11	3.00	3.00	2.029	2.05 (1)	-2.0	1.788	1.79 (9)
O12	4.00	4.00	2.121	2.06 (1)	-2.0	2.002	2.2 (1)
O13	4.00	4.00	2.114	2.10 (1)	-2.0	1.959	2.5 (1)
O14	3.00	3.00	2.071	2.04 (1)	-2.0	1.745	2.22 (9)
O15	4.00	4.00	2.199	2.19 (1)	-2.0	1.858	1.83 (8)

### 3.3.5 XANES analyses of $\text{Na}_{4-x}\text{Fe}_3(\text{PO}_4)_2(\text{P}_2\text{O}_7)$

The desodiation mechanism was further analyzed by XANES to monitor the redox reaction. Figure 3-11a clearly shows that the XANES spectrum shifts to the right during the first charging, indicating oxidation of iron from  $\text{Fe}^{2+}$  to  $\text{Fe}^{3+}$ . An  $\text{Na}_4\text{Fe}_3(\text{PO}_4)_2(\text{P}_2\text{O}_7)$  powder sample was used as an  $\text{Fe}^{2+}$  reference, since its oxidation state was previously identified using Fe Mössbauer analysis.<sup>10</sup> The XANES spectrum shifts back to lower valence states with progress of the discharge reaction. Finally, iron recovers its original oxidation state,  $\text{Fe}^{2+}$ , at the discharge state of 1.7 V, as shown in Figure 3-11b. The tendency of XANES spectra during the second cycle was almost identical to that of the initial charge state (see Figure 3-12). The XANES spectra of the as-prepared state and of the end of the charge/discharge states are compared in Figure 3-11c. The iron oxidation state of the as-prepared and cycled electrode was consistent with the  $\text{Fe}^{2+}$  reference material, and the oxidation state of fully charged samples corresponded to  $\text{Fe}^{3+}$ . Supplementary XANES spectra from chemically prepared samples indicated the same trend, and are provided in Figure 3-13.

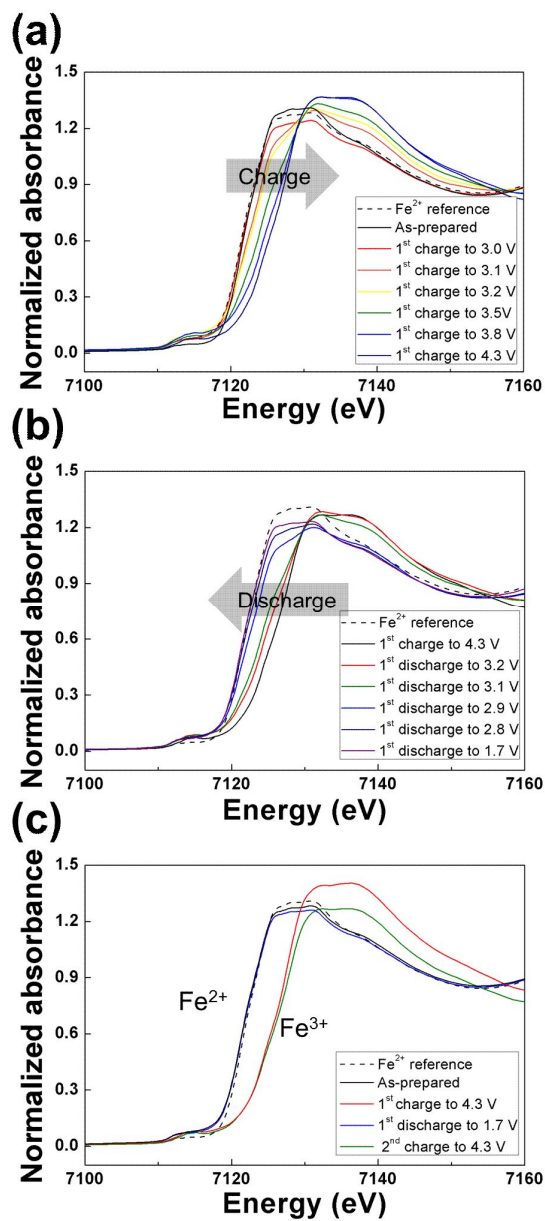


**Figure 3-11.** XANES spectra during first (a) charge and (b) discharge. XANES spectra of the as-prepared state and of the end of charge and end of discharge states are shown in (c).

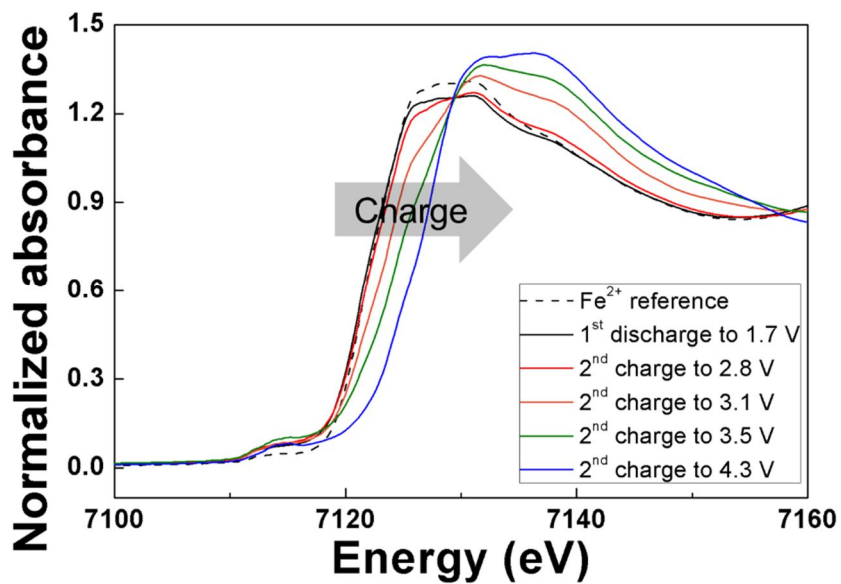


**Figure 3-12.** X-ray absorption near-edge structure (XANES) spectra of the  $\text{Na}_x\text{Fe}_3(\text{PO}_4)_2(\text{P}_2\text{O}_7)$  electrode during the second charge.

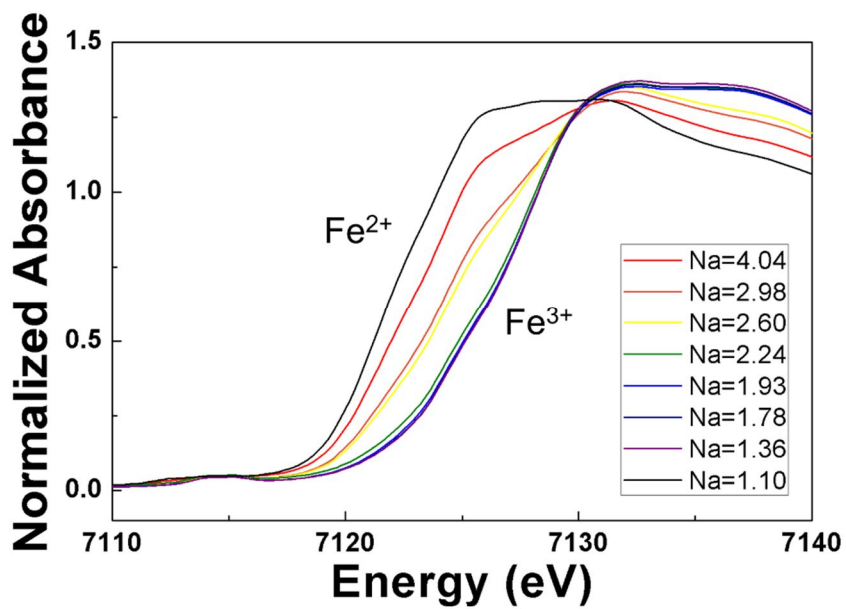


**Figure 3-13.** XANES spectra of chemically prepared  $\text{Na}_x\text{Fe}_3(\text{PO}_4)_2(\text{P}_2\text{O}_7)$  ( $1 \leq x \leq 4$ ) samples.

### 3.3.6 Electrochemical mechanism studies using GITT and PITT

The nature of the de/intercalation process of  $\text{Na}_4\text{Fe}_3(\text{PO}_4)_2(\text{P}_2\text{O}_7)$  was additionally confirmed from electrochemical PITT measurements, as shown in Figure 3-14(a,b). The PITT experiment was carried out using a voltage step of 5 mV and a cut-off current corresponding to the C/50 rate. “Cottrel-type” curves that represent the one-phase reaction were observed throughout the range of the charge and discharge steps.<sup>23</sup> This result is consistent with the *ex situ* XRD and first principles calculations.

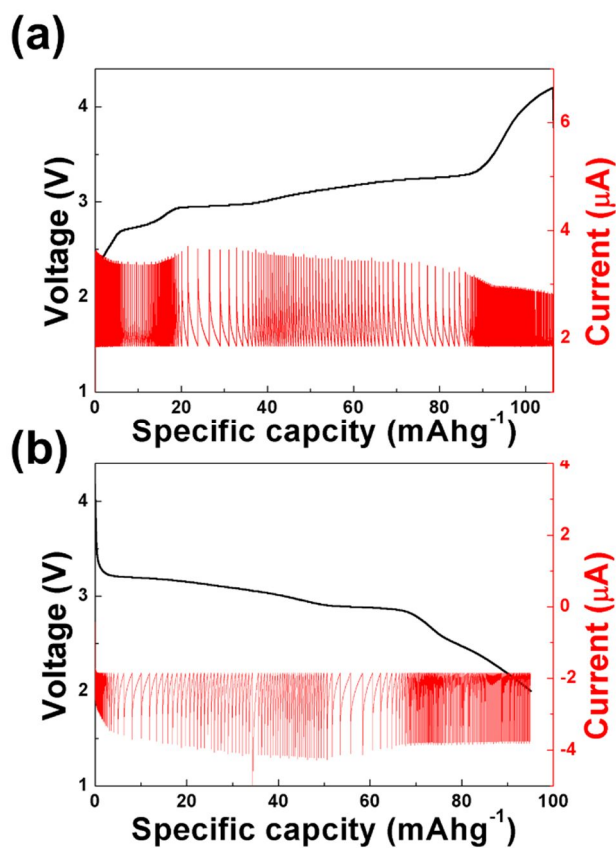


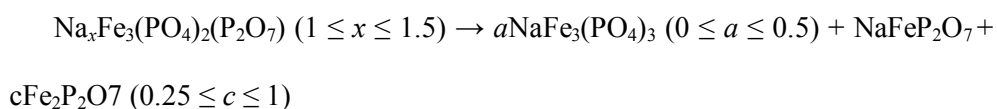
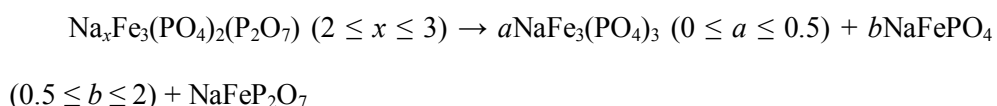
**Figure 3-14.** PITT measurements of  $\text{Na}_4\text{Fe}_3(\text{PO}_4)_2(\text{P}_2\text{O}_7)$  during (a) charging and (b) discharging.

### 3.3.7 Phase diagram of $\text{Na}_{4-x}\text{Fe}_3(\text{PO}_4)_2(\text{P}_2\text{O}_7)$

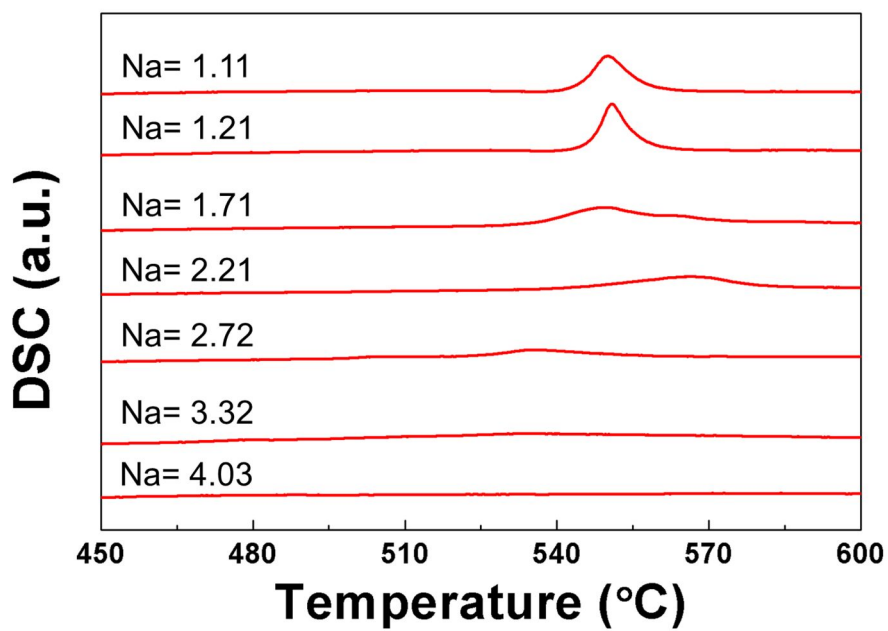
Finally, the safety of the  $\text{Na}_4\text{Fe}_3(\text{PO}_4)_2(\text{P}_2\text{O}_7)$  electrode at high temperature was examined by evaluating the thermal stability of partially desodiated phases. A series of samples with different SOC's was prepared through chemical desodiation, and the stability of the samples was investigated using DSC and *in situ* high-temperature XRD analyses. Figure 3-15 shows the DSC curves of partially charged samples, which illustrate that all of the partially charged samples were stable up to 500 °C. Exothermal peaks began to appear only above 500 °C for each sample, and the intensity of the exothermal peaks increased with the SOC. *In situ* high temperature XRD, Figure 3-16(a–d), also confirmed the superior thermal stability of  $\text{Na}_x\text{Fe}_3(\text{PO}_4)_2(\text{P}_2\text{O}_7)$  irrespective of the SOC. The desodiated phases followed various decomposition routes depending on the remaining Na composition. For example, the slightly desodiated sample  $\text{Na}_{3.2}\text{Fe}_3(\text{PO}_4)_2(\text{P}_2\text{O}_7)$  decomposed mainly into Na-rich compounds, such as  $\text{Na}_3\text{Fe}_2(\text{PO}_4)_3$  and  $\text{NaFePO}_4$ , starting at 550 to 650 °C. As the Na composition in the phase decreased, Na-poor phases such as  $\text{NaFe}_3(\text{PO}_4)_3$ ,  $\text{NaFeP}_2\text{O}_7$ , and  $\text{Fe}_2\text{P}_2\text{O}_7$  were preferentially evolved as decomposition products. The fully charged sample,  $\text{NaFe}_3(\text{PO}_4)_2(\text{P}_2\text{O}_7)$ , yielded  $\text{Fe}_2\text{P}_2\text{O}_7$  and  $\text{NaFeP}_2\text{O}_7$  at the same temperature.<sup>10</sup>

Figure 3-17 summarizes the decomposed phases of  $\text{Na}_x\text{Fe}_3(\text{PO}_4)_2(\text{P}_2\text{O}_7)$  ( $1 < x < 4$ ) upon heating. Solid solution of  $\text{Na}_x\text{Fe}_3(\text{PO}_4)_2(\text{P}_2\text{O}_7)$  ( $1 < x < 4$ ) was maintained

up to 530 °C at all SOC. However, at temperatures higher than 530 °C, the phases began to decompose, yielding a few different products depending on the remaining Na content in the phases. Although it is difficult to precisely describe the decomposition reaction as a chemical formula due to the complex feature involving many phases, the decomposition process of  $\text{Na}_x\text{Fe}_3(\text{PO}_4)_2(\text{P}_2\text{O}_7)$  ( $x \leq 3$ ) can be estimated as follows.

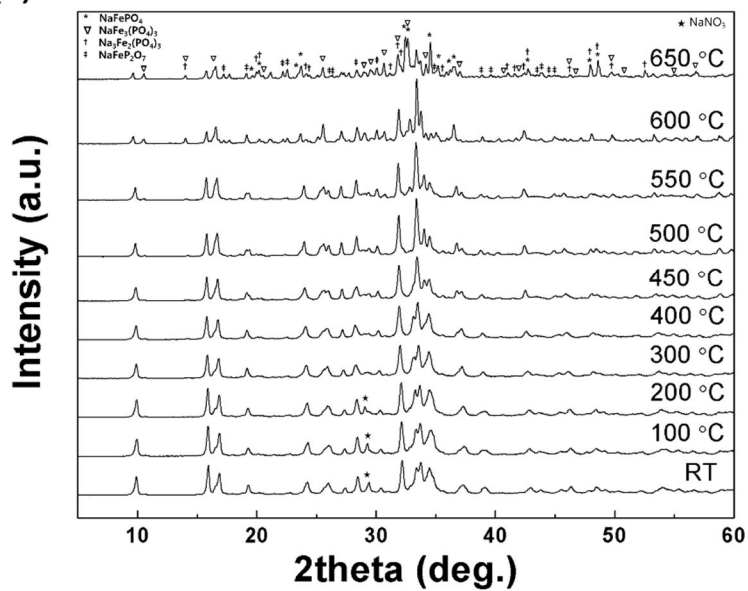


The high stability at all SOCs is notable and is comparable to that of the safest polyanion cathodes for Na rechargeable batteries,<sup>9,24,25</sup> illustrating the inherently safe characteristics of low voltage sodium-based polyanion compounds which have low oxygen chemical potential in desodiated phases.<sup>19,26</sup> We believe that the outstanding safety characteristics of  $\text{Na}_x\text{Fe}_3(\text{PO}_4)_2(\text{P}_2\text{O}_7)$  ( $x < 4$ ) at all SOCs is one of its strongest advantages as a cathode for Na rechargeable battery. However, it should be also noted that for the safe Na batteries; the safety characteristics of other components, not only the electrodes, should be considered, since the recent report has shown that the use of perchlorate salts in the electrolyte, for example, can cause a danger for explosion.<sup>27</sup>

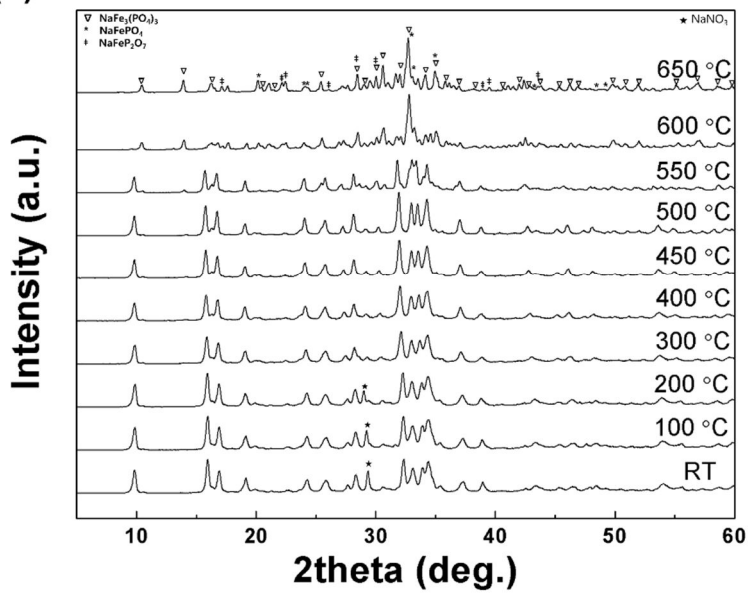


**Figure 3-15.** Differential scanning calorimetry (DSC) spectra of  $\text{Na}_x\text{Fe}_3(\text{PO}_4)_2(\text{P}_2\text{O}_7)$  ( $1 \leq x \leq 4$ ).

(a)



(b)



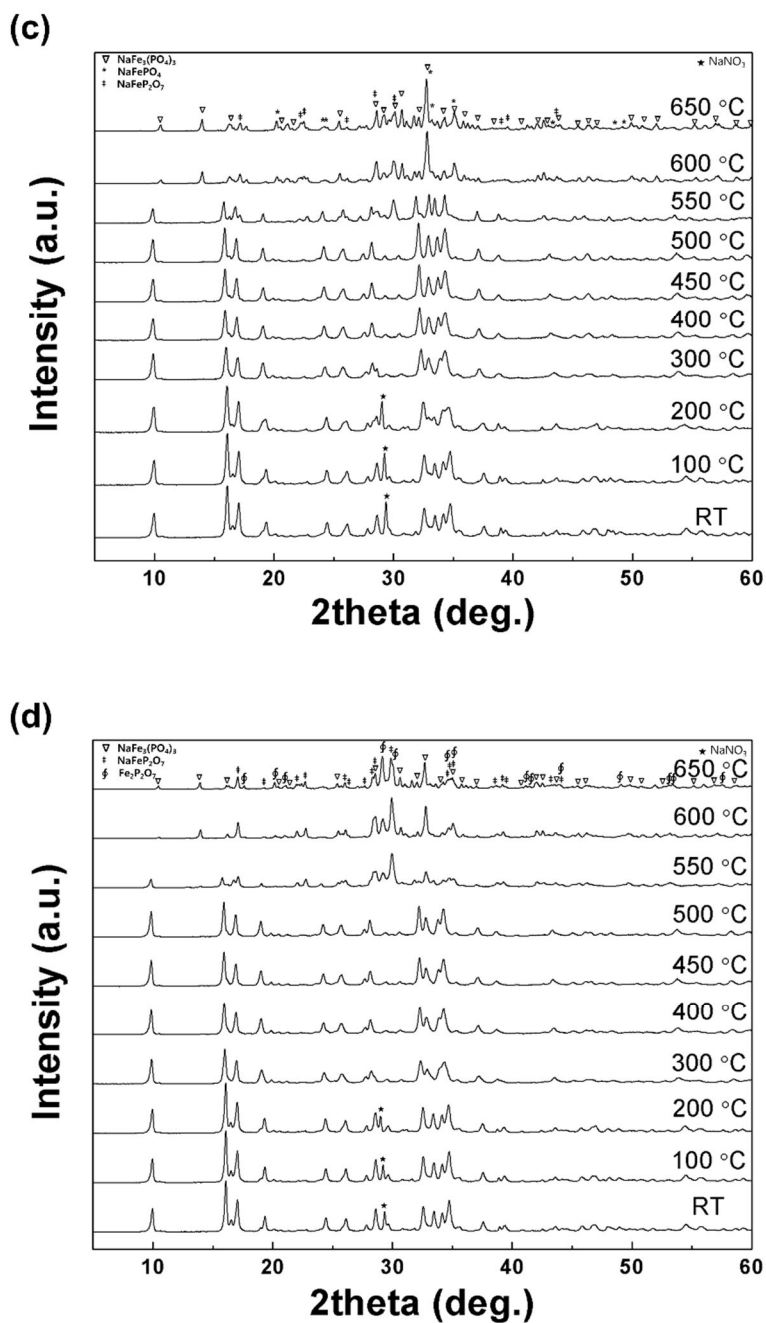


**Figure 3-16.** *In situ* high-temperature XRD of desodiated powder samples of  $\text{Na}_x\text{Fe}_3(\text{PO}_4)_2(\text{P}_2\text{O}_7)$  at (a)  $x = 3.2$ , (b)  $x = 2.72$ , (c)  $x = 2.21$ , and (d)  $x = 1.71$ .

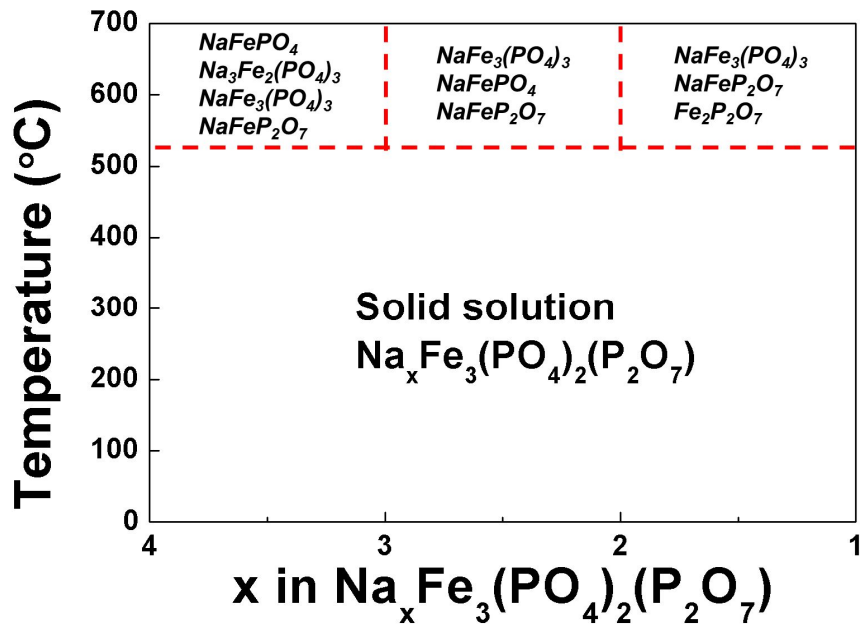


Figure 3-17. Phase diagram of  $\text{Na}_x\text{Fe}_3(\text{PO}_4)_2(\text{P}_2\text{O}_7)$  ( $1 < x < 4$ ).

### 3.4 Conclusion

Detailed structural evolution of  $\text{Na}_4\text{Fe}_3(\text{PO}_4)_2(\text{P}_2\text{O}_7)$  during charging and discharging was examined by XRD, ND, XAS, first-principles calculations, and electrochemical measurements. We clarified that the electrochemical reaction of  $\text{Na}_4\text{Fe}_3(\text{PO}_4)_2(\text{P}_2\text{O}_7)$  in a Na-ion cell is governed mainly by a one-phase reaction with a reversible structural evolution that includes  $\text{P}_2\text{O}_7$  distortion. The unusually small volume change observed during cycling is expected to contribute to stable cycle retention. Furthermore, the partially desodiated phases were thermally stable up to 530 °C at all SOCs. With an open framework and one-phase reaction, high voltage ( $\sim 3.2$  V vs. Na), low volume change ( $\sim 4$  %), and high safety,  $\text{Na}_4\text{Fe}_3(\text{PO}_4)_2(\text{P}_2\text{O}_7)$  should be a promising candidate for Na rechargeable battery electrodes.

### 3.5 References

- (1) J. -M. Tarascon, M. Armand, *Nature* **2001**, *414*, 359–367.
- (2) M. Armand, J. -M. Tarascon, *Nature* **2008**, *451*, 652–657.
- (3) K. Kang, Y. S. Meng, J. Breger, C. P. Grey, G. Ceder, *Science* **2006**, *311*, 977–980.
- (4) P. Moreau, P.; D. Guyomard, J. Gaubicher, F. Boucher. *Chem. Mater.* **2010**, *22*, 4126–4128.
- (5) K. T. Lee, T. N. Ramesh, F. Nan, G. Botton, L. F. Nazar, *Chem. Mater.* **2011**, *23*, 3593-3600.
- (6) B. L. Ellis, W. R. M. Makahnouk, Y. Makimura, K. Toghill, L. F. Nazar, *Nat. Mater.* **2007**, *6*, 749-753.
- (7) P. Barpanda, J. Chotard, N. Recham, C. Delacourt, M. Ati, L. Dupont, M. Armand, J. -M. Tarascon, *Inorg. Chem.* **2010**, *49*, 7401–7413.
- (8) P. Barpanda, T. Ye, S. Nishimura, S. -C. Chung, Y. Yamada, M. Okubo, H. Zhou, A. Yamada, *Electrochem. Commun.* **2012**, *24*, 116–119.
- (9) H. Kim, R. A. Shakoor, C. Park, S. -Y. Lim, J. -S. Kim, Y. -N. Jo, W. Cho, K. Miyasaka, R. Kahraman, Y. Jung, J. -W. Choi, *Adv. Funct. Mater.* **2012**, *23*, 1147–1155.
- (10) H. Kim, I. Park, D. -H. Seo, S. Lee, S. -W. Kim, W. J. Kwon, Y. -U. Park, C. S. Kim, S. Jeon, K. Kang, *J. Am. Chem. Soc.* **2012**, *134*, 10369–10372.

- (11) A. R. Wizansky, P. E. Rauch, F. J. DiSalvo, *J. Solid State. Chem.* **1989**, *81*, 203–207.
- (12) G. Kresse, J. Furthmuller, *Comput. Mater. Sci.* **1996**, *6*, 15.
- (13) J. P. Perdew, K. Burke, M. Ernzerhof, *Phys. Rev. Lett.* **1996**, *77*, 3865.
- (14) V. I. Anisimov, J. Zaanen, O. K. Andersen, *Phys. Rev. B* **1991**, *44*, 943.
- (15) V. I. Anisimov, F. Aryasetiawan, A. I. Lichtenstein, *J. Phys. Condens. Matter* **1997**, *9*, 767.
- (16) G. Hautier, C. C. Fischer, A. Jain, T. Mueller, G. Ceder, *Chem. Mater.* **2010**, *22*, 3762–3767.
- (17) A. Jain, G. Hautier, C. Moore, B. Kang, J. Lee, H. Chen, N. Twu, G. Ceder, *J. Electrochem. Soc.* **2012**, *159*, A622–A633.
- (18) H. Chen, G. Hautier, G. Ceder, *J. Am. Chem. Soc.* **2012**, *134*, 19619–19627.
- (19) G. Hautier, A. Jain, T. Mueller, C. Moore, S. P. Ong, G. Ceder, *Chem. Mater.* **2013**, *25*, 2064–2074.
- (20) P. P. Ewald, *Annalen der Physik.*, **1921**, *369*, 253–287.
- (21) A. Van der Ven, M. K. Aydinol, G. Ceder, *Phys. Rev. B* **1998**, *58*, 2975–2987.
- (22) R. Malik, F. Zhou, G. Ceder, *Nat. Mater.* **2011**, *10*, 587–590.
- (23) N. Meethong, H. –Y. Huang, S. A. Speakman, W. C. Carter, Y. –M. Chiang, *Adv. Funct. Mater.* **2007**, *17*, 1115–1123.

- (24) S. -W. Kim, J. Kim, H. Gwon, K. Kang, *J. Electrochem. Soc.* **2009**, *156*, A635–A638.
- (25) P. Barpanda, J. -M. Chotard, N. Recham, C. Delacourt, M. Ati, L. Dupont, M. Armand, J. -M. Tarascon, *Inorg. Chem.* **2010**, *49*, 7401–7413.
- (26) S. P. Ong, A. Jain, G. Hautier, B. Kang, G. Ceder, *Electrochem. Commun.* **2010**, *12*, 427–430.
- (27) A. Ponrouch, E. Marchante, M. Courty, J. -M. Tarascon, M. R. Palacin, *Energy Environ. Sci.* **2012**, *5*, 8572–8583.

## **Chapter 4. Anomalous Jahn-Teller behavior in manganese-based mixed-phosphate cathode for sodium ion batteries**

(The essence of this chapter has been published in *Energy & Environmental Science*. Reproduced from [H. Kim et al., *Energy Environ. Sci.* **2015**, 8, 3325-3335.] with permission from The Royal Society of Chemistry)

### **4.1 Introduction**

The recent rapid growth in demand for energy has led to increasing interest in sustainable energy resources, such as solar and wind power, in addition to energy generation from conventional fossil fuel resources. An important component in the exploitation of sustainable energy resources is efficient energy storage technology. Large-scale energy storage systems (ESSs) have become an important area of research in recent years.<sup>1,2</sup> Na-ion batteries (NIBs) are promising candidates for these applications because of the availability and low cost of sodium, as well as the similar electrochemistry to the established Li-ion battery technology.<sup>3-5</sup> However, the low energy density, poor cycle stability and slow sodium kinetics of the existing electrode materials have inhibited the widespread uptake of NIBs.

A number of promising layered sodium-intercalation materials with a high energy density have recently been reported for applications as electrodes in NIBs.<sup>3-</sup>

<sup>5</sup> However, exploitation of sodium in these layered structures with a large number

of cycles remains challenging. The large volume change (>10%) during cycling and the phase instability of desodiated structure are among the largest obstacles, and the theoretical capacity remains far from that demonstrated using these layered electrode materials.<sup>6-8</sup> Prussian blue analogues (PBAs) have also been intensively investigated in recent years as promising electrodes for NIBs due to their low element cost, easy synthesis at room temperature and large alkali-ion channel with low activation barriers.<sup>9-11</sup> Although earlier PBAs with a hydrated form showed poor electrochemical activities in Na-ion cells, recent theoretical and experimental studies revealed that the dehydrated PBAs exhibit promising electrochemical properties. The vacuum-dried  $\text{Na}_2\text{MnFe}(\text{CN})_6$  cathode displays superior electrochemical properties compared to other reported PBAs with a hydrated form.<sup>12-13</sup> Polyanion-based compounds have received a wider attention due to its structural stability and the chemical diversity.<sup>14-21</sup> The strong X-O (X = P, S, B, Si) covalent bonding in the structure could offer great structural stability during electrochemical cycling. Furthermore, the rigid open crystal structure is less vulnerable to oxygen evolution at high temperature and exhibits a relatively small volume change associated with sodium-ion insertion/extraction.<sup>14-16</sup> To date, the search for the new polyanion electrodes has focused on iron- and vanadium-based compounds. Iron-based materials, including  $\text{Na}_2\text{FeP}_2\text{O}_7$ ,  $\text{Na}_2\text{Fe}_2(\text{SO}_4)_3$ ,  $\text{Na}_4\text{Fe}_3(\text{PO}_4)_2(\text{P}_2\text{O}_7)$ ,  $\text{Na}_2\text{FePO}_4\text{F}$ ,  $\text{NaFePO}_4$ ,  $\text{NaFeSO}_4\text{F}$ ,  $\text{Na}_2\text{Fe}(\text{SO}_4)_2 \cdot 2\text{H}_2\text{O}$ ,  $\text{Na}_{4-x}\text{Fe}_{2+x/2}(\text{P}_2\text{O}_7)_2$  and  $\text{Na}_{2.24}\text{FePO}_4\text{CO}_3$ , are low-cost cathode materials due to the availability of Fe.<sup>14-21</sup> Vanadium-based cathodes include  $\text{Na}_3\text{V}_2(\text{PO}_4)_3$ ,  $\text{Na}_{1.5}\text{VPO}_5$ .

$\delta\text{F}_{0.5+\delta}$ ,  $\text{Na}_{1.5}\text{VPO}_4\text{F}_{1.5}$ ,  $\text{Na}_7\text{V}_4(\text{P}_2\text{O}_7)_4\text{PO}_4$  and  $\text{NaVPO}_4\text{F}$  are of interest because of the high voltage and corresponding high energy density.<sup>22-26</sup> There are, however, a number of challenges which must be addressed; these include the low energy density of iron-based cathodes due to the low voltage (typically less than 3.2 V), and the cost issue and environmental impact of vanadium-based compounds.

Along with the iron-based compounds, manganese-based polyanion compounds are attractive alternatives, due to the abundance and ready availability. Recently identified electrode materials include  $\text{Na}_2\text{MnPO}_4\text{F}$ ,  $\text{Na}_2\text{MnP}_2\text{O}_7$  and  $\text{Na}_3\text{MnPO}_4\text{CO}_3$ , which exhibit electrochemical activity with a higher voltage than is typical for iron-based electrodes.<sup>27-30</sup> While these manganese-based materials have attracted much attention, none have yet been shown to provide sufficiently high performance as electrodes, as they typically suffer from an unacceptably low rate capability and a poor cycle stability. Limited cycle performance of below 30 cycles has been reported.<sup>27-30</sup> Moreover, the large overpotential during charge/discharge even at low current densities has led to a low usable energy density, as well as a low power density. These observations have been made with most manganese-based electrodes, and have been attributed to Jahn–Teller distortion ( $\text{Mn}^{3+}$ ) of the structure during battery cycling. These severe structural distortions lead to deteriorations of the mobility of the ions and of the structural stability, thus rapidly degrading the electrochemical activity of manganese-based cathodes in NIBs.

Here we describe a novel high-voltage mixed-phosphate cathode based on manganese; i.e.,  $\text{Na}_4\text{Mn}_3(\text{PO}_4)_2(\text{P}_2\text{O}_7)$ , for applications as electrodes in NIBs. This

mixed phosphate compound allows fast sodium intercalation kinetics regardless of the state of charges and exhibits a voltage of 3.8 V, which is the highest among known manganese-based NIB cathodes. Furthermore, a reversible capacity of 121 mAh g<sup>-1</sup> and an energy density of 416 Wh kg<sup>-1</sup> could be delivered at a rate of C/20 in Na-ion cells, which also represents the largest energy density among manganese-based polyanion NIB cathodes. In addition, our Na-ion cells exhibited stable electrochemical performance over 100 cycles, with 86% retention at a rate of C/5. We attribute this outstanding electrochemical performance to a unique structural feature of our new material where the ionic mobility of sodium is not decreased by the structural changes induced by the Jahn–Teller distortion, rather is actually increased. First principles calculations reveal that this is due to the unique Jahn–Teller distortion of Mn<sup>3+</sup>, which opens up sodium diffusion channels, enhancing the sodium insertion/extraction kinetics.

## 4.2 Experimental

**Synthesis of  $\text{Na}_4\text{Mn}_3(\text{PO}_4)_2(\text{P}_2\text{O}_7)$ :**  $\text{Na}_4\text{Mn}_3(\text{PO}_4)_2(\text{P}_2\text{O}_7)$  was synthesized *via* a conventional solid-state reaction. A stoichiometric quantity of  $\text{Na}_4\text{P}_2\text{O}_7$  (95 %, Aldrich),  $\text{Mn}_2\text{C}_2\text{O}_4 \cdot 2\text{H}_2\text{O}$  (99%, Alfa Aesar) and  $\text{NH}_4\text{H}_2\text{PO}_4$  (98% ACS reagent, Aldrich) was mixed using wet ball milling at 200 rpm for 12 hours in acetone. Following ball-milling, the acetone was dried out at 70°C for 12 hours. The mixture was calcinated at 300°C for 6 hours in air, and the resulting powder was pelletized under a pressure of 200 kg cm<sup>-2</sup>, and sintered again at 600°C for 6 hours in air. Carbon coating of the  $\text{Na}_4\text{Mn}_3(\text{PO}_4)_2(\text{P}_2\text{O}_7)$  sample was carried out to enhance the electrical conductivity using pyromellitic acid (PA) ( $\text{C}_{10}\text{H}_6\text{O}_2$ , 96%, Alfa Aesar).  $\text{Na}_4\text{Mn}_3(\text{PO}_4)_2(\text{P}_2\text{O}_7)$ , and PA were mixed using a planetary ball-milling with a mass ratio of 9:1, and the ground mixture was annealed at 600°C for 2 hours under an Ar atmosphere. The carbon content was approximately 3 wt% of the total powder sample.

**Characterization methods:** High resolution powder X-ray diffraction (XRD) data of  $\text{Na}_4\text{Mn}_3(\text{PO}_4)_2(\text{P}_2\text{O}_7)$  were obtained from the Beamline 9B at Pohang Accelerator Laboratory (PAL), Republic of Korea. The data were collected over a  $2\theta$  range of 10–130°, with a step size of 0.01°, a step time of 7 s and wavelength of  $\lambda = 1.54950 \text{ \AA}$ . Neutron diffraction (ND) data of  $\text{Na}_4\text{Mn}_3(\text{PO}_4)_2(\text{P}_2\text{O}_7)$  were recorded using a high-resolution powder diffractometer (HRPD) at the HANARO facility in the Korea Atomic Energy Research Institute (KAERI). The measurements were performed over a  $2\theta$  range of 0–180° with a step size of 0.05°

using a constant wavelength of  $\lambda = 1.834333 \text{ \AA}$  supplied via a Ge (331) monochromator. The particle size of the samples was examined using field-emission scanning electron microscopy (FESEM) (SUPRA 55VP/Carl Zeiss) and transmission electron microscopy (TEM) (Tecnal F20/FEI). XRD patterns of *ex situ* electrode samples were collected over a  $2\theta$  range of  $8\text{--}60^\circ$  with a step size of  $0.02^\circ$  and step time of 2 s using an X-ray diffractometer (Bruker, D2 PHASER). The valence states and local environment of Mn in the structure of  $\text{Na}_{4-x}\text{Mn}_3(\text{PO}_4)_2(\text{P}_2\text{O}_7)$  ( $0 \leq x \leq 3$ ) were characterized using X-ray absorption near edge structure (XANES) and X-ray absorption fine structure (EXAFS) analyses. The XANES and EXAFS spectra were obtained from Beamline 7D and 8C at the PAL, Republic of Korea. The Mn k-edge spectra were collected in transmission mode with the electron energy of 2.5 GeV and a current of 200 mA. Mn reference spectra were obtained simultaneously from Mn metal foil.

***First-principles calculations:*** Density functional theory (DFT) calculations were performed to investigate the phase stability, structural evolution during desodiation, and Na diffusion kinetics of  $\text{Na}_4\text{Mn}_3(\text{PO}_4)_2(\text{P}_2\text{O}_7)$ . All calculations were carried out using spin-polarized generalized gradient approximation (GGA) parameterized using the Perdew–Burke–Ernzerhof (PBE) exchange model.<sup>31</sup> We further introduced a Hubbard parameter  $U$  for Mn, to correct the self-interaction error with the GGA method;<sup>32</sup> we used  $U_{\text{eff}} = 4.5 \text{ eV}$ , which were taken from a study on olivine  $\text{LiMnPO}_4$ .<sup>33</sup> Since our study includes both  $\text{Mn}^{2+}$  and  $\text{Mn}^{3+}$ , we adopted the average value of  $U_{\text{eff}}$  from each species. We used projector-augmented wave (PAW)

pseudopotentials as implemented in the Vienna *ab initio* simulation package (VASP).<sup>34, 35</sup> After performing the convergence test, a kinetic energy cut-off of 500 eV was used for all calculations, and  $1 \times 3 \times 2$  k-point grid was used for geometric relaxations. The structures were relaxed until the remaining force in the unit cell converged within  $0.05 \text{ eV \AA}^{-1}$ . We used ferromagnetic ordering of Mn ions because no clear magnetic structure is found by experiments, and our test shows that free energy differences between various magnetic configurations are within a few meVs per formula unit (see Figure 4-1).<sup>36</sup>

To investigate the phase stability and structural evolution, we generated all possible configurations of Na and the vacancies in several Na compositions using four formula units of  $\text{Na}_{4-x}\text{Mn}_3(\text{PO}_4)_2(\text{P}_2\text{O}_7)$  ( $0 \leq x \leq 3$ ) implemented using the CASM software package.<sup>37</sup> Although larger supercells generally yield more accurate results, our unit cell generated more than 16,500 configurations throughout Na compositions, which are large enough to determine the most stable configuration in each Na composition. The 40 lowest electrostatic energy configurations were identified for each composition, as calculated using the Ewald summation method.<sup>38</sup> Further DFT calculations resulted in a convex hull of  $\text{Na}_{4-x}\text{Mn}_3(\text{PO}_4)_2(\text{P}_2\text{O}_7)$  ( $0 \leq x \leq 3$ ), which provided information on the feasible phase reactions and the voltage profiles.

The activation barriers for Na diffusion in the  $\text{Na}_{4-x}\text{Mn}_3(\text{PO}_4)_2(\text{P}_2\text{O}_7)$  ( $x = 0, 1, 3$ ) structures were determined using the nudged elastic band (NEB) method.<sup>39</sup> A supercell of eight formula units was used to calculate the Na ion diffusion within

$\text{Na}_{4-x}\text{Mn}_3(\text{PO}_4)_2(\text{P}_2\text{O}_7)$  ( $x = 0, 1, 3$ ). After the initial and final configurations of Na diffusion were determined, five intermediate images were generated *via* linear interpolation of the initial and final images. These were structurally relaxed to provide activation barriers for Na diffusion. The lattice parameters were fixed, whereas all the internal degrees of freedom were allowed to relax.

**Electrochemical tests:** The electrodes were prepared using  $\text{Na}_4\text{Mn}_3(\text{PO}_4)_2(\text{P}_2\text{O}_7)$ , super P and polyvinylidene fluoride (PVDF) with a final mass ratio of 70:20:10. N-methyl-2-pyrrolidone (NMP) (99.5%, Aldrich) was used as a solvent to prepare a slurry of the mixture. The well-mixed slurry was pasted onto Al foil with a 250  $\mu\text{m}$  thickness using a doctor blade, and the NMP was evaporated at 120°C for 1 hour. The loading of  $\text{Na}_4\text{Mn}_3(\text{PO}_4)_2(\text{P}_2\text{O}_7)$  was approximately 2  $\text{mg cm}^{-2}$ . The Na half-cell was assembled into a CR2032 coin cell using metallic Na (Sodium cube 99%, Aldrich) as a counter electrode, a glass microfiber filter (grade GF/F; Whatman, US) as a separator. All of the electrochemical tests were carried out by using 1M  $\text{NaBF}_4$  in EC/PC as an electrolyte which exhibited the most stable electrochemical properties at both room temperature and 60 °C. Galvanostatic measurements of the charge/discharge of the  $\text{Na}_4\text{Mn}_3(\text{PO}_4)_2(\text{P}_2\text{O}_7)$  electrode were performed with various C-rates (C/20, C/10, C/5, 1C, 2C, 5C, 10C and 20C) at room temperature and at 60°C with cut-off voltages of 1.7 and 4.5 V (*vs.*  $\text{Na}^+/\text{Na}$ ). *Ex situ* electrode samples at different states of charge (SOCs) were prepared at a rate of C/20 with a relaxation time of 6 hours to measure the quasi-equilibrium state of the electrodes.

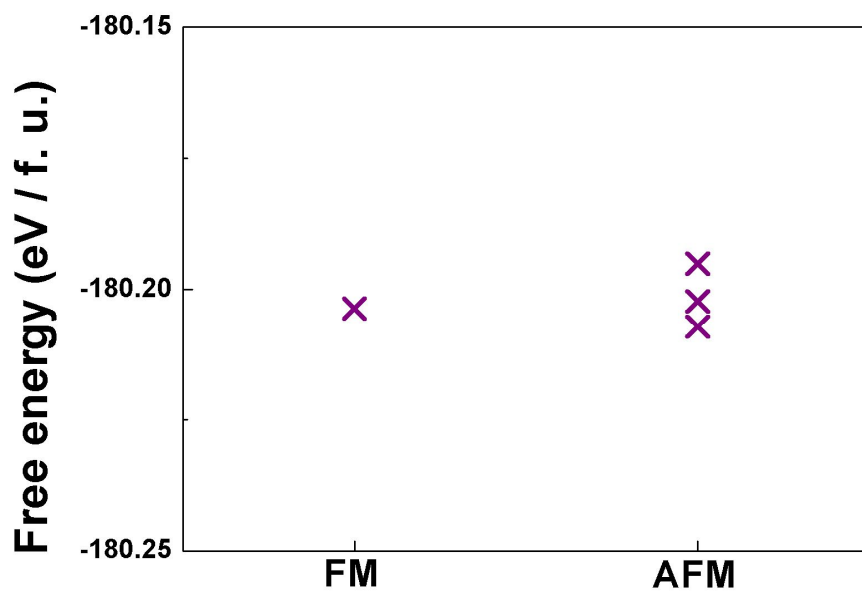


**Figure 4-1.** Free energies of  $\text{Na}_4\text{Mn}_3(\text{PO}_4)_2\text{P}_2\text{O}_7$  with various magnetic configurations.



## 4.3 Result and Discussion

### 4.3.1 Synthesis and characterization of $\text{Na}_4\text{Mn}_3(\text{PO}_4)_2(\text{P}_2\text{O}_7)$

$\text{Na}_4\text{Mn}_3(\text{PO}_4)_2(\text{P}_2\text{O}_7)$  was successfully synthesized *via* a solid-state reaction at 600°C in air. The crystal structure of the  $\text{Na}_4\text{Mn}_3(\text{PO}_4)_2(\text{P}_2\text{O}_7)$  was investigated using synchrotron X-ray sources, as shown in Figure 4-2a. The crystal structure was determined to be orthorhombic  $Pn2_1a$ , with the following lattice parameters:  $a = 18.02651(7) \text{ \AA}$ ,  $b = 6.65673(2) \text{ \AA}$  and  $c = 10.76886(4) \text{ \AA}$ , with a unit volume of  $1292.237(8) \text{ \AA}^3$  using Rietveld refinement; this is in a good agreement with a previous report of the crystal structure.<sup>36</sup> The fitting was satisfactory with low reliability factors of  $R_I = 3.53\%$ ,  $R_F = 2.14\%$ ,  $R_p = 6.84\%$  and  $R_{wp} = 9.82\%$ . A trace amount of  $\text{NaMnPO}_4$  ( $< 4\%$ ) was detected. The detailed atomic parameters of  $\text{Na}_4\text{Mn}_3(\text{PO}_4)_2(\text{P}_2\text{O}_7)$  were further investigated using ND analysis, which provides detailed information on the light elements (i.e., Na, P and O), as shown in Figure 4-2b.  $\text{Na}_4\text{Mn}_3(\text{PO}_4)_2(\text{P}_2\text{O}_7)$  is isostructural to the existing cathode materials  $\text{Na}_4\text{Co}_3(\text{PO}_4)_2(\text{P}_2\text{O}_7)$  and  $\text{Na}_4\text{Fe}_3(\text{PO}_4)_2(\text{P}_2\text{O}_7)$ , but with larger lattice constants, which are attributed to the larger ionic radius of  $\text{Mn}^{2+}$  (the ionic radius of  $\text{Mn}^{2+}$  is  $0.83 \text{ \AA}$ , compared with  $0.78 \text{ \AA}$  of  $\text{Fe}^{2+}$  and  $0.745 \text{ \AA}$  for  $\text{Co}^{2+}$ ).<sup>16, 36, 40, 41</sup> Figure 4-2c shows a schematic diagram of the structure of  $\text{Na}_4\text{Mn}_3(\text{PO}_4)_2(\text{P}_2\text{O}_7)$  based on the refinement results of the XRD and ND analyses. The structure is composed of the infinite chains of  $[\text{Mn}_3\text{P}_2\text{O}_{13}]_\infty$  blocks along the  $bc$ -plane, and these blocks are connected along the  $a$ -axis *via* diphosphate ( $\text{P}_2\text{O}_7$ ) groups, which provides the 3D open structure.<sup>16, 36</sup> Three crystallographically distinguishable Mn octahedra sites

were identified in the crystal, and these octahedra were connected *via* edge or corner sharing. Detailed structural information, including the atomic parameters and bond valances determined from Rietveld refinement, are listed in Table 4-1.

The morphology of the  $\text{Na}_4\text{Mn}_3(\text{PO}_4)_2(\text{P}_2\text{O}_7)$  powder was analyzed using scanning electron microscopy (SEM) and transmission electron microscopy (TEM). Figure 4-3a shows an SEM image, which indicates that the primary particle size of the as-prepared  $\text{Na}_4\text{Mn}_3(\text{PO}_4)_2(\text{P}_2\text{O}_7)$  powder was 0.5–1  $\mu\text{m}$ . Following annealing during the carbon coating process, the particle size reduced to 200–500 nm, due to the ball-milling process with PA, as shown in Figure 4-3b. The TEM image shown in Figure 4-3c reveals that the carbon was coated onto the surface of the  $\text{Na}_4\text{Mn}_3(\text{PO}_4)_2(\text{P}_2\text{O}_7)$  particles.

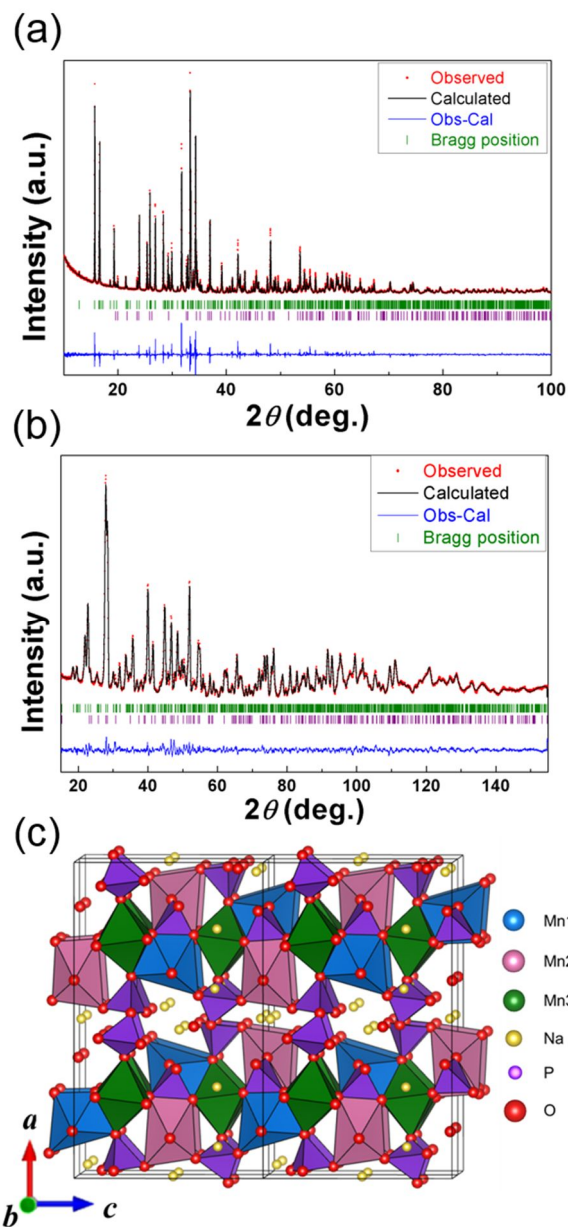


**Figure 4-2.** Rietveld refinement of (a) XRD and (b) ND patterns of  $\text{Na}_4\text{Mn}_3(\text{PO}_4)_2(\text{P}_2\text{O}_7)$ . The  $\text{NaMnPO}_4$  impurities are shown by the purple markers. (c) Schematic representation of  $\text{Na}_4\text{Mn}_3(\text{PO}_4)_2(\text{P}_2\text{O}_7)$  based on the ND analyses.

**Table 4-1.** The structural data on  $\text{Na}_4\text{Mn}_3(\text{PO}_4)_2(\text{P}_2\text{O}_7)$  analyzed using Rietveld refinement of the XRD and ND patterns. Details of the measurement conditions, lattice parameters, reliability factors, atomic positions and bond valence data are also listed.

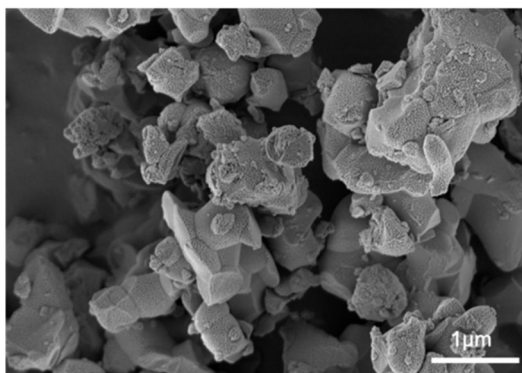
Formula	$\text{Na}_4\text{Mn}_3(\text{PO}_4)_2(\text{P}_2\text{O}_7)$
Crystal system	Orthorhombic
Space group	$Pn2_1a$ (No. 33)
Lattice parameters	
a (Å)	18.02651 (7)
b (Å)	6.65673 (2)
c (Å)	10.76886 (4)
Unitcell volume (Å <sup>3</sup> )	1290.07 (8)
Source	X-ray
Temperature (K)	300
Wave length (Å)	1.54950
2θ range (°)	10 – 100
Number of data points	12045
Number of reflections	1316
R <sub>p</sub> (%)	6.84
R <sub>wp</sub> (%)	9.82
R <sub>I</sub> (%)	3.53
R <sub>F</sub> (%)	2.14

Formula	$\text{Na}_4\text{Mn}_3(\text{PO}_4)_2(\text{P}_2\text{O}_7)$
Crystal system	Orthorhombic
Space group	$Pn2_1a$ (No. 33)
Lattice parameters	
a (Å)	18.0201 (7)
b (Å)	6.6508 (2)
c (Å)	10.7642 (4)
Unitcell volume (Å <sup>3</sup> )	1290.07 (8)
Source	Neutron
Temperature (K)	300
Wave length (Å)	1.834333
2θ range (°)	10 – 100
Number of data points	0 – 180
Number of reflections	3200
R <sub>p</sub> (%)	956
R <sub>wp</sub> (%)	3.25
R <sub>l</sub> (%)	4.22
R <sub>F</sub> (%)	3.11

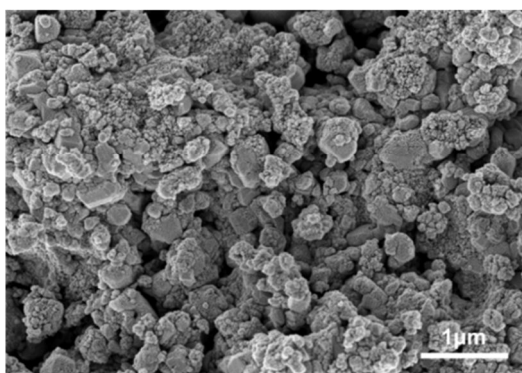
<b>Atom</b>	<b>x (Å)</b>	<b>y (Å)</b>	<b>z (Å)</b>	<b>B<sub>iso</sub></b>	<b>Occupancy</b>
Mn1	0.3435 (7)	0.060 (4)	0.5087 (17)	0.80 (17)	1.00
Mn2	0.1436 (7)	0.538 (4)	0.4837 (17)	0.80 (17)	1.00
Mn3	0.2443 (9)	0.272 (3)	0.741 (2)	0.80 (17)	1.00
P1	0.2991 (5)	0.547 (3)	0.5044 (13)	0.26 (9)	1.00
P2	0.1806 (5)	0.032 (3)	0.4770 (10)	0.26 (9)	1.00
P3	0.5603 (6)	0.422 (3)	0.7452 (12)	0.26 (9)	1.00
P4	0.4455 (5)	0.121 (3)	0.7265 (11)	0.26 (9)	1.00
Na1	0.5033 (12)	0.788 (4)	0.9823 (11)	0.34 (13)	1.00
Na2	0.2862 (7)	0.795 (3)	0.7513 (20)	0.34 (13)	1.00
Na3	0.3985 (8)	0.408 (3)	0.2602 (18)	0.34 (13)	1.00
Na4	0.4674 (10)	0.63488	0.5492 (14)	0.34 (13)	1.00
O1	0.2435 (6)	0.516 (3)	0.6134 (11)	1.19 (5)	1.00
O2	0.3507 (7)	0.375 (3)	0.4869 (11)	1.19 (5)	1.00
O3	0.3433 (6)	0.747 (3)	0.5330 (11)	1.19 (5)	1.00
O4	0.2528 (6)	0.564 (3)	0.3836 (10)	1.19 (5)	1.00
O5	0.2329 (6)	0.075 (3)	0.6006 (10)	1.19 (5)	1.00
O6	0.1279 (6)	-0.144 (3)	0.5032 (13)	1.19 (5)	1.00
O7	0.2357 (6)	0.011 (3)	0.3779 (12)	1.19 (5)	1.00
O8	0.1404 (7)	0.230 (3)	0.4496 (10)	1.19 (5)	1.00
O9	0.4784 (6)	0.336 (3)	0.7040 (9)	1.19 (5)	1.00
O10	0.5574 (6)	0.522 (3)	0.8691 (9)	1.19 (5)	1.00
O11	0.6201 (5)	0.242 (3)	0.7406 (12)	1.19 (5)	1.00
O12	0.5755 (5)	0.573 (3)	0.6450 (9)	1.19 (5)	1.00
O13	0.4670 (6)	0.048 (3)	0.8631 (11)	1.19 (5)	1.00
O14	0.3615 (5)	0.132 (3)	0.7116 (10)	1.19 (5)	1.00
O15	0.4792 (6)	-0.016 (3)	0.6360 (12)	1.19 (5)	1.00

<b>Atom</b>	<b>Coordination number</b>	<b>Average Distance (Å)</b>	<b>Expected valence</b>	<b>Bond valence Summation</b>
Mn1	6.00	2.22 (1)	2.00	1.95 (6)
Mn2	6.00	2.23 (1)	2.00	1.91 (6)
Mn3	6.00	2.16 (1)	2.00	2.28 (7)
P1	4.00	1.54 (1)	5.00	4.9 (1)
P2	4.00	1.55 (1)	5.00	4.9 (1)
P3	4.00	1.56 (1)	5.00	4.7 (1)
P4	4.00	1.54 (1)	5.00	5.0 (1)
Na1	6.00	2.40 (1)	1.00	1.26 (4)
Na2	7.00	2.53 (1)	1.00	1.03 (3)
Na3	5.00	2.47 (1)	1.00	0.78 (3)
Na4	6.00	2.492 (8)	1.00	1.04 (3)
O1	4.00	2.12 (1)	-2.00	-2.00 (6)
O2	4.00	2.25 (1)	-2.00	-2.0 (1)
O3	4.00	2.16 (1)	-2.00	-1.88 (9)
O4	4.00	2.06 (1)	-2.00	-2.17 (7)
O5	4.00	2.14 (1)	-2.00	-1.86 (6)
O6	3.00	1.99 (2)	-2.00	-1.90 (9)
O7	4.00	2.11 (1)	-2.00	-2.25 (7)
O8	4.00	2.20 (1)	-2.00	-2.0 (1)
O9	3.00	1.94 (1)	-2.00	-2.19 (9)
O10	4.00	2.14 (1)	-2.00	-2.10 (8)
O11	3.00	2.04 (1)	-2.00	-1.60 (7)
O12	4.00	2.11 (1)	-2.00	-2.16 (9)
O13	4.00	2.15 (1)	-2.00	-1.78 (6)
O14	4.00	2.19 (1)	-2.00	-1.90 (5)
O15	4.00	2.23 (1)	-2.00	-1.98 (9)

(a)



(b)



(c)

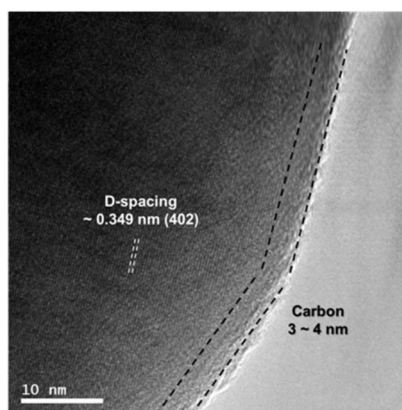


**Figure 4-3.** SEM images of (d) the as-synthesized and (e) carbon-coated  $\text{Na}_4\text{Mn}_3(\text{PO}_4)_2(\text{P}_2\text{O}_7)$ . (f) TEM image of the carbon-coated  $\text{Na}_4\text{Mn}_3(\text{PO}_4)_2(\text{P}_2\text{O}_7)$ .

### 4.3.2 Electrochemical properties of $\text{Na}_4\text{Mn}_3(\text{PO}_4)_2(\text{P}_2\text{O}_7)$

Galvanostatic charge/discharge tests of the  $\text{Na}_4\text{Mn}_3(\text{PO}_4)_2(\text{P}_2\text{O}_7)$  electrodes were carried out at room temperature using Na-ion cells, as shown in Figure 4-4a. Almost 100 % of the theoretical capacity (i.e., one electron per Mn atom, giving 129.55 mAh g<sup>-1</sup>) was obtained during the first charge, and 85 % of the charge capacity (109 mAh g<sup>-1</sup>) was delivered during continued discharge at a rate of C/20. Subsequent charge and discharge cycles revealed that the electrochemical reaction of the  $\text{Na}_4\text{Mn}_3(\text{PO}_4)_2(\text{P}_2\text{O}_7)$  electrode was highly reversible, without a notable change in the electrochemical profile. Stable cycle performance was observed, with 82 % capacity retention after 100 cycles. Note that the average voltage of the  $\text{Mn}^{2+}/\text{Mn}^{3+}$  redox couple in  $\text{Na}_{4-x}\text{Mn}_3(\text{PO}_4)_2(\text{P}_2\text{O}_7)$  ( $0 \leq x \leq 3$ ) was 3.84 V. This is the largest  $\text{Mn}^{2+}/\text{Mn}^{3+}$  redox potential (vs.  $\text{Na}^+/\text{Na}$ ) among Mn-based cathodes yet reported, and comparable to that of the well-known high voltage olivine  $\text{LiMnPO}_4$  (vs.  $\text{Li}^+/\text{Li}$ ).<sup>27-30, 42</sup> We believe that the high voltage exhibited by the  $\text{Na}_4\text{Mn}_3(\text{PO}_4)_2(\text{P}_2\text{O}_7)$  electrode is partly due to the Mn octahedra surrounded by the electron-drawing  $\text{P}_2\text{O}_7$  groups, which have a strong inductive effect.<sup>14, 20, 25, 29, 40, 43</sup> In addition, the edge-sharing geometry of the  $\text{Mn1-O}_6$  and  $\text{Mn3-O}_6$  polyhedra is expected to lead to a strong  $\text{Mn}^{3+}-\text{Mn}^{3+}$  repulsion in the desodiated structure, which destabilizes the charged state of the electrode, leading to an increased voltage.<sup>15, 43, 44</sup> The average voltage of 3.84 V is clearly shown in the  $dQ/dV$  curves shown in Figure 4-4b; three anodic peaks at 3.96, 3.89 and 3.85 V can be clearly distinguished, in addition to the cathodic peaks at 3.87, 3.77, 3.64 V. The multiple

peaks in the  $dQ/dV$  profiles imply complex reactions during electrochemical cycling; this will be discussed in detail later in the paper.

We find that the  $\text{Na}_4\text{Mn}_3(\text{PO}_4)_2(\text{P}_2\text{O}_7)$  electrode was capable of reversibly delivering a discharge capacity that was close to theoretical limit when the kinetic limitations were alleviated. At an elevated temperature of 60 °C, a capacity of 121 mAh  $\text{g}^{-1}$  (i.e., 93 % of theoretical capacity) could be delivered at a rate of C/20. This corresponds to an energy density of the  $\text{Na}_4\text{Mn}_3(\text{PO}_4)_2(\text{P}_2\text{O}_7)$  electrode of 416 Wh  $\text{kg}^{-1}$ , which is the largest of manganese-based NIB cathodes. Note that the energy density of 385 Wh  $\text{kg}^{-1}$  at 25°C also exceeds that of previously reported manganese-based polyanion cathodes.<sup>27-30</sup> Battery tests at higher current rates show that the  $\text{Na}_4\text{Mn}_3(\text{PO}_4)_2(\text{P}_2\text{O}_7)$  electrode retained significant rate capability both at room temperature and 60°C. Figure 4-5c and d show discharge profiles of  $\text{Na}_4\text{Mn}_3(\text{PO}_4)_2(\text{P}_2\text{O}_7)$  at rates of C/20, C/10, C/5, 1C, 2C, 5C, 10C and 20C at 25°C and 60 °C. A capacity of approximately 112 mAh  $\text{g}^{-1}$  was delivered at a rate of 2C at 60°C, and 90 mAh  $\text{g}^{-1}$  was achieved at a rate of 1C at room temperature. More than a half of the theoretical capacity was retained at rates of up to 10C, both at room temperature and 60 °C. The Ragone plot shown in Figure 4-6 shows the energy and power density of  $\text{Na}_4\text{Mn}_3(\text{PO}_4)_2(\text{P}_2\text{O}_7)$  under various conditions, which is also shown compared with other representative manganese-based polyanion cathodes, as well as recently reported iron-based cathodes for NIBs.<sup>15, 27, 28, 30, 45, 46</sup> It is remarkable that  $\text{Na}_4\text{Mn}_3(\text{PO}_4)_2(\text{P}_2\text{O}_7)$  exhibited the largest gravimetric energy and power densities among these compounds, and these metrics are comparable to

those of electrode materials for Li-ion batteries. Moreover, this electrochemical performance was obtained from  $\text{Na}_4\text{Mn}_3(\text{PO}_4)_2(\text{P}_2\text{O}_7)$  with relatively large particles (i.e., 2–500 nm in diameter).

Promising cycle performance was obtained at a rate of C/5 with the cycle retention of 86 % and a Coulombic efficiency of 98.5 % following 100 cycles, as shown in Figure 4-7a. Such capacity retention is unprecedented among manganese-based polyanion compounds, which typically suffer from significant structural distortion due to the presence of Jahn–Teller active  $\text{Mn}^{3+}$ . Operation at 60°C also exhibited stable retention of 70 % at a rate of 1C following 200 cycles, with a Coulombic efficiency of 98.5 %, as shown in Figure 4-7b. This cycle stability is markedly superior to that of typical manganese-based cathodes at the elevated temperatures, which exhibit rapid capacity decay due to accelerated Mn dissolution.<sup>47</sup>

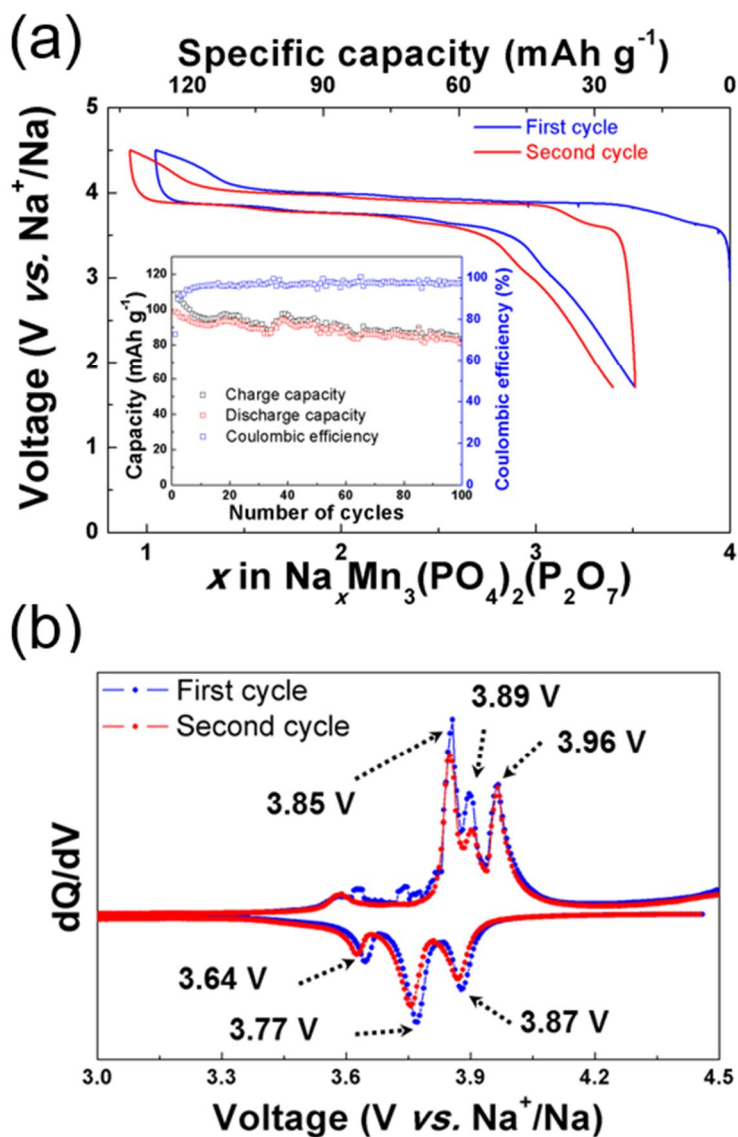


**Figure 4-4.** (a) Charge/discharge profiles of  $\text{Na}_4\text{Mn}_3(\text{PO}_4)_2(\text{P}_2\text{O}_7)$  at a rate of  $\text{C}/20$ . Cycles at a rate of  $\text{C}/20$  are shown in the inset. (b)  $dQ/dV$  plots for  $\text{Na}_4\text{Mn}_3(\text{PO}_4)_2(\text{P}_2\text{O}_7)$ .

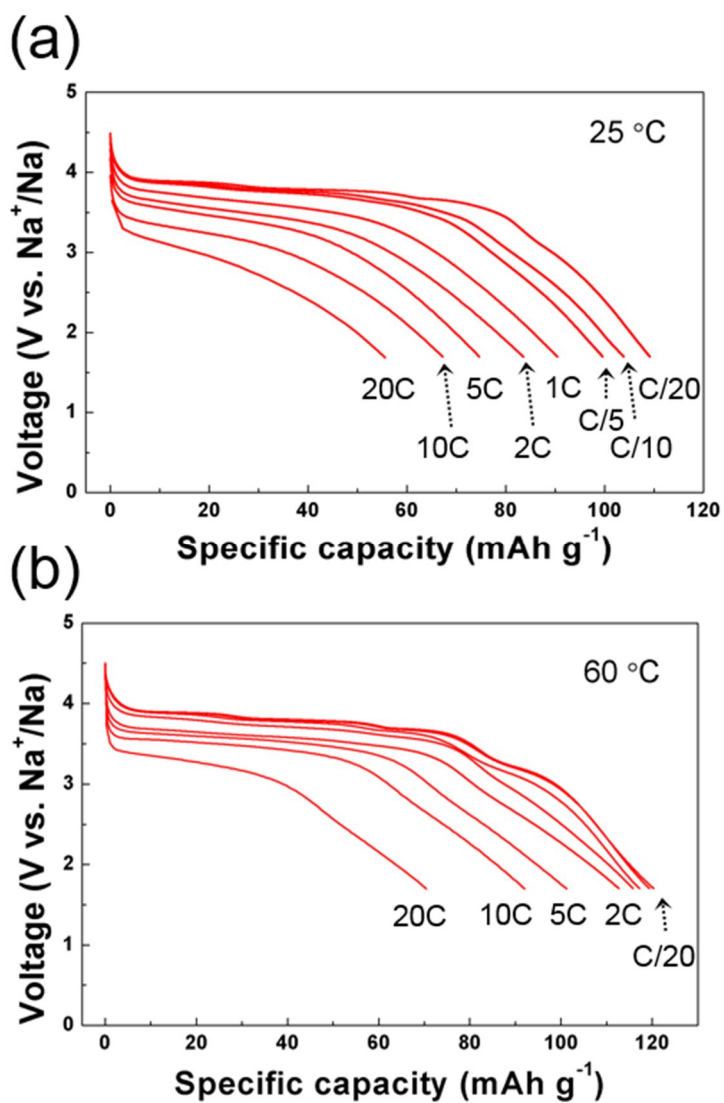


**Figure 4-5.** The discharge profiles of  $\text{Na}_4\text{Mn}_3(\text{PO}_4)_2(\text{P}_2\text{O}_7)$  at various rates of C/20 to 20C at (c) 25°C and (d) 60°C.

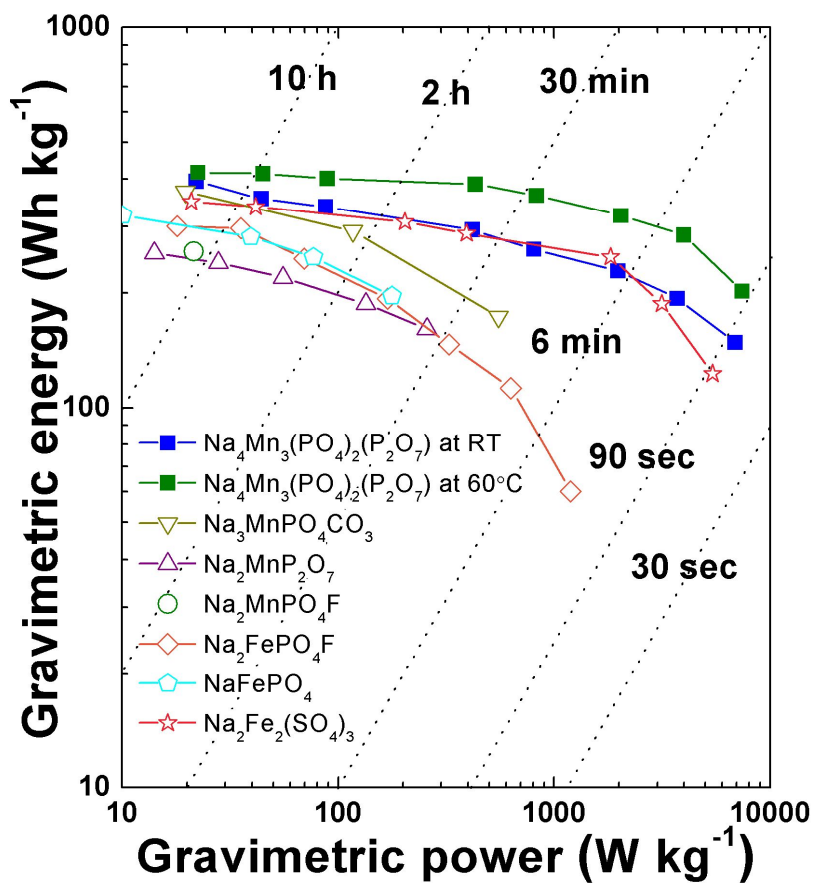


**Figure 4-6.** A Ragone plot of Na<sub>4</sub>Mn<sub>3</sub>(PO<sub>4</sub>)<sub>2</sub>(P<sub>2</sub>O<sub>7</sub>) and other representative Fe- and Mn-based polyanion cathode materials for NIBs. <sup>15, 27, 28, 30, 45, 46</sup>

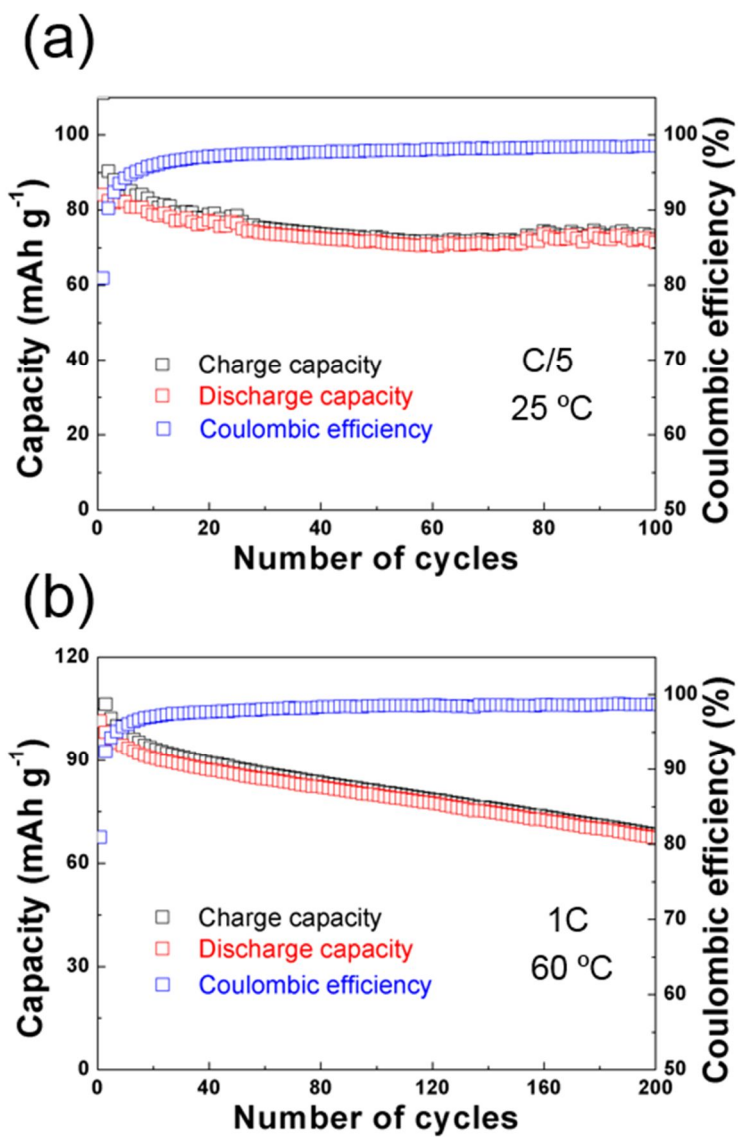


**Figure 4-7.** The cycle performance of  $\text{Na}_4\text{Mn}_3(\text{PO}_4)_2(\text{P}_2\text{O}_7)$  in Na-ion cells at (f) C/5 and 25°C, and (g) 1C and 60°C.

### 4.3.3 Structural evolution of the $\text{Na}_{4-x}\text{Mn}_3(\text{PO}_4)_2(\text{P}_2\text{O}_7)$ electrode during cycling ( $0 \leq x \leq 3$ )

To understand the electrochemical activity of  $\text{Na}_4\text{Mn}_3(\text{PO}_4)_2(\text{P}_2\text{O}_7)$  in the Na cell, *ex situ* XRD analysis of the electrodes was performed at different SOCs. Figure 4-8a and b show *ex situ* XRD patterns of the electrodes during intermediate charge/discharge states. Several multi-phase reactions appeared during cycling, which is consistent with the  $dQ/dV$  data shown in Figure 4-4b, which is in marked contrast to the isostructural  $\text{Na}_4\text{Fe}_3(\text{PO}_4)_2(\text{P}_2\text{O}_7)$  electrode, where a single phase electrode reaction occurs throughout the entire charge/discharge process.<sup>48</sup> Nevertheless, slight shifts of the (200), (011) and (210) peaks were observed following charging up to 3.86 V, which is indicative of solid solution behavior of  $\text{Na}_{4-x}\text{Mn}_3(\text{PO}_4)_2(\text{P}_2\text{O}_7)$  ( $\alpha$ -phase) during the initial charging process. The *a*- and *b*-lattice constants exhibited negligible change in this solid-solution region, as shown in Figure 4-8c and d, whereas the *c* lattice parameter and the cell volume decreased continuously, as shown in Figure 4-8e and f. Following charging to 3.9V, which corresponds to the extraction of approximately 1.64 Na ion, the *a* and *c* lattice parameters underwent relatively large changes, and new peaks appeared in the XRD patterns. This is indicative of the evolution of a new phase ( $\beta$ ) in the  $\alpha$ -phase matrix. The  $\alpha$ -phase fully transformed to  $\beta$ -phase at the Na composition of 2.24 in  $\text{Na}_{4-x}\text{Mn}_3(\text{PO}_4)_2(\text{P}_2\text{O}_7)$ , and Rietveld refinement of this  $\beta$ -phase reveals that *a* and *c* lattice parameters differed significantly to those of the  $\alpha$ -phase. We speculate that the large lattice mismatch between the  $\alpha$ - and  $\beta$ -phases is the cause of the

significant distortion of the  $a$  and  $c$  lattice parameters of the  $\alpha$ -phase during this stage, as well as the apparent phase separation. During charging above 4 V, an additional Na-poor phase ( $\gamma$ -phase) was detected. The new  $\gamma$ -phase exhibited comparable  $a$  and  $c$  lattice parameters to those of the  $\beta$ -phase, which in an interesting contrast to the case of the phase transition from  $\alpha$  to  $\beta$ . Figure 4-9a shows the results of Rietveld refinement of the fully charged state ( $\gamma$ -phase). It indicates that after complete charging, the electrode experiences volume contraction of about 7 % (compared to the pristine state). This is larger than that of the isostructural  $\text{Na}_4\text{Fe}_3(\text{PO}_4)_2(\text{P}_2\text{O}_7)$  electrode ( $\sim 4$  %);<sup>48</sup> however, it should be noted that this volume change following full charging is one of the lowest among manganese-based electrodes (*e.g.*, O3- $\text{NaNi}_{0.5}\text{Mn}_{0.5}\text{O}_2$  exhibits a volume change of 18 %, P2- $\text{Na}_x\text{Fe}_{0.5}\text{Mn}_{0.5}\text{O}_2$  of 11 % and olivine  $\text{LiMnPO}_4$  of 10 %).<sup>6, 8, 42</sup> Whereas a large volume change is typically observed for most manganese-based electrodes, due to the occurrence of the significant  $\text{Mn}^{3+}$  Jahn–Teller distortion during charging, the small volume change of  $\text{Na}_{4-x}\text{Mn}_3(\text{PO}_4)_2(\text{P}_2\text{O}_7)$  is attributed to the unique local environment of Mn in the structure, which will be discussed in more detail in the following section. The *ex situ* XRD patterns of subsequent discharge exhibit a reversible structural evolution from the  $\gamma$ -phase to the  $\alpha$ -phase via the occurrence of an intermediate  $\beta$ -phase, indicating a reversible electrode reaction. However, a  $\delta$ -phase also appeared as an additional intermediate phase between  $\beta$ -phase and  $\alpha$ -phase. It is uncertain as to the origin of this  $\delta$ -phase during discharge; however, we speculate that it may arise from specific Na-vacancy ordering, which occurs

preferentially in the structure.<sup>18, 25</sup> Detailed structural investigations of this particular composition is part of our ongoing work. Nevertheless, the XRD patterns of the fully discharged electrode were completely restored to its initial as-prepared state, as shown in Figure 4-9b. Furthermore, the evolution of XRD patterns during the subsequent charge/discharge cycle was identical to that in the first cycle, as shown in Figure 4-10.

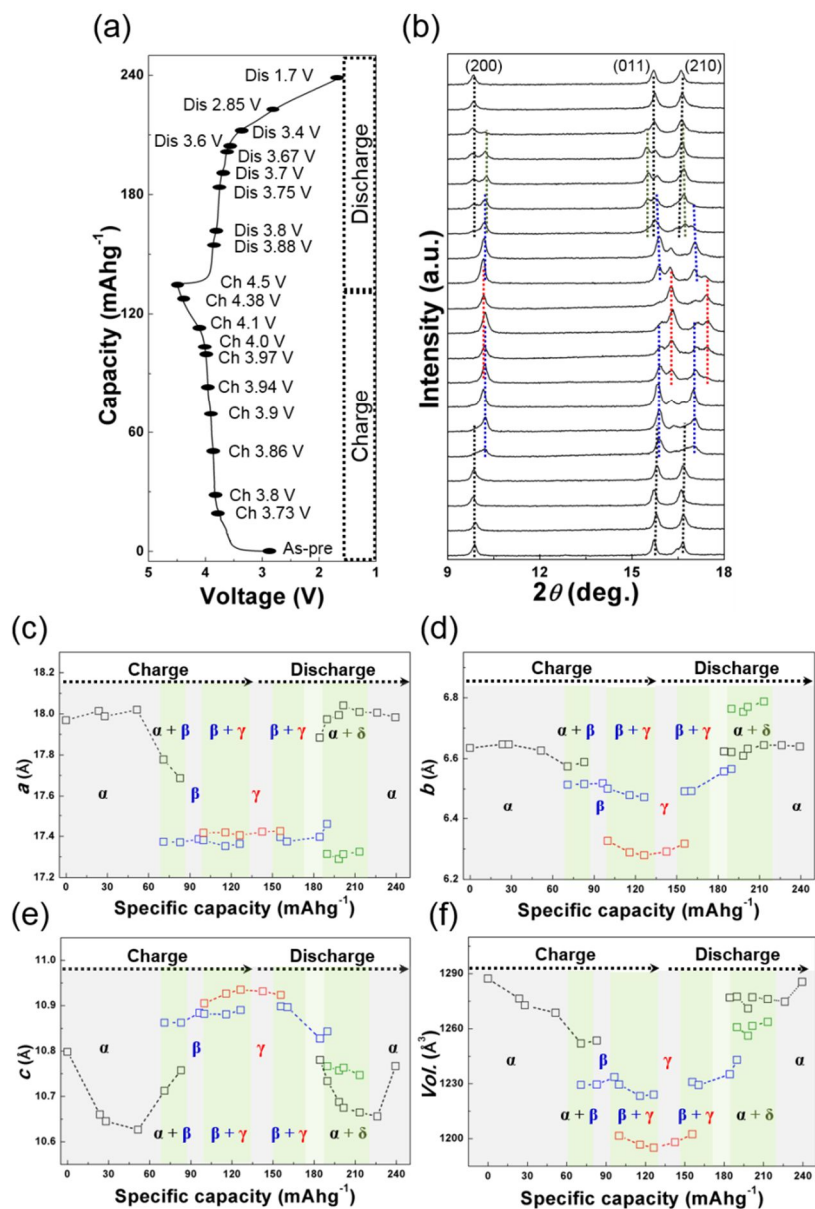


**Figure 4-8.** (a) Galvanostatic charge/discharge profiles of  $\text{Na}_4\text{Mn}_3(\text{PO}_4)_2(\text{P}_2\text{O}_7)$  at a rate of C/20. (b) *Ex situ* XRD patterns of  $\text{Na}_4\text{Mn}_3(\text{PO}_4)_2(\text{P}_2\text{O}_7)$  electrodes during charge/discharge in a Na-ion cell. Changes in the (c)  $a$ , (d)  $b$ , (e)  $c$  lattice parameters and (f) the lattice volume following charging and discharging.

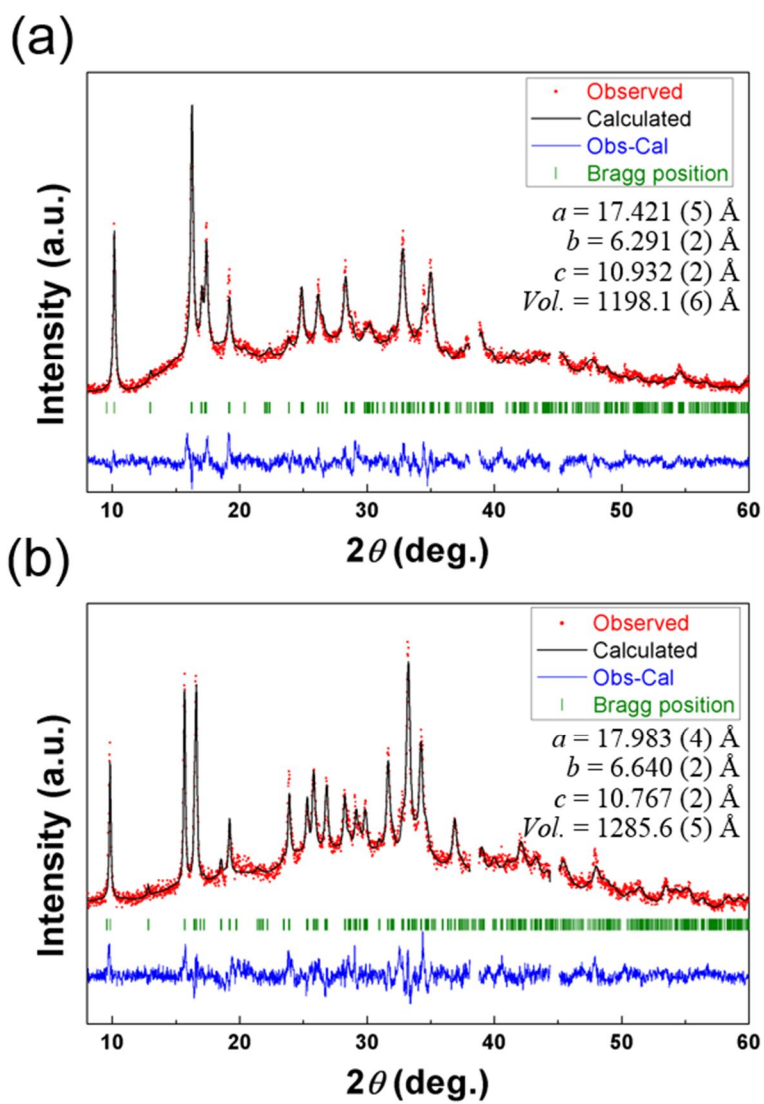


**Figure 4-9.** Rietveld refinement of the XRD patterns of (c) fully charged and (d) discharged electrodes.

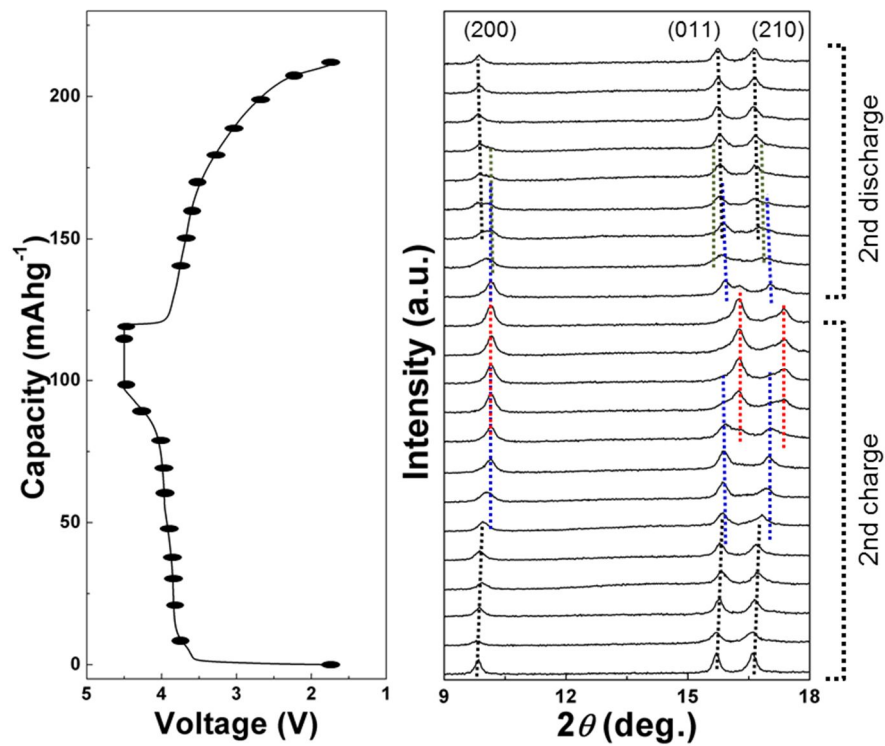


**Figure 4-10.** *Ex situ* XRD patterns of  $\text{Na}_{4-x}\text{Mn}_3(\text{PO}_4)_2(\text{P}_2\text{O}_7)$  during the second charge/discharge cycle. The black, red, blue and green dotted curves corresponds to the  $\alpha$ -,  $\beta$ -,  $\gamma$ - and  $\delta$ -phases, respectively.

#### 4.3.4 Local structural analyses of $\text{Na}_{4-x}\text{Mn}_3(\text{PO}_4)_2(\text{P}_2\text{O}_7)$ ( $0 \leq x \leq 3$ )

##### using *ex situ* XAS

The structural evolution during electrochemical cycling was further analyzed using XAS to monitor the oxidation state and local environment of Mn. Figure 4-11a shows XANES spectra of the  $\text{Na}_{4-x}\text{Mn}_3(\text{PO}_4)_2(\text{P}_2\text{O}_7)$  ( $0 \leq x \leq 3$ ) electrodes during the initial charge process. The clear rightward shift of the XANES spectrum is indicative of oxidation from  $\text{Mn}^{2+}$  to  $\text{Mn}^{3+}$ . In addition, the XANES profile gradually altered, showing an isosbestic point at 6559 eV, which is commonly observed in electrode materials that operate *via* a two-phase reaction.<sup>49, 50</sup> The XANES spectrum shifted back to the initial valence state during the discharge process, and the form of the profile also returned to the initial state, as shown in Figure 4-11b; this indicates that the electrochemical reaction of  $\text{Na}_{4-x}\text{Mn}_3(\text{PO}_4)_2(\text{P}_2\text{O}_7)$  was reversible in the region of  $0 \leq x \leq 3$ . EXAFS analyses also provide information on the local environment of Mn during electrochemical cycling. Figure 4-11c shows Fourier transformed (FT) EXAFS spectra of the electrode during charging. The peak corresponding to Mn-O bonds at 1.56 Å exhibited a gradual increase during the initial charging step, and split into two. This suggests the occurrence of Jahn–Teller active  $\text{Mn}^{3+}$  (indicated by the blue arrow in the figure) in the distorted  $\text{MnO}_6$  octahedron, with two long Mn-O bonds and four short Mn-O bonds.<sup>50</sup> The length of the long Mn-O bond was found to be 1.72 Å, whereas that of the short Mn-O bond was 1.35 Å. The FT-EXFAS signals during subsequent discharging to 1.7 V exhibited a completely reversible behavior, as shown in the red arrow in Figure 4-11d. The XANES and EXAFS spectra during

second charge/discharge cycle were found to be identical to those of the first cycle, as shown in Figure 4-12.

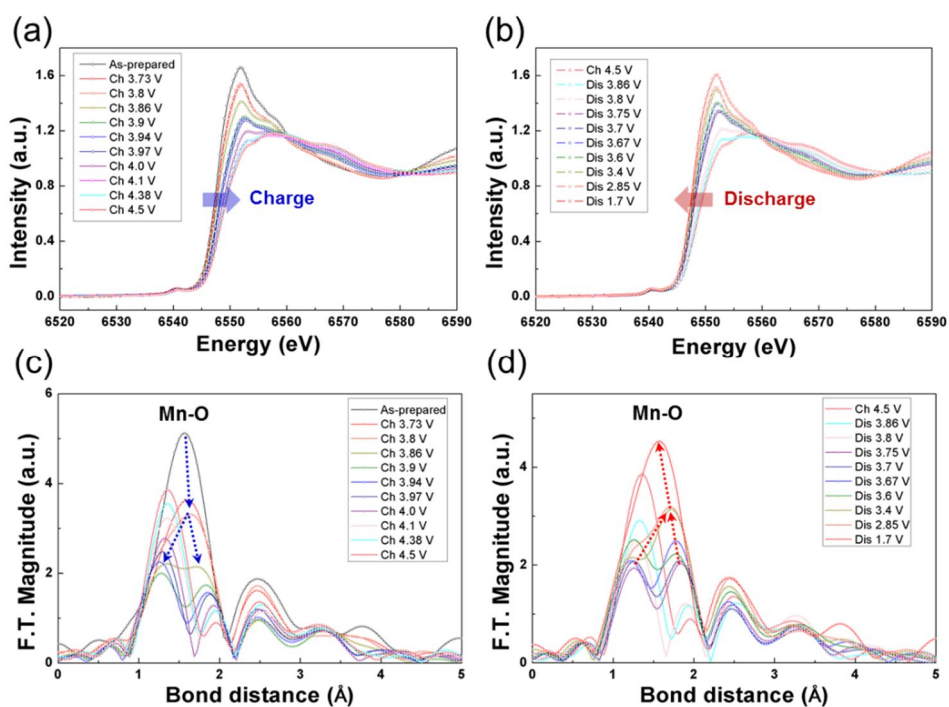


**Figure 4-11.** The XANES spectra of *ex situ* electrode samples of  $\text{Na}_{4-x}\text{Mn}_3(\text{PO}_4)_2(\text{P}_2\text{O}_7)$  ( $0 \leq x \leq 3$ ) during (a) charge and (b) discharge. The EXAFS spectra of *ex situ* electrode samples of  $\text{Na}_{4-x}\text{Mn}_3(\text{PO}_4)_2(\text{P}_2\text{O}_7)$  ( $0 \leq x \leq 3$ ) during (c) charge and (d) discharge.

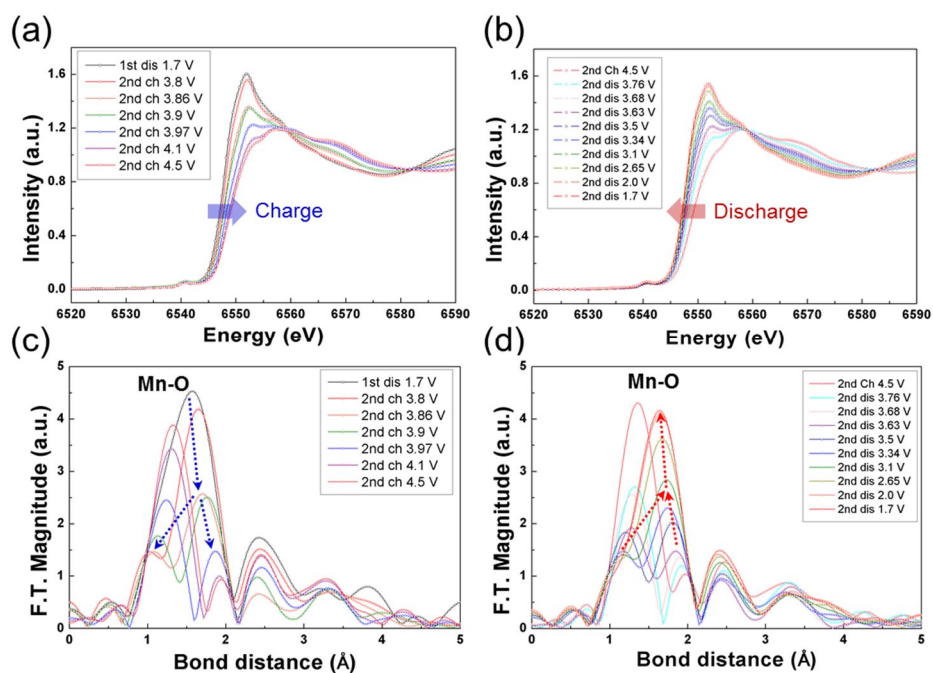


**Figure 4-12.** XANES spectra of the *ex situ* electrode samples of  $\text{Na}_{4-x}\text{Mn}_3(\text{PO}_4)_2(\text{P}_2\text{O}_7)$  ( $0 \leq x \leq 3$ ) during (a) the second charging and (b) discharging. *Ex situ* EXAFS spectra of  $\text{Na}_{4-x}\text{Mn}_3(\text{PO}_4)_2(\text{P}_2\text{O}_7)$  ( $0 \leq x \leq 3$ ) electrode samples (c) during the second charging and (d) discharging.

#### 4.3.5 DFT study on $\text{Na}_{4-x}\text{Mn}_3(\text{PO}_4)_2(\text{P}_2\text{O}_7)$ ( $0 \leq x \leq 3$ )

DFT calculations were carried out to gain insight into the phase reaction of  $\text{Na}_4\text{Mn}_3(\text{PO}_4)_2(\text{P}_2\text{O}_7)$  following desodiation. Figure 4-13a shows the formation energy of  $\text{Na}_{4-x}\text{Mn}_3(\text{PO}_4)_2(\text{P}_2\text{O}_7)$  at a few important sodium contents of  $x$  ( $0 \leq x \leq 3$ ). This energy diagram predicts that  $\text{Na}_4\text{Mn}_3(\text{PO}_4)_2(\text{P}_2\text{O}_7)$  undergoes a single-phase reaction until one Na is extracted from the structure, and further Na extraction leads to a two-phase reaction. This behavior corresponds well with our experimental observations (see Figure 4-8c–f); however, differs in that a single two-phase reaction is predicted to occur between the  $\alpha$  and  $\gamma$ -phases. The absence of a  $\beta$ -phase in the calculations may imply that the  $\beta$ -phase is a kinetically driven intermediate phase between the  $\alpha$ - and  $\gamma$ -phases, which is structurally similar to both the  $\alpha$ - and  $\gamma$ -phases, even though its origin is not clearly understood. The change in the lattice parameters during desodiation also matches well with the experimental observations, as shown in Figure 4-13b. We find negligible changes in the  $a$  and  $b$  lattice parameters ( $< 1\%$ ) within the initial solid–solution reaction, and a larger decrease in  $c$  lattice parameter is shown. Following the extraction of one sodium ion, further charging induces the  $\gamma$ -phase, which has significantly smaller  $a$  and  $b$  lattice parameters, and a larger  $c$  lattice parameter than the  $\alpha$ -phase, which is also in a good agreement with experimental results.

Pristine  $\text{Na}_4\text{Mn}_3(\text{PO}_4)_2(\text{P}_2\text{O}_7)$  has four crystallographically distinguishable Na sites and three Mn sites, as shown in Figure 4-13c. Upon charging, preferential Na

extraction was observed among these sites, along with the corresponding oxidation of Mn, as listed in Table 4-2. Na ions in the Na2 site are preferentially extracted (i.e., removed first), and oxidation of Mn ions in the Mn3 site occurs simultaneously, which was determined from the spin number numerically integrated around the Mn ion, as shown in Figure 4-14. The Mn oxidation preference is also confirmed by the Bader charge analysis and partial density of states (pDOS) calculation (See Table 4-3 and Figure 4-15). The selective oxidation of Mn results in Jahn–Teller distortion in the structure, inducing an increase of the *a* lattice parameter and decrease of *b* and *c* lattice parameters. However, because of the origin distorted nature of the Mn3-O<sub>6</sub> octahedron in the pristine Na<sub>4</sub>Mn<sub>3</sub>(PO<sub>4</sub>)<sub>2</sub>(P<sub>2</sub>O<sub>7</sub>), only a small decrease (~0.1 Å) in the bond lengths in the *bc*-plane occurs, accompanied by a slight elongation of bond lengths in the *a*-direction, as shown in Figure 4-13. This appears to be reason for such small changes in the *a* and *b* lattice parameters, despite the Jahn–Teller active Mn<sup>3+</sup> ion.

The fully desodiated phase, NaMn<sub>3</sub>(PO<sub>4</sub>)<sub>2</sub>(P<sub>2</sub>O<sub>7</sub>), has one quarter of the Na occupancy in the Na1 and Na3 sites, and half of the Na occupancy in the Na4 (see Table 4-2). All of the Mn ions are in 3+ oxidation states, regardless of their sites, leading to Jahn–Teller distortion of each of the Mn octahedra. Following oxidation to Mn<sup>3+</sup>, edge-sharing octahedra of Mn1-O<sub>6</sub> and Mn3-O<sub>6</sub> change to corner-sharing (denoted by the circle in Figure 4-13c), which is similar to what is observed in NaFe<sub>3</sub>(PO<sub>4</sub>)<sub>2</sub>(P<sub>2</sub>O<sub>7</sub>).<sup>48</sup> This phenomenon may be attributed to strong repulsion of between Mn<sup>3+</sup> ions in the [Mn<sub>3</sub>P<sub>2</sub>O<sub>13</sub>]<sub>∞</sub> chain. To accommodate this repulsion, the

$P_2O_7$  dimer distorts to adopt the corner-sharing of the Mn1 and Mn3 octahedra, increasing the distance between Mn1 and Mn3 sites from 3.36 Å to 3.66 Å. This distortion results in a shift of the Mn1 along the *c*-direction, increasing the *c* lattice parameter, which is also verified by the comparison of simulated XRD patterns and experimental ones as shown in Figure 4-17. Interestingly, the nature of the Jahn–Teller distortion in the Mn3-O<sub>6</sub> octahedra significantly changes at this stage, as shown in Fig. S8. The initial distortion of the Mn3-O<sub>6</sub> octahedra in Na<sub>3</sub>Mn<sub>3</sub>(PO<sub>4</sub>)<sub>2</sub>(P<sub>2</sub>O<sub>7</sub>) contains two long Mn-O bonds in the *a*-direction (Mn3-O11 and Mn3-O14) and four short bonds in the *bc*-plane (indicated by the yellow and white arrows, respectively, in the centre of Figure 4-16). However, this changes to the octahedral form with two long Mn-O bonds in the *bc*-plane (Mn3-O1 and Mn3-O4) and four remaining short Mn-O bonds in the *a*-direction and in the *bc*-plane of NaMn<sub>3</sub>(PO<sub>4</sub>)<sub>2</sub>(P<sub>2</sub>O<sub>7</sub>) (see the right-hand side of Figure 4-16). This is primarily due to the concurrent manifestation of Jahn–Teller distortions in the Mn1-O<sub>6</sub> and Mn2-O<sub>6</sub> octahedra of the fully desodiated state. Because the Mn-O bonds in the Mn1-O<sub>6</sub> and Mn2-O<sub>6</sub> octahedra are shortened along *bc*-plane due to the Jahn–Teller distortion, the Mn3-O<sub>6</sub> octahedron stretches along the *bc*-plane, as shown by yellow arrows in Figure 4-13c. This results in the elongation of the Mn3-O1 and Mn3-O4 bonds, and the remaining four Mn-O bonds of Mn3-O<sub>6</sub> octahedron are shortened to maintain the energy gain from the Jahn–Teller distortion.<sup>51, 52</sup>

The structural distortion induced by the Jahn–Teller active Mn<sup>3+</sup> has an important effect on the mobility of Na ions in the structure. Figure 4-18a–c show

the Na diffusion pathways in the  $\text{Na}_{4-x}\text{Mn}_3(\text{PO}_4)_2(\text{P}_2\text{O}_7)$  ( $x = 0, 1, 3$ ) structures. A 3D network of interconnected Na diffusion pathways can be clearly seen. One interesting point to note is that, unlike most reported manganese-based cathode materials, Na diffusion is not significantly retarded by the structural changes induced by the Jahn–Teller distortion.<sup>50, 53</sup> While distortion of the  $\text{P}_2\text{O}_7$  dimer in  $\text{NaMn}_3(\text{PO}_4)_2(\text{P}_2\text{O}_7)$  causes atomic rearrangements of Mn, P and O ions in the structure (see Figure 4-19), according to our calculations of the various Na diffusion pathways, the activation barriers for Na hopping do not increase after the local distortion (see Table 4-4). It is worthwhile to note that  $\text{Na}_4\text{Fe}_3(\text{PO}_4)_2(\text{P}_2\text{O}_7)$ , which shows similar structural evolution to  $\text{Na}_4\text{Mn}_3(\text{PO}_4)_2(\text{P}_2\text{O}_7)$ , exhibits slow Na kinetics at this state of charge because of the  $\text{P}_2\text{O}_7$  distortion and atomic rearrangement which narrows the Na diffusion channels.<sup>48</sup> In the case of  $\text{Na}_4\text{Fe}_3(\text{PO}_4)_2(\text{P}_2\text{O}_7)$ , the activation barriers in most Na diffusion paths increase after Fe oxidation as shown in Table 4-5. After Fe oxidation, there are only limited plausible Na diffusion pathways remaining for  $\text{NaFe}_3(\text{PO}_4)_2(\text{P}_2\text{O}_7)$ , as activation barriers of Na1 – Na4, Na2 – Na4, Na3 – Na2, Na3 – Na4 paths become higher than 500 eV. In particular, as the Na3 – Na2 path closes down due to significantly higher barrier, the 3-dimensional diffusion channel of  $\text{Na}_4\text{Fe}_3(\text{PO}_4)_2(\text{P}_2\text{O}_7)$  does not remain intact (See Figure 4-20). In case of  $\text{NaMn}_3(\text{PO}_4)_2(\text{P}_2\text{O}_7)$ , on the contrary, activation barriers of most pathways considerably decrease and 3-dimensional connection of Na diffusion pathways is maintained due to the anomalous behavior of Mn ion distortion.

In order to understand why the activation barriers of most Na diffusion pathways decrease in  $\text{Na}_4\text{Mn}_3(\text{PO}_4)_2(\text{P}_2\text{O}_7)$ , we took a closer look at Na1 – Na4 diffusion pathway (denoted by the circle in Figure 4-18a and c). We found that Jahn-Teller distortion of Mn1-O<sub>6</sub> and Mn2-O<sub>6</sub> octahedra in  $\text{NaMn}_3(\text{PO}_4)_2(\text{P}_2\text{O}_7)$  induces a shift of each site in the c-direction; however, the Mn1-O5 and Mn2-O1 bond length increases in the c-direction due to the Jahn–Teller distortion, opening up an Na diffusion channel; *i.e.*, the Na1 – Na4 channel (see Table 4-4), as shown in Figure 4-21a-b and Figure 4-16. Closer inspection of the local environment for diffusion between Na1 and Na4 sites indicates that, in the intermediate states of Na diffusion, the distance between the diffusing Na ions and the 6 adjacent O ions, which forms the tunnel space, increases due to the oxidation of Mn1 and Mn2 (see Table 4-6). The volume of Na-O<sub>6</sub> octahedra in the intermediate state increases from 14.20 Å<sup>3</sup> to 15.70 Å<sup>3</sup>. Accordingly, the activation barrier drastically decreases from 560 meV to 306 meV. This is in clear contrast to the case for Na diffusion in  $\text{NaFe}_3(\text{PO}_4)_2(\text{P}_2\text{O}_7)$ , where the channel narrows significantly due to the shift of Fe1 sites in *a*-direction and distortion of P<sub>2</sub>O<sub>7</sub>, which critically increases the activation barrier from 599 meV to 922 meV. (See Table 4-6 and Figure 4-22). Considering that the ionic mobility depends critically on the space of the diffusion pathways, it is reasonable to expect that the activation barrier for Na ions in the Na1 – Na4 pathway is smaller with  $\text{NaMn}_3(\text{PO}_4)_2(\text{P}_2\text{O}_7)$ , despite the stronger repulsive interaction between Mn<sup>3+</sup> in the charged state.<sup>54, 55</sup> This unique structural evolution can explain the high rate capability and cycle stability of  $\text{Na}_4\text{Mn}_3(\text{PO}_4)_2(\text{P}_2\text{O}_7)$

observed from the experiments. It is also consistent with the observation that the polarization remains small at the final state of charge in galvanostatic intermittent titration technique (GITT) profiles of  $\text{Na}_4\text{Mn}_3(\text{PO}_4)_2(\text{P}_2\text{O}_7)$ , whereas a dramatic increase of overpotential is observed in  $\text{Na}_4\text{Fe}_3(\text{PO}_4)_2(\text{P}_2\text{O}_7)$  (see Figure 4-23). Furthermore, this provides an important example structure whereby the Jahn–Teller distortion facilitates Na diffusion that than retarding, it has been reported for most Mn-based cathode materials.<sup>27-30, 50, 53</sup>

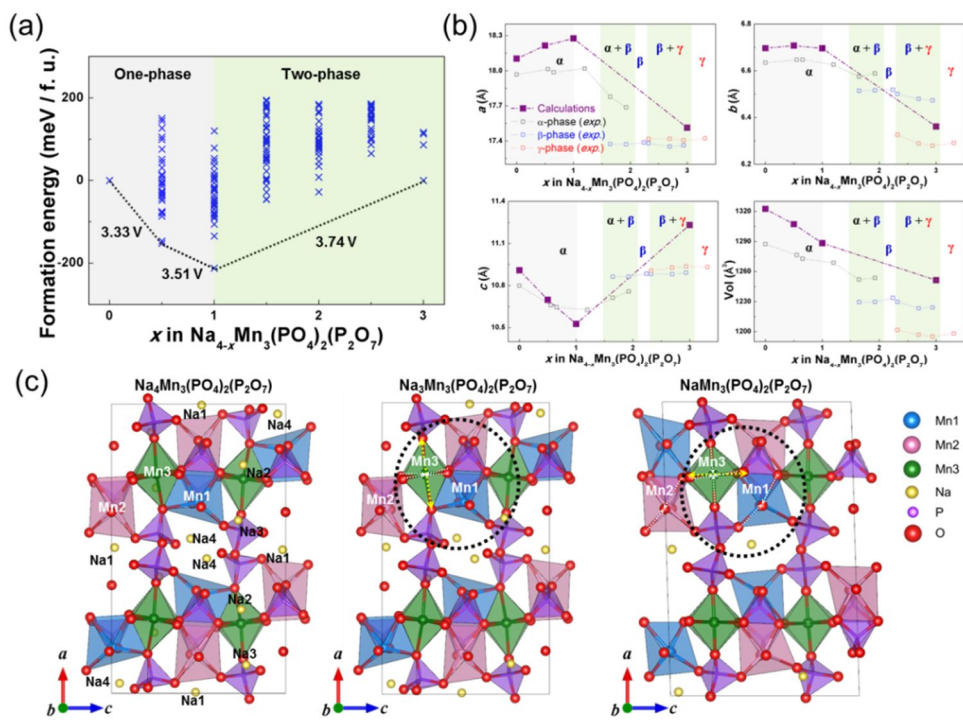


**Figure 4-13.** (a) Formation energy plot of  $\text{Na}_{4-x}\text{Mn}_3(\text{PO}_4)_2(\text{P}_2\text{O}_7)$  ( $0 \leq x \leq 3$ ). (b) Lattice parameters of each phase in  $\text{Na}_{4-x}\text{Mn}_3(\text{PO}_4)_2(\text{P}_2\text{O}_7)$  ( $0 \leq x \leq 3$ ), both from the DFT calculations and the experiments. (c) Calculated structures of (left)  $\text{Na}_4\text{Mn}_3(\text{PO}_4)_2(\text{P}_2\text{O}_7)$ , (centre)  $\text{Na}_3\text{Mn}_3(\text{PO}_4)_2(\text{P}_2\text{O}_7)$  and (right)  $\text{NaMn}_3(\text{PO}_4)_2(\text{P}_2\text{O}_7)$ .

**Table 4-2.** Desodiation sequence and Mn oxidation states upon charging of  $\text{Na}_{4-x}\text{Mn}_3(\text{PO}_4)_2(\text{P}_2\text{O}_7)$  ( $0 \leq x \leq 3$ ) based on the DFT calculations.

Sites	Occupancy				Valence state		
	Na1	Na2	Na3	Na4	Mn1	Mn2	Mn3
$\text{Na}_4\text{Mn}_3(\text{PO}_4)_2(\text{P}_2\text{O}_7)$	1	1	1	1	2+	2+	2+
$\text{Na}_{3.5}\text{Mn}_3(\text{PO}_4)_2(\text{P}_2\text{O}_7)$	1	0.5	1	1	2+	2+	2+/3+
$\text{Na}_3\text{Mn}_3(\text{PO}_4)_2(\text{P}_2\text{O}_7)$	1	0	1	1	2+	2+	3+
$\text{NaMn}_3(\text{PO}_4)_2(\text{P}_2\text{O}_7)$	0.25	0	0.25	0.5	3+	3+	3+

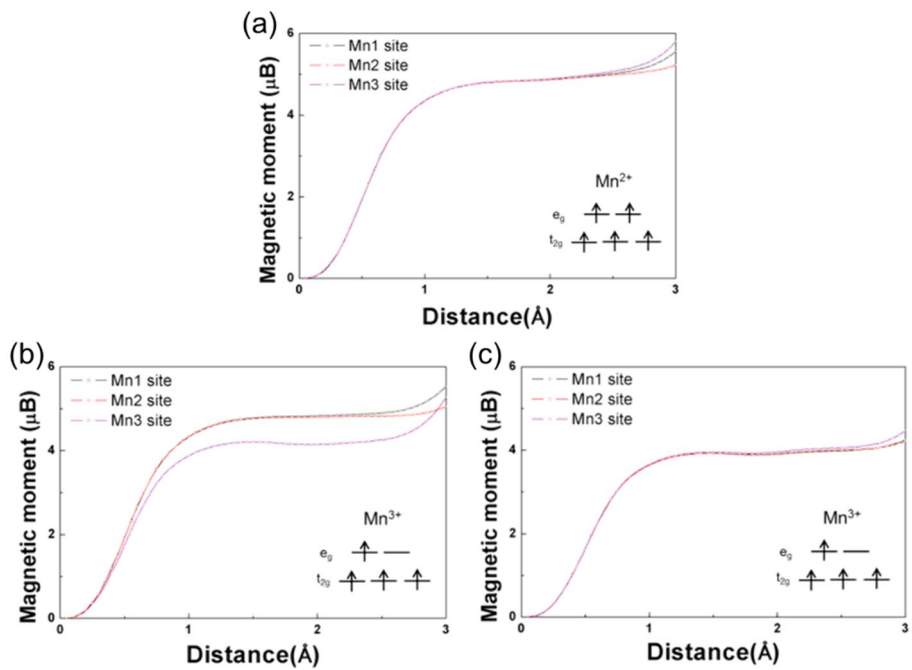


**Figure 4-14.** Spin integration of Mn ions in (a)  $\text{Na}_4\text{Mn}_3(\text{PO}_4)_2(\text{P}_2\text{O}_7)$ , (b)  $\text{Na}_3\text{Mn}_3(\text{PO}_4)_2(\text{P}_2\text{O}_7)$  and (c)  $\text{NaMn}_3(\text{PO}_4)_2(\text{P}_2\text{O}_7)$ .

**Table 4-3.** Bader charge analysis on  $\text{Na}_4\text{Mn}_3(\text{PO}_4)_2(\text{P}_2\text{O}_7)$  upon desodiation.

Sites	Bader charge		
	Mn1	Mn2	Mn3
$\text{Na}_4\text{Mn}_3(\text{PO}_4)_2(\text{P}_2\text{O}_7)$	+1.50	+1.50	+1.51
$\text{Na}_3\text{Mn}_3(\text{PO}_4)_2(\text{P}_2\text{O}_7)$	+1.52	+1.53	+1.74
$\text{NaMn}_3(\text{PO}_4)_2(\text{P}_2\text{O}_7)$	+1.75	+1.78	+1.78

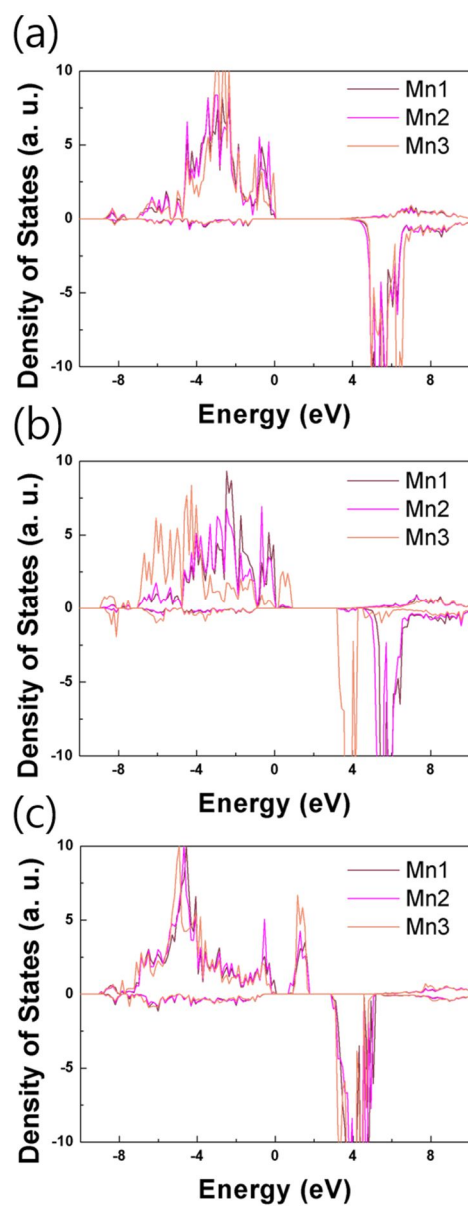
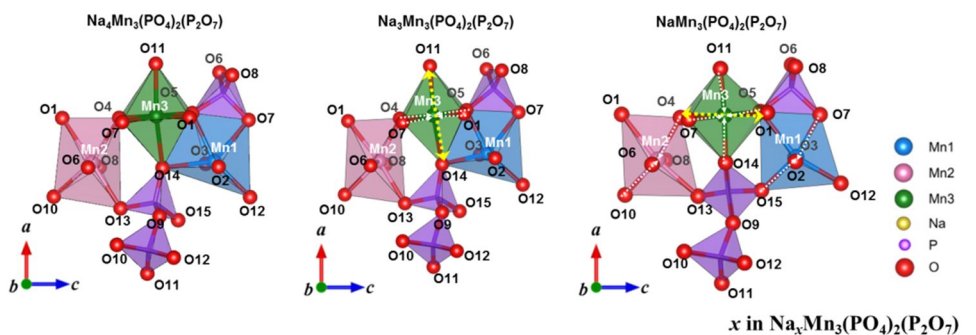


**Figure 4-15.** Partial Density of States (pDOS) of (a)  $\text{Na}_4\text{Mn}_3(\text{PO}_4)_2(\text{P}_2\text{O}_7)$ , (b)  $\text{Na}_3\text{Mn}_3(\text{PO}_4)_2(\text{P}_2\text{O}_7)$  and (c)  $\text{NaMn}_3(\text{PO}_4)_2(\text{P}_2\text{O}_7)$ .



$x$ in $\text{Na}_x\text{Mn}_3(\text{PO}_4)_2(\text{P}_2\text{O}_7)$											
	$x = 4$	$x = 3$	$x = 1$		$x = 4$	$x = 3$	$x = 1$		$x = 4$	$x = 3$	$x = 1$
<b>Mn1-O12</b>	2.19359	2.14609	2.12345	<b>Mn2-O1</b>	2.30757	2.32009	2.34324	<b>Mn3-O11</b>	2.26099	<u>2.26949</u>	1.90277
<b>Mn1-O5</b>	2.27667	2.20061	2.34099	<b>Mn2-O13</b>	2.335	2.25696	2.22463	<b>Mn3-O14</b>	2.44977	<u>2.41048</u>	1.91366
<b>Mn1-O7</b>	2.34478	2.3876	1.96494	<b>Mn2-O6</b>	2.13627	2.1887	1.95271	<b>Mn3-O1</b>	2.14498	1.99636	<u>2.37308</u>
<b>Mn1-O15</b>	2.29278	2.21251	1.98209	<b>Mn2-O8</b>	2.1425	2.13742	1.99626	<b>Mn3-O4</b>	2.13777	1.99852	<u>2.31788</u>
<b>Mn1-O3</b>	2.15481	2.13651	1.98471	<b>Mn2-O10</b>	2.20473	2.18322	1.96033	<b>Mn3-O5</b>	2.15207	2.03149	1.96856
<b>Mn1-O2</b>	2.1573	2.21453	1.94916	<b>Mn2-O4</b>	2.25386	2.18287	1.96624	<b>Mn3-O7</b>	2.16584	2.00348	1.99423

**Figure 4-16.** The magnified local structure of  $\text{Na}_{4-x}\text{Mn}_3(\text{PO}_4)_2(\text{P}_2\text{O}_7)$  ( $x = 0, 1, 3$ ).

The bond lengths between Mn and O ions are listed in the table below.

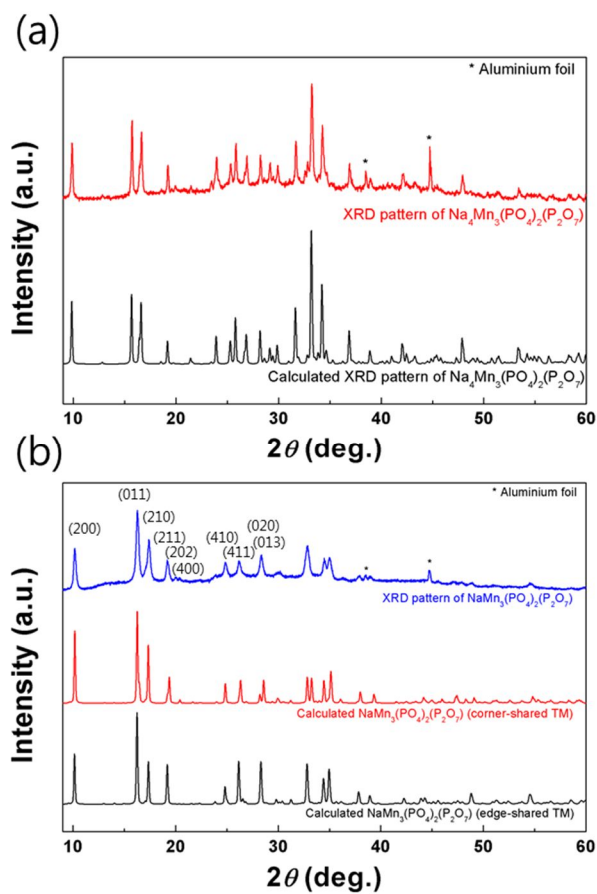


**Figure 4-17.** The XRD patterns of  $\text{Na}_{4-x}\text{Mn}_3(\text{PO}_4)_2(\text{P}_2\text{O}_7)$  ((a)  $x = 0$ , (b)  $x = 3$ ) from experiments and DFT calculations.

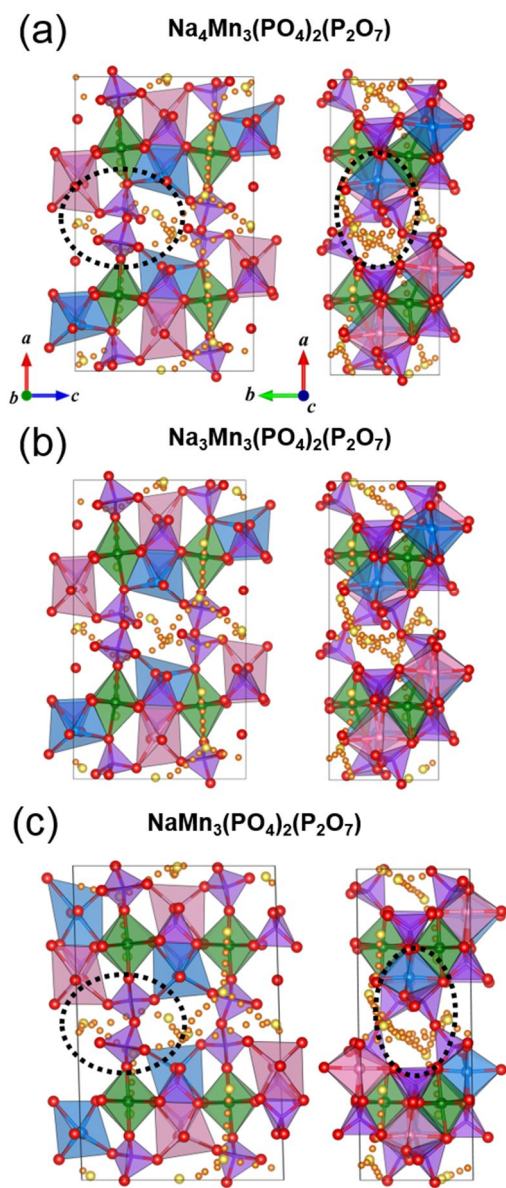


**Figure 4-18.** Na diffusion pathways in (a)  $\text{Na}_4\text{Mn}_3(\text{PO}_4)_2(\text{P}_2\text{O}_7)$ , (b)  $\text{Na}_3\text{Mn}_3(\text{PO}_4)_2(\text{P}_2\text{O}_7)$  and (c)  $\text{NaMn}_3(\text{PO}_4)_2(\text{P}_2\text{O}_7)$ .

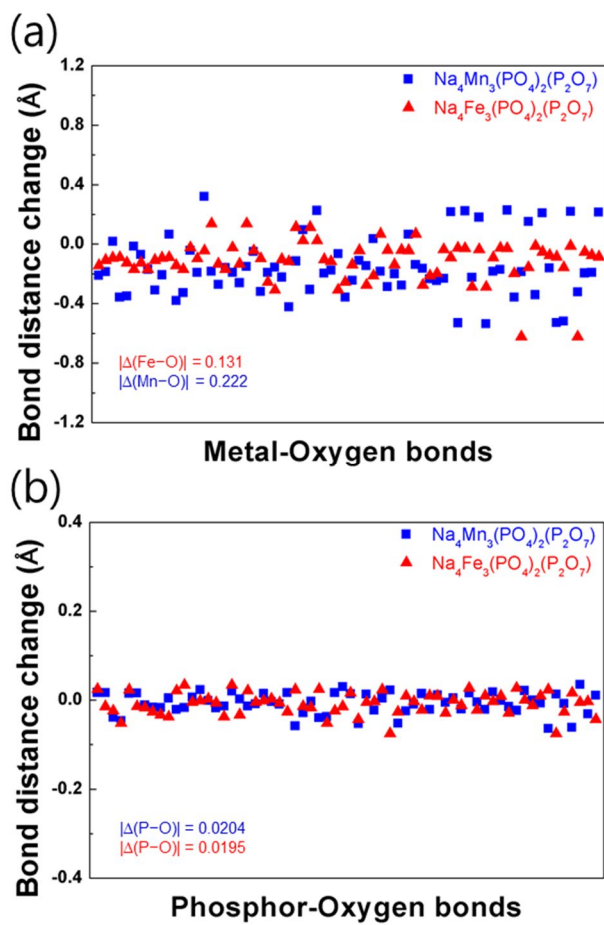


**Figure 4-19.** Bond distance change of (a)  $\Delta(\text{Me-O})$  and (b)  $\Delta(\text{P-O})$  in  $\text{Na}_4\text{Me}_3(\text{PO}_4)_2(\text{P}_2\text{O}_7)$  (Me=Mn, Fe) after full charge.

**Table 4-4.** The calculated activation barriers for Na diffusion in  $\text{Na}_4\text{-}_x\text{Mn}_3(\text{PO}_4)_2(\text{P}_2\text{O}_7)$ . ( $x = 0, 1, 3$ )

<b>From (Na site)</b>	<b>To (Na site)</b>	<b><math>E_a</math>, (meV) <math>x = 4</math></b>	<b><math>E_a</math>, (meV) <math>x = 3</math></b>	<b><math>E_a</math>, (meV) <math>x = 1</math></b>
1	1	306	168	282
1	4	560	242	306
2	4	492	>1000	>1000
3	1	209	238	674
3	2	246	243	98
3	4	499	583	288
4	4	271	432	147

**Table 4-5.** The calculated activation barriers for Na diffusion in  $\text{Na}_{4-x}\text{Fe}_3(\text{PO}_4)_2(\text{P}_2\text{O}_7)$ . ( $x = 0, 3$ )

<b>From (Na site)</b>	<b>To (Na site)</b>	<b><math>E_a</math> (meV) <math>\text{Na}_4\text{Fe}_3(\text{PO}_4)_2(\text{P}_2\text{O}_7)</math></b>	<b><math>E_a</math> (meV) <math>\text{NaFe}_3(\text{PO}_4)_2(\text{P}_2\text{O}_7)</math></b>
1	1	256	349
1	4	599	922
2	4	481	853
3	1	540	269
3	2	344	558
3	4	685	630
4	4	544	325

s

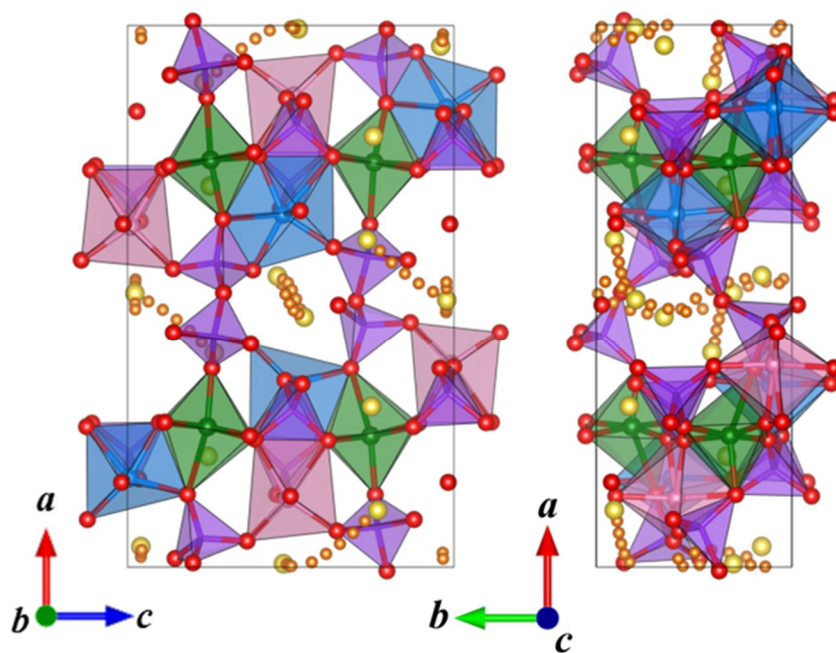


**Figure 4-20.** Na diffusion pathways in  $\text{NaFe}_3(\text{PO}_4)_2(\text{P}_2\text{O}_7)$  with an activation energy below 500 meV.

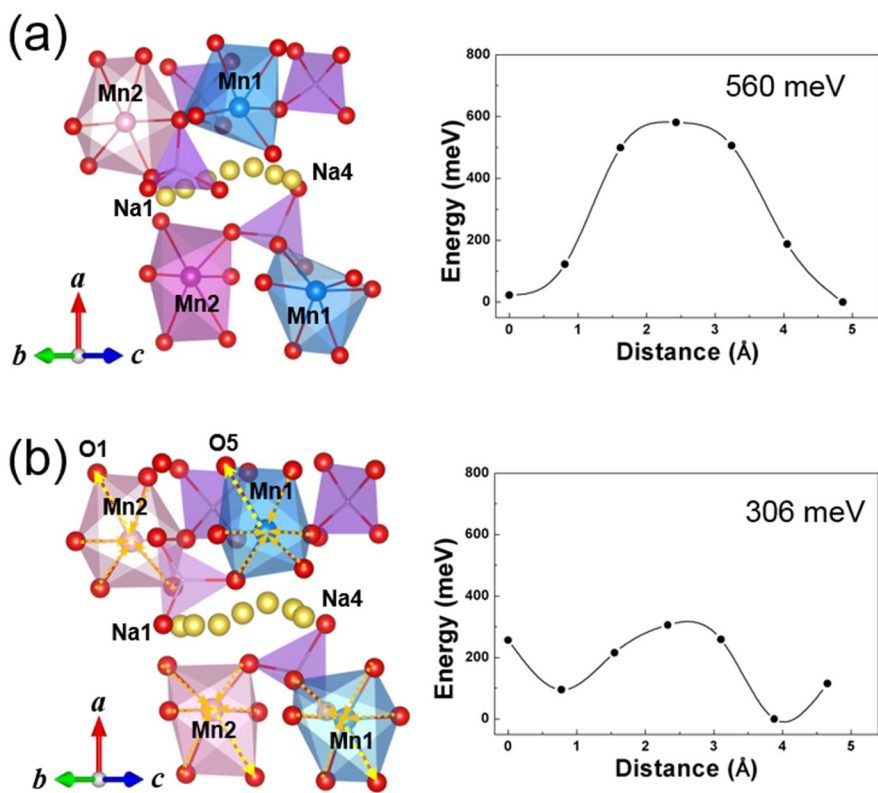


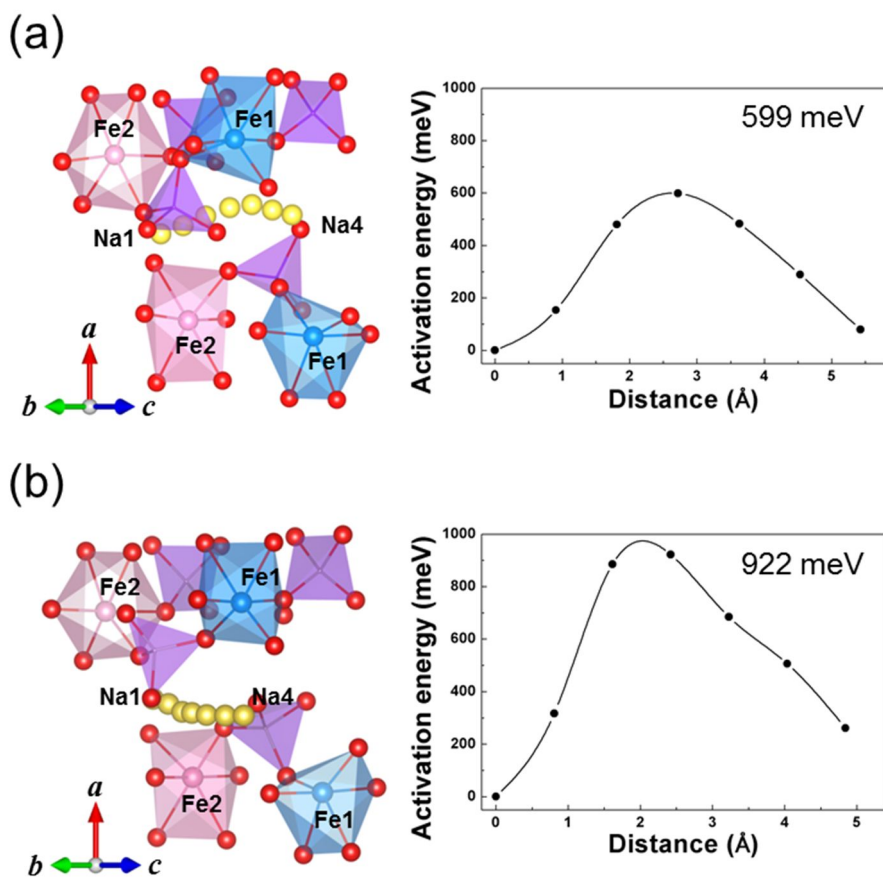
**Figure 4-21.** Magnified diffusion pathways of Na ions from the Na1 to Na4 sites (shown by the black circles in Figure 4-18a and c) in (a) Na<sub>4</sub>Mn<sub>3</sub>(PO<sub>4</sub>)<sub>2</sub>(P<sub>2</sub>O<sub>7</sub>) and (b) NaMn<sub>3</sub>(PO<sub>4</sub>)<sub>2</sub>(P<sub>2</sub>O<sub>7</sub>).

**Table 4-6.** Distance from diffusing Na ions in the intermediate state to adjacent Mn ions and O ions.

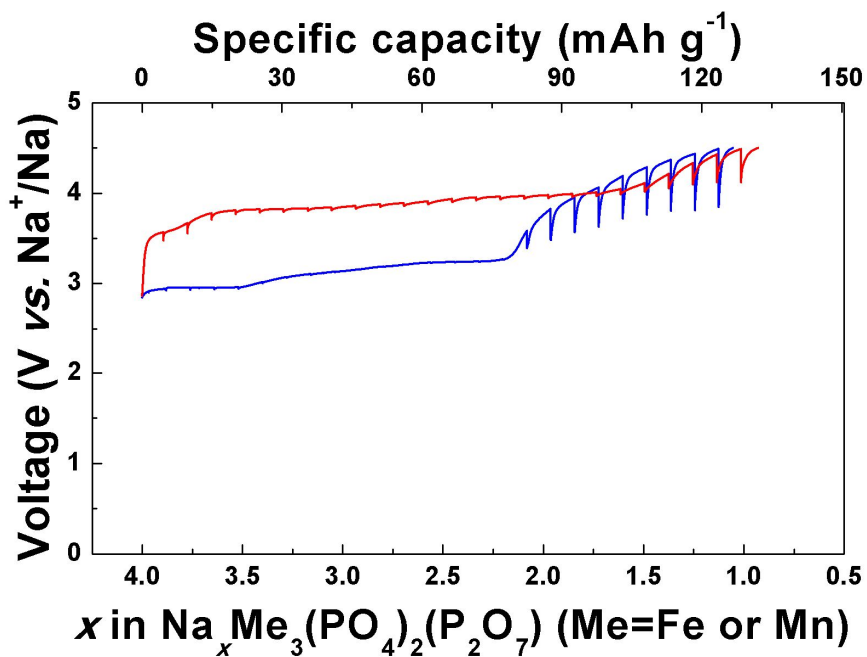
<b>Distance from migrating Na</b>	<b>Na<sub>4</sub>Mn<sub>3</sub>(PO<sub>4</sub>)<sub>2</sub>(P<sub>2</sub>O<sub>7</sub>)</b>	<b>NaMn<sub>3</sub>(PO<sub>4</sub>)<sub>2</sub>(P<sub>2</sub>O<sub>7</sub>)</b>
Mn1	4.31(2+)	4.24(3+)
Mn2	3.62(2+)	3.81(3+)
O8	2.52	3.19
O9	2.51	2.84
O10	2.51	2.62
O12	2.83	2.38
O13	2.69	2.17
O15	2.56	2.58

<b>Distance from migrating Na</b>	<b>Na<sub>4</sub>Fe<sub>3</sub>(PO<sub>4</sub>)<sub>2</sub>(P<sub>2</sub>O<sub>7</sub>)</b>	<b>NaFe<sub>3</sub>(PO<sub>4</sub>)<sub>2</sub>(P<sub>2</sub>O<sub>7</sub>)</b>
Fe1	4.36(2+)	4.40(3+)
Fe2	3.85(2+)	4.08(3+)
O8	2.60	-
O9	2.49	-
O10	2.38	2.93
O12	2.92	1.99
O13	2.83	2.26
O15	2.35	2.41
O6	-	2.90
O10	-	2.93



**Figure 4-22.** Magnified diffusion pathways of Na ions from Na1 to Na4 site in (a)  $\text{Na}_4\text{Fe}_3(\text{PO}_4)_2(\text{P}_2\text{O}_7)$  and (b)  $\text{NaFe}_3(\text{PO}_4)_2(\text{P}_2\text{O}_7)$ .



**Figure 4-23.** Galvanostatic intermittent titration technique (GITT) profiles of  $\text{NaMn}_3(\text{PO}_4)_2(\text{P}_2\text{O}_7)$  and  $\text{Na}_4\text{Fe}_3(\text{PO}_4)_2(\text{P}_2\text{O}_7)$  in Na-ion cells.

## 4.4 Conclusion

We have described a 3.8-V Mn-based mixed-phosphate; i.e.,  $\text{Na}_4\text{Mn}_3(\text{PO}_4)_2(\text{P}_2\text{O}_7)$ , which was successfully synthesized, and promising electrochemical activity was characterized for the first time. The  $\text{Mn}^{2+}/\text{Mn}^{3+}$  redox potential of 3.84 V vs.  $\text{Na}^+/\text{Na}$  is the largest yet reported among manganese-based cathode materials, resulting in a significant increase in the energy density compared with existing materials, representing the largest value yet reported (i.e.,  $416 \text{ Wh kg}^{-1}$ ). The high power capability and cycle stability of a manganese-based cathode was observed in Na-ion cells, and is attributed to the unique Jahn–Teller distortion that occurs in this material, which opens up Na diffusion channels, as shown by first principles DFT calculations. The multi-phase reaction with a small lattice volume change of approximately 7% during the electrochemical cycling was found, which also enables the remarkable cycle stability of this material. We believe that the low-cost, stable cycle performances, and high energy density makes  $\text{Na}_4\text{Mn}_3(\text{PO}_4)_2(\text{P}_2\text{O}_7)$  a particularly promising material for cathodes in large-scale Na rechargeable batteries.

## 4.5 References

- (1) J. M. Tarascon and M. Armand, *Nature*, **2001**, *414*, 359-367.
- (2) M. Armand and J. M. Tarascon, *Nature*, **2008**, *451*, 652-657.
- (3) S.-W. Kim, D.-H. Seo, X. Ma, G. Ceder and K. Kang, *Adv. Energy Mater.*, **2012**, *2*, 710-721.
- (4) H. Pan, Y.-S. Hu and L. Chen, *Energy Environ. Sci.*, **2013**, *6*, 2338-2360.
- (5) N. Yabuuchi, K. Kubota, M. Dahbi and S. Komaba, *Chem. Rev.*, **2014**, *114*, 11636-11682.
- (6) N. Yabuuchi, M. Kajiyama, J. Iwatate, H. Nishikawa, S. Hitomi, R. Okuyama, R. Usui, Y. Yamada and S. Komaba, *Nat. Mater.*, **2012**, *11*, 512-517.
- (7) R. Berthelot, D. Carlier and C. Delmas, *Nat. Mater.*, **2011**, *10*, 74-80.
- (8) S. Komaba, N. Yabuuchi, T. Nakayama, A. Ogata, T. Ishikawa and I. Nakai, *Inorg. Chem.*, **2012**, *51*, 6211-6220.
- (9) Y. Lu, L. Wang, J. Cheng and J. B. Goodenough, *Chem. Commun.* **2012**, *48*, 6544-6546.
- (10) L. Wang, Y. Lu, J. Liu, M. Xu, J. Cheng, D. Zhang and J. B. Goodenough, *Angew. Chem. Int. Ed.* **2013**, *52*, 1964-1967.
- (11) Y. You, X. -L. Wu, Y. -X. Yin and Y. -G. Guo, *Energy Environ. Sci.* **2014**, *7*, 1643-1647.

- (12) J. Song, L. Wang, Y. Lu, J. Liu, B. Guo, P. Xiao, J. -J. Lee, X. -Q. Yang, G. Henkelman and J. B. Goodenough, *J. Am. Chem. Soc.* **2015**, *137*, 2658-2664.
- (13) P. Xiao, J. Song, L. Wang, J. B. Goodenough and G. Henkelman, *Chem. Mater.* **2015**, *27*, 3763.
- (14) P. Barpanda, T. Ye, S.-i. Nishimura, S.-C. Chung, Y. Yamada, M. Okubo, H. Zhou and A. Yamada, *Electrochem. Commun.*, **2012**, *24*, 116-119.
- (15) P. Barpanda, G. Oyama, S.-i. Nishimura, S.-C. Chung and A. Yamada, *Nat. Commun.*, **2014**, *5*, 4358.
- (16) H. Kim, I. Park, D.-H. Seo, S. Lee, S.-W. Kim, W. J. Kwon, Y.-U. Park, C. S. Kim, S. Jeon and K. Kang, *J. Am. Chem. Soc.*, **2012**, *134*, 10369-10372.
- (17) B. L. Ellis, W. R. M. Makahnouk, Y. Makimura, K. Toghill and L. F. Nazar, *Nat. Mater.*, **2007**, *6*, 749-753.
- (18) K. T. Lee, T. N. Ramesh, F. Nan, G. Botton and L. F. Nazar, *Chem. Mater.*, **2011**, *23*, 3593-3600.
- (19) P. Barpanda, G. Oyama, C. D. Ling and A. Yamada, *Chem. Mater.*, **2014**, *26*, 1297-1299.
- (20) K.-H. Ha, S. H. Woo, D. Mok, N.-S. Choi, Y. Park, S. M. Oh, Y. Kim, J. Kim, J. Lee, L. F. Nazar and K. T. Lee, *Adv. Energy Mater.*, **2013**, *3*, 689-689.
- (21) W. Huang, J. Zhou, B. Li, J. Ma, S. Tao, D. Xia, W. Chu and Z. Wu, *Sci. Rep.*, **2014**, *4*, 4188.

- (22) Z. Jian, W. Han, X. Lu, H. Yang, Y.-S. Hu, J. Zhou, Z. Zhou, J. Li, W. Chen, D. Chen and L. Chen, *Adv. Energy Mater.*, **2013**, *3*, 156-160.
- (23) Y.-U. Park, D.-H. Seo, H.-S. Kwon, B. Kim, J. Kim, H. Kim, I. Kim, H.-I. Yoo and K. Kang, *J. Am. Chem. Soc.*, **2013**, *135*, 13870-13878.
- (24) R. A. Shakoor, D.-H. Seo, H. Kim, Y.-U. Park, J. Kim, S.-W. Kim, H. Gwon, S. Lee and K. Kang, *J. Mater. Chem.*, **2012**, *22*, 20535-20541.
- (25) S. Y. Lim, H. Kim, J. Chung, J. H. Lee, B. G. Kim, J.-J. Choi, K. Y. Chung, W. Cho, S.-J. Kim, W. A. Goddard, Y. Jung and J. W. Choi, *Proc. Nat. Acad. Sci. U. S. A.*, **2013**, *111*, 599-604.
- (26) H. Zhuo, X. Wang, A. Tang, Z. Liu, S. Gamboa and P. J. Sebastian, *J. Power Sources*, **2006**, *160*, 698-703.
- (27) S.-W. Kim, D.-H. Seo, H. Kim, K.-Y. Park and K. Kang, *Phys. Chem. Chem. Phys.*, **2012**, *14*, 3299-3303.
- (28) C. S. Park, H. Kim, R. A. Shakoor, E. Yang, S. Y. Lim, R. Kahraman, Y. Jung and J. W. Choi, *J. Am. Chem. Soc.*, **2013**, *135*, 2787-2792.
- (29) P. Barpanda, T. Ye, M. Avdeev, S.-C. Chung and A. Yamada, *J. Mater. Chem. A*, **2013**, *1*, 4194-4197.
- (30) H. Chen, Q. Hao, O. Zivkovic, G. Hautier, L.-S. Du, Y. Tang, Y.-Y. Hu, X. Ma, C. P. Grey and G. Ceder, *Chem. Mater.*, **2013**, *25*, 2777-2786.
- (31) J. P. Perdew, K. Burke and M. Ernzerhof, *Phys. Rev. Lett.*, **1996**, *77*, 3865-3868.

- (32) V. I. Anisimov, J. Zaanen and O. K. Andersen, *Phys. Rev. B*, **1991**, *44*, 943-954.
- (33) F. Zhou, M. Cococcioni, C. A. Marianetti, D. Morgan and G. Ceder, *Phys. Rev. B*, **2004**, *70*, 235121.
- (34) P. E. Blöchl, *Phys. Rev. B*, **1994**, *50*, 17953-17979.
- (35) G. Kresse and J. Furthmüller, *Comput. Mater. Sci.*, **1996**, *6*, 15-50.
- (36) F. Sanz, C. Parada, J. M. Rojo and C. Ruíz-Valero, *Chem. Mater.*, **2001**, *13*, 1334-1340.
- (37) A. Van der Ven, J. C. Thomas, Q. Xu and J. Bhattacharya, *Math. Comput. Simulat.*, **2010**, *80*, 1393-1410.
- (38) A. Y. Toukmaji and J. A. Board Jr, *Comput. Phys. Commun.*, **1996**, *95*, 73-92.
- (39) G. Henkelman, B. P. Uberuaga and H. Jónsson, *J. Chem. Phys.*, **2000**, *113*, 9901-9904.
- (40) M. Nose, H. Nakayama, K. Nobuhara, H. Yamaguchi, S. Nakanishi and H. Iba, *J. Power Sources*, **2013**, *234*, 175-179.
- (41) R. Shannon, *Acta Crystallogr. Sect. A*, **1976**, *32*, 751-767.
- (42) G. Li, H. Azuma and M. Tohda *Electrochem. Solid-State Lett.*, **2002**, *5*, A135-A137.
- (43) S.-i. Nishimura, M. Nakamura, R. Natsui and A. Yamada, *J. Am. Chem. Soc.*, **2010**, *132*, 13596-13597.

- (44) P. Barpanda, M. Ati, B. C. Melot, G. Rousse, J. N. Chotard, M. L. Doublet, M. T. Sougrati, S. A. Corr, J. C. Jumas and J. M. Tarascon, *Nat. Mater.*, **2011**, *10*, 772-779.
- (45) A. Langrock, Y. Xu, Y. Liu, S. Ehrman, A. Manivannan and C. Wang, *J. Power Sources*, **2013**, *223*, 62-67.
- (46) S.-M. Oh, S.-T. Myung, J. Hassoun, B. Scrosati and Y.-K. Sun, *Electrochem. Commun.*, **2012**, *22*, 149-152.
- (47) Y. Xia, Y. Zhou and M. Yoshio, *J. Electrochem. Soc.*, **1997**, *144*, 2593-2600.
- (48) H. Kim, I. Park, S. Lee, H. Kim, K.-Y. Park, Y.-U. Park, H. Kim, J. Kim, H.-D. Lim, W.-S. Yoon and K. Kang, *Chem. Mater.*, **2013**, *25*, 3614-3622.
- (49) Y. Orikasa, T. Maeda, Y. Koyama, H. Murayama, K. Fukuda, H. Tanida, H. Arai, E. Matsubara, Y. Uchimoto and Z. Ogumi, *Chem. Mater.*, **2013**, *25*, 1032-1039.
- (50) L. F. J. Piper, N. F. Quackenbush, S. Sallis, D. O. Scanlon, G. W. Watson, K. W. Nam, X. Q. Yang, K. E. Smith, F. Omenya, N. A. Chernova and M. S. Whittingham, *J. Phys. Chem. C*, **2013**, *117*, 10383-10396.
- (51) I. B. Bersuker, *Chem. Rev.*, **2013**, *113*, 1351-1390.
- (52) H. A. Jahn and E. Teller *Proc. R. Soc. A.*, **1937**, *161*, 220.
- (53) B. Xu and S. Meng, *J. Power Sources*, **2010**, *195*, 4971-4976.
- (54) K. Kang and G. Ceder, *Phys. Rev. B*, **2006**, *74*, 094105.

(55) J. Lee, A. Urban, X. Li, D. Su, G. Hautier and G. Ceder, *Science*, **2014**, *343*, 519-522.

# **Chapter 5. Highly stable iron- and manganese-based cathodes for long-lasting sodium rechargeable batteries**

## **5.1 Introduction**

Developing cost-efficient large scale ESSs that may connect to renewable energy sources is one of the key issues in the 21st century to cope with ever growing energy demands. Although recent advances in Li-ion battery (LIB) technology have increased the energy density to the level applicable to large scale ESSs, the cost issues arising from the use of costly transition metals in current LIB chemistry and the concern on the uneven global distribution of lithium around world are still great challenges.<sup>1</sup> In this respect, Na-ion battery (NIB) can be the attractive alternative to LIB due to the unlimited Na resources and similar electrochemistry to LIB. Furthermore, the NIBs using redox couples based on earth-abundant transition metal such as Fe or Mn would offer an optimal option for large scale ESSs.

Accordingly, the intensive researches have focused on searching for new low-cost electrodes for NIBs.<sup>2-6</sup> Recent studies introduced a few important groups of potential electrode materials such as layered oxides and Prussian blue analogues based on Fe or Mn as well as transition metal-free organic electrodes with promising electrochemical properties.<sup>2-4,6</sup> While these materials possess clear potential merits, the insufficient cycle performance typically well below 1,000 cycles arising from a large volume change of most layered oxides or the dissolution

issues of Prussian blue and organic cathodes in the electrolyte are still challenging to address.<sup>7-11</sup> Also, the absence of Na ions in Prussian blue analogues and the organic cathodes requires the use of metallic Na as the counter electrode, which raises another level of issues that need to be resolved.<sup>8,12-13</sup> The polyanion-based compounds including phosphate-, fluorophosphates-, pyrophosphate-, sulfate- and carbonophosphate materials have also been extensively studied as an important group of potential electrode materials.<sup>14-27</sup> The structure based on the polyanions generally provides the structural stability due to the strong X-O (X = P, S, B, Si) covalent bonding, and the open rigid framework is beneficial for maintaining a small volume change upon electrochemical cycling with a fast ionic mobility compared to common layered materials. Moreover, its diversity in chemistry in terms of polyanion species, transition metals and the crystal structure offers many opportunities in identifying new electrode materials with high-performance and low-cost.

Recently, we reported a new crystalline framework based on mixed-polyanion of  $(\text{PO}_4)^{3-}$  and  $(\text{P}_2\text{O}_7)^{4-}$ ;  $\text{Na}_4\text{Fe}_3(\text{PO}_4)_2(\text{P}_2\text{O}_7)$  and  $\text{Na}_4\text{Mn}_3(\text{PO}_4)_2(\text{P}_2\text{O}_7)$  for the use of Na rechargeable batteries.<sup>28-30</sup> The open framework structure of these compounds supports a three-dimensional diffusion of Na ions in the crystal with low activation barriers for hopping enabling the fast Na de/insertion during electrochemical cycling in Na-ion cells. In the case of  $\text{Na}_4\text{Fe}_3(\text{PO}_4)_2(\text{P}_2\text{O}_7)$ , a theoretical capacity of 129 mAh g<sup>-1</sup> with an average voltage of 3.2 V vs. Na<sup>+</sup>/Na was achievable *via* one-phase reaction with a volume change of ~4 % during the charge/discharge

processes.<sup>29</sup> A high voltage approximately 3.8 V vs. Na<sup>+</sup>/Na and the energy density of 416 Wh kg<sup>-1</sup> could be obtained for the Na<sub>4</sub>Mn<sub>3</sub>(PO<sub>4</sub>)<sub>2</sub>(P<sub>2</sub>O<sub>7</sub>) electrode.<sup>30</sup> In contrast to Na<sub>4</sub>Fe<sub>3</sub>(PO<sub>4</sub>)<sub>2</sub>(P<sub>2</sub>O<sub>7</sub>), the Mn-based electrode operated *via* multi-phase reaction during charge/discharge processes with a volume change about 7 %. Although these electrode materials display promising electrochemical activities in Na-ion cells, the low energy density of Na<sub>4</sub>Fe<sub>3</sub>(PO<sub>4</sub>)<sub>2</sub>(P<sub>2</sub>O<sub>7</sub>) electrode and the large volume change with multiple structural transitions in Na<sub>4</sub>Mn<sub>3</sub>(PO<sub>4</sub>)<sub>2</sub>(P<sub>2</sub>O<sub>7</sub>) electrode upon electrochemical cycling remain to be resolved for NIBs suitable to large-scale ESSs.

In order to address this issue, herein we attempt to tune the electrochemical properties of this family of materials within the binary mixed-phosphate phases, Na<sub>4</sub>Mn<sub>x</sub>Fe<sub>3-x</sub>(PO<sub>4</sub>)<sub>2</sub>(P<sub>2</sub>O<sub>7</sub>) ( $x = 1, 2$ ), which is successfully synthesized for the first time. To our surprise, the binary system exhibits the smaller volume change (~ 2%) upon cycling and the higher practical power/energy density compared to their end members. The electrochemical characterization illustrates that high energy density is attributed to the combined (i) high potential of Mn<sup>2+</sup>/Mn<sup>3+</sup> redox couples as well as the upshifted Fe<sup>2+</sup>/Fe<sup>3+</sup> redox potential and (ii) the faster intercalation kinetics. Moreover, Na<sub>4</sub>MnFe<sub>2</sub>(PO<sub>4</sub>)<sub>2</sub>(P<sub>2</sub>O<sub>7</sub>) electrode is capable of exhibiting a remarkable cycle stability up to 3,000 cycles at a current rate of 1C at room temperature. *Ex situ* X-ray diffraction (XRD) and X-ray absorption near edge structure (XANES) analyses at intermediate charge/discharge state of Na<sub>4</sub>Mn<sub>x</sub>Fe<sub>3-x</sub>(PO<sub>4</sub>)<sub>2</sub>(P<sub>2</sub>O<sub>7</sub>) ( $x = 1, 2$ ) electrodes reveal that the stable electrochemical properties are ascribed to the

minimal structural change with a topotactic Na de/intercalation reaction upon electrochemical cycling.

## 5.2 Experimental

**Synthesis of  $\text{Na}_4\text{Mn}_x\text{Fe}_{3-x}(\text{PO}_4)(\text{P}_2\text{O}_7)$  ( $x = 0, 1, 2, 3$ ):**  $\text{Na}_4\text{Mn}_x\text{Fe}_{3-x}(\text{PO}_4)(\text{P}_2\text{O}_7)$  ( $x = 1, 2$ ) powder samples were synthesized *via* solid-state method. A stoichiometric amount of  $\text{Na}_4\text{P}_2\text{O}_7$  (95 %, Aldrich),  $x\text{MnC}_2\text{O}_4 \cdot 2\text{H}_2\text{O}$  (99 %, Alfa Aesar),  $(1-x)\text{FeC}_2\text{O}_4 \cdot 2\text{H}_2\text{O}$  (99 %, Aldrich) and 5 wt% of pyromellitic acid (PA) ( $\text{C}_{10}\text{H}_6\text{O}_2$ , 96 %, Alfa Aesar) was mixed using planetary ball-milling at 400 rpm for 12 hours. The precursors were sealed in Ar glove box to avoid the oxidation of Fe during ball-milling process. The well ground mixture was calcinated at 300 °C for 6 hours under an Ar flow. The resulting powder was ground and pelletized under a pressure of 250 kg cm<sup>-2</sup>, and sintered again at 600 °C for 12 hours under an Ar flow. Carbon-coated  $\text{C}/\text{Na}_4\text{Mn}_x\text{Fe}_{3-x}(\text{PO}_4)(\text{P}_2\text{O}_7)$  ( $x = 1, 2$ ) samples were prepared *via* post annealing method with PA carbon sources. 5 wt% PA was mixed again with  $\text{Na}_4\text{Mn}_x\text{Fe}_{3-x}(\text{PO}_4)(\text{P}_2\text{O}_7)$  ( $x = 1, 2$ ) samples using dry-ball milling at 80 rpm, and the mixture was annealed at 600 °C for 2 hours under an Ar atmosphere. The carbon contents in carbon-coated samples were confirmed to be 6 wt%.  $\text{C}/\text{Na}_4\text{Mn}_3(\text{PO}_4)_2(\text{P}_2\text{O}_7)$  and  $\text{Na}_4\text{Fe}_3(\text{PO}_4)_2(\text{P}_2\text{O}_7)$  powder samples were prepared via the same method with previous reports.<sup>29-30</sup>

**Characterization methods:** The crystal structure of as-prepared  $\text{Na}_4\text{Mn}_x\text{Fe}_{3-x}(\text{PO}_4)(\text{P}_2\text{O}_7)$  ( $x = 0, 1, 2, 3$ ) powder and *ex situ* electrode samples of  $\text{Na}_{4-y}\text{Mn}_x\text{Fe}_{3-x}(\text{PO}_4)(\text{P}_2\text{O}_7)$  ( $x = 1, 2, 0 \leq y \leq 3$ ) were analyzed by using X-ray diffractometer (Bruker, D2 PHASER) equipped with Cu K $\alpha$  radiation ( $\lambda = 1.5406 \text{ \AA}$ ). The data was recorded over a  $2\theta$  range of 8 to 60 ° with a step size of 0.02 and a step time of 1

sec. High resolution powder diffraction (HRPD) analyses using synchrotron X-ray and neutron sources were performed to determine the atomic configuration of Fe and Mn in the structure. Synchrotron X-ray diffraction (XRD) data were obtained from the Beamline 9B at Pohang Accelerator Laboratory (PAL), Republic of Korea. The data was collected over a  $2\theta$  range of 8 to 148.5 ° with a step size of 0.02 and a step time of 7 sec using a constant wavelength of  $\lambda = 1.4647 \text{ \AA}$ . ND data were obtained from the HANARO facility in the Korea Atomic Energy Research Institute (KAERI). The measurement was conducted at a  $2\theta$  range of 0–180° with a step size of 0.05° using a wavelength of  $\lambda = 1.834333 \text{ \AA}$ . The particle size of the samples were evaluated using field-emission scanning electron microscopy (FESEM) (SUPRA 55VP/Carl Zeiss). Atomic ratios between Na to Fe and Mn were determined by inductively coupled plasma-atomic emission spectroscopy (ICP-AES) (Thermo Jarrel Ash, Polyscan 60E, U. S. A.) The carbon contents in the  $\text{C}/\text{Na}_4\text{Mn}_x\text{Fe}_{3-x}(\text{PO}_4)(\text{P}_2\text{O}_7)$  ( $x = 1, 2$ ) samples were analyzed by using elemental analyzer (EA 1108 CHNS-O, FISOONS Instruments). The valence states of Mn and Fe in the structure of  $\text{Na}_{4-y}\text{Mn}_x\text{Fe}_{3-x}(\text{PO}_4)_2(\text{P}_2\text{O}_7)$  ( $x = 1, 2, 0 \leq y \leq 3$ ) were characterized using X-ray absorption near edge structure (XANES) analysis. The XANES spectra were obtained from Beamline 8C at the PAL, Republic of Korea. The Mn and Fe k-edge spectra were collected in transmission and fluorescence mode with the electron energy of 2.5 GeV and a current of 300 mA. Fe and Mn reference spectra were obtained simultaneously from each metal foil.

**Electrochemical tests:** The electrodes were prepared using of  $\text{Na}_4\text{Mn}_x\text{Fe}_{3-x}(\text{PO}_4)(\text{P}_2\text{O}_7)$  ( $x = 0, 1, 2, 3$ ), super P and polyvinylidene fluoride (PVDF) binder with a mass ratio of 7:2:1 in N-methyl-2-pyrrolidone (NMP) (99.5%, Aldrich) solvent. The slurry was pasted onto Al foil with a 250  $\mu\text{m}$  thickness. After NMP was evaporated at 120  $^\circ\text{C}$  for 1 hour, the electrode was pressed using roll press machine. The loading of  $\text{Na}_4\text{Mn}_x\text{Fe}_{3-x}(\text{PO}_4)(\text{P}_2\text{O}_7)$  ( $x = 0, 1, 2, 3$ ) was approximately 2  $\text{mg cm}^{-2}$ . The electrochemical test was conducted with a Na half-cell which was assembled into CR2032 coin cell using metallic Na (Sodium cube 99%, Aldrich) as a counter electrode. A glass microfiber filter (grade GF/F; Whatman, US) and 1-M solution of  $\text{NaBF}_4$  in an ethyl carbonated/prophylene carbonate electrolyte (EC/PC, 1:1, Anhydrous, Aldrich) were used as a separator and electrolyte, respectively. Galvanostatic measurement of  $\text{Na}_4\text{Mn}_x\text{Fe}_{3-x}(\text{PO}_4)(\text{P}_2\text{O}_7)$  ( $x = 0, 1, 2, 3$ ) electrode samples was performed with various C-rates (C/20, C/10, C/5, 1C, 5C, 10C and 20C) at room temperature and at 60 $^\circ\text{C}$  with cut-off voltages of 1.7 and 4.5 V (vs.  $\text{Na}^+/\text{Na}$ ). Galvanostatic intermittent titration technique (GITT) measurement of the electrodes was performed with a current rate of C/50 and 4 hour relaxation time. The Cyclic voltammetry (CV) measurement of the electrodes was conducted over the voltage range of 1.7 to 4.5 V at a scan rate of 0.1  $\text{mV s}^{-1}$ .

## 5.3 Result and Discussion

### 5.3.1 Synthesis and structural characterization of $\text{Na}_4\text{Mn}_x\text{Fe}_{3-x}(\text{PO}_4)_2(\text{P}_2\text{O}_7)$ ( $x = 0, 1, 2, 3$ )

The binary transition metal (TM) mixed-phosphates,  $\text{Na}_4\text{Mn}_x\text{Fe}_{3-x}(\text{PO}_4)_2(\text{P}_2\text{O}_7)$  ( $x = 1, 2$ ), were successfully synthesized *via* the conventional solid-state synthesis involving a relatively low temperature heat treatment ( $\sim 600$  °C) under Ar atmosphere. The crystal structure of these compounds were characterized using XRD analyses, which confirmed that  $\text{Na}_4\text{Mn}_x\text{Fe}_{3-x}(\text{PO}_4)_2(\text{P}_2\text{O}_7)$  ( $x = 1, 2$ ) with the orthorhombic  $Pn2_1a$  were obtained without noticeable impurities, as shown in Figure 5-1a.<sup>29-30</sup> in Figure 5-1b shows the variation of the cell parameters as a function of Mn contents ( $x$ ) in  $\text{Na}_4\text{Mn}_x\text{Fe}_{3-x}(\text{PO}_4)_2(\text{P}_2\text{O}_7)$ . The lattice parameters and the volume linearly change upon Mn substitution, indicating a complete solid solution between two end phases of  $\text{Na}_4\text{Fe}_3(\text{PO}_4)_2(\text{P}_2\text{O}_7)$  and  $\text{Na}_4\text{Mn}_3(\text{PO}_4)_2(\text{P}_2\text{O}_7)$ . The increase of the cell volume is attributed to a larger ionic radius of  $\text{Mn}^{2+}$  (0.83 Å) compared to  $\text{Fe}^{2+}$  (0.61 Å) in the structure. The cell parameters and R-factors from Rietveld refinement are tabulated in Figure 5-2. We performed XANES analyses using synchrotron X-ray sources to probe the valence states of Fe and Mn in the binary compounds. XANES spectra at Fe k-edge in Figure 5-3a illustrate that the oxidation state of Fe in  $\text{Na}_4\text{Mn}_x\text{Fe}_{3-x}(\text{PO}_4)_2(\text{P}_2\text{O}_7)$  ( $x = 1, 2$ ) remains 2+ comparable to the reference state in  $\text{Na}_4\text{Fe}_3(\text{PO}_4)_2(\text{P}_2\text{O}_7)$ .<sup>[29]</sup> Also, the valence state of Mn is determined to be 2+ using  $\text{Na}_4\text{Mn}_3(\text{PO}_4)_2(\text{P}_2\text{O}_7)$  reference as shown in Figure 5-3b.<sup>30</sup> The local environment around Fe and Mn examined by EXAFS

fittings showed that the bonding nature around Fe and Mn in  $\text{Na}_4\text{Mn}_x\text{Fe}_{3-x}(\text{PO}_4)_2(\text{P}_2\text{O}_7)$  ( $x = 1, 2$ ) remains almost identical to the single metal mixed phosphates (See the inset of Figure 5-3a and b).<sup>29-30</sup> However, it is interesting to note that Fe-O length slightly increases as Mn contents ( $x$ ) increases, while the bond length Mn-O remains constant. The increase in the Fe-O bond length is attributed to the distortion induced by the neighboring larger Mn ion sharing the polyhedron edges whose detailed structure and effect on the electrochemistry will be discussed later.

Combined X-ray and neutron diffraction study was performed to determine the detailed atomic position as well as the configuration of Fe and Mn in the  $\text{Na}_4\text{Mn}_x\text{Fe}_{3-x}(\text{PO}_4)_2(\text{P}_2\text{O}_7)$  ( $x = 1, 2$ ), as shown Figure 5-4(a-b) and Figure 5-1(c-d). The atomic positions of heavy elements such as Fe and Mn were investigated using XRD analysis, whereas light elements (*i.e.* O, P, Na) were primarily analyzed by ND. Furthermore, a possible atomic ordering of Fe and Mn in the structure was examined using ND studies, which exhibit a significant contrast of neutron scattering length between Mn and Fe ions (*i.e.* Fe = 9.45 fm and Mn = -3.73 fm). It is worthwhile to note that the ND pattern of  $\text{Na}_4\text{MnFe}_2(\text{PO}_4)_2(\text{P}_2\text{O}_7)$  in Figure 5-1c show different peak intensity ratios at a whole  $2\theta$  range compared to  $\text{Na}_4\text{Mn}_2\text{Fe}(\text{PO}_4)_2(\text{P}_2\text{O}_7)$ , while the overall crystal structure remains the same. This is attributed to distinct Fe and Mn occupancy ratios in three symmetrically inequivalent TM sites shown in the inset of Figure 5-1(c-d). To quantify the Fe and Mn occupancies, we carefully simulated the ND patterns by varying the Fe and

Mn ratios in three different TM sites based on the atomic position derived from synchrotron XRD results, as shown in Figure 5-5. The resulting Fe and Mn occupancies from Rietveld refinement are described in Table 5-1. It reveals that Mn has a clear preference in TM1 sites both in  $\text{Na}_4\text{MnFe}_2(\text{PO}_4)_2(\text{P}_2\text{O}_7)$  and  $\text{Na}_4\text{Mn}_2\text{Fe}(\text{PO}_4)_2(\text{P}_2\text{O}_7)$ . Nevertheless, additional new peaks from a specific ordering of Mn and Fe in the structure could not be detected. The detailed structural information along with the measurement conditions are presented in Table 5-2. The particle morphology of carbon-coated  $\text{Na}_4\text{Mn}_x\text{Fe}_{3-x}(\text{PO}_4)_2(\text{P}_2\text{O}_7)$  ( $x = 0, 1, 2, 3$ ) was investigated in Figure 5-6, which showed that all the samples have similar particle sizes of 200nm ~1 $\mu\text{m}$ .

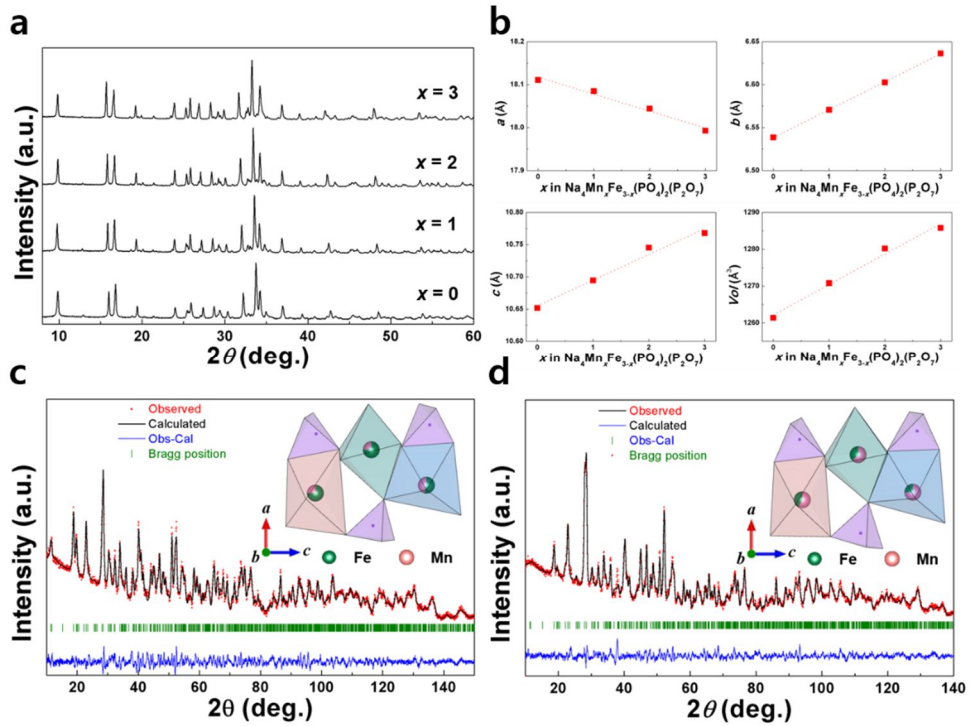
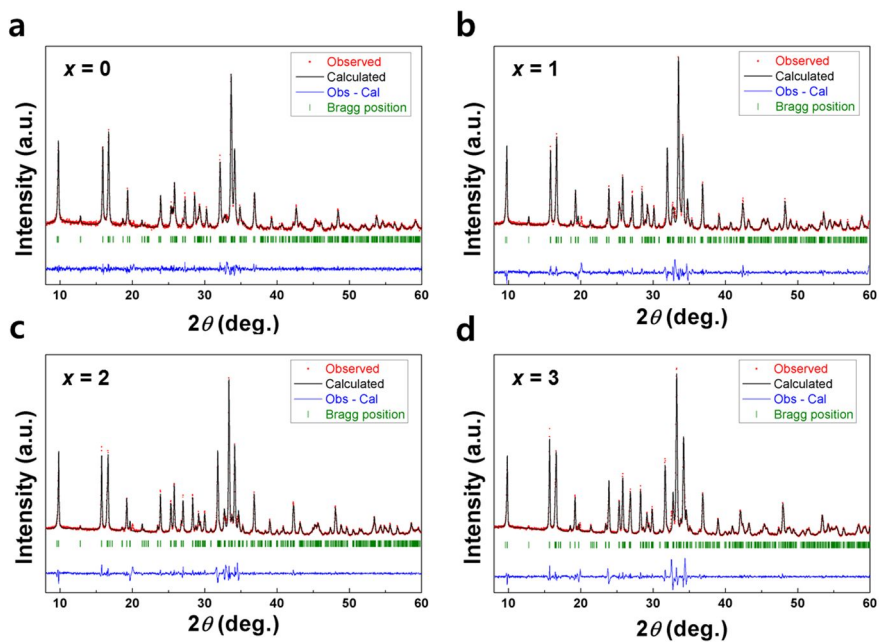


**Figure 5-1.** a) XRD patterns and b) cell parameters of  $\text{Na}_4\text{Mn}_x\text{Fe}_{3-x}(\text{PO}_4)_2(\text{P}_2\text{O}_7)$  ( $x = 0, 1, 2, 3$ ). Rietveld refinement of ND patterns of  $\text{Na}_4\text{Mn}_x\text{Fe}_{3-x}(\text{PO}_4)_2(\text{P}_2\text{O}_7)$  (c)  $x = 1$ , d)  $x = 2$ ). Occupied Fe and Mn ions in three different transition metal sites with their fraction in color are described in the inset of ND patterns.



$x$ (ICP)	$a$ (Å)	$b$ (Å)	$c$ (Å)	$Vol$ (Å <sup>3</sup> )	$R_p$ (%)	$R_{wp}$ (%)	$R_t$ (%)	$R_f$ (%)
0 (0)	18.111 (2)	6.5387 (5)	10.6518 (7)	1261.4 (2)	4.14	5.36	0.739	0.616
1 (0.93)	18.085 (1)	6.5708 (5)	10.6945 (7)	1270.8 (1)	4.85	7.06	1.35	1.25
2 (1.92)	18.0443 (9)	6.6027 (3)	10.7453 (6)	1280.2 (1)	5.06	7.48	0.918	0.762
3 (3.0)	17.993 (1)	6.6364 (4)	10.7680 (7)	1285.8 (1)	5.99	9.23	1.17	0.739

**Figure 5-2.** Rietveld refinement of the XRD patterns of  $\text{Na}_4\text{Mn}_x\text{Fe}_{3-x}(\text{PO}_4)_2(\text{P}_2\text{O}_7)$  (a)  $x = 0$ , b)  $x = 1$ , c)  $x = 2$ , d)  $x = 3$ ). The elemental composition from inductively coupled plasma (ICP) analyses and the cell parameters and reliability factors from Rietveld refinement are illustrated in the table.

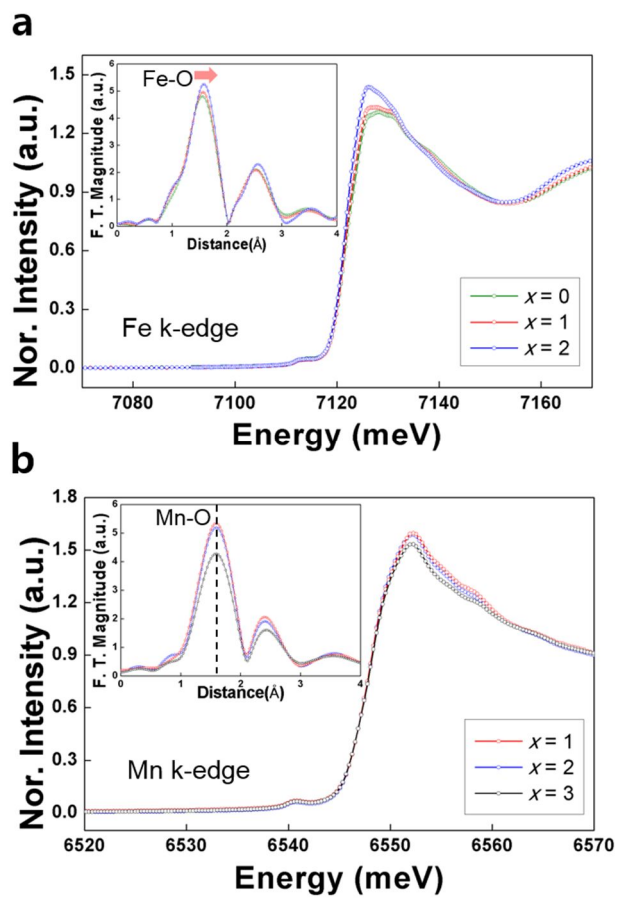


**Figure 5-3.** XANES spectra at c) Fe and d) Mn k-edges of  $\text{Na}_4\text{Mn}_x\text{Fe}_{3-x}(\text{PO}_4)_2(\text{P}_2\text{O}_7)$  ( $x = 0, 1, 2, 3$ ). EXAFS spectra are shown in the inset.

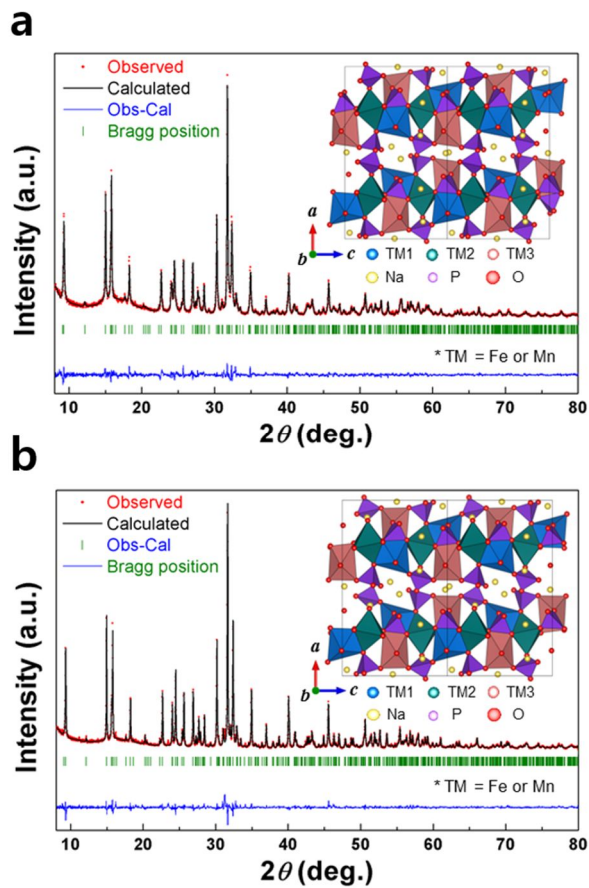


**Figure 5-4.** Rietveld refinement of synchrotron XRD patterns of  $\text{Na}_4\text{Mn}_x\text{Fe}_{3-x}(\text{PO}_4)_2(\text{P}_2\text{O}_7)$  (a)  $x = 1$ , b)  $x = 2$  ). Structure schematics are presented in the inset of XRD patterns.

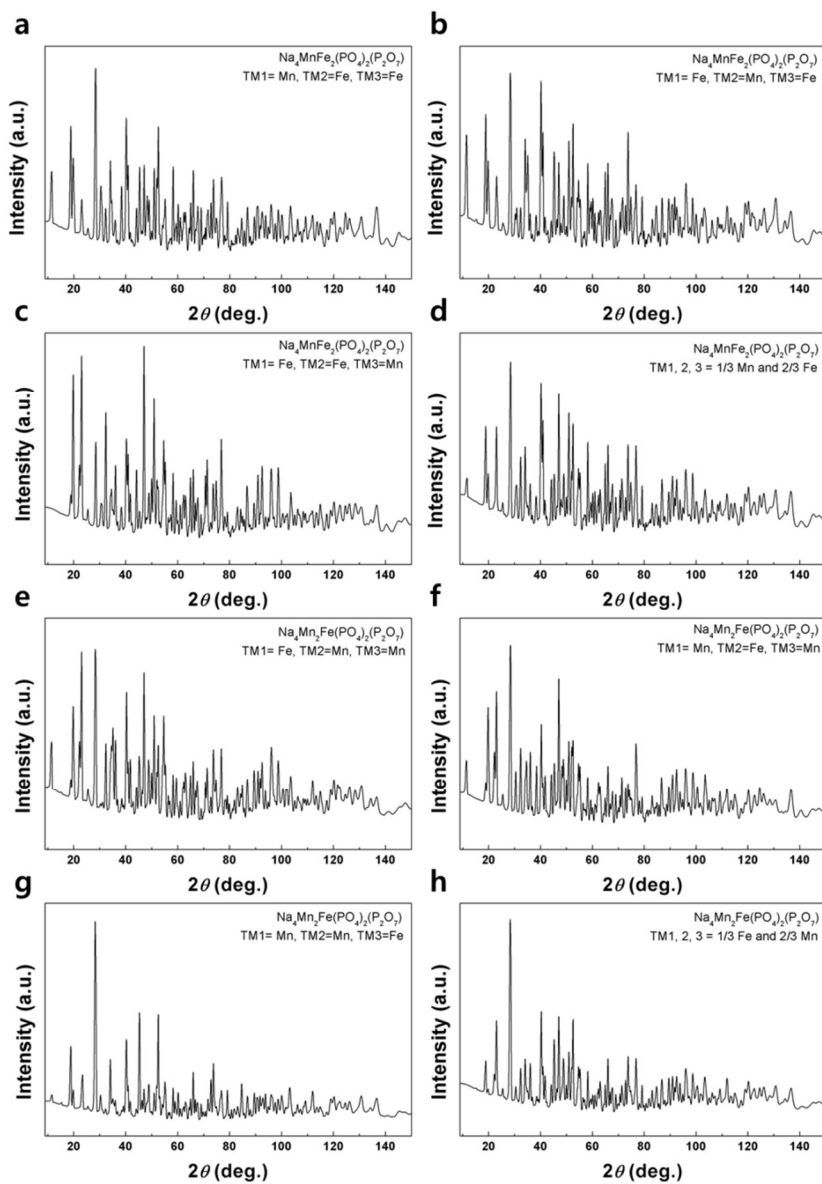


**Figure 5-5.** Simulated neutron diffraction (ND) patterns of  $\text{Na}_4\text{Mn}_x\text{Fe}_{3-x}(\text{PO}_4)_2(\text{P}_2\text{O}_7)$  (a-d)  $x = 1$ , (e-h)  $x = 2$ . Four different simulated models are presented at each composition ( $x = 1, 2$ ) with a different atomic distribution of Fe and Mn in three different transition metal sites.

**Table 5-1.** Fe and Mn occupancies in three different transition metal sites (TM1, 2 and TM3 sites).

<b>Phase</b>	<b>Site</b>	<b>Atom</b>	<b>Occupancy (<math>\text{\AA}^3</math>)</b>
$x = 1$	TM1	Fe	0.482 (7)
		Mn	0.518 (7)
	TM2	Fe	0.828 (5)
		Mn	0.172 (5)
	TM3	Fe	0.725 (6)
		Mn	0.275 (6)
$x = 2$	TM1	Fe	0.171 (7)
		Mn	0.829 (7)
	TM2	Fe	0.406 (7)
		Mn	0.594 (7)
	TM3	Fe	0.434 (8)
		Mn	0.536 (8)

**Table 5-2.** The detailed structural information of  $\text{Na}_4\text{Mn}_x\text{Fe}_{3-x}(\text{PO}_4)_2(\text{P}_2\text{O}_7)$  ( $x = 1, 2$ ). The measurement conditions and atomic information from Rietveld refinements are presented.

Formula	$\text{Na}_4\text{MnFe}_2(\text{PO}_4)_2(\text{P}_2\text{O}_7)$	
Crystal system	Orthorhombic	
Space group	$Pn2_1a$ (No. 33)	
Lattice parameters		
$a$ (Å)	18.046 (2)	18.0752 (3)
$b$ (Å)	6.5713 (6)	6.57257 (6)
$c$ (Å)	10.7015 (9)	10.7022 (1)
Unitcell volume (Å <sup>3</sup> )	1269.04 (20)	1271.43 (3)
Source	Neutron	X-ray
Temperature (K)	300 K	300 K
Wave length (Å)	1.834333	1.46470
$2\theta$ range	0 – 180°	8 – 128°
Number of data points	3200	6020
Number of reflections	948	1474
$R_p$ (%)	2.20	5.63
$R_{wp}$ (%)	2.83	7.29
$R_I$ (%)	2.40	3.79
$R_F$ (%)	1.21	2.53
$\chi^2$	4.43	2.00

Formula	Na <sub>4</sub> Mn <sub>2</sub> Fe(PO <sub>4</sub> ) <sub>2</sub> (P <sub>2</sub> O <sub>7</sub> )	
Crystal system	Orthorhombic	
Space group	<i>Pn2<sub>1</sub>a</i> (No. 33)	
Lattice parameters		
<i>a</i> (Å)	18.014 (2)	18.0425 (1)
<i>b</i> (Å)	6.6054 (6)	6.60315 (4)
<i>c</i> (Å)	10.7410 (8)	10.7493 (1)
Unitcell volume (Å <sup>3</sup> )	1278.11 (18)	1280.64 (2)
Source	Neutron	X-ray
Temperature (K)	300 K	300 K
Wave length (Å)	1.834333	1.46470
2θ range	0 – 180°	8 – 128°
Number of data points	3200	6020
Number of reflections	953	1428
R <sub>p</sub> (%)	2.31	6.46
R <sub>wp</sub> (%)	2.96	8.83
R <sub>l</sub> (%)	4.49	3.37
R <sub>F</sub> (%)	2.22	2.49
χ <sup>2</sup>	4.13	2.85

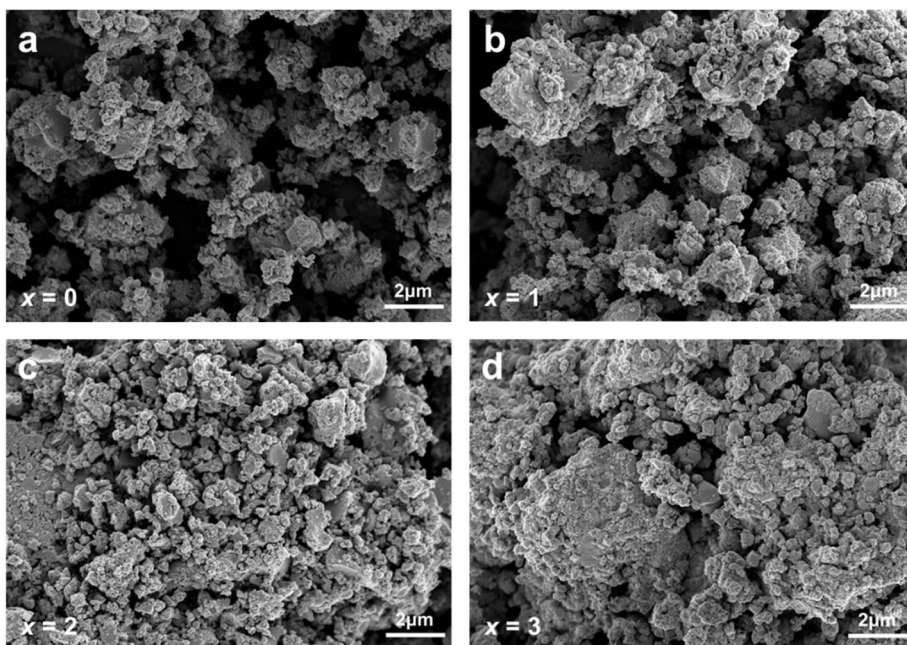


**Figure 5-6.** Scanning electron microscopy (SEM) images of  $\text{Na}_4\text{Mn}_x\text{Fe}_{3-x}(\text{PO}_4)_2(\text{P}_2\text{O}_7)$  ((a)  $x = 0$ , (b)  $x = 1$ , (c)  $x = 2$ , (d)  $x = 3$ ).

### 5.3.2 Electrochemical investigation of $\text{Na}_4\text{Mn}_x\text{Fe}_{3-x}(\text{PO}_4)_2(\text{P}_2\text{O}_7)$ ( $x = 0, 1, 2, 3$ ) electrodes

Galvanostatic charge/discharge measurements of  $\text{Na}_4\text{Mn}_x\text{Fe}_{3-x}(\text{PO}_4)_2(\text{P}_2\text{O}_7)$  ( $x = 0, 1, 2, 3$ ) were conducted using Na metal as a counter electrode. Figure 5-7a and b show the typical charge/discharge profiles of the four different electrodes ( $x = 0, 1, 2, 3$ ) at a current rate of  $C/20$  at room temperature. All the electrodes delivered similar capacities about  $110 \text{ mAh g}^{-1}$  which correspond to about 85 % of the theoretical capacity (*i.e.* one electron per TM, giving  $\sim 129 \text{ mAh g}^{-1}$ ). The substitution of Mn into the structure induces the electrochemical activity at the redox potential  $\sim 3.8 \text{ V}$  involving a  $\text{Mn}^{2+}/\text{Mn}^{3+}$  redox couple from both charge and discharge profiles. The activation of Mn redox couple resulted in a higher energy density for Mn rich samples, as shown in Figure 5-8. It was noteworthy that  $\text{Na}_4\text{Mn}_2\text{Fe}(\text{PO}_4)_2(\text{P}_2\text{O}_7)$  could display the energy density of about  $380 \text{ Wh kg}^{-1}$  at room temperature which is comparable to that of pure Mn-phase probably due to the enhanced kinetics with the addition of Fe in the structure. Interestingly, the large energy density was obtained from not only  $\text{Mn}^{2+}/\text{Mn}^{3+}$  redox activity but also upshifted  $\text{Fe}^{2+}/\text{Fe}^{3+}$  redox potentials. The magnified figure of discharge curves around  $\text{Fe}^{2+}/\text{Fe}^{3+}$  redox potentials in Figure 5-7c and cyclic voltammetry (CV) plots in Figure 5-9(a-c) indicate that the potential of  $\text{Fe}^{2+}/\text{Fe}^{3+}$  redox reaction upshifts to higher value in both anodic and cathodic scans. Onset potential of  $\text{Fe}^{2+}/\text{Fe}^{3+}$  increases from 2.89 to 3.06 V vs.  $\text{Na}^+/\text{Na}$  in anodic scan and from 2.78 to 2.89 V vs.  $\text{Na}^+/\text{Na}$  in cathodic scan as the Mn content ( $x$ ) increases from 0 to 2 in  $\text{Na}_4\text{Mn}_x\text{Fe}_3$ .

$x(\text{PO}_4)_2(\text{P}_2\text{O}_7)$ . The upshift of  $\text{Fe}^{2+}/\text{Fe}^{3+}$  redox potential was also found in GITT profiles as shown in Figure 5-10. Similar upshift of  $\text{Fe}^{2+}/\text{Fe}^{3+}$  redox couple has been previously reported for  $\text{Li}(\text{Fe}_{1-y}\text{Mn}_y)\text{PO}_4$ ,  $\text{Li}(\text{Mn}_{1/3}\text{Fe}_{1/3}\text{Co}_{1/3})\text{PO}_4$  and  $\text{Li}_2(\text{Fe}_{1-y}\text{Mn}_y)\text{P}_2\text{O}_7$  with higher Mn contents.<sup>31-35</sup> Malik et al. claimed that the upshift of redox potential of  $\text{Fe}^{2+}/\text{Fe}^{3+}$  in binary metal olivine can be understood by considering the unfavorable interaction between the oxidized  $\text{Fe}^{3+}$  and remaining  $\text{Li}^+$ , which could lead to the increased energy of intermediate compounds.<sup>35</sup> Similarly, we speculate that unfavorable  $\text{Na}^+ - \text{Fe}^{3+}$  and/or  $\text{V}_{\text{Na}} - \text{Mn}^{2+}$  pairs in  $\text{Na}_{4-y}\text{Mn}_x\text{Fe}_{3-x}(\text{PO}_4)_2(\text{P}_2\text{O}_7)$  ( $0 < y < 3$ ) may also increase the Gibbs free energy of intermediate states, resulting in a higher  $\text{Fe}^{2+}/\text{Fe}^{3+}$  redox potential compared to a  $\text{Na}_{4-y}\text{Fe}_3(\text{PO}_4)_2(\text{P}_2\text{O}_7)$ . Also, the variation in Fe-O bond lengths in  $\text{Na}_4\text{Mn}_x\text{Fe}_{3-x}(\text{PO}_4)_2(\text{P}_2\text{O}_7)$  as observed above would affect on the potential of  $\text{Fe}^{2+}/\text{Fe}^{3+}$  redox couple. Considering the longer TM-O bond length generally induces higher ionic character of TM in the structure based on the inductive effect descriptor, an increased average bond length between Fe and O in  $\text{Na}_4\text{Mn}_x\text{Fe}_{3-x}(\text{PO}_4)_2(\text{P}_2\text{O}_7)$  would result in a higher Fe redox potential (See Figure 5-3 and Table 5-3).<sup>31,36</sup>

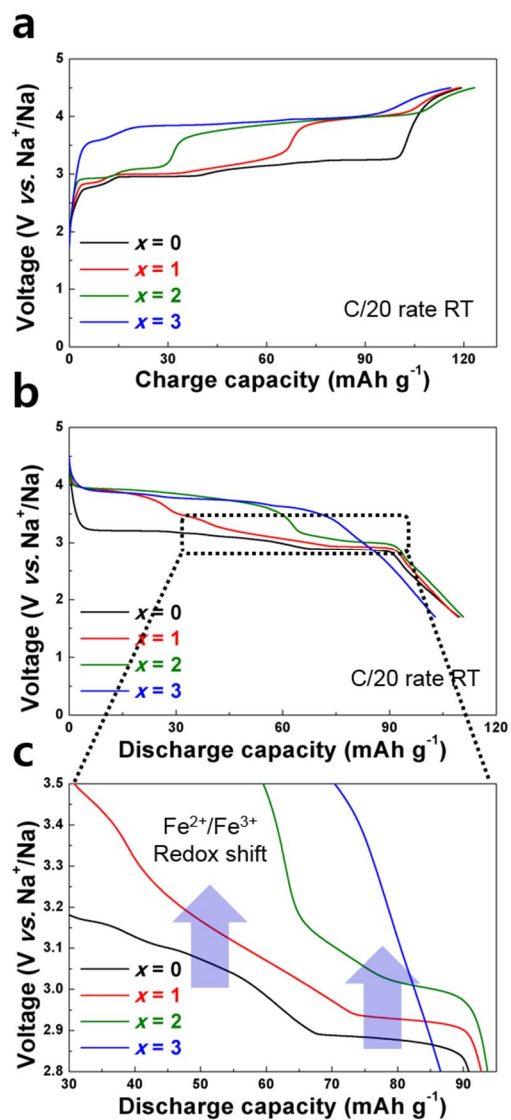


**Figure 5-7.** Galvanostatic a) charge / b) discharge curves of  $\text{Na}_4\text{Mn}_x\text{Fe}_{3-x}(\text{PO}_4)_2(\text{P}_2\text{O}_7)$  ( $x = 0, 1, 2, 3$ ) at the C-rate of C/20. c) The magnified figure of discharge curves around  $\text{Fe}^{2+}/\text{Fe}^{3+}$  redox potentials. For the clear comparison of electrochemical profiles, we used the data from second charge/discharge reaction.

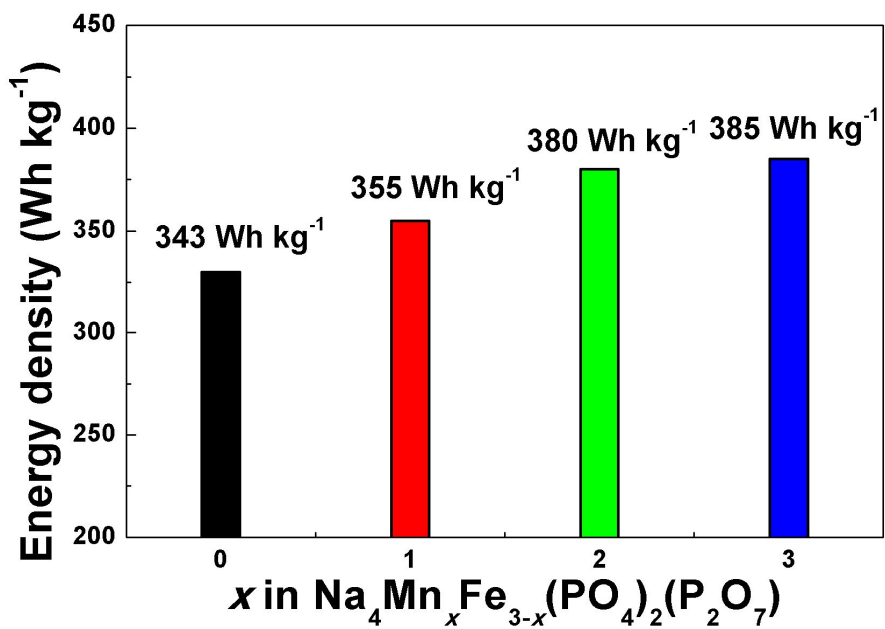


**Figure 5-8.** Energy densities of Na<sub>4</sub>Mn<sub>x</sub>Fe<sub>3-x</sub>(PO<sub>4</sub>)<sub>2</sub>(P<sub>2</sub>O<sub>7</sub>) (x = 0, 1, 2, 3) electrodes at the C-rate of C/20 at room temperature.

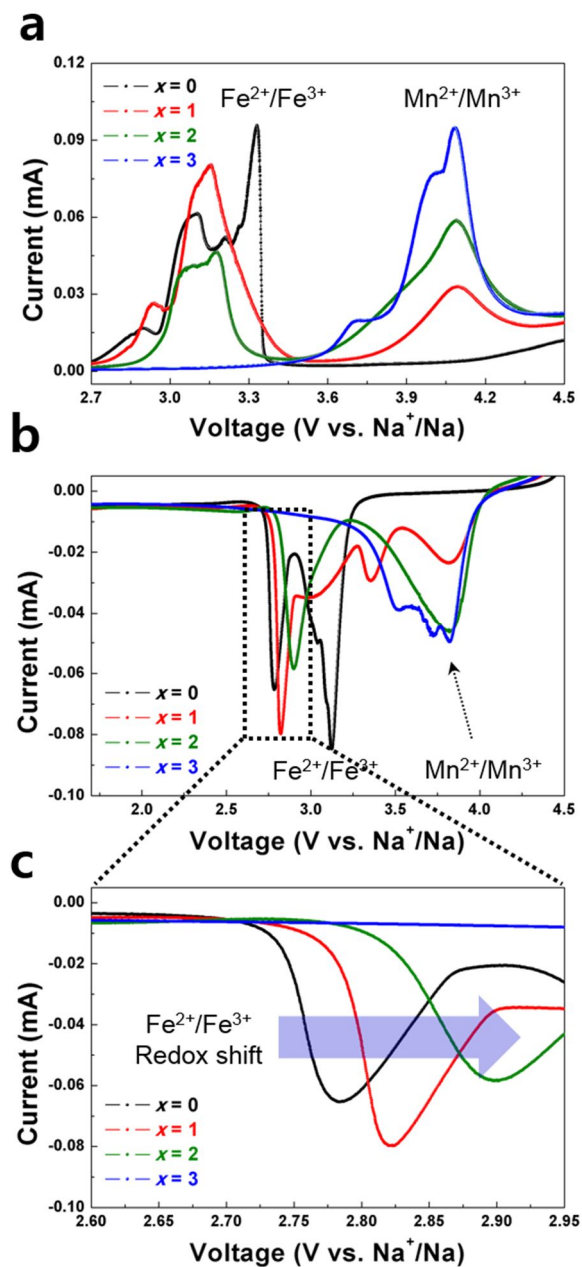


**Figure 5-9.** CV curves upon a) anodic and b) cathodic scans. c) The magnified figure of CV plot around 2.8 V upon cathodic scan.

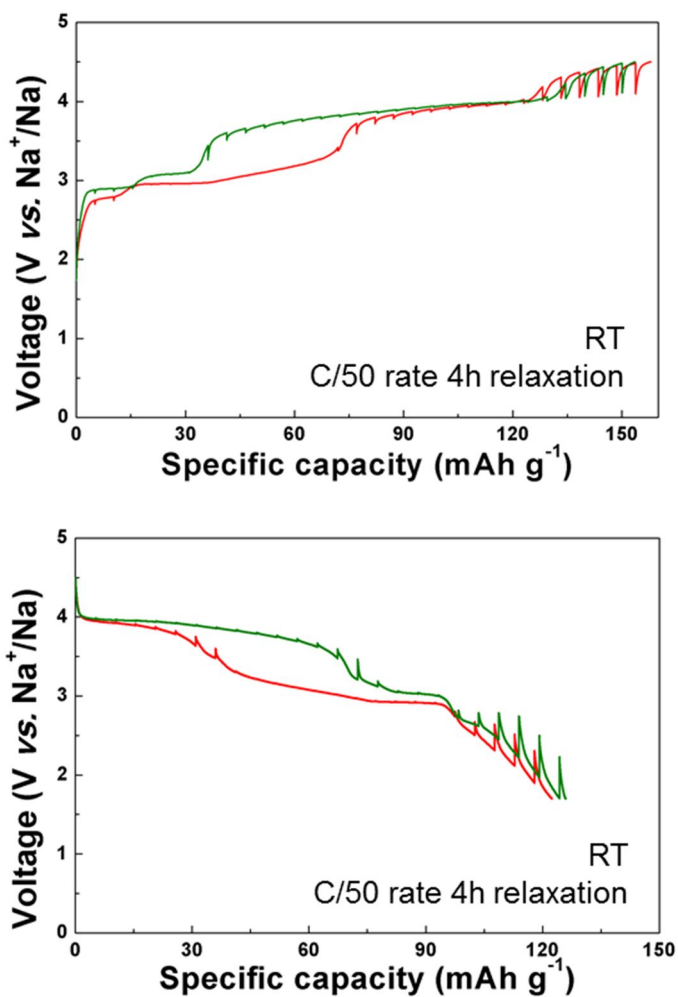


**Figure 5-10.** Galvanostatic intermittent titration technique (GITT) profiles of  $\text{Na}_4\text{Mn}_x\text{Fe}_{3-x}(\text{PO}_4)_2(\text{P}_2\text{O}_7)$  ( $x = 1, 2$ ) at the C-rate of C/50 with 4h relaxation times.

**Table 5-3.** TM-O bond lengths in  $\text{Na}_4\text{Mn}_x\text{Fe}_{3-x}(\text{PO}_4)_2(\text{P}_2\text{O}_7)$  ( $x = 0, 1, 2, 3$ ).

---

<b>Bond length</b>	<b>TM1-O (Å)</b>	<b>TM2-O (Å)</b>	<b>TM3-O (Å)</b>	<b>TM-O Average (Å)</b>
<b><math>x = 0</math></b>	2.0875	2.2001	2.1896	2.159067
<b><math>x = 1</math></b>	2.1873	2.2023	2.2030	2.197533
<b><math>x = 2</math></b>	2.2188	2.2089	2.1971	2.208267
<b><math>x = 3</math></b>	2.2226	2.2252	2.1822	2.21

---

### 5.3.3 Electrochemical mechanism of $\text{Na}_4\text{Mn}_x\text{Fe}_{3-x}(\text{PO}_4)_2(\text{P}_2\text{O}_7)$ ( $x = 1, 2$ ) electrodes upon charge/discharge processes

To understand the structural evolution of  $\text{Na}_4\text{Mn}_x\text{Fe}_{3-x}(\text{PO}_4)_2(\text{P}_2\text{O}_7)$  ( $x = 1, 2$ ) during electrochemical reaction, we performed *ex situ* XRD at various state of charges (SOCs). Figure 5-11a shows *ex situ* XRD patterns of  $\text{Na}_4\text{MnFe}_2(\text{PO}_4)_2(\text{P}_2\text{O}_7)$  at intermediate states of charge and discharge processes. Continuous peak shift of XRD pattern was observed for the entire process, which indicates the one-phase reaction of  $\text{Na}_{4-x}\text{MnFe}_2(\text{PO}_4)_2(\text{P}_2\text{O}_7)$ . Peaks of (200), (011) and (210) shift to higher angles during charge, and return to the initial  $2\theta$  during subsequent discharge reaction. The  $\text{Na}_4\text{Mn}_2\text{Fe}(\text{PO}_4)_2(\text{P}_2\text{O}_7)$  electrode also operates *via* the one-phase reaction during electrochemical cycling with a continuous shift of XRD peaks, as shown in Figure 5-11b. (See Figure 5-12 for the XRD patterns at a  $2\theta$  range of 8 to  $60^\circ$ ). It is noted that the one-phase based Na de/intercalation behavior is similar to  $\text{Na}_4\text{Fe}_3(\text{PO}_4)_2(\text{P}_2\text{O}_7)$ , but is in marked contrast to the  $\text{Na}_4\text{Mn}_3(\text{PO}_4)_2(\text{P}_2\text{O}_7)$  electrode, where a multi-phase reaction occurs during electrochemical reaction with two intermediate phases ( $\beta$ ,  $\delta$ -phases).<sup>30</sup>

Figure 5-11c displays the lattice parameter change of  $\text{Na}_4\text{Mn}_x\text{Fe}_{3-x}(\text{PO}_4)_2(\text{P}_2\text{O}_7)$  ( $x = 1, 2$ ) electrodes with cycling. Upon Na extraction from the  $\text{Na}_4\text{MnFe}_2(\text{PO}_4)_2(\text{P}_2\text{O}_7)$ , *a*-lattice parameter linearly decreases, while *b*-lattice parameter exhibits negligible change ( $< 1\%$ ). In the case of *c*-lattice parameter, it only slightly increases up to 3.1 V corresponding to one Na extraction per formula unit, but suddenly jumps up with more than one Na extraction ( $\sim 3.3$  V). The opposite evolution of lattice

parameters occurs during the discharge reaction. The unusual change of *c*-lattice parameter is similar to what has been observed for  $\text{Na}_4\text{Fe}_3(\text{PO}_4)_2(\text{P}_2\text{O}_7)$  electrode in our previous work and was attributed to the  $\text{P}_2\text{O}_7$  distortion and the shift of the center of TM octahedron.<sup>29</sup> The overall cell volume decreases linearly with Na extraction. Note that the Fe-rich mixed-phosphate electrode,  $\text{Na}_4\text{MnFe}_2(\text{PO}_4)_2(\text{P}_2\text{O}_7)$ , experiences a volume contraction about 2.07 % after a full charging. This value is smaller than those of the representative Fe- and Mn-based cathodes such as  $\text{Na}_{2/3}\text{Fe}_{1/2}\text{Mn}_{1/2}\text{O}_2$  (~11 %),  $\text{NaFePO}_4$  (~17 %),  $\text{Na}_2\text{FePO}_4\text{F}$  (3.7 %) and  $\text{Na}_2\text{FeP}_2\text{O}_7$  (~2.6 %),  $\text{Na}_4\text{Fe}_3(\text{PO}_4)_2(\text{P}_2\text{O}_7)$  (~4 %) and  $\text{Na}_4\text{Mn}_3(\text{PO}_4)_2(\text{P}_2\text{O}_7)$  (~7 %), and comparable to that of recently reported  $\text{Na}_2\text{Fe}_2(\text{SO}_4)_3$  electrode (~1.6 %). (See Figure 5-11d)<sup>15,17,23,29-30,37-38</sup> Until now, it is unclear as to the origin of the low volume change with a particular Fe and Mn ratios, however, we speculate that it is related to the preferential occupancies of Fe and Mn in the symmetrically distinguishable TM sites and corresponding sequential distortion of TM along with the desodiation procedure.<sup>29-30</sup> *b*- and *c*-lattice constants from Mn-rich electrode,  $\text{Na}_4\text{Mn}_2\text{Fe}(\text{PO}_4)_2(\text{P}_2\text{O}_7)$ , display a similar tendency with that of  $\text{Na}_4\text{MnFe}_2(\text{PO}_4)_2(\text{P}_2\text{O}_7)$  during charge and discharge reactions. However, the change of *a*-lattice parameter is much larger with a collapse at a certain composition of more than one Na extraction, which may come from the Jahn-Teller distortion of  $\text{Mn}^{3+}$  as was previously observed for  $\text{Na}_4\text{Mn}_3(\text{PO}_4)_2(\text{P}_2\text{O}_7)$ <sup>30</sup> As a result, the lattice volume contraction is larger about 4.08 % after a full charging. The valence state of transition metals in  $\text{Na}_4\text{Mn}_x\text{Fe}_{3-x}(\text{PO}_4)_2(\text{P}_2\text{O}_7)$  ( $x = 1, 2$ ) during

electrochemical reaction was evaluated using XANES analyses, as shown in Figure 5-11e. It clearly shows that Fe k-edge spectrum of  $\text{Na}_4\text{MnFe}_2(\text{PO}_4)_2(\text{P}_2\text{O}_7)$  shifts to right during the initial charging up to 3.5 V vs.  $\text{Na}^+/\text{Na}$ , indicating  $\text{Fe}^{2+}/\text{Fe}^{3+}$  redox reactions. The negligible shift of the Fe k-edge spectrum was found in the following charging up to 4.5 V. Instead,  $\text{Mn}^{2+}/\text{Mn}^{3+}$  redox reaction occurs in this region. While the shift of XANES spectra was not clear from the Mn-k edge, the pre-edge shifts to the right at the voltage range of 3.5 V to 4.5 V as shown in the inset of Mn k-edge spectra. The reversible  $\text{Fe}^{2+}/\text{Fe}^{3+}$  and  $\text{Mn}^{2+}/\text{Mn}^{3+}$  redox reactions take place during subsequent discharge processes as shown in Figure 5-13. Similarly, the Fe k-edge spectra of  $\text{Na}_4\text{Mn}_2\text{Fe}(\text{PO}_4)_2(\text{P}_2\text{O}_7)$  electrode primarily shift to rightward until charging up to 3.85 V, which is followed by the main shift of Mn k-edge until the end of the charging reaction. Based on the XANES analyses, we can confirm that the capacities at low potential below 3.5 V and high potential above 3.8 V were delivered from  $\text{Fe}^{2+}/\text{Fe}^{3+}$  and  $\text{Mn}^{2+}/\text{Mn}^{3+}$  redox reaction, respectively.

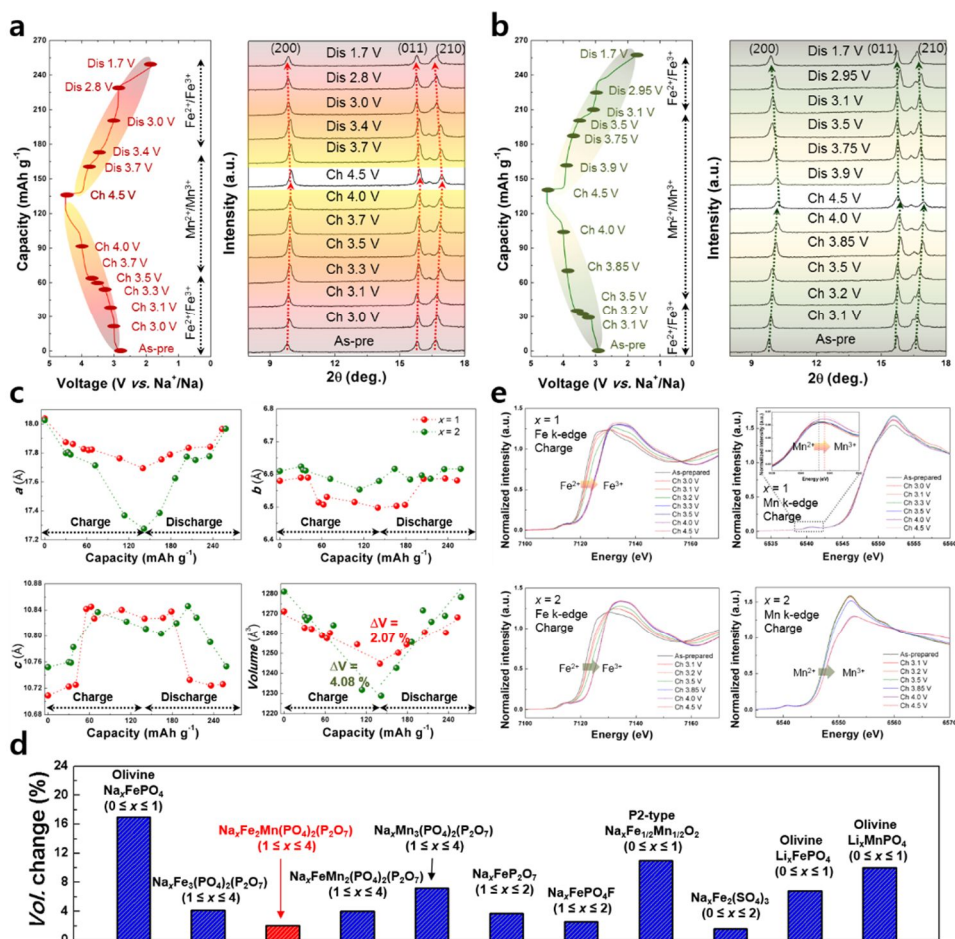


**Figure 5-11.** *Ex situ* XRD patterns of Na<sub>4</sub>Mn<sub>x</sub>Fe<sub>3-x</sub>(PO<sub>4</sub>)<sub>2</sub>(P<sub>2</sub>O<sub>7</sub>) (a)  $x = 1$ , b)  $x = 2$ ) during electrochemical charge/discharge reactions in Na-ion cells. c) Lattice parameter and cell volume changes upon charge/discharge reactions in Na-ion cells. d) Comparison of volume changes on charging in various Fe- and Mn-based cathodes for Na-ion batteries. e) The Fe and Mn k-edge XANES spectra of Na<sub>4</sub>Mn<sub>x</sub>Fe<sub>3-x</sub>(PO<sub>4</sub>)<sub>2</sub>(P<sub>2</sub>O<sub>7</sub>) ( $x = 1, 2$ ) upon charge reactions in Na-ion cells.

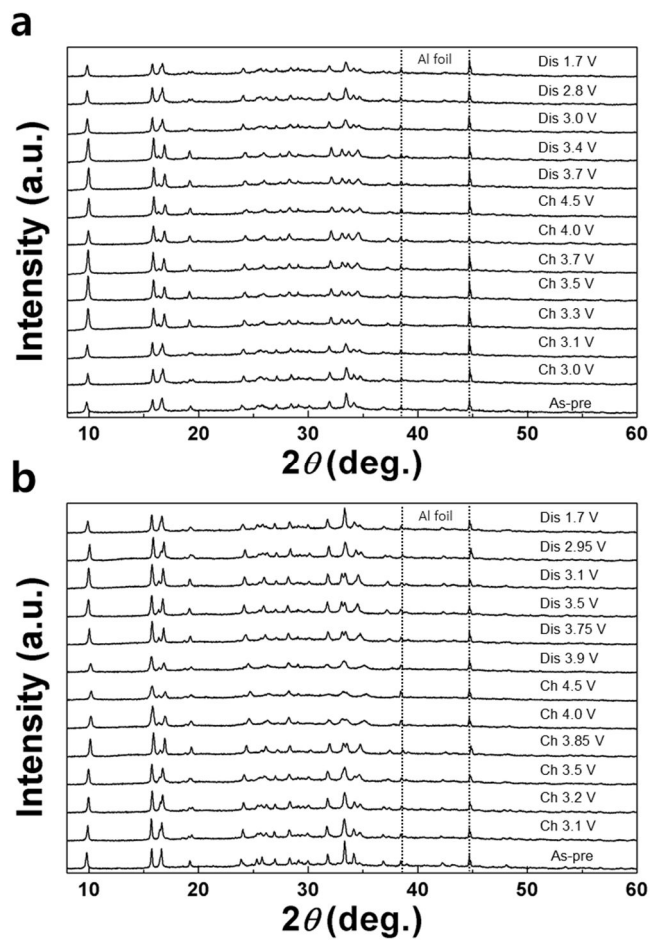


**Figure 5-12.** *Ex situ* XRD patterns of  $\text{Na}_4\text{Mn}_x\text{Fe}_{3-x}(\text{PO}_4)_2(\text{P}_2\text{O}_7)$  (a)  $x = 1$ , b)  $x = 2$  during charge/discharge reactions in Na-ion cells.

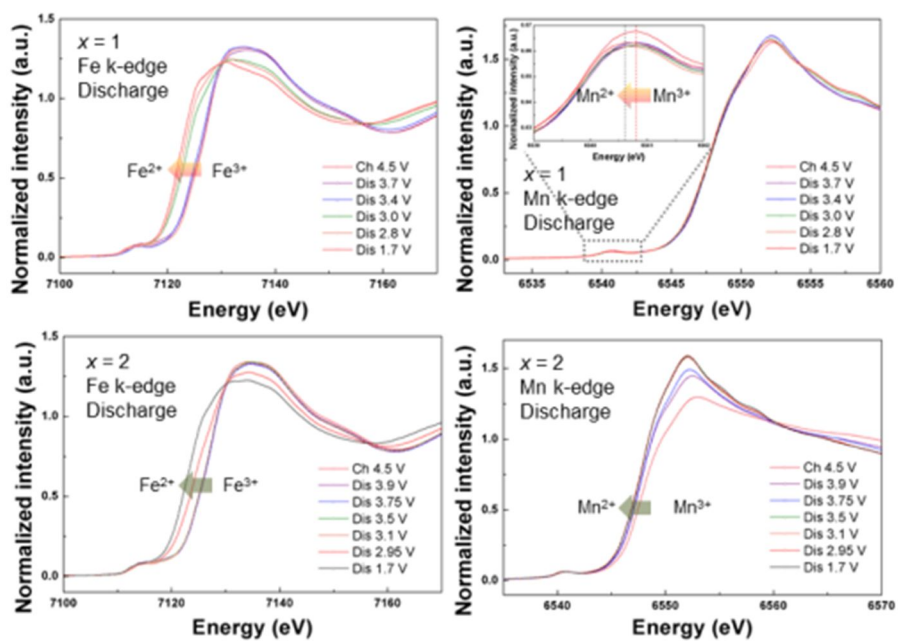


**Figure 5-13.** X-ray absorption near edge structure (XANES) spectra near to Fe and Mn k-edges of  $\text{Na}_{4-y}\text{Mn}_x\text{Fe}_{3-x}(\text{PO}_4)_2(\text{P}_2\text{O}_7)$  ( $x = 1, 2; 0 \leq y \leq 3$ ) upon discharge reaction.

### 5.3.4 Electrochemical properties of $\text{Na}_4\text{Mn}_x\text{Fe}_{3-x}(\text{PO}_4)_2(\text{P}_2\text{O}_7)$ ( $x = 1, 2$ ) electrodes at various conditions

Galvanostatic charge/discharge experiments at various C-rates were carried out at room temperature using coin-type Na cells. Figure 5-14a displays the discharge profiles of  $\text{Na}_4\text{MnFe}_2(\text{PO}_4)_2(\text{P}_2\text{O}_7)$  at various C-rates. About 87 % ( $112 \text{ mAh g}^{-1}$ ) of the theoretical capacity was delivered at a C/20 rate, and a capacity of approximately  $101 \text{ mAh g}^{-1}$  was retained at a current rate of 2C. Furthermore, we can obtain more than 60 % of the theoretical capacity even at a 3 minute discharging procedure (20C).  $\text{Na}_4\text{Mn}_2\text{Fe}(\text{PO}_4)_2(\text{P}_2\text{O}_7)$  electrode also shows a high rate performances up to 20 C rate in Figure 5-14b. A capacity of  $113 \text{ mAh g}^{-1}$  was delivered from C/20, and more than a half of the theoretical capacity was retained at 20C. The high energy density about  $380 \text{ Wh kg}^{-1}$  was obtained at C/20, and this value is comparable to those of polyanion cathodes such as  $\text{Na}_4\text{Mn}_3(\text{PO}_4)_2(\text{P}_2\text{O}_7)$  and  $\text{Na}_2\text{Fe}_2(\text{SO}_4)_3$ .<sup>23,30</sup> The Ragone plot of  $\text{Na}_4\text{Mn}_x\text{Fe}_{3-x}(\text{PO}_4)_2(\text{P}_2\text{O}_7)$  ( $x = 1, 2$ ) compared with other representative Fe- and Mn-based polyanion compounds (*i.e.*  $\text{NaFePO}_4$ ,  $\text{Na}_2\text{FePO}_4\text{F}$ ,  $\text{Na}_2\text{Fe}_2(\text{SO}_4)_3$ ,  $\text{Na}_3\text{MnPO}_4\text{CO}_3$ ,  $\text{Na}_2\text{MnP}_2\text{O}_7$ ,  $\text{Na}_2\text{MnPO}_4\text{F}$  and  $\text{Na}_4\text{Mn}_3(\text{PO}_4)_2(\text{P}_2\text{O}_7)$ ) in Figure 5-15 reveals that both  $\text{Na}_4\text{Mn}_x\text{Fe}_{3-x}(\text{PO}_4)_2(\text{P}_2\text{O}_7)$  ( $x = 1, 2$ ) electrodes exhibit outstandingly large gravimetric energy and power densities at room temperature compared to them.<sup>16,18,23,26,30,39-40</sup> Notable is that higher rate performances of the  $\text{Na}_4\text{Mn}_x\text{Fe}_{3-x}(\text{PO}_4)_2(\text{P}_2\text{O}_7)$  ( $x = 1, 2$ ) electrodes were also observed at  $60 \text{ }^\circ\text{C}$  in Figure 5-16 delivering the capacity near theoretical capacity ( $> 95 \%$ ) with the energy density of  $376 \text{ Wh kg}^{-1}$  and  $418 \text{ Wh kg}^{-1}$ ,

respectively. We speculate that such a high rate performance basically roots from the open framework structure of  $\text{Na}_4\text{Mn}_x\text{Fe}_{3-x}(\text{PO}_4)_2(\text{P}_2\text{O}_7)$  and from the de/sodiation involving a low volume change ( $\sim 2\%$  for  $x = 1$ ,  $\sim 4\%$  for  $x = 2$ ) during electrochemical cycling.

Remarkable cycle stability was achieved for both  $\text{Na}_4\text{Mn}_x\text{Fe}_{3-x}(\text{PO}_4)_2(\text{P}_2\text{O}_7)$  ( $x = 1, 2$ ) electrodes in Na cells. Figure 5-17a shows that approximately 96 % and 95 % of the initial capacities were retained from  $\text{Na}_4\text{MnFe}_2(\text{PO}_4)_2(\text{P}_2\text{O}_7)$  and  $\text{Na}_4\text{Mn}_2\text{Fe}(\text{PO}_4)_2(\text{P}_2\text{O}_7)$  electrodes, respectively after 50 cycles at C/20. The discharge profile was also well preserved after 20 and 50 cycles without the significant voltage decay as shown in the inset of Figure 5-17a. It is worthy of noting that  $\text{Na}_4\text{MnFe}_2(\text{PO}_4)_2(\text{P}_2\text{O}_7)$  electrode demonstrates an unprecedentedly stable cycle property at a current rate of 1C and room temperature. Approximately 83 % of the initial capacity was retained after 3,000 cycles with a Coulombic efficiency of 99.8% in Figure 5-17b. To the best of knowledge, this is the first demonstration of such superior cycle stability for Fe- or Mn-based polyanion cathodes for Na-ion batteries. Electrode operation of  $\text{Na}_4\text{Mn}_x\text{Fe}_{3-x}(\text{PO}_4)_2(\text{P}_2\text{O}_7)$  ( $x = 1, 2$ ) at 60°C also exhibited a stable cycle retention up to 200 cycles as shown in Figure 5-17c.  $\text{Na}_4\text{Mn}_x\text{Fe}_{3-x}(\text{PO}_4)_2(\text{P}_2\text{O}_7)$  ( $x = 1, 2$ ) electrodes showed a retention of 93 % ( $x = 1$ ) and 75 % ( $x = 2$ ) after the 200 cycles. Considering that the long-term cycle stability is one of the key factors in the success of large scale ESSs, we believe that  $\text{Na}_4\text{MnFe}_2(\text{PO}_4)_2(\text{P}_2\text{O}_7)$  could be a strong competitor among various cost-efficient cathode materials.

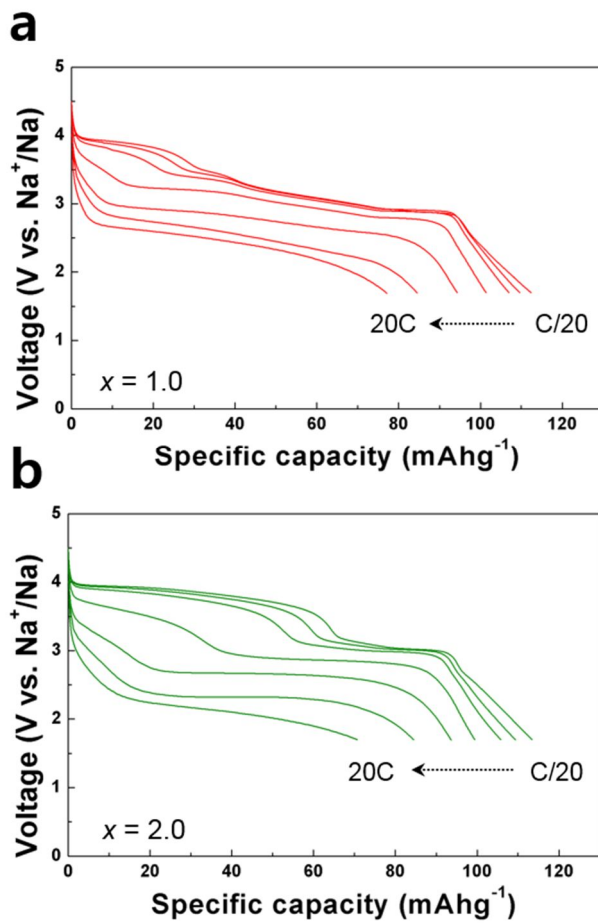


**Figure 5-14.** Galvanostatic discharge profiles of  $\text{Na}_4\text{Mn}_x\text{Fe}_{3-x}(\text{PO}_4)_2(\text{P}_2\text{O}_7)$  (a)  $x = 1$ , b)  $x = 2$ ) at different C-rates (C/20, C/10, C/5, 1C, 2C, 5C, 10C and 20C). The charge was conducted at a current rate of C/20.

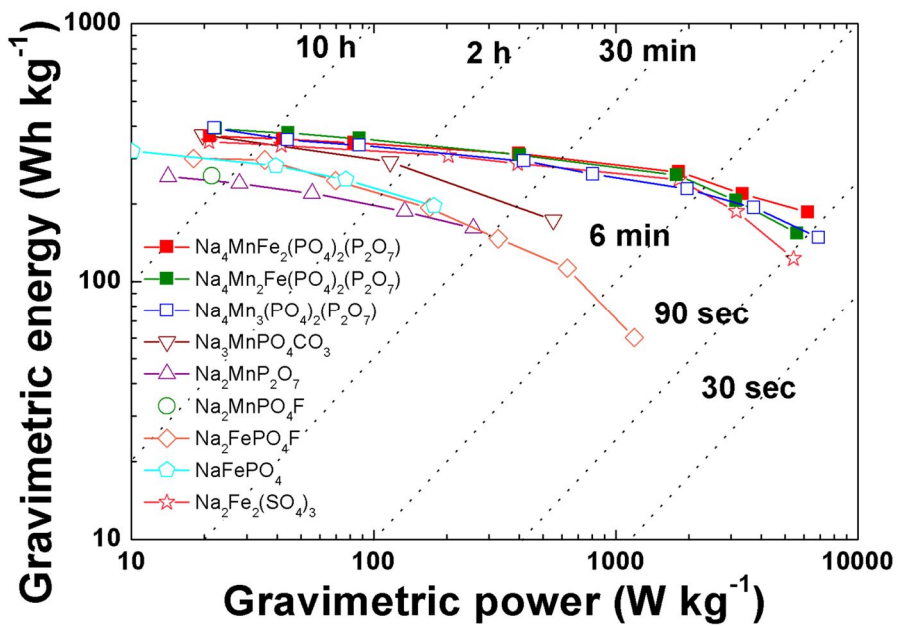
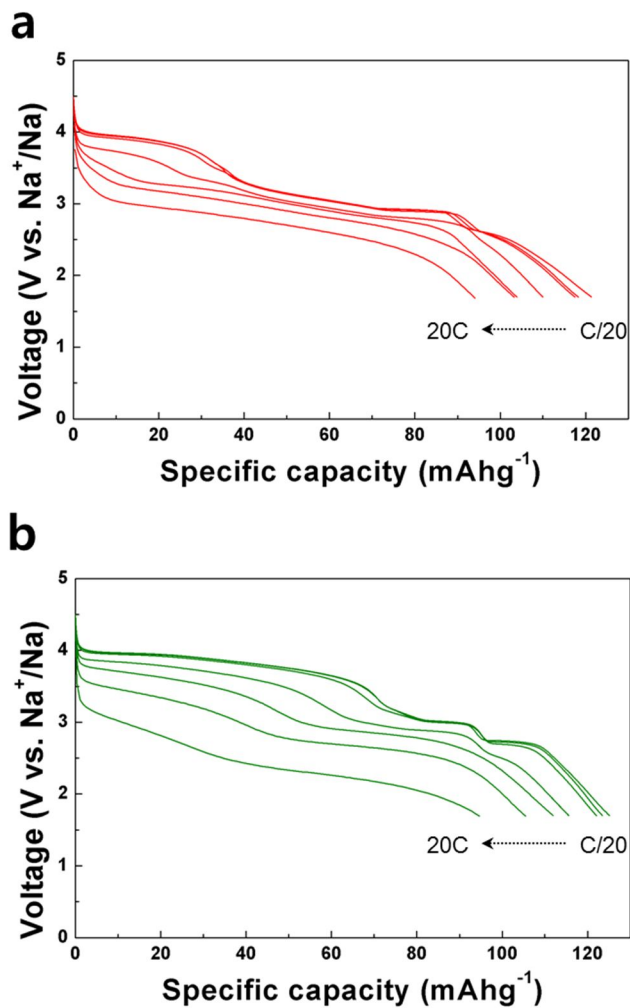
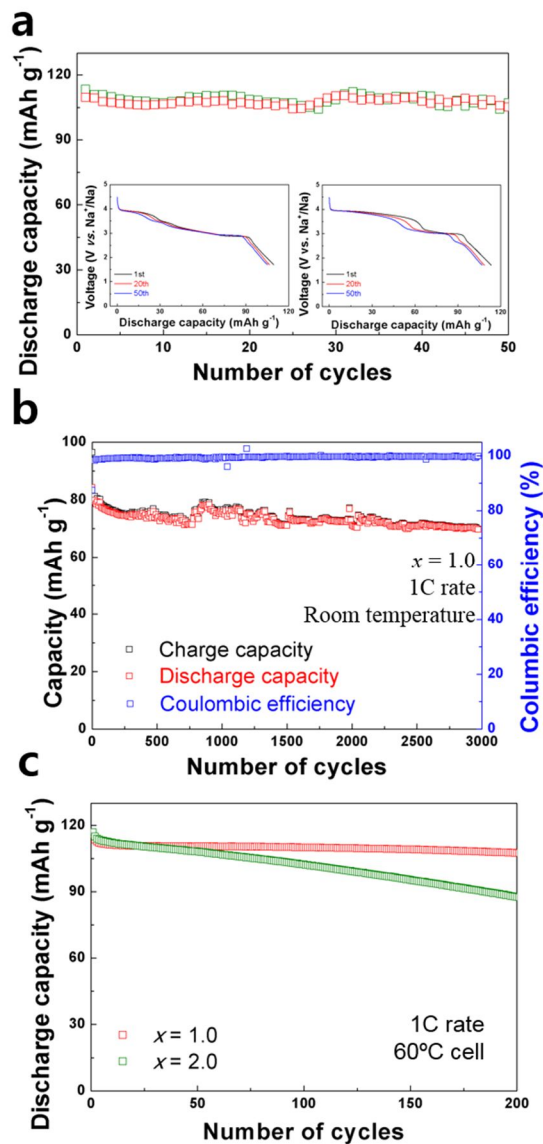


Figure 5-15. A Ragone plot of Na<sub>4</sub>Mn<sub>x</sub>Fe<sub>3-x</sub>(PO<sub>4</sub>)<sub>2</sub>(P<sub>2</sub>O<sub>7</sub>) and other representative Fe- and Mn-based polyanion cathode materials for NIBs. <sup>15,17,22,25,29,36-37</sup>



**Figure 5-16.** Galvanostatic discharge profiles of  $\text{Na}_4\text{Mn}_x\text{Fe}_{3-x}(\text{PO}_4)_2(\text{P}_2\text{O}_7)$  (a)  $x = 1$ , b)  $x = 2$ ) at different C-rates (C/20, C/10, C/5, 1C, 2C, 5C, 10C and 20C) in 60°C cell. The charge was conducted at a current rate of C/20.



**Figure 5-17.** a) The cycle performances of  $\text{Na}_4\text{Mn}_x\text{Fe}_{3-x}(\text{PO}_4)_2(\text{P}_2\text{O}_7)$  ( $x = 1, 2$ ) at C/20 and  $25^\circ\text{C}$ . b) The cycle performance of  $\text{Na}_4\text{MnFe}_2(\text{PO}_4)_2(\text{P}_2\text{O}_7)$  at 1C and

25 °C. c) The cycle performance of  $\text{Na}_4\text{Mn}_x\text{Fe}_{3-x}(\text{PO}_4)_2(\text{P}_2\text{O}_7)$  ( $x = 1, 2$ ) at C/20 and 60 °C.

## 5.4 Conclusion

We successfully synthesized solid-solution phases of  $\text{Na}_4\text{Mn}_x\text{Fe}_{3-x}(\text{PO}_4)_2(\text{P}_2\text{O}_7)$  ( $x = 1, 2$ ) for the first time, and characterized the structure by using ND, XRD and XANES analyses. The high energy density (*i.e.* 376 Wh  $\text{kg}^{-1}$  for  $x = 1$  and 418 Wh  $\text{kg}^{-1}$  for  $x = 2$ ) was obtained from both electrodes by utilizing  $\text{Mn}^{2+}/\text{Mn}^{3+}$  and  $\text{Fe}^{2+}/\text{Fe}^{3+}$  redox couple in Na-ion cells. Both electrodes operate *via* one-phase solution reaction with a remarkably small volume change (*i.e.* 2 % for  $x = 1$  and 4% for  $x = 2$ ).  $\text{Na}_4\text{MnFe}_2(\text{PO}_4)_2(\text{P}_2\text{O}_7)$  electrode could exhibit outstanding rate and cycle performances at both room temperature and 60°C on the merit of open framework structure and the low volume change ( $\sim 2$  %). The electrode operation at 1C at room temperature showed unprecedentedly stable cycle retention of 83 % until 3000 charge/discharge cycles. We believe that the combination of high energy density, long-term cycle stability and low element cost of Fe and Mn makes the  $\text{Na}_4\text{MnFe}_2(\text{PO}_4)_2(\text{P}_2\text{O}_7)$  electrode as a strong competitor for large-scale Na-ion battery cathodes.

## 5.5 References

- (1) J.-M. Tarascon, *Nat. Chem.* **2010**, *2*, 510-510.
- (2) N. Yabuuchi, K. Kubota, M. Dahbi, S. Komaba, *Chem. Rev.* **2014**, *114*, 11636-11682.
- (3) S.-W. Kim, D.-H. Seo, X. Ma, G. Ceder, K. Kang, *Adv. Energy Mater.* **2012**, *2*, 710-721.
- (4) H. Pan, Y.-S. Hu, L. Chen, *Energy Environ. Sci.* **2013**, *6*, 2338-2360.
- (5) C. Masquelier, L. Croguennec, *Chem. Rev.* **2013**, *113*, 6552-6591.
- (6) D. Kundu, E. Talaie, V. Duffort, L. F. Nazar, *Angew. Chem. Int. Ed.* **2015**, *54*, 3431-3448.
- (7) H. Chen, M. Armand, G. Demailly, F. Dolhem, P. Poizot, J.-M. Tarascon, *ChemSusChem* **2008**, *1*, 348-355.
- (8) Y. Liang, Z. Tao, J. Chen, *Adv. Energy Mater.* **2012**, *2*, 742-769.
- (9) M. Lee, J. Hong, H. Kim, H.-D. Lim, S. B. Cho, K. Kang, C. B. Park, *Adv. Mater.* **2014**, *26*, 2558-2565.
- (10) Y. You, X. Yu, Y. Yin, K.-W. Nam, Y.-G. Guo, *Nano Res.* **2015**, *8*, 117-128.
- (11) M. Pasta, C. D. Wessells, N. Liu, J. Nelson, M. T. McDowell, R. A. Huggins, M. F. Toney, Y. Cui, *Nat. Commun.* **2014**, *5*.
- (12) Y. You, X.-L. Wu, Y.-X. Yin, Y.-G. Guo, *Energy Environ. Sci.* **2014**, *7*, 1643-1647.

- (13) Y. Lu, L. Wang, J. Cheng, J. B. Goodenough, *Chem. Commun.* **2012**, *48*, 6544-6546.
- (14) K. T. Lee, T. N. Ramesh, F. Nan, G. Botton, L. F. Nazar, *Chem. Mater.* **2011**, *23*, 3593-3600.
- (15) B. L. Ellis, W. R. M. Makahnouk, Y. Makimura, K. Toghill, L. F. Nazar, *Nat. Mater.* **2007**, *6*, 749-753.
- (16) S.-W. Kim, D.-H. Seo, H. Kim, K.-Y. Park, K. Kang, *Phys. Chem. Chem. Phys.* **2012**, *14*, 3299-3303.
- (17) P. Barpanda, T. Ye, S.-i. Nishimura, S.-C. Chung, Y. Yamada, M. Okubo, H. Zhou, A. Yamada, *Electrochem. Commun.* **2012**, *24*, 116-119.
- (18) C. S. Park, H. Kim, R. A. Shakoor, E. Yang, S. Y. Lim, R. Kahraman, Y. Jung, J. W. Choi, *J. Am. Chem. Soc.* **2013**, *135*, 2787-2792.
- (19) P. Barpanda, G. Liu, Z. Mohamed, C. D. Ling, A. Yamada, *Solid State Ionics* **2014**, *268*, Part B, 305-311.
- (20) J. Kim, H. Kim, I. Park, Y.-U. Park, J.-K. Yoo, K.-Y. Park, S. Lee, K. Kang, *Energy Environ. Sci.* **2013**, *6*, 830-834.
- (21) J. Kim, H. Kim, K.-Y. Park, Y.-U. Park, S. Lee, H.-S. Kwon, H.-I. Yoo, K. Kang, *J. Mater. Chem. A* **2014**, *2*, 8632-8636.
- (22) K.-H. Ha, S. H. Woo, D. Mok, N.-S. Choi, Y. Park, S. M. Oh, Y. Kim, J. Kim, J. Lee, L. F. Nazar, K. T. Lee, *Adv. Energy Mater.* **2013**, *3*, 770-776.

- (23) P. Barpanda, G. Oyama, S.-i. Nishimura, S.-C. Chung, A. Yamada, *Nat. Commun.* **2014**, *5*.
- (24) J. Ming, P. Barpanda, S.-i. Nishimura, M. Okubo, A. Yamada, *Electrochem. Commun.* **2015**, *51*, 19-22.
- (25) P. Barpanda, G. Oyama, C. D. Ling, A. Yamada, *Chem. Mater.* **2014**, *26*, 1297-1299.
- (26) H. Chen, Q. Hao, O. Zivkovic, G. Hautier, L.-S. Du, Y. Tang, Y.-Y. Hu, X. Ma, C. P. Grey, G. Ceder, *Chem. Mater.* **2013**, *25*, 2777-2786.
- (27) W. Huang, J. Zhou, B. Li, J. Ma, S. Tao, D. Xia, W. Chu, Z. Wu, *Sci. Rep.* **2014**, *4*.
- (28) H. Kim, I. Park, D.-H. Seo, S. Lee, S.-W. Kim, W. J. Kwon, Y.-U. Park, C. S. Kim, S. Jeon, K. Kang, *J. Am. Chem. Soc.* **2012**, *134*, 10369-10372.
- (29) H. Kim, I. Park, S. Lee, H. Kim, K.-Y. Park, Y.-U. Park, H. Kim, J. Kim, H.-D. Lim, W.-S. Yoon, K. Kang, *Chem. Mater.* **2013**, *25*, 3614-3622.
- (30) H. Kim, G. Yoon, I. Park, K.-Y. Park, B. Lee, J. Kim, Y.-U. Park, S.-K. Jung, H.-D. Lim, D. Ahn, S. Lee, K. Kang, *Energy Environ. Sci.* **2015**, *8*, 3325-3335.
- (31) G. Kobayashi, A. Yamada, S.-i. Nishimura, R. Kanno, Y. Kobayashi, S. Seki, Y. Ohno, H. Miyashiro, *J. Power Sources* **2009**, *189*, 397-401.
- (32) N. Furuta, S.-i. Nishimura, P. Barpanda, A. Yamada, *Chem. Mater.* **2012**, *24*, 1055-1061.

- (33) D.-H. Seo, H. Gwon, S.-W. Kim, J. Kim, K. Kang, *Chem. Mater.* **2010**, *22*, 518-523.
- (34) T. Ye, P. Barpanda, S.-i. Nishimura, N. Furuta, S.-C. Chung, A. Yamada, *Chem. Mater.* **2013**, *25*, 3623-3629.
- (35) R. Malik, F. Zhou, G. Ceder, *Phys. Rev. B* **2009**, *79*, 214201.
- (36) P. Barpanda, M. Ati, B. C. Melot, G. Rousse, J. N. Chotard, M. L. Doublet, M. T. Sougrati, S. A. Corr, J. C. Jumas, J. M. Tarascon, *Nat. Mater.* **2011**, *10*, 772-779.
- (37) N. Yabuuchi, M. Kajiyama, J. Iwatate, H. Nishikawa, S. Hitomi, R. Okuyama, R. Usui, Y. Yamada, S. Komaba, *Nat. Mater.* **2012**, *11*, 512-517.
- (38) J. Lu, S. C. Chung, S.-i. Nishimura, A. Yamada, *Chem. Mater.* **2013**, *25*, 4557-4565.
- (39) S.-M. Oh, S.-T. Myung, J. Hassoun, B. Scrosati, Y.-K. Sun, *Electrochem. Commun.* **2012**, *22*, 149-152.
- (40) A. Langrock, Y. Xu, Y. Liu, S. Ehrman, A. Manivannan, C. Wang, *J. Power Sources* **2013**, *223*, 62-67.

## Chapter 6. Summary

This thesis is mainly about on designing new mixed-phosphate electrode materials composed of  $(\text{PO}_4)^{3-}$  and  $(\text{P}_2\text{O}_7)^{4-}$  as well as cost efficient transition metals such as Fe and Mn. The contents are composed of four parts: (i) a new iron-based mixed-phosphate cathodes for Li and Na Rechargeable Batteries, (ii) Understanding the electrochemical mechanism of  $\text{Na}_4\text{Fe}_3(\text{PO}_4)_2(\text{P}_2\text{O}_7)$  in a Na rechargeable battery, (iii) a new 3.8 V-class manganese-based mixed-phosphate electrode with anomalous Jahn-Teller behavior of  $\text{Mn}^{3+}$  and (iv) Highly reversible iron- and manganese-based mixed-phosphate cathodes,  $\text{Na}_4\text{Mn}_x\text{Fe}_{3-x}(\text{PO}_4)_2(\text{P}_2\text{O}_7)$  ( $x = 1, 2$ ), for sodium rechargeable batteries.

In the first part of this dissertation, new mixed-polyanion-based compounds,  $\text{Li}_x\text{Na}_{4-x}\text{Fe}_3(\text{PO}_4)_2(\text{P}_2\text{O}_7)$  ( $x = 0, 3$ ), were firstly proposed as new promising electrodes for Li and Na rechargeable batteries. I showed that the combination of  $(\text{PO}_4)^{3-}$  and  $(\text{P}_2\text{O}_7)^{4-}$  polyanion groups and low cost transition metal of Fe could provide a new crystal framework with a promising electrochemical properties. This research suggests that significant opportunity exists to explore new low-cost, high-performance electrodes in mixed-polyanion materials.

In the second part, structural evolution of  $\text{Na}_{4-x}\text{Fe}_3(\text{PO}_4)_2(\text{P}_2\text{O}_7)$  during charge/discharge was examined by experiments and first-principles calculations. I revealed that the electrode operates *via* a one-phase reaction with a reversible structural

evolution that includes  $P_2O_7$  distortion. Furthermore, the structural stability of partially desodiated phases at high temperature was examined.

The third part demonstrates a new 3.8-V Mn-based mixed-phosphate,  $Na_4Mn_3(PO_4)_2(P_2O_7)$ , with a high  $Mn^{2+}/Mn^{3+}$  redox potential of 3.84 V and energy density of  $416 \text{ Wh kg}^{-1}$ . The high power capability and cycle stability was observed in Na-ion cells, which is attributed to the unique Jahn–Teller distortion of  $Mn^{3+}$  in this material. Also, the multi-phase reaction with a lattice volume change of approximately 7% during the electrochemical cycling was found.

In the final part, I introduced highly reversible  $Na_4Mn_xFe_{3-x}(PO_4)_2(P_2O_7)$  ( $x = 1, 2$ ) electrodes for the first time, and characterized the structure by using ND, XRD and XANES analyses. Among  $Na_4Me_3(PO_4)_2(P_2O_7)$  ( $Me = Fe$  or  $Mn$ ) families, the highest energy density (*i.e.*  $418 \text{ Wh kg}^{-1}$  for  $x = 2$ ) was obtained from  $Na_4Mn_2Fe(PO_4)_2(P_2O_7)$  electrode by utilizing  $Mn^{2+}/Mn^{3+}$  redox couple as well as an upshifting of  $Fe^{2+}/Fe^{3+}$  redox potential in Na-ion cells. Also, I showed that  $Na_4MnFe_2(PO_4)_2(P_2O_7)$  electrode exhibits remarkable rate and cycle performances over 3000 cycles at fast charge/discharge rates on the merit of open framework structure, low volume change ( $\sim 2 \%$ ) with a solid-solution reaction. I believe that the mixed-phosphate compounds,  $Na_4Me_3(PO_4)_2(P_2O_7)$  ( $Me = Fe$  or  $Mn$ ), introduced here could be a strong competitor for large-scale Na-ion battery cathodes based on their high energy density, long-term cycle stability and low element cost of Fe and Mn.

## Abstract in Korean

### 초 록

지구 온난화와 오일 매장량 감소로 인하여 지속 가능한 에너지원에 대한 개발이 많은 관심을 받고 있다. 또한, 계속 증가하고 있는 에너지 수요에 대비하고, 친환경 에너지에 대한 원활한 공급을 위해서 대용량 에너지 저장장치에 대한 개발은 최근 매우 중요한 연구로 떠올랐다. 여러 가지 에너지 저장장치 중에서 소듐이차전지의 경우 높은 가격경쟁력 및 리튬이차전지와 비슷한 chemistry 등의 장점을 기반으로 가장 유망한 차세대 배터리로 각광받고 있으며, 이에 따라, 낮은 가격을 갖는 철 및 망간 기반의 새로운 전극 소재를 찾는 것이 매우 중요하다.

본 연구에서는 최적의 소듐이차전지용 전극 소재를 design 하기 위해서 철 및 망간기반의 복합인산염계 소재에 대한 연구를 진행하였다. 제 2 장에서는 새로운 철 기반의 소재  $\text{Na}_4\text{Fe}_3(\text{PO}_4)_2(\text{P}_2\text{O}_7)$ 에 대한 연구를 다루고 있다. 3 차원 채널을 갖는 신규 전극 소재의 경우 X-선 회절과 중성자 회절 분석을 통해서 분석하였으며, 소듐이온셀에서 3.2 V (vs.  $\text{Na}^+/\text{Na}$ )의 전압과  $320 \text{ Wh kg}^{-1}$ 의 에너지 밀도를 보였다. 또한, 이온교환법을 통해 합성한  $\text{Li}_3\text{NaFe}_3(\text{PO}_4)_2(\text{P}_2\text{O}_7)$  소재의 경우 리튬이온셀에서  $140\text{mAh g}^{-1}$ 의 용량과 3.4 V (vs.  $\text{Li}^+/\text{Li}$ )의 전압을 보였다. 이 연구의 경우  $(\text{PO}_4)^{3-}$ 와  $(\text{P}_2\text{O}_7)^{4-}$  조합을 통해 새로운 열린 구조의 전극 소재를 디자인 할 수 있다는 점에 그 의의가 있다.

제 3 장에서는  $\text{Na}_x\text{Fe}_3(\text{PO}_4)_2(\text{P}_2\text{O}_7)$  ( $1 \leq x \leq 4$ ) 소재에 대한 전기화학 분석에 대한 내용을 다루고 있다. 위 소재에 대한 분석의 경우 실험과 제일계산이 동시에 이용되었다.  $\text{Na}_x\text{Fe}_3(\text{PO}_4)_2(\text{P}_2\text{O}_7)$  전극이 철의 산화환원반응과 one-phase 반응을 통해 소듐이 삽입/탈리 됨을 확인하였으며, 부피팽창이 충/방전 동안 4% 이내임을 확인하였다. 이러한 낮은 부피 변화는 소재의 열린 구조와 구조내  $\text{P}_2\text{O}_7$  의 거동에 기인한다. 비록 충전 마지막 과정에서 낮은 Na kinetic 으로 인해 이론용량의 82% 밖에 소듐이 활용되지 않았으나, 높은 파워밀도가 C/20 부터 C/5 까지 확인되었다. 또한, 20 사이클까지 안정적인 거동을 보였다. 추가적으로, *In situ* X-선 회절분석과 DSC 분석을 통해서 모든 충전상인  $\text{Na}_x\text{Fe}_3(\text{PO}_4)_2(\text{P}_2\text{O}_7)$  ( $1 \leq x \leq 4$ ) 에서 530 도까지 안정함을 확인 하였다. 이러한 충/방전 거동에 대한 구조 분석은 향후 위 소재의 최적화 방향을 제시 할 수 있을 것으로 예상된다.

제 4 장에서는 새로운 3.8 V 기반의 소듐이차전지용 망간 복합인산염계 양극 소재  $\text{Na}_4\text{Mn}_3(\text{PO}_4)_2(\text{P}_2\text{O}_7)$  에 대한 연구를 소개 하였다. 위 전극의 경우 소듐이온셀에서 매우 가역적인 전기화학 특성을 보였으며, 3.84 V 의 전압 (vs.  $\text{Na}^+/\text{Na}$ ) 과  $416 \text{ Wh kg}^{-1}$  의 높은 에너지 밀도를 보였다. 또한, *Ex situ* X-선 회절 및 산란 분석을 통해서 위 소재가 다상 반응을 통해 작동함을 확인하였다. 망간 3 개의 안-텔러 거동으로 인해 충/방전 동안 ~7 % 의 높은 부피변화를 보였으나, 충전 후 Na 이온의 이동성은 오히려 증가하는 현상을 보였다. 이는 구조내의 소듐 채널을 여는 특별한 안-텔러 거동에 의한 것으로 확인 되었다. 이러한 구조적 현상을 통해 위 소재는 소듐이온셀에서 높은 파워 특성과 사이클 안정성을 보였다. 망간기반의 새로운 복합인산염계 소재는 높은 전압,

에너지 밀도 등을 기반으로 매우 우수한 소듐이차전지용 양극 소재가 될 것으로 기대한다.

제 2-3 장에서 소개한 철과 망간 기반 소재의 경우 소듐이온셀에서 우수한 전기화학 특성을 보였으나  $\text{Na}_4\text{Fe}_3(\text{PO}_4)_2(\text{P}_2\text{O}_7)$  소재의 경우 낮은 에너지 밀도를 보였으며,  $\text{Na}_4\text{Mn}_3(\text{PO}_4)_2(\text{P}_2\text{O}_7)$  소재의 경우 다상 반응에 의한 충/방전 동안 큰 부피변화를 보였다. 이러한 특성으로 인해서 위 소재들을 대용량에너지 저장장치에 적용하기에는 그 한계가 있으며, 이를 해결하기 위한 노력으로써 제 5 장에서는 Fe-Mn 기반의  $\text{Na}_4\text{Mn}_x\text{Fe}_{3-x}(\text{PO}_4)_2(\text{P}_2\text{O}_7)$  ( $x = 1, 2$ ) 소재에 대해서 최초로 소개하고자 한다. 전기화학 분석을 통해서 구조 내 망간 함량 증가에 따른 에너지 밀도 증가를 확인하였으며, 이는  $\text{Mn}^{2+}/\text{Mn}^{3+}$  산화환원전위의 부분 증가와  $\text{Fe}^{2+}/\text{Fe}^{3+}$  전압 향상에 의한 것을 확인하였다. Ex situ 구조 분석을 통해서 위 소재들이 one-phase 반응을 통해 작동함을 확인하였으며,  $\text{Na}_4\text{MnFe}_2(\text{PO}_4)(\text{P}_2\text{O}_7)$  소재의 경우 충/방전 동안 2.07 % 의 매우 낮은 부피변화를 보임을 확인하였다. 열린 구조와 낮은 부피변화의 장점을 통해서 50% 이상의 이론용량이 20C 에서 발현되었으며, 1C 에서 3000 사이클 이상의 안정적인 사이클을 보였다. 위 소재들의 경우 낮은 가격, 높은 에너지 밀도, 안정적인 사이클 특성 등을 기반으로 대용량 에너지 저장장치용 양극 소재로서 큰 가치가 있을 것으로 기대된다.

**주요어:** 에너지 저장장치, 소듐이온전지, 높은 가격경쟁력, 양극 소재, 복합인산염계 소재

**학번 :** 2012-30917